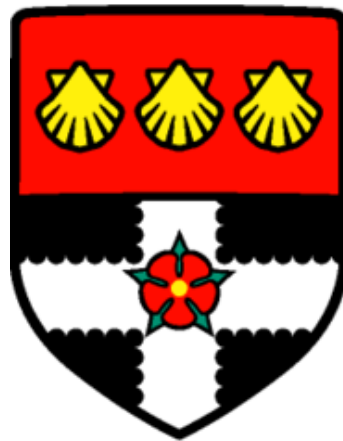


Exploring the Dynamics of Summer-time Arctic Cyclones and Sea Ice Interaction



Hannah Croad

Department of Meteorology

University of Reading

A thesis presented for the degree of

Doctor of Philosophy

June 2024



Declaration

I confirm that this is my own work and the use of all material from other sources has been properly and fully acknowledged.

Hannah Croad

Abstract

Arctic cyclones pose the major weather hazard to the increasing human activity in the summer-time Arctic, producing strong winds that can have large impacts on the depleting sea ice cover. Whilst the dynamics of mid-latitude cyclones have been studied for decades, summer-time Arctic cyclones have received less attention. This thesis advances our understanding of summer-time Arctic cyclone dynamics and their interaction with sea ice.

In this work cyclone evolution in the summer-time Arctic is split into two classes. A climatological analysis demonstrates that $\sim 65\%$ of cyclones have a low-level-dominant (LLD) vorticity structure during growth, whilst the remaining $\sim 35\%$ have an upper-level-dominant (ULD) vorticity structure and commonly develop with axisymmetric vortices on the tropopause. These two subsets of cyclones have different characteristics, and hence, this work represents a starting point for developing conceptual models in the future. However, regardless of structure during growth, summer-time Arctic cyclones tend to transition to a persistent columnar vortex structure after maturity, unlike mid-latitude cyclones.

The fundamental mechanisms by which friction and sensible heat fluxes over sea ice impact summer-time Arctic cyclones are diagnosed using a potential vorticity framework, with frictional processes identified as having different effects on the dynamics of LLD and ULD cyclones. The results indicate that the columnar vortex structure of mature summer-time Arctic cyclones with friction may be dynamically unstable, and an idealised quasi-geostrophic model is used to characterise this instability. Finally, the sensitivity of summer-time Arctic forecasts to sea ice coupling representation in a numerical weather prediction model is examined. It is found that cyclones have a large impact on sea ice, but

that cyclone forecasts are largely insensitive to sea ice coupling choice.

This thesis provides novel insights into summer-time Arctic cyclones, with regards to their atmospheric dynamics and interaction with sea ice, providing a platform for further research.

Acknowledgements

Firstly, a massive thank you to my all-star supervisory team of John Methven, Ben Harvey, Sarah Keeley, and Ambrogio Volonté, whose guidance over the past 4 years have made this work possible. It cannot be overstated how much I have appreciated your input of ideas and time, technical support, feedback, and encouragement throughout the project. I have really valued the different expertise and perspectives that you have each brought to the project, and I have learnt so much from all of you.

Being part of the wider Arctic Summer-time Cyclones community has also been incredibly beneficial for my scientific development and understanding of the world of academia. In particular, thank you to Sue Gray, Ian Renfrew, Steven Cavallo, and Dave Parsons for the interesting discussions and advice. I would also like to thank my monitoring committee members, Len Shaffrey and Nigel Arnell, for always encouraging me to see the bigger picture with my work and keeping me on track.

The Department of Meteorology has been an incredibly friendly and supportive environment in which to work towards my PhD. In particular, thank you to SCENARIO cohort 7: Alanna, Blair, Brian, Charlie, Harriet, Helen, Isabel, and Natalie. I feel very lucky to have completed my PhD alongside such a wonderful group of like-minded people. Isabel and Charlie, through the stress of undergraduate exams, a year abroad in Oklahoma, and the PhD journey, our friendship over the past 8 years has been so important to me. Thanks also to my running buddies, Brian, my half marathon training partner, and Harriet, my vegetable/pumpkin relay co-organiser. More generally, thank you to the PhD students in the department for being such a lovely, supportive group of people, and of course for all the fun and silliness.

To my Mum and Dad, Sarah and Andrew, thank you for all of your support and understanding despite my being at university for so long, and for always being there to pick up the pieces when it all gets a bit much. Thanks also to my brother Adam, my sister Chloe, and my Nan Tina, for making my visits home so fun and fulfilling. To the best group of friends that anyone could ask for, Isabel, Eleanor, and Rebecca, thanks for all of the laughs and craziness, and for always being the best distractions from work!

Finally, thank you to Lewis, for being a constant source of laughter and happiness, for always being the voice of calm and reason during difficult times, and for your love and support over the years.

Authorship of papers

This thesis is structured around four papers. The first, second and fourth papers have been published, whilst the third is in draft format. The content of the papers presented here is largely unchanged from the published manuscripts (with only a few minor additions made in the preparation of this thesis). The estimated percentage contribution of the candidate (HLC) is provided below, along with a description of the specific contributions from each of the co-authors:

1. **Croad, H. L.**, J. Methven, B. Harvey, S. P. E. Keeley, and A. Volonté (2023): The role of boundary layer processes in summer-time Arctic cyclones. *Weather and Climate Dynamics*, **4 (3)**, 617-638, <https://doi.org/10.5194/wcd-4-617-2023>.

Estimated contribution: 80%. HLC designed the study and conducted the analysis detailed in this paper, with supervision from JM, BH, SPEK, and AV. SPEK set up the ECMWF IFS model configurations which were run by HLC. HLC took responsibility to write this paper, with feedback from JM, BH, SPEK, and AV. Three anonymous reviewers provided comments on an earlier version of the manuscript.

2. **Croad, H. L.**, J. Methven, B. Harvey, S. P. E. Keeley, A. Volonté, and K. I. Hodges (2023): A climatology of summer-time Arctic cyclones using a modified phase space. *Geophysical Research Letters*, **50 (22)**, e2023GL105993, <https://doi.org/10.1029/2023GL105993>.

Estimated contribution: 80%. The study was conceptualised by HLC with input from JM, BH and AV. HLC developed the methodology and performed the formal analysis (using reanalysis data curated by AV and cyclone tracks provided by KH)

with supervision from JM, BH, SPEK, and AV. HLC took responsibility to write this paper, with feedback from JM, BH, SPEK, AV and KH. Two anonymous reviewers provided comments on an earlier version of the manuscript.

3. **Croad, H. L.**, B. Harvey, and J. Methven: The stability of axisymmetric vortex columns with friction and relevance to summer-time Arctic cyclones. In prep. for *Journal of the Atmospheric Sciences*.

Estimated contribution: 70%. BH conceptualised the study (with input from HLC and JM), formulated the linear stability analysis, and provided the quasi-geostrophic model. HLC developed the methodology and performed the formal analysis and model runs with supervision from BH and JM. HLC took responsibility to write this paper, with feedback from BH and JM.

4. **Croad, H. L.**, S. P. E. Keeley, J. Methven, B. Harvey, and A. Volonté (2025): Examining the sensitivity of ECMWF IFS weather forecasts to sea-ice coupling for the summer-time Arctic and cyclones. *Quarterly Journal of the Royal Meteorological Society*, **151(766)**, e4899, <https://doi.org/10.1002/qj.4899>.

Estimated contribution: 80%. The study was conceptualised by HLC, SPEK and JM. SPEK set up the ECMWF IFS model configurations which were run by HLC. HLC developed the methodology and performed the formal analysis with supervision from SPEK, JM, BH, and AV. HLC took responsibility to write this paper with feedback from SPEK, JM, BH, and AV. Two anonymous reviewers provided comments on an earlier version of the manuscript.

Contents

Declaration	iii
Abstract	v
Acknowledgements	vii
Authorship of papers	ix
Contents	xi
1 Motivation	1
1.1 The Arctic: an environment undergoing rapid change	1
1.2 An emerging focus on Arctic weather forecasting	4
1.3 Summer-time Arctic cyclones	6
1.4 Aims of the thesis	9
1.5 Structure of the thesis	10
2 Background theory and literature review	13
2.1 Extratropical atmospheric dynamics	13
2.1.1 Atmospheric balance	13
2.1.2 Potential vorticity	14
2.1.3 Baroclinic instability	16
2.1.4 Polar vs. mid-latitude regions	18
2.2 Extratropical cyclones	19
2.2.1 Cyclone structure in cyclone phase space	20
2.2.2 Other approaches to cyclone classification	22

2.2.3	Summer-time Arctic cyclones	24
2.3	The impact of the surface on extratropical cyclones	29
2.3.1	The boundary layer	29
2.3.2	Boundary layer processes in extratropical cyclones	29
2.4	Sea ice	33
2.4.1	The boundary layer over sea ice	33
2.4.2	Sea ice in numerical weather prediction	34
2.4.3	Cyclone-sea ice interactions	35
3	The role of boundary layer processes in summer-time Arctic cyclones	39
3.1	Introduction	40
3.2	Methodology	46
3.2.1	Reanalysis data	46
3.2.2	IFS model runs	47
3.2.3	Arctic cyclone tracking	47
3.2.4	A modified cyclone phase space	47
3.2.5	PV framework	49
3.2.6	Depth-integrated PV budget	52
3.3	Arctic cyclone case studies	54
3.4	Results	60
3.4.1	Boundary Layer PV tendencies	60
3.4.2	Cyclone depth-integrated PV budget	62
3.4.3	Cyclone structural evolution	67
3.5	Discussion	71
3.6	Conclusions	74
4	A climatology of summer-time Arctic cyclones using a modified phase space	79
4.1	Introduction	80
4.2	Methodology	82
4.2.1	Reanalysis data	82
4.2.2	Arctic cyclone tracking	82
4.2.3	A modified cyclone phase space	83

4.3	Results	85
4.3.1	Cyclone structure and evolution	85
4.3.2	Cyclone characteristics	89
4.3.3	Extreme cyclones	90
4.4	Conclusions	92
5	The stability of axisymmetric vortex columns with friction and relevance to summer-time Arctic cyclones	95
5.1	Introduction	96
5.2	Methodology	100
5.2.1	The two-layer QG model	100
5.2.2	Numerical integration of the two-layer QG model	101
5.2.3	Reanalysis data	102
5.3	Key physical parameters and scales	102
5.4	Linear stability analysis	105
5.4.1	Defining the basic state	105
5.4.2	Characterising the instability of the basic state	108
5.5	Non-linear numerical simulation results	110
5.5.1	Comparison with the linear stability analysis	110
5.5.2	Earlier stages in cyclone lifecycle	115
5.6	Discussion	117
5.7	Conclusions	120
6	Examining the sensitivity of ECMWF IFS weather forecasts to sea ice coupling for the summer-time Arctic and cyclones	125
6.1	Introduction	126
6.2	Methodology	130
6.2.1	Experiments	130
6.2.2	Evaluation	133
6.2.3	Cyclone tracks	133
6.3	Results	134
6.3.1	Forecasts of sea ice	134

6.3.2	Forecasts of the atmospheric boundary layer	138
6.3.3	Forecasts of Arctic cyclones	149
6.4	Conclusions	152
7	Conclusions	157
7.1	Summary and Discussion	157
7.2	Implications and future work	162
A	Appendix to Chapter 5: Linear stability analysis	167
A.1	Adding a perturbation	167
A.2	Time evolution of the perturbation without friction	169
A.3	Time evolution of the perturbation with friction	171
	References	173

Chapter 1

Motivation

1.1 The Arctic: an environment undergoing rapid change

The Arctic is a fragile environment unlike any other on Earth. The Arctic, commonly defined as those regions north of the Arctic circle at $66^{\circ} 33'$ N or north of the climatological July 10°C isotherm (Arctic Portal, 2024), comprises the Arctic Ocean basin surrounded by the northern landmasses of Scandinavia, Russia, the United States, Canada and Greenland. Large portions of the ocean surface are covered by sea ice, whilst the surrounding land is partially covered by glaciers and ice sheets, and is underlain by permafrost (Figure 1.1). The Arctic is an environment of extreme cold, seasonality, and weather, conducive to a unique ecosystem that has adapted to the harsh conditions (Barry et al., 2013).

At the same time, the Arctic region is one the most rapidly changing environments in the world, driven primarily by increasing temperatures as a result of anthropogenic climate change. Since the 1970s the Arctic has warmed nearly four times faster than the global average in a process called Arctic Amplification (Chylek et al., 2022; Rantanen et al., 2022). The most visible sign of global warming and climate change in the Arctic is the dramatic decline in sea ice, especially in summer (see Figure 1.1). Total sea ice extent has shown a declining trend through all months, with the largest trend in September (Meier et al., 2014). September Arctic sea ice extent during 1979–2023 has shown an average decline of 12.2% per decade (National Snow and Ice Data Center, 2023; Figure 1.2). The increasing temperatures are also contributing to the melting of Arctic land ice, contributing to global sea level rise (Aschwanden et al., 2019; Box et al., 2018), and the thawing

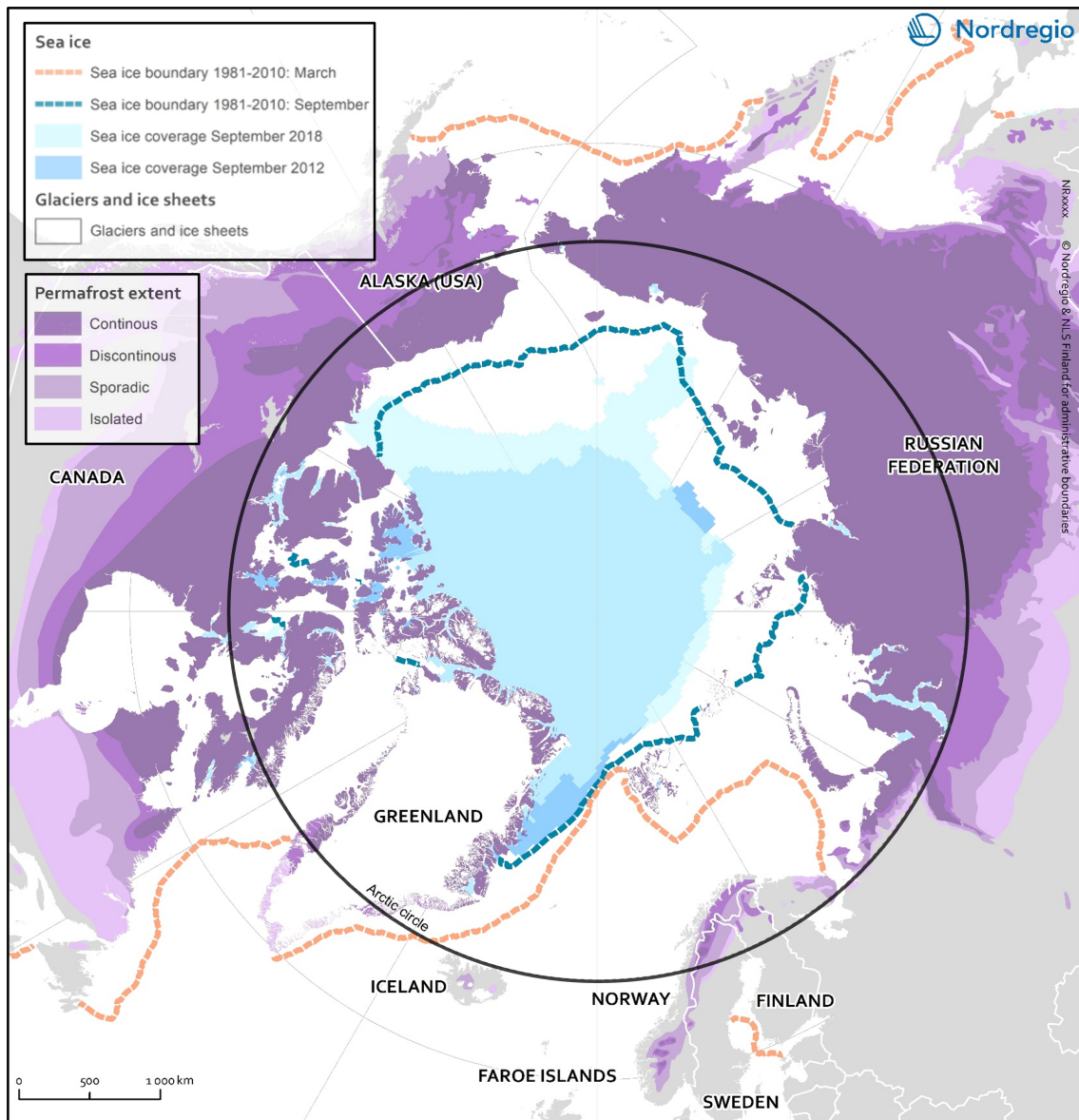


Figure 1.1: Map of the Arctic region (with the Arctic circle marked by the bold solid black line) and the main components of the cryosphere: sea ice, glaciers and ice sheets, and permafrost. Adapted from Nordregio (2019) at <https://nordregio.org/maps/components-of-the-cryosphere-in-the-arctic/>, designed by Eeva Turunen using permafrost and ground-ice data (Brown et al., 2002) and sea ice data (U.S. National Ice Center et al., 2010) from National Snow and Ice Data Center.

of permafrost which is associated with the further release of greenhouse gases due to the microbial breakdown of previously frozen organic carbon (Schuur et al., 2015).

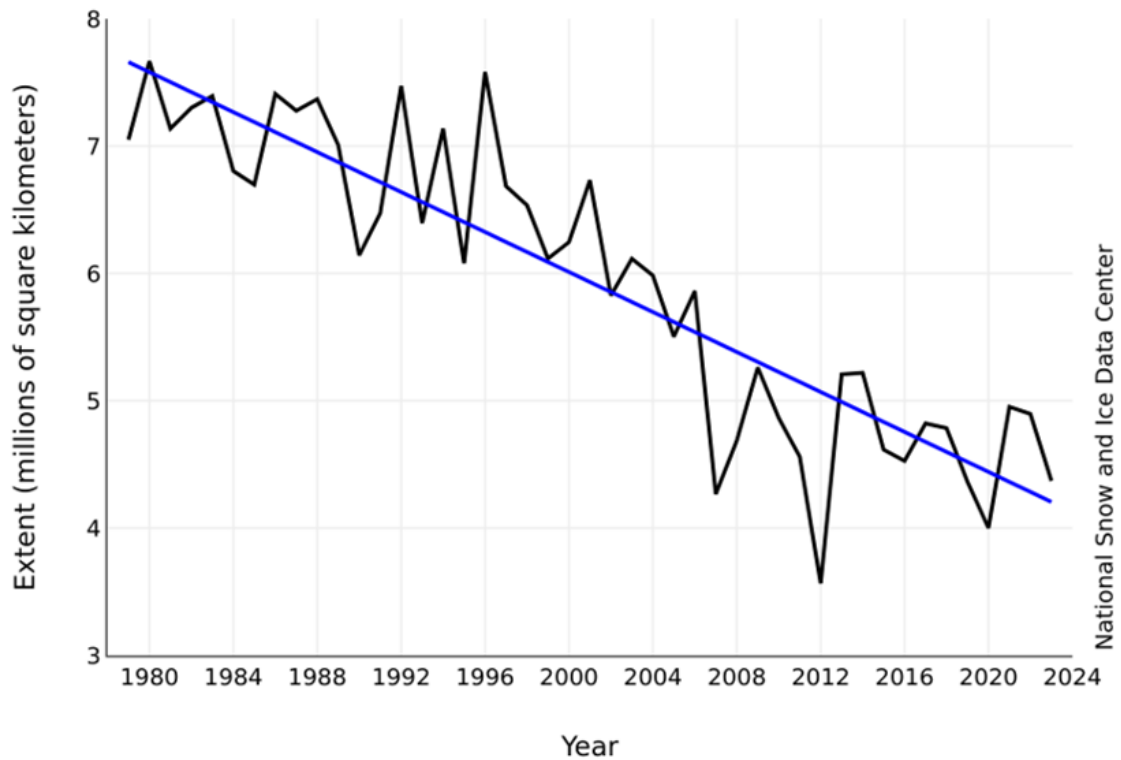


Figure 1.2: Average September Arctic sea ice extent during 1979–2023 (black line) with linear trend (blue line) overlaid showing a decline of 12.2% per decade relative to the 1981–2010 average. Image courtesy of the National Snow and Ice Data Center (2023) at <https://nsidc.org/sea-ice-today/analyses/sun-sets-arctic-melt-season>.

Climate-induced changes in Arctic terrestrial, ocean and sea ice environments are threatening existing ecosystems (e.g. Barry et al., 2013), for example, polar bear populations are exhibiting range contraction and decline (Bromaghin et al., 2015; Laidre et al., 2018). The changing Arctic environment directly impacts human activity (e.g. Jaskólski, 2021), with permafrost thaw and accelerated coastal erosion (due to reduced sea ice and increased exposure to storm waves) threatening existing infrastructure (e.g. Isaev et al., 2019; Karjalainen et al., 2019; Nicu et al., 2020). These abrupt environmental changes hinder the hunting opportunities of indigenous communities (e.g. Hauser et al., 2021) and threatens their way of life (Irrgang et al., 2019; Jaskólski, 2021).

1.2 An emerging focus on Arctic weather forecasting

The transformation of the Arctic environment is destabilising to the existing ecosystems, whilst also offering new economic potential. The loss of sea ice increases the accessibility of the Arctic, especially in summer, opening up opportunities for resource extraction, shipping and tourism (Andrew, 2014; Stephenson et al., 2011). The Arctic is abundant in natural resources, with geological assessments estimating that $\sim 30\%$ and $\sim 13\%$ of the Earth's undiscovered natural gas and oil respectively are present in the Arctic circle (Bird et al., 2008; Gautier et al., 2009). Reductions in sea ice extent and thickness permit increased maritime activities, with increasing interest in transit shipping via the Northern Sea Route and Northwest Passage during the summer (Arctic Council, 2009). These routes offer considerable reductions in distance between European and Pacific ports compared to traditional shipping routes via the Suez and Panama Canals (Figure 1.3), and will become an increasingly viable option for non-specialised open water vessels as sea ice continues to decline in the coming decades (Melia et al., 2016).

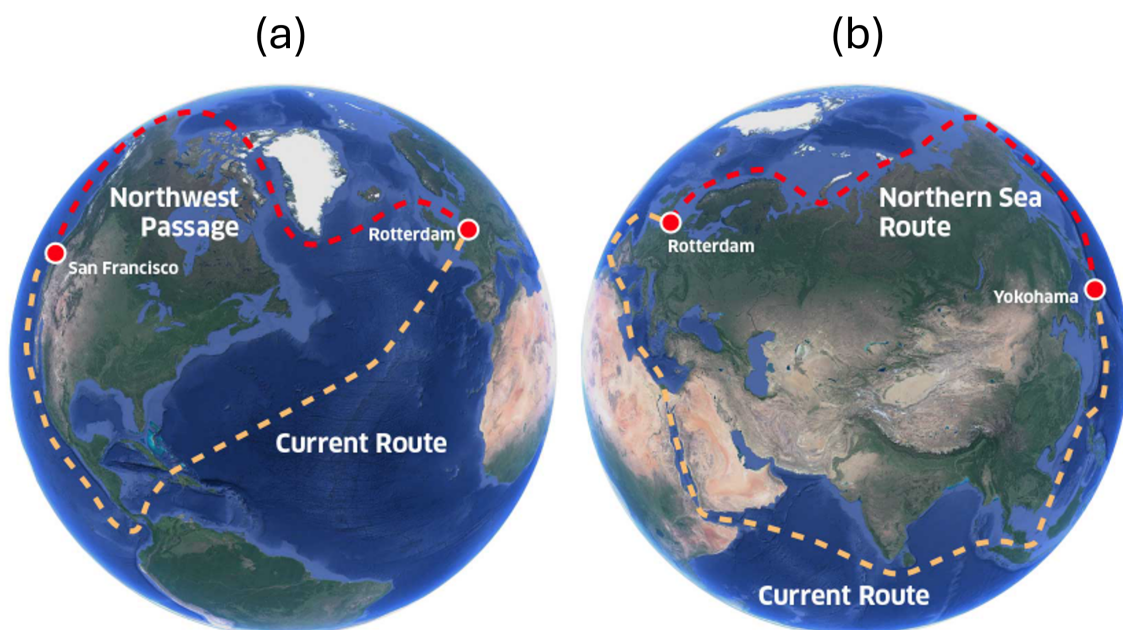


Figure 1.3: Arctic shipping routes: (a) The Northwest Passage and (b) The Northern Sea Route (red dashed lines) compared to traditional routes via the Panama and Suez Canals respectively (yellow dashed lines). Image produced by discoveringthearctic.org at <https://discoveringthearctic.org.uk/arctic-challenges/troubled-water/northwest-northeast-passages/>.

As human activity increases in the Arctic, it is going to be increasingly exposed to the hazards of the Arctic environment. For example, in November 2021 more than 20 ships became stranded in thick ice along the eastern part of the Northern Sea Route after earlier than expected freeze-up and challenging sea ice conditions associated with strong winds of up to 30 m s^{-1} took shippers by surprise (High North News, 2021; The Barents Observer, 2021). Operations in the Arctic require detailed information about the spatial distribution of sea ice. Although 2007 had the third lowest pan-Arctic sea ice extent on record at the time of writing, throughout the summer the Northern Sea Route was blocked by sea ice, illustrating that reduced total Arctic sea ice extent does not guarantee open shipping routes (Melia et al., 2016). These examples demonstrate the need for accurate forecasts of weather and sea ice for supporting operations in the Arctic.

Indeed, in recent years there has been increased focus on weather in the polar regions, which have previously received less attention than tropical and mid-latitude regions (e.g. Jung et al., 2013). Numerical weather prediction (NWP) in the Arctic is more challenging than lower latitude regions due to the relative scarcity of in-situ observations (e.g. Naakka et al., 2019) and difficulties assimilating satellite data over snow and sea ice (Lawrence et al., 2019) to constraint forecast initial conditions. Recently in NWP there has been an advance towards Earth system models with coupled atmosphere, ocean and sea ice (e.g. Keeley and Mogensen, 2018; Smith et al., 2018), which has the potential to improve Arctic forecasts where these three Earth system components intersect. Improved predictions of Arctic weather are not just beneficial for supporting human activity in the Arctic, but also for improving mid-latitude forecasts due to linkages in the weather in the two regions (e.g. Jung et al., 2014; Lawrence et al., 2019). Jung and Matsueda (2016) assessed the forecast skill of nine different global NWP systems in the Arctic, and found that forecast skill for 500 hPa geopotential height and 2 m temperature was comparable to mid-latitudes, but more variable, and that analysis uncertainty was larger in the Arctic. The performance of NWP forecasts for individual weather events in the Arctic, which is of greater interest to end users (especially in summer when the Arctic is most accessible to human activity), has received less attention.

1.3 Summer-time Arctic cyclones

Arctic cyclones are the dominant weather hazard in the Arctic. Arctic cyclones are synoptic-scale low pressure systems in the Arctic that can be generated locally, or originate in the mid-latitudes before moving poleward into the Arctic. These systems produce some of the most impactful Arctic weather, with extreme surface winds and ocean waves (Thomson and Rogers, 2014; Waseda et al., 2018, 2021) that can have large impacts on sea ice (Asplin et al., 2012; Lukovich et al., 2021; Peng et al., 2021). Figure 1.4 indicates the presence of an Arctic cyclone in the East Siberian Sea in early November 2021, which was likely responsible for the strong winds and rapidly changing sea ice conditions that trapped ships on the Northern Sea Route at this time (High North News, 2021; The Barents Observer, 2021).

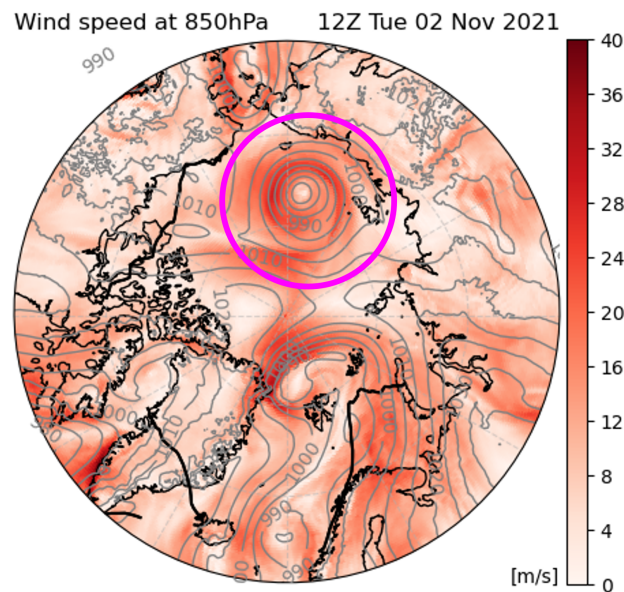


Figure 1.4: Map of 850 hPa wind speed (shading) and mean sea level pressure (grey contours) at 12Z 02 November 2021, with the magenta circle highlighting an Arctic cyclone. Plot produced by Ben Harvey from ECMWF operational analysis.

The focus of this thesis is Arctic cyclones that occur during the summer, when the Arctic is most accessible to human activity. In this thesis summer is defined as May-September, capturing the main period of sea ice melt in the Arctic. Case studies of extreme cyclones have indicated that summer-time Arctic cyclones can be extremely long-lived and have

a different lifecycle to mid-latitude cyclones (Aizawa and Tanaka, 2016; Simmonds and Rudeva, 2012; Tanaka et al., 2012; Tao et al., 2017; Yamagami et al., 2017). The best known example is the Great Arctic cyclone of 2012 (henceforth C12), due to it being the strongest August Arctic cyclone on record and its long lifetime of almost 13 days (Simmonds and Rudeva, 2012). C12 was also noteworthy due to its large size (Figure 1.5), and the fact that it achieved a long-lived axisymmetric vortex structure after maturity (Aizawa and Tanaka, 2016). This structure has also been identified in other extreme summer-time Arctic cyclones (e.g. Vessey et al., 2022), and is a striking contrast to mid-latitude cyclones which have a tilted asymmetric structure and dissipate quickly after maturity. However, it is not clear how typical these cases are, and whether there are different varieties of cyclone evolutions in the summer-time Arctic. While different varieties of cyclone evolution in the mid-latitudes are relatively well understood (e.g. Bjerknes, 1919; Shapiro and Keyser, 1990), conceptual models for Arctic cyclones have yet to be established. Previous literature on summer-time Arctic cyclones has been mostly constrained to case studies and has been descriptive in nature, with less focus on the atmospheric dynamics of these systems. In particular, our understanding of the axisymmetric vortex phase of summer-time Arctic cyclones is lacking.

The interaction between Arctic cyclones and sea ice is an important consideration in summer, when the ice extent and thickness is reduced. The record-low sea ice extent in 2012 was shown to be exacerbated by C12, due to enhanced ice melt associated with increased ocean heat transport and strong winds (Zhang et al., 2013). As ice cover continues to thin it will become increasingly vulnerable to the impacts of cyclone activity. Changing sea ice cover also impacts the overlying atmosphere, which will likely feed back on the development of Arctic cyclones. For example, a reduction in sea ice extent means that more of the ocean surface is exposed, associated with an increase in heat transfer from the surface to the atmosphere and potentially increased energy for Arctic cyclones in summer (Simmonds and Keay, 2009). In addition, as the climate warms, the summer-time Arctic is becoming increasingly dominated by the marginal ice zone (MIZ; Rolph et al., 2020; Strong and Rigor, 2013), a band of fragmented ice floes separating the ice-free ocean and the main ice pack (Figure 1.6). Sea ice in the MIZ is thinner, more mobile, and rougher

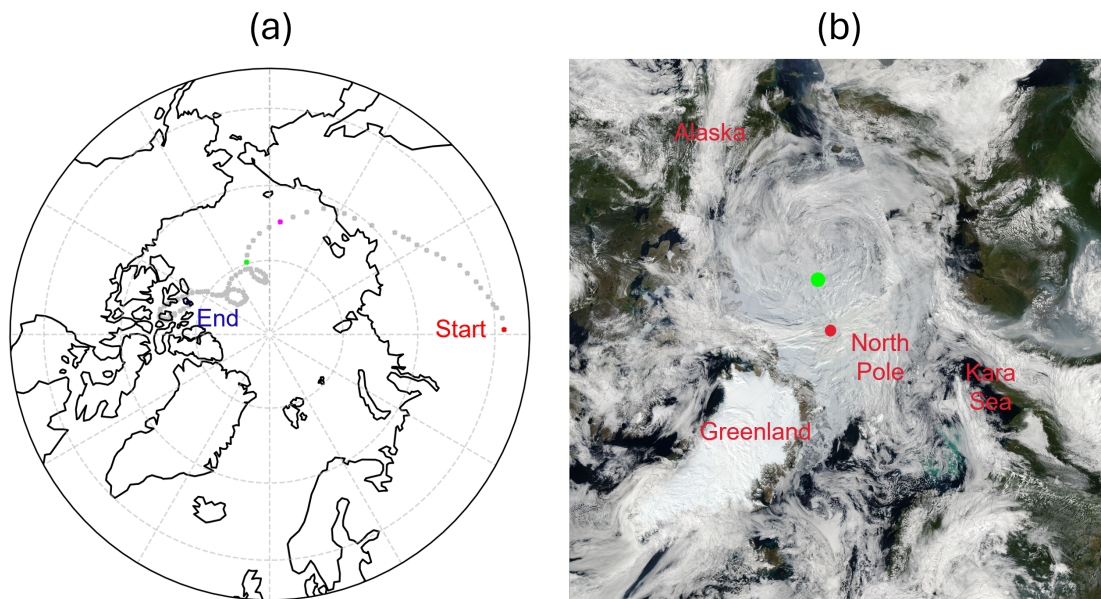


Figure 1.5: (a) The 3-hourly track positions of C12 (grey dots) during 09Z 2 August - 03Z 15 August 2012 from the TRACK algorithm (Hodges, 1995). The red and blue dots mark the start and end time respectively, whilst the magenta and green dots mark the time of maximum growth rate and maximum intensity respectively. (b) Satellite image on 6 August 2012 when the cyclone was at its maximum intensity. Image by Jeff Schmaltz, LANCE/EOSDIS Rapid Response (courtesy of NASA Earth Observatory, <https://earthobservatory.nasa.gov/images/78812/2012-arctic-cyclone>). Geographical references overlaid in red, and the approximate cyclone center marked by the green dot, were added by Hannah Croad.

than pack ice, such that interactions with atmospheric weather systems like Arctic cyclones may be enhanced in summer. However, the mechanisms by which the surface impacts cyclone evolution in the Arctic are not well understood at present.

That our understanding of the physical mechanisms acting in Arctic cyclones is incomplete is epitomised by the fact that the forecast skill of Arctic cyclones is lower than that of mid-latitude cyclones in the Northern Hemisphere (Capute and Torn, 2021; Yamagami et al., 2018a). Yamagami et al. (2018a) found that the forecast skill for 10 “extraordinary” summer-time Arctic cyclones was lower than that of mid-latitude cyclones in the Northern Hemisphere across 5 different forecasting systems. For example, a 500 km position error of summer-time Arctic cyclones was found at 3.5–5 days (Yamagami et al., 2018a), compared to 5–6 days for Northern Hemisphere mid-latitude cyclones (Froude, 2010), although this is more similar to Southern Hemisphere mid-latitude cyclones (Froude, 2011). Yamagami et al. (2018b) examined the predictability of C12 in detail, showing that ac-



Figure 1.6: The marginal ice zone at 50 ft. Photo taken by Ian Renfrew onboard the research aircraft during the Arctic Summer-time Cyclones field campaign (Flight 364 on 30 July 2022).

curate forecasts of the position and intensity were not available until 2–3 days before it reached maximum intensity, and that the best forecasts were produced by the ensemble members that captured the upper-level vortex dynamics. The relative sparsity of the observation network and consequent larger uncertainty in initial conditions are likely one of the reasons for the lower forecast skill. However, the case of C12 illustrates that certain synoptic situations in the summer-time Arctic can also limit predictability, and demonstrates the need for improved understanding of the mechanisms that determine Arctic cyclone dynamics. It might be expected that recent progress in developing coupled NWP systems would improve weather forecasts of Arctic cyclones, due to the capability to represent complex interactions between the atmosphere, ocean and sea ice. However, this is yet to be examined or established.

1.4 Aims of the thesis

As motivated in the previous section, there are many gaps in our knowledge of the physical mechanisms acting in summer-time Arctic cyclones, with regards to their atmospheric dynamics and their interaction with sea ice. Furthermore, the impact of coupled atmosphere-ocean-sea ice in NWP models on forecasts of summer-time Arctic cyclones has not yet

been assessed. On these matters, the thesis addresses the following key questions (KQs):

1. What is the variability in the occurrence of summer-time Arctic cyclones, and can they be categorized into classes with distinct structural evolutions and characteristics?
2. By what mechanisms does the surface impact summer-time Arctic cyclone evolution?
3. Which physical parameters determine the dynamics and stability of summer-time Arctic cyclones during their axisymmetric columnar vortex phase, and what is the impact of surface processes?
4. How does sea ice coupling representation impact weather forecasts of summer-time Arctic cyclones in NWP?

KQs 1–3 deal with the dynamics of summer-time Arctic cyclones, whilst KQ 4 concerns their representation in NWP models. Each of these KQs broadly corresponds to a work chapter in the main body of the text (Chapters 3–6), although there is some overlap (see details below). More specific research questions are posed in each of the work chapters.

1.5 Structure of the thesis

Prerequisite background theory and literature underpinning the main scientific results of the thesis are presented in Chapter 2. The four chapters comprising the main body of this thesis are re-formatted papers (Chapters 3–6), with further specific literature reviewed at the start of each of these work chapters. To ensure the papers can stand alone, some introductory material from Chapter 2 is repeated in the work chapters, though efforts have been made to minimize this repetition.

In Chapter 3 (“The role of boundary layer processes in summer-time Arctic cyclones”, published in *Weather and Climate Dynamics* in July 2023), the fundamental frictional and thermodynamic mechanisms by which the surface impacts the evolution of summer-time Arctic cyclones are examined, focusing on two cases from summer 2020. The two

case studies have contrasting development, with one being low-level dominant (LLD) in terms of vorticity structure, and the other being upper-level dominant (ULD). This chapter predominantly focuses on answering KQ2, but is presented first as the method and terminology used in Chapter 4 are first introduced here (thereby also touching on KQ1).

Answering KQ1 is the main focus of Chapter 4 (“A climatology of summer-time Arctic cyclones using a modified phase space”, published in *Geophysical Research Letters* in November 2023). In this chapter a climatology of the structure of summer-time Arctic cyclones is performed from 1979–2021, building on Chapter 3 by formalising the LLD or ULD development classification for summer-time Arctic cyclones and investigating the characteristic cyclone behaviour of the two groups.

The results from Chapters 3 and 4 indicate that the axisymmetric columnar vortex structure of mature summer-time Arctic cyclones with friction may be dynamically unstable. The focus of Chapter 5 (“The stability of axisymmetric vortex columns with friction and relevance to summer-time Arctic cyclones”, a paper in draft format that will be submitted to *Journal of the Atmospheric Sciences* after some further analysis) is to quantify the instability of this vortex setup with friction using an idealised model, and then relate the results to the real world (answering KQ3).

In Chapter 6 (“Examining the sensitivity of ECMWF IFS weather forecasts to sea ice coupling for the summer-time Arctic and cyclones”, published in *Quarterly Journal of the Royal Meteorological Society* in January 2025), the impact of sea ice coupling representation in an operational NWP model on forecasts of summer-time Arctic cyclones during a summer period in 2020 are examined, thereby answering KQ4.

A summary and discussion of the main findings of the four work chapters follows in Chapter 7. Suggestions for future work arising from this thesis are also provided.

Chapter 2

Background theory and literature review

2.1 Extratropical atmospheric dynamics

In order to discuss the dynamics of extratropical cyclones, it is useful to first introduce the concepts of atmospheric balance, potential vorticity (PV) and baroclinic instability. Differences between the atmospheric dynamics of mid-latitude and polar regions are also discussed.

2.1.1 Atmospheric balance

The fundamentals of large-scale atmospheric balance have been covered in many meteorological textbooks (e.g. Hoskins and James, 2014; Vallis, 2017), but the basic concepts are stated here for completeness. In the extratropics, large-scale motions are close to geostrophic and hydrostatic balance. These balances can be written in terms of a geostrophic streamfunction (which is related to perturbations in pressure), ψ_g :

$$u_g = -\frac{\partial\psi_g}{\partial y}, \quad v_g = \frac{\partial\psi_g}{\partial x}, \quad b' = f_0\frac{\partial\psi_g}{\partial z} \quad (2.1)$$

where (u_g, v_g) is the geostrophic wind, $b' = g\frac{\theta'}{\theta_0}$ is the buoyancy (θ is potential temperature, θ' is the horizontal potential temperature anomaly from a reference value θ_0 , g is the gravitational acceleration), $f_0 = 2\Omega\sin(\phi)$ is the Coriolis parameter (i.e. the vertical component of the planetary vorticity at given latitude where Ω is the angular velocity of the Earth and ϕ is the latitude), and x, y, z are the zonal, meridional and vertical coordinates respectively. In combination, these equations imply thermal wind balance, relating

horizontal temperature gradients to vertical gradients in horizontal wind:

$$\frac{\partial u_g}{\partial z} = -\frac{1}{f_0} \frac{\partial b'}{\partial y}, \quad \frac{\partial v_g}{\partial z} = \frac{1}{f_0} \frac{\partial b'}{\partial x}, \quad \frac{\partial \xi_g}{\partial z} = \frac{1}{f_0} \nabla_H^2 b' \quad (2.2)$$

where $\xi_g = \frac{\partial v_g}{\partial x} - \frac{\partial u_g}{\partial y}$ is the vertical component of the geostrophic relative vorticity, and ∇_H^2 is the horizontal Laplacian.

2.1.2 Potential vorticity

PV is one of the most important unifying concepts in meteorology, first introduced by Rossby (1940) and Ertel (1942), describing the atmosphere's dynamic and thermal state. The Rossby-Ertel PV (P) is a measure of the circulation of a fluid parcel between two potential temperature surfaces (i.e. isentropes), defined as:

$$P = \frac{1}{\rho} \vec{\zeta}_a \cdot \nabla \theta \quad (2.3)$$

where ρ is the density of air, $\vec{\zeta}_a$ is the absolute vorticity (the sum of the planetary and relative vorticity), and ∇ is the three-dimensional gradient operator. It was demonstrated by Ertel (1942) that P is conserved following fluid parcels (i.e. $\frac{DP}{Dt} = 0$) for adiabatic and frictionless motions. A typical order of magnitude of P for the mid-latitude upper troposphere is $10^{-6} \text{ K m}^2 \text{ kg}^{-1} \text{ s}^{-1}$, and this quantity is referred to as 1 “potential vorticity unit” or PVU. P generally increases with latitude (with increasing planetary vorticity), and with height from the troposphere into the stratosphere (due to increasing stratification), with the tropopause commonly defined to be the 2 PVU surface (referred to as the “dynamic tropopause”).

PV is a powerful concept due to its conservation law, but also due to its invertibility. The “invertibility principal” states that if the global distribution of PV is known, then (with specified balance and boundary conditions) the PV field can be inverted to obtain the wind and potential temperature fields everywhere in the domain (Hoskins et al., 1985). This is most readily demonstrated mathematically by considering quasi-geostrophic (QG) PV (QGPV), a quantity whose advection on horizontal surfaces mimics the advection of the full Rossby-Ertel PV under the approximations of QG theory (in which it is assumed

that the atmosphere stays close to geostrophic balance; e.g. Chapter 5 in Vallis, 2017). QGPV is conserved following the horizontal geostrophic flow in the absence of friction and diabatic effects:

$$QGPV = \underbrace{f_0 + \beta y}_f + \underbrace{\nabla_H^2 \psi_g}_{\xi_g} + \frac{1}{\rho} \frac{\partial}{\partial z} \left(\rho \frac{f_0^2}{N^2} \frac{\partial \psi_g}{\partial z} \right) \quad (2.4)$$

where the planetary vorticity f is assumed to vary linearly with the meridional gradient $\beta = \frac{2\Omega \cos(\phi)}{a}$ (i.e. the β -plane approximation where a is the Earth's radius) and $N = \sqrt{\frac{g}{\theta} \frac{\partial \theta}{\partial z}}$ is the Brunt-Väisälä frequency. By making the Boussinesq approximation (i.e. that ρ and N are approximately constant) and assuming that β is small (a valid assumption in the polar regions), the QGPV anomaly from the background planetary vorticity is given by:

$$q = QGPV - f_0 = \nabla_H^2 \psi_g + \frac{f_0^2}{N^2} \frac{\partial^2 \psi_g}{\partial z^2} = \left(\frac{\partial^2}{\partial x^2} + \frac{\partial^2}{\partial y^2} + \frac{f_0^2}{N^2} \frac{\partial^2}{\partial z^2} \right) \psi_g = \widehat{\nabla}^2 \psi_g \quad (2.5)$$

where $\widehat{\nabla}^2$ is the three dimensional Laplacian with the vertical coordinate scaled by $\frac{f_0}{N}$. This is a form of Poisson equation, where q can be inverted mathematically given suitable boundary conditions to find the geostrophic streamfunction, ψ_g . Equation 2.5 describes how a PV anomaly influences the streamfunction equally in all directions, thereby inducing anomalies in wind and buoyancy (via Equation 2.1) that decay with distance from the anomaly. This principle is called ‘‘action-at-a-distance’’. Whilst demonstrated with QGPV with approximations for the sake of mathematical simplicity, this concept is also true for the full Rossby-Ertel PV (e.g. Hoskins et al., 1985).

Schematic diagrams showing the inversion of isolated PV anomalies to obtain their associated circulation and potential temperature fields are presented in Figure 2.1. In the Northern Hemisphere, a lowering of the tropopause is associated with an upper-level positive PV anomaly (Figure 2.1a), which corresponds to a cyclonic circulation and an increase in static stability, with a tropospheric cold anomaly established below due to isentropes bowing upwards towards the positive PV anomaly. In contrast, a rising of the tropopause

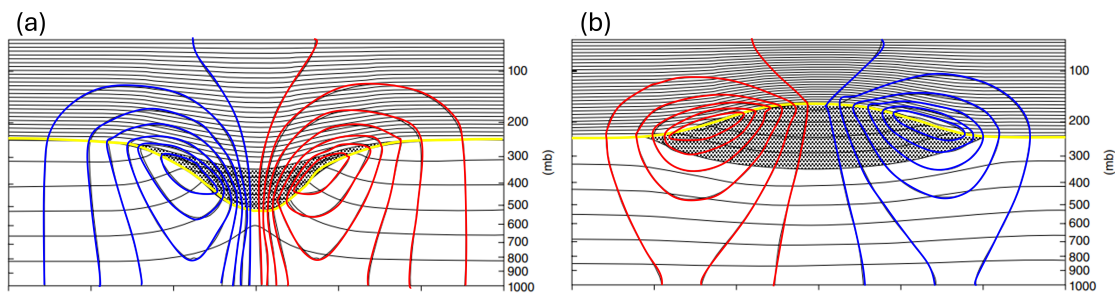


Figure 2.1: A schematic diagram adapted from Hoskins and James (2014, Figure 10.4, originally Figure 15 in Hoskins et al., 1985) showing the inversion of isolated (a) positive and (b) negative PV anomalies (stippled) on the tropopause (yellow line) in the Northern Hemisphere. The inversion of the PV anomalies gives the wind (with red and blue lines denoting wind into and out of the page respectively) which is cyclonic in (a) and anticyclonic in (b), and potential temperature (black lines) fields.
 © 1985 Royal Meteorological Society. Reproduced with permission from Wiley.

is associated with an upper-level negative PV anomaly (Figure 2.1b), corresponding to an anticyclonic circulation and a decrease in static stability with a tropospheric warm anomaly below.

2.1.3 Baroclinic instability

Baroclinic instability is the primary growth mechanism of extratropical cyclones, and occurs in regions of strong horizontal temperature gradients. On the planetary scale, the mid-latitude regions are characterised by a strong meridional temperature gradient between the relatively warm equatorial regions and cold polar regions, associated with vertical shear in zonal wind due to thermal wind balance (Equation 2.2). This leads to an upper-level mid-latitude jet, and a basic state that is dynamically unstable to small perturbations. These small perturbations can grow (converting potential energy into kinetic energy) into cyclones which act to mix warm air polewards and cold air equatorwards (i.e. ultimately reducing the meridional temperature gradient).

The baroclinic instability mechanism can be understood as arising from the vertical interaction between two Rossby waves (PV-conserving motions owing their existence to the meridional gradient of PV; also see Section 2.1.4) that are out of phase in the zonal direction (e.g. Heifetz et al., 2004). The concept can be understood in the simplest way by considering an upper-level PV anomaly that is positioned over a low-level baroclinic

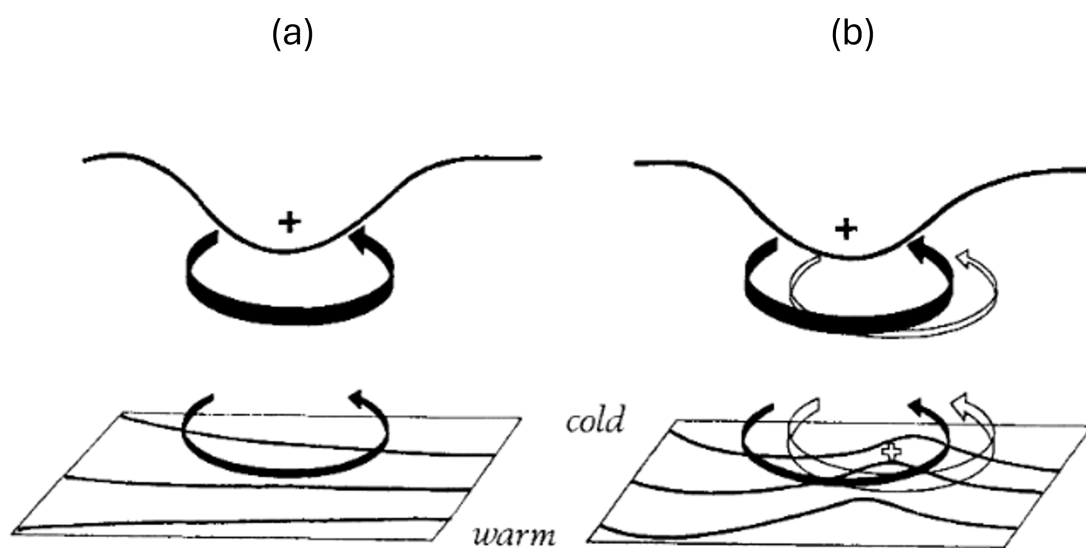


Figure 2.2: A schematic diagram from Hoskins et al. (1985, Figure 21) of baroclinic instability with an upper-level positive PV anomaly positioned over a low-level baroclinic zone (as described in the text). The circulation induced by the upper-level PV anomaly is marked with black arrows in (a), with the resulting low-level warm anomaly and induced circulation marked with white arrows in (b).

© 1985 Royal Meteorological Society. Reproduced with permission from Wiley.

zone, with a mean state where upper-level PV increases with latitude and low-level temperature decreases with latitude (see schematic in Figure 2.2). An upper-level positive PV anomaly (e.g. a trough in the jet stream) is associated with a cyclonic circulation, that is greatest in the upper levels but extends down to the surface through action-at-a-distance (Figure 2.2a). The cyclonic circulation near the surface acts to distort the meridional temperature gradient, moving warm air polewards ahead of the PV anomaly, and cold air equatorwards behind. A warm anomaly at the surface can be thought of as resulting from a positive PV anomaly concentrated at the surface (Bretherton, 1966), and therefore is associated with its own cyclonic circulation. Through action at-a-distance, this cyclonic circulation extends to the upper-levels, with equatorward flow behind the warm anomaly advecting higher-PV air equatorward and amplifying the upper-level PV anomaly (Figure 2.2b). Hence, the upper and lower level circulations are acting to enhance the other in mutual amplification, leading to the growth of a baroclinic wave.

Necessary (but not sufficient) conditions for baroclinic instability arise from mathematical stability analysis of idealised basic states (e.g. Charney and Stern, 1962; Pedlosky, 1964).

A key result that emerges is the Charney-Stern-Pedlosky (CSP) condition for instability, which is satisfied (i.e. indicating that baroclinic instability is possible) by several criteria (e.g. Section 9.4.3 in Vallis, 2017), essentially requiring that the meridional gradient of PV exhibits both positive and negative values somewhere in the domain (e.g. Section 14.2 in Hoskins and James, 2014). This condition is required for the phase locking and mutual amplification mechanism described above to occur, and is typically manifested in the atmosphere via a positive gradient of PV in the upper troposphere and a negative gradient of PV at the surface associated with the equator-to-pole reduction of surface temperature.

2.1.4 Polar vs. mid-latitude regions

The equator-pole meridional temperature gradient is strongest in the mid-latitudes, so the baroclinic instability mechanism associated with the upper-level jet stream is more relevant to the mid-latitudes than the polar regions. However, some cyclones may be initiated in the mid-latitudes before moving into the Arctic region. Furthermore, horizontal temperature gradients can also be established regionally (e.g. due to a land-sea contrast), which means that baroclinic instability can still be a relevant mechanism away from the mid-latitude jet. In particular, the Arctic coastline is associated with a strong horizontal temperature gradient in summer between the relatively warm land to the south and the colder ocean to the north. This baroclinic zone is commonly referred to as the “Arctic Frontal Zone”, and is discussed in more detail in Section 2.2.3.

The mid-latitude flow is dominated by Rossby waves (e.g. alternating troughs and ridges on the jet stream), key to which is the planetary vorticity which increases with latitude. The planetary vorticity (f) is greatest at the poles, however, its meridional gradient (β) is very weak in polar regions, such that conditions are less favourable for Rossby wave propagation. Woollings et al. (2023) performed a lag correlation analysis of 500 hPa geopotential height (Figure 2.3) to highlight the typical observed flow structures as a function of latitude (in the Southern Hemisphere, although the results are qualitatively true for the Northern Hemisphere also). There is a clear signature of Rossby wave-like behaviour at 45°S, with eastward propagation of alternating wave packets (Figure 2.3a). A similar flow structure is observed at 60°S, although the zonal propagation of wave pack-

ets is weaker (Figure 2.3b). Further poleward at 75°S no wave-like behaviour is seen on average, with Figure 2.3c illustrating a coherent vortex embedded within broader annular flow. Woollings et al. (2023) suggest that the flow in polar regions can be conceptualised as an interplay between geostrophic turbulence and Rossby wave propagation (like mid-latitudes; e.g. Rhines, 1975), but with a larger dominance of turbulent flow compared to mid-latitude regions. Hence, isolated vortices often dominate in the polar regions (although some wave-like structures do occur), with one example being “tropopause polar vortices”, which are commonly observed features of the summer-time Arctic (discussed in more detail in Section 2.2.3). The authors also suggest that high-latitude waves are less dispersive, due to a smaller value of β , so that downstream development does not play such a strong role in the decay of eddies as it does in mid-latitudes. This may result in more persistent weather phenomena in the polar regions (Woollings et al., 2023).

2.2 Extratropical cyclones

Extratropical cyclones, synoptic-scale low pressure systems, are the primary weather systems outside of the tropics. In this section the characteristics of extratropical cyclones are discussed. Firstly a cyclone phase space for classifying a spectrum of cyclone structures is introduced, followed by a brief overview of discrete conceptual models used for classifying mid-latitude cyclones. Following this, a review on the current state of knowledge

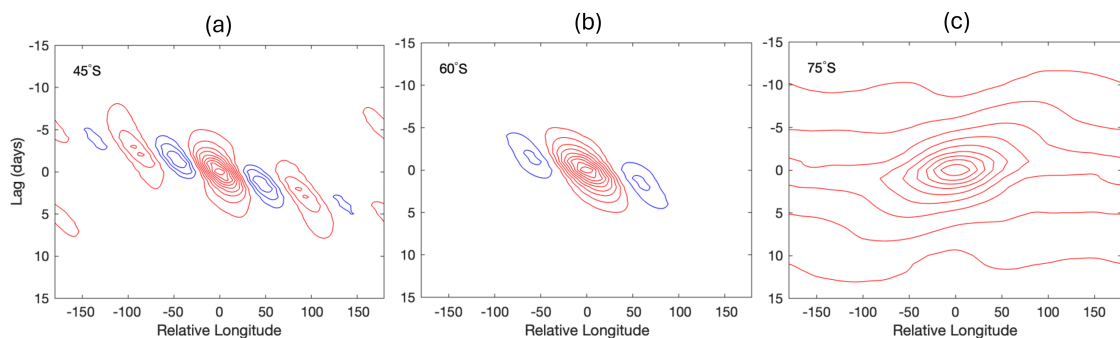


Figure 2.3: Adapted from Woollings et al. (2023, Figure 7). Lag correlation of daily mean 500 hPa geopotential height at (a) 45°S, (b) 60°S and (c) 75°S, calculated at 12 base points equally spaced around the hemisphere and then averaged over the period 1979–2018 in the December–January–February season. The contour interval is 0.1 (red and blue lines indicating positive and negative correlations respectively) with the zero correlation lines omitted.

Reproduced under the terms of the Creative Commons Attribution 4.0 License.

of summer-time Arctic cyclones is provided.

2.2.1 Cyclone structure in cyclone phase space

A cyclone phase space for objectively classifying the structure of cyclones throughout their lifecycle was proposed by Hart (2003). The cyclone phase space provides a flexible approach towards classification of cyclone structure, allowing for a continuum of structures, and is suitable for classifying both tropical and extratropical cyclones. The cyclone phase space describes a cyclone's thermal asymmetry (i.e. whether it is axisymmetric and non-frontal or asymmetric and frontal), and its thermal wind structure (whether it is warm-core and cyclonic winds decrease with height, or cold-core and cyclonic winds increase with height). The thermal asymmetry of a cyclone is defined as the storm-motion-relative 900–600 hPa thickness asymmetry across a cyclone within a 500 km radius of its centre:

$$B = h \left(\overline{Z_{600 \text{ hPa}} - Z_{900 \text{ hPa}}|_R} - \overline{Z_{600 \text{ hPa}} - Z_{900 \text{ hPa}}|_L} \right) \quad (2.6)$$

calculated by splitting a cyclone into two semi-circles that are to the right (R) and left (L) of the cyclone motion vector, where Z is isobaric height, the overbar indicates the areal mean over a semi-circle, and h takes the value of ± 1 in the Northern/Southern Hemisphere. This parameter essentially captures the horizontal temperature gradient across a cyclone, since the thickness of a layer is proportional to its average temperature. A threshold of $B = 10 \text{ m}$ is used for classification, below which a cyclone is considered to be symmetric, and above which a cyclone is considered to have an asymmetric structure. The cyclone thermal wind structure is determined by the vertical gradient of the cyclone isobaric height perturbation on a pressure level ($\Delta Z = Z_{max} - Z_{min}$):

$$\left. \frac{\partial(\Delta Z)}{\partial \ln p} \right|_{p_2}^{p_1} = -|V_T| \quad (2.7)$$

calculated in both a lower layer ($p_1 = 600 \text{ hPa}$, $p_2 = 900 \text{ hPa}$) and upper layer ($p_1 = 300 \text{ hPa}$, $p_2 = 600 \text{ hPa}$) of the troposphere using a linear regression fit to give a scaled thermal wind ($-|V_T|$), where p is pressure. In essence, this parameter describes whether the cyclone winds increase or decrease with height in a layer. If $-|V_T|$ is positive, then wind speed decreases with height, indicative of a warm-core cyclone by thermal wind balance

(Equation 2.2), whilst a negative $-|V_T|$ indicates increasing wind speed with height and a cold-core cyclone.

The structure of a cyclone throughout its lifetime can be plotted in a phase space diagram defined by Equations 2.6 and 2.7, as demonstrated in Figure 2.4 for a mid-latitude cyclone (Figure 2.4a) and a tropical cyclone (Figure 2.4b) respectively (showing only the thermal wind in the lower layer for brevity). Mid-latitude cyclones are characterised by high asymmetry that peaks during their growth phase, consistent with growth by baroclinic instability which requires horizontal temperature gradients, in contrast to tropical cyclones which are symmetric. Tropical cyclones are warm-core systems (throughout the troposphere), whilst mid-latitude cyclones can be warm-core or cold-core in different vertical layers depending on their dynamics. In Figure 2.4a the mid-latitude cyclone has a cold-core structure, although some mid-latitude cyclones can develop a warm seclusion which would lead to a low-level warm-core structure (see Section 2.2.2).

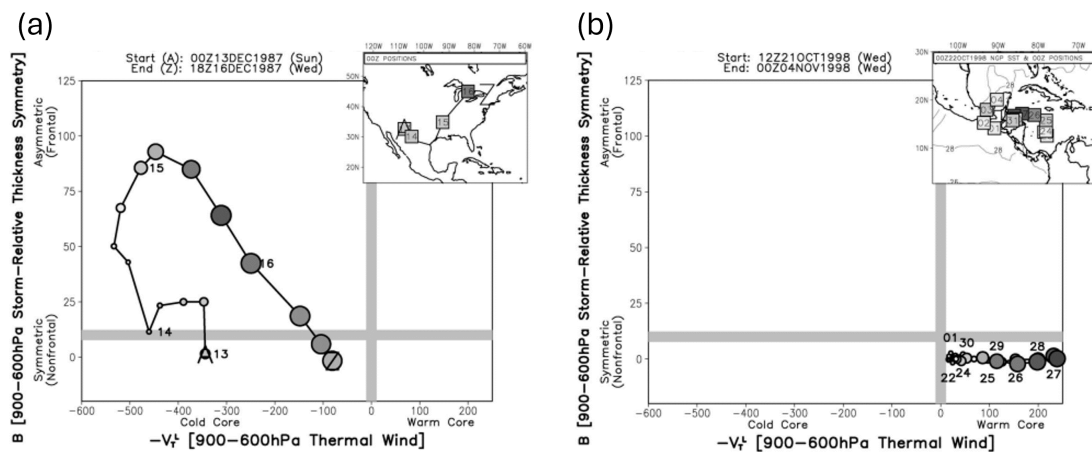


Figure 2.4: Adapted from Hart (2003, Figures 4a and 5a). The lifecycle of (a) a mid-latitude cyclone and (b) a tropical cyclone in the cyclone phase space diagram, with 6-hourly markers starting at “A” and ending in “Z”, with darker shading and larger markers indicating a stronger cyclone.

© American Meteorological Society. Used with permission.

The objective nature of a cyclone phase space means that theoretically it can be used to examine the lifecycle of Arctic cyclones without any substantial alterations (although in practice it is beneficial to make some minor changes to improve suitability for the Arctic

environment and optimise scientific understanding). However, the lifecycles of Arctic cyclones have not previously been examined in the cyclone phase space. A modified form of the cyclone phase space is presented in Chapter 4.

2.2.2 Other approaches to cyclone classification

Although in nature the evolution of cyclone structure occurs on a spectrum of behaviours, conceptual models and classification schemes have been developed to explain variability in extratropical cyclone dynamics and to enhance understanding. The classification approaches presented here have been based on the observation and study of mid-latitude cyclones.

The lifecycles of mid-latitude cyclones are highlighted by conceptual models (two of which are described here for the purpose of introducing the key features of extratropical cyclones). One of the first such models was the Norwegian cyclone model (Bjerknes, 1919; Bjerknes and Solberg, 1922) which describes a cyclone as consisting of a warm and a cold air mass separated by sharp boundaries (i.e. fronts). The model describes the development of a frontal wave into a eastward-travelling low pressure system with the warm air mass (i.e. the “warm sector”) flanked by a warm front ahead and a cold front to the rear (Figure 2.5a). The cyclone continues to grow, but ultimately cold air from the rear side of the cyclone cuts off the warm sector forming an occlusion (Figure 2.5a), at which point the cyclone starts to weaken (Schultz and Vaughan, 2011). Although constructed from relatively sparse near-surface observations, the core principles of the Norwegian model remain largely adequate to describe mid-latitude cyclone evolution in the present day. However, more modern observations collected from field campaigns in the 1980s suggested that not all cyclones evolve in the same manner. Using these observations, Shapiro and Keyser (1990) proposed a new conceptual model for the lifecycles of mid-latitude cyclones. This Shapiro-Keyser model differs from the Norwegian model in that frontal fracture occurs near the cyclone centre, with the cold front becoming oriented perpendicular to the warm front in a characteristic “T-bone” structure (Figure 2.5b). In the occlusion process, warm air becomes wrapped up and trapped in the cyclone centre (indicated by a “bent-back” warm front), forming a warm seclusion (Figure 2.5b), after

which the cyclone weakens (Schultz and Vaughan, 2011).

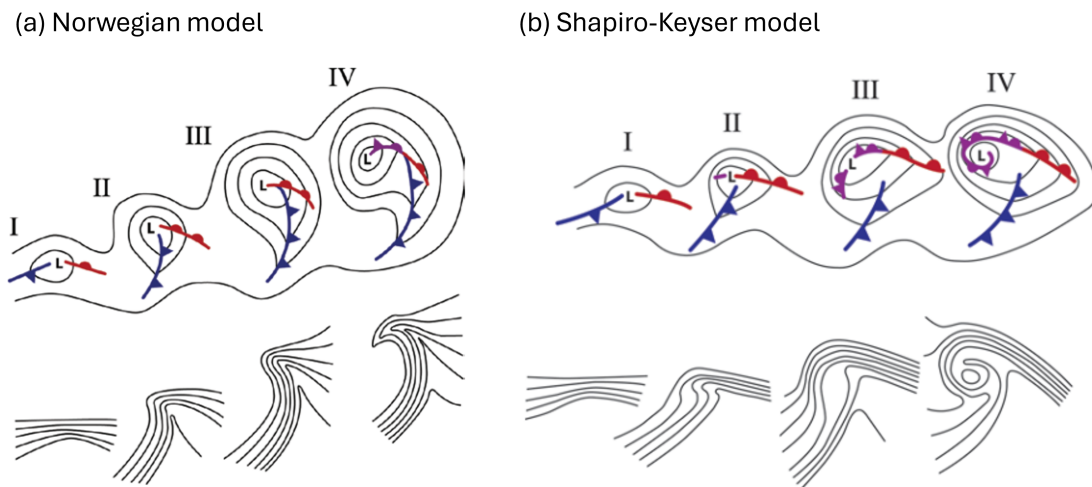


Figure 2.5: Adapted from Schultz and Vaughan (2011, Figures 2 and 12). The (a) Norwegian and (b) Shapiro-Keyser conceptual models of cyclone evolution showing (top) lower-tropospheric geopotential height and fronts, and (bottom) lower-tropospheric potential temperature. (a) Norwegian cyclone model: (I) incipient frontal cyclone, (II) and (III) narrowing warm sector, (IV) occlusion; (b) Shapiro-Keyser cyclone model: (I) incipient frontal cyclone, (II) frontal fracture, (III) frontal T-bone and bent-back front, (IV) frontal T-bone and warm seclusion.

© American Meteorological Society. Used with permission.

Taking a more process-based approach, Petterssen and Smebye (1971) proposed that mid-latitude cyclones can be classified as one of two types, based on the relative contribution of the lower- and upper-level forcing during cyclogenesis. Type A cyclones are those where the low-level forcing dominates the cyclone growth, forming in a low-level baroclinic region with no pre-existing upper-level trough (although one may develop as the cyclone grows). In contrast, Type B cyclones are those where the upper-level forcing dominates cyclone growth, where an upper-level trough moves over a relatively weak baroclinic region at low-levels, that strengthens as the low-level cyclone grows. In more recent years the Petterssen and Smebye (1971) classification scheme has been extended to include Type C cyclones, initially proposed by Deveson et al. (2002), in which the cyclone development is dominated by strong mid-level latent heating (e.g. Ahmadi-Givi et al., 2004; Plant et al., 2003).

Classification is important for enhancing scientific understanding and ultimately for anticipating the location and nature of cyclone hazards. For example, Gray and Dacre (2006)

demonstrated that the strongest North Atlantic cyclones are most likely to be classified as Type A cyclones, and least likely to be identified as Type C. For the North Atlantic basin, Type A cyclogenesis is prevalent to the east of the Rockies, Type B cyclogenesis dominates off the east coast of the US, and Type C cyclogenesis occurs most commonly over ocean regions of weaker low-level baroclinicity (Gray and Dacre, 2006). Schultz et al. (1998) suggested that cyclones occurring in confluent flow may develop in closer resemblance to the Shapiro-Keyser model, whilst cyclones in diffluent flow more closely resemble the Norwegian model lifecycle. This suggests that Shapiro-Keyser cyclones may be more prevalent over the western North Atlantic Ocean, in the confluence region of the upper-level jet, whereas Norwegian cyclones may be more prevalent over the eastern North Atlantic Ocean (Clark and Gray, 2018). Shapiro-Keyser cyclones can potentially be associated with sting jets, which cause very strong near-surface winds (Clark and Gray, 2018). Despite the importance of these classification schemes for understanding the potential hazards associated with a cyclone, none have yet been developed with specific focus on Arctic cyclones.

2.2.3 Summer-time Arctic cyclones

The subject of this thesis is Arctic cyclones, defined as synoptic-scale low-pressure systems that develop or move into the Arctic region, during summer. Note that these synoptic-scale cyclones are distinct from mesoscale “polar lows”, the short-lived (< 2 days), intense depressions that regularly develop over high-latitude oceans in winter in association with deep convection (e.g. Emanuel and Rotunno, 1989; Moreno-Ibáñez et al., 2021).

Zhang et al. (2004) found that Arctic cyclones in summer are more frequent, less intense, and longer-lived than winter-time Arctic cyclones, although Vessey et al. (2020) found that cyclone frequency counts were dependent on the choice of reanalysis product and tracking variable. In winter, Arctic cyclones most commonly track in the Greenland, Barents and Kara Seas in the Atlantic sector of the Arctic, whilst in summer cyclone activity is greatest along the Russian coastline and in the central Arctic (Crawford and Serreze, 2016; Vessey et al., 2020). In summer, Arctic cyclones that form in mid-latitudes and move poleward tend to be stronger than those that are generated locally, whilst cyclones

that enter the central Arctic (north of $>70^{\circ}\text{N}$) are especially long-lived (Zhang et al., 2004). Vessey et al. (2022) demonstrated that the mean lifetime of summer-time Arctic cyclones is 3 days greater than winter-time Arctic cyclones, and 4 days greater than winter-time mid-latitude cyclones in the North Atlantic.

The Arctic coastline in summer is commonly referred to as the “Arctic Frontal Zone” (AFZ), due to the presence of a strong meridional temperature gradient established by the proximity of the relatively warm land to cool ocean (Figure 2.6). This strong meridional temperature gradient means that the AFZ is a key region for baroclinic instability in the summer-time Arctic. Crawford and Serreze (2016) demonstrated that Arctic cyclone activity is greatest along the Eurasian coastline in summer, with the AFZ acting to intensify cyclones that form over Eurasia via the baroclinic instability mechanism. Furthermore, years with a stronger AFZ are characterised by increased cyclone numbers and cyclone intensity (Day and Hodges, 2018). The AFZ has shown a strengthening trend in recent decades, due to the land surface warming faster than the ocean surface (Day and Hodges, 2018).

An important feature of the summer-time Arctic, with regards to cyclone development, is the presence of tropopause polar vortices (TPVs), coherent circulation features on the tropopause with horizontal scales of less than 1500 km, and lifetimes that can exceed 1 month (Cavallo and Hakim, 2010). TPVs are a common feature of the Arctic (in summer but also the other seasons), owing their presence to the lack of a zonal jet stream and wind shear which would act to destroy such features in the mid-latitudes. TPVs are positive axisymmetric PV anomalies on the tropopause, associated with a tropospheric cold anomaly, a stratospheric warm anomaly, and strong cyclonic winds on the tropopause that extend the depth of the troposphere (Figure 2.7), closely resembling the idealised positive PV anomaly on the tropopause in Figure 2.1a. TPVs are intensified by longwave radiative cooling above the tropopause, whilst shortwave radiation and mid-tropospheric latent heating acts to weaken them (Cavallo and Hakim, 2009, 2012, 2013). TPVs are known to excite and interact with surface cyclones, with Gray et al. (2021) demonstrating that one third of all summer-time Arctic cyclones develop in the vicinity of TPVs.

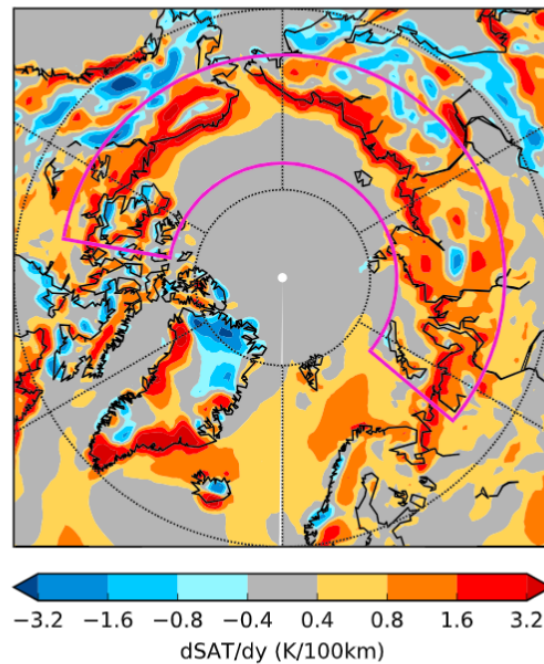


Figure 2.6: Adapted from Day and Hodges (2018, Figure 1a). Map of June-July-August mean (1979–2016) equatorward 2 m temperature (SAT) gradient. The magenta box marks the Arctic Frontal Zone.

© 2018. The Authors. Reproduced with permission from Wiley.

Our knowledge of the lifecycles of summer-time Arctic cyclones has largely been based on case studies. As introduced in Chapter 1, the Great Arctic Cyclone of 2012 (C12) is the most studied case, being extremely strong and long-lived (Simmonds and Rudeva, 2012). C12 formed over the Eurasian continent and then moved north-eastward over the Eurasian coastline where it intensified by baroclinic instability on the AFZ, before moving into the central Arctic where it reached its maximum intensity and remained for over 1 week (Simmonds and Rudeva, 2012; also see Figure 1.5a). The cyclone initially had a warm-core tilted structure during growth, with peak winds in the lower troposphere (Aizawa and Tanaka, 2016). This structure is not unlike that of mid-latitude cyclones that develop on a low-level baroclinic zone in the absence of an upper-level anomaly (i.e. Type A cyclogenesis). However, after maximum intensity the cyclone underwent a structural transition, attaining a deep vertically-stacked cold-core structure with cyclonic winds (maximum on the tropopause) established throughout the troposphere (Aizawa and Tanaka, 2016). This columnar vortex structure has also been reported in other extreme summer-time Arctic cyclone cases, with the low-level cyclone interacting with, and becoming vertically stacked

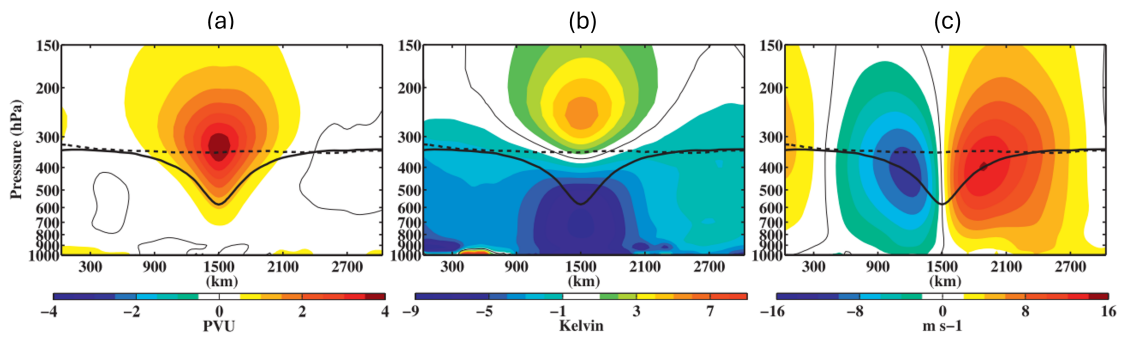


Figure 2.7: Adapted from Cavallo and Hakim (2010, Figure 9a-c). The composite structure of 568 TPVs identified during 2 August 2007–31 July 2009 over the Canadian Archipelago region. Plots show west-east cross-vortex sections of anomalous (a) Rossby-Ertel PV, (b) temperature, and (c) meridional wind. The thick solid (dashed) contour is the composite (background) tropopause.

© American Meteorological Society. Used with permission.

below, a TPV at upper-levels (e.g. Tanaka et al., 2012; Tao et al., 2017). This long-lived axisymmetric vortex structure is unlike that of mid-latitude cyclones, which exhibit a tilted structure during growth and then usually quickly dissipate after maturity. Cyclone merger can also be an important process in the evolution of summer-time Arctic cyclones, for example, a cyclone in August 2016 (C16) lived for over 1 month due to repeated cyclone mergings (Yamagami et al., 2017).

Building on these case studies, Vessey et al. (2022) showed that the composite structure of intense summer-time Arctic cyclone cases is distinct from that of intense winter-time Arctic and mid-latitude cyclone cases, with a structural transition at around the time of maximum intensity from a tilted baroclinic wave structure to an axisymmetric cold-core structure. Rather than undergoing occlusion and dissipating like mid-latitude cyclones, the composite cold-core structure persists and strengthens for up to 8 days after maximum intensity (Figure 2.8). Furthermore, Gray et al. (2021) considered variability in cyclone structure in the summer-time Arctic, performing a climatology of cyclones that are “unmatched” or “matched” with TPVs during development. Unmatched cyclones (two-thirds) were initially dominated by low-level vorticity, and most commonly tracked on the Eurasian coastline, in association with high baroclinicity on the AFZ. In contrast, matched cyclones (one-third) were initially dominated by upper-level vorticity, with reduced system tilt and a single columnar vortex structure at maximum intensity (like in Vessey et al., 2022). Matched cyclones most commonly track along the North American

coastline, which is consistent with the climatological occurrence of TPVs (Cavallo and Hakim, 2010).

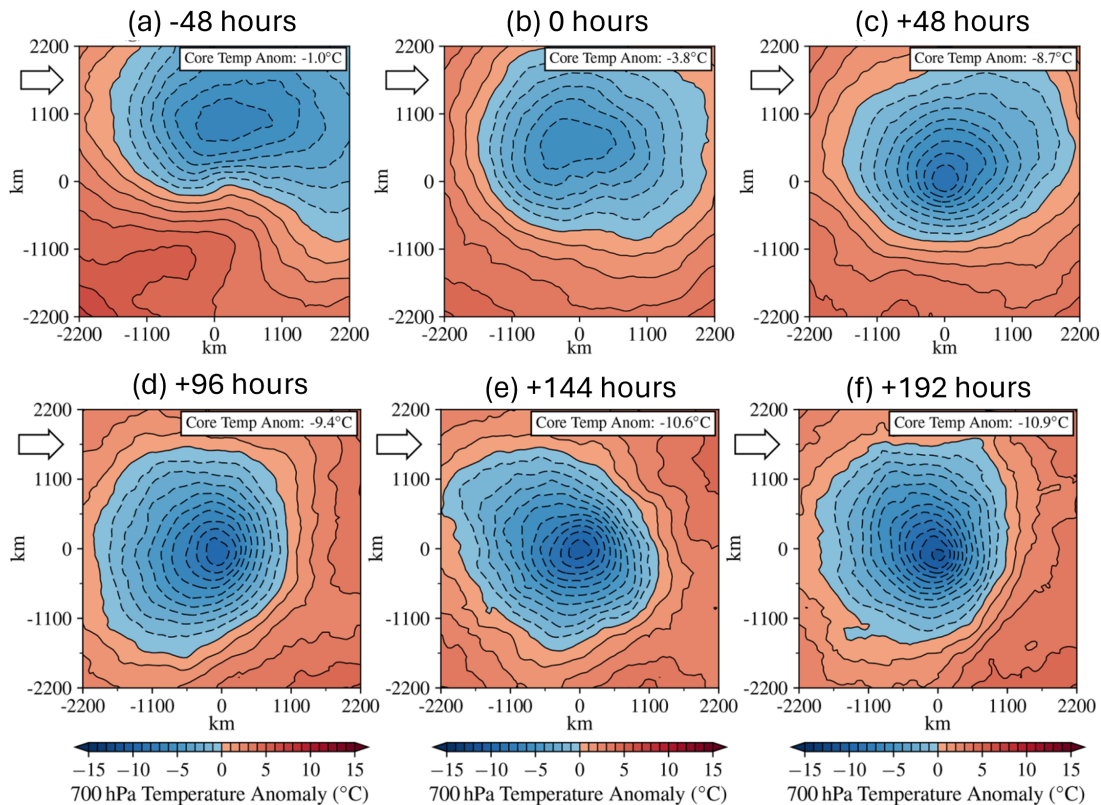


Figure 2.8: Adapted from Vessey et al. (2022, Figures 6g-i and 7). Horizontal 700 hPa temperature anomaly composite structure of 100 intense summer-time (June, July, August) Arctic cyclones at (a) 48 hours before maximum intensity, (b) maximum intensity, and at (c) 48, (d) 96, (e) 144, (f) 192 hours after maximum intensity. The large arrow indicates the direction of cyclone propagation, and the inset contains the core temperature anomaly.

Reproduced under the terms of the Creative Commons Attribution 4.0 License.

Recent works examining trends in the behaviour and characteristics of Arctic cyclones have yielded contrasting results. Zhang et al. (2023) found that integrated Arctic cyclone activity has increased over the last seven decades in three different reanalysis datasets, with cyclones becoming stronger and longer-lived in all seasons. However, in contrast, Valkonen et al. (2021) did not find any significant trends in the number or intensity of summer-time Arctic cyclones in their examination of three different reanalysis datasets during 1979–2015. Hence, for now it remains unclear as to whether there are trends in the occurrence of summer-time Arctic cyclones, with results being highly sensitive to choice of reanalysis dataset, cyclone tracking method and metrics.

2.3 The impact of the surface on extratropical cyclones

2.3.1 The boundary layer

The boundary layer (BL) is the portion of the atmosphere which is directly influenced by Earth's surface, and responds to surface forcings on a timescale of an hour or less (Stull, 1988). The presence of the surface enforces gradients in wind (since the wind vanishes at the surface), temperature, and humidity with the overlying atmosphere, leading to the development of turbulent eddies which continuously act to redistribute momentum, heat, and moisture in the vertical. "Turbulent exchange" refers to these turbulent fluxes of momentum, heat and moisture between the surface and the atmosphere. The vertical extent of these turbulent eddies determines the BL depth, which is quite variable in time and space but is typically on the order of one kilometre.

Turbulent transport in the BL modifies the force balance from geostrophic and hydrostatic balance (which ultimately impacts the free troposphere and weather systems through continuity). In neutrally or stably stratified conditions, a theoretical BL often discussed is the Ekman BL, in which there is a horizontal force balance between the pressure gradient, Coriolis, and frictional forces. The turbulent transport of momentum by eddies is assumed to be driven by the vertical gradient of the local mean wind, and the wind speed increases from zero at the surface to the geostrophic value at the top of the BL (Holton and Hakim, 2012). However, in reality, turbulent mixing (mechanical or buoyancy-driven) commonly leads to the formation of a well-mixed layer (above a near-surface layer), in which wind speed and potential temperature are nearly constant with height, and turbulent fluxes vary approximately linearly with height (Holton and Hakim, 2012). Although the structure of the BL in the real world is quite different from the Ekman BL, qualitative features of its solution are valid for explaining how BL friction impacts the free troposphere (see below).

2.3.2 Boundary layer processes in extratropical cyclones

The effects of surface friction on cyclone development are most commonly explained using the Ekman pumping mechanism. For flow in geostrophic balance (i.e. above the BL

where the flow is approximately frictionless), the pressure gradient and Coriolis forces balance each other such that air parcels travel parallel to isobars (Figure 2.9a). However, friction in the (Ekman) BL modifies the force balance such that the wind is weakened and has a cross-isobaric component that turns towards low pressure (Figure 2.9b). This means that the BL wind in a cyclonic vortex turns in towards the low centre, with low-level convergence forcing ascent (since the surface prevents descent) by continuity at the top of the BL. The consequences of this Ekman pumping on a cyclonic vortex are demonstrated in a schematic in Figure 2.9c. The ascent at the top of the BL forces a secondary circulation in which a slow outward radial flow in the free troposphere acts to weaken the primary azimuthal flow. This can be understood by considering that the Coriolis force for the outward flow is directed in an anticyclonic sense, exerting a torque opposite to the direction of the cyclonic circulation of the vortex (Holton and Hakim, 2012). This cyclone spin-down mechanism can also be understood as Ekman pumping acting to squash the free tropospheric column, which is associated with a reduction in relative vorticity due to the conservation of circulation.

The explanation of Ekman pumping above assumes a barotropic vortex (i.e. a symmetric vortex with a neutrally stratified atmosphere). In reality the extratropical atmosphere is usually stably stratified, and extratropical cyclones exhibit an asymmetric structure with strong temperature gradients in frontal regions. Hence, it is clear that the Ekman pumping mechanism alone cannot explain the impact of friction on extratropical cyclones. A more comprehensive understanding can be achieved by utilising a PV framework (and this is the most natural way to view extratropical cyclones given the role of both relative vorticity and temperature gradients). Friction in the BL means that PV is not conserved following fluid parcels. The PV framework also captures the non-conservation of PV due to diabatic effects (i.e. sensible and latent heat fluxes), which have not been discussed so far. In the presence of friction and diabatic effects, the Lagrangian tendency of PV is:

$$\frac{DP}{Dt} = -\frac{1}{\rho} \left[(\nabla \times \vec{F}) \cdot \nabla \theta + \vec{\zeta} \cdot \nabla \left(\frac{D\theta}{Dt} \right) \right] \quad (2.8)$$

where \vec{F} is the frictional force vector. The first term on the right hand side represents

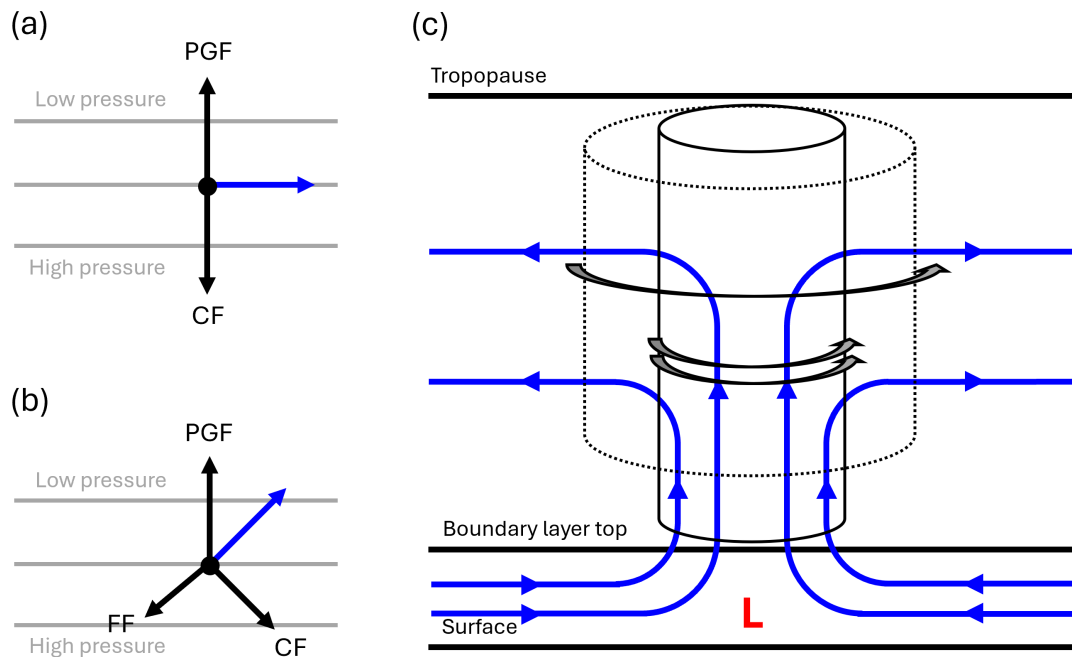


Figure 2.9: Schematics showing the force balance on an air parcel for (a) frictionless flow in the free troposphere (i.e. geostrophic balance) and (b) flow in the BL, with grey lines denoting isobars, black arrows representing the pressure gradient force (PGF), the Coriolis force (CF), and the frictional force (FF), and the blue arrow denoting the parcel velocity. (c) Schematic diagram of the Ekman pumping mechanism in a barotropic vortex. The solid cylinder illustrates the initial vortex tube with the double grey arrows demonstrating the primary azimuthal circulation. Ekman pumping forces a secondary circulation, denoted by the blue streamlines, in which the vortex column is squashed (dotted cylinder) and the cyclone primary azimuthal circulation is weakened (single grey arrow).

frictional effects on PV, whilst the second represents the diabatic effects (which can be split into sensible and latent contributions). From this equation, Cooper et al. (1992) derived a simplified expression for the depth-averaged BL PV tendencies associated with friction and sensible heat fluxes, by assuming a constant density and a linear-flux gradient (i.e. fluxes decrease linearly with height from the surface to zero at the BL top). The depth-averaged BL PV tendency equation highlights the mechanisms by which friction or sensible heating in the BL generate or destroy PV. The processes and their impacts on extratropical cyclones are briefly described below (but are discussed in more detail in Chapter 3). Note that this framework has only previously been applied to mid-latitude cyclones, with the identified BL mechanisms understood in the context of the typical structure of a mid-latitude cyclone. This framework has not been applied to summer-time

Arctic cyclones before, which is the focus of Chapter 3.

From this framework, two frictional processes are apparent, with the first being the PV-version of Ekman pumping. Friction acts to weaken the BL winds in a cyclone (from the geostrophic value above the BL), thereby reducing the azimuthal circulation and vertical component of relative vorticity. The ascent associated with Ekman pumping also lifts isentropes away from the surface, which reduces static stability in the BL. In combination this frictional process generates negative PV in the BL (assuming the BL is stably stratified). To understand the cyclone spin-down mechanism aspect of Ekman pumping in this framework, consider that the rising isentropes lead to increased static stability above the BL which, if PV is to be conserved, means that relative vorticity must decrease there (e.g. Section 17.6 in Hoskins and James, 2014). The second frictional process is the baroclinic generation of PV, which occurs in frontal regions where there are strong horizontal temperature gradients. Wind in the BL increases from zero at the surface to the geostrophic value at the BL top, with vertical shear that constitutes a large horizontal component of relative vorticity. When coincident with large horizontal temperature gradients, large PV anomalies can be generated. Adamson et al. (2006) described the “baroclinic PV mechanism”, by which positive PV generated in the BL along the warm front is advected above the BL by the warm conveyor belt (an air flow in extratropical cyclones that ascends northward from the warm sector over the warm front) and over the cyclone centre, with increased static stability restricting the mutual growth of the upper and lower levels, acting to reduce the cyclone growth rate.

The PV framework of Cooper et al. (1992) also highlights the role of sensible heat fluxes. Surface sensible heat fluxes alter the temperature of near-surface air and the vertical stratification of the BL, thereby impacting PV. For example, upward sensible heat fluxes (i.e. heat transfer from the surface to the overlying air) are associated with a reduction in BL static stability (if the BL is stably stratified), which results in a negative PV anomaly in regions of positive vertical relative vorticity (e.g. behind the cold front of mid-latitude cyclones; Chagnon et al., 2013). The direct effect of surface sensible heat fluxes is to weaken mid-latitude cyclone development by reducing the low-level temperature gra-

dient, although this impact is relatively small compared to friction (Plant and Belcher, 2007) and latent heating (Bui and Spengler, 2021; Hualand and Spengler, 2020). This PV framework can also be extended to include the impact of latent heating in the BL (e.g. Vanni re et al., 2016). The moisture in ascending air parcels (e.g. in the warm conveyor belt) will condense and release latent heat, associated with an increase in static stability and a positive PV anomaly below (and a decrease in static stability and negative PV anomaly above). Hence, the impact of latent heat release at low levels is to impose a positive PV anomaly on the cyclonic circulation that would exist without latent heating (Davis et al., 1993). Latent heat fluxes are likely smaller in the Arctic than mid-latitudes due to reduced temperature and absolute humidity, although Terpstra et al. (2015) suggested that this can still be significant for the development of polar cyclones. However, latent heat fluxes are not a key focus in this thesis.

2.4 Sea ice

2.4.1 The boundary layer over sea ice

The presence of sea ice has a strong influence on the overlying BL due to its influence on radiative and turbulent fluxes (e.g. Notz, 2012). Sea ice typically has a higher albedo than other land surfaces due to its white colour, although the albedo is highly variable in summer in the presence of melt ponds and the absence of fresh snow (Perovich and Polashenski, 2012). The high albedo means that more shortwave radiation is reflected back to space, and reduces the amount of solar energy absorbed at the surface, keeping the surface cold. The cool and dry conditions over sea ice are conducive to a BL that is stable or near-neutral for most of the year (e.g. Persson and Vihma, 2017). In summer, when sea ice is in a melting regime, the surface temperature over ice is locked at 0 C as the phase change from ice to water occurs.

Surface roughness over sea ice is typically smaller than over land (Andreas et al., 1996), although considerable variations in surface roughness can occur in regions of marginal ice, ridging and melt ponds (e.g. Guest and Davidson, 1991). The marginal ice zone

(MIZ), the heterogeneous band of fragmented ice floes separating the ocean and main ice pack, is becoming an increasingly dominant sea ice state in the summer-time Arctic (Rolph et al., 2020; Strong and Rigor, 2013). The MIZ is defined as regions where sea ice fraction (SIF), the areal fraction of sea ice cover in a given region or grid box, is between 0.15 and 0.8. Although the surface roughness can vary significantly by region and ice morphology, surface roughness typically peaks in the MIZ at SIF values between 0.5 and 0.8 (e.g. Elvidge et al., 2016; Lüpkes and Birnbaum, 2005).

The MIZ is associated with gradients in roughness, temperature, and humidity that result in turbulent exchange of momentum, heat and moisture with the atmosphere. Turbulent momentum fluxes peak in the MIZ where there is high surface roughness, primarily due to form drag over ice flow edges (e.g. Elvidge et al., 2016). Off-ice flow, such as during cold-air outbreaks, is associated with cold air moving over the warmer ocean surface. The flow undergoes a transition from a BL that is stable or neutral over ice to one that is unstable over ocean, with upward turbulent sensible and latent heat fluxes on the order of 100 W m^{-2} during winter (e.g. Elvidge et al., 2021; Renfrew and Moore, 1999). In contrast, the BL is cooled and dried during on-ice flow, such as warm air intrusions (e.g. Pithan et al., 2018). Turbulent fluxes of sensible and latent heat are typically much smaller in summer than in winter (on the order of 10 W m^{-2} or less; e.g. Andreas et al., 2010; Persson et al., 2002), indicating that temperatures over sea ice and ocean are more similar.

2.4.2 Sea ice in numerical weather prediction

Sea ice has previously been treated rather crudely in NWP, for example, with a constant roughness length often being prescribed for all sea ice morphologies (e.g. Notz, 2012), which does not consider changes in surface roughness across the MIZ. Furthermore, it was previously assumed that sea ice did not change significantly on the timescales of weather forecasts, with operational NWP systems typically keeping sea ice fields fixed throughout the forecast. However, Keeley and Mogensen (2018) demonstrated that static sea ice is a very poor assumption for NWP, with more than 5% of the Arctic ice field exhibiting significant changes over 5-day periods during June–November 2017. In recent years, there has been much progress in this regard.

For example, turbulent momentum fluxes between the atmosphere and sea ice are commonly parametrized as being directly proportional to a drag coefficient, which increases with surface roughness. Figure 2.10 presents the negatively-skewed distribution of the drag coefficient as a function of SIF estimated from aircraft observations collected over the MIZ during an Arctic field campaign, with a maximum value between 0.6 and 0.8 (Elvidge et al., 2016). Recent work demonstrates that physical parametrizations for surface momentum, heat and moisture fluxes that depend on SIF (derived from field campaign observations) do improve the representation of surface turbulent exchange over sea ice (e.g. Elvidge et al., 2021; Renfrew et al., 2019). Indeed, in the most recent implementation of the European Centre for Medium-Range Weather Forecasts (ECMWF) IFS (model cycle 48r1, released in June 2023), the roughness length for momentum (which informs the drag coefficient) is dependent on SIF, although the roughness lengths for heat and moisture still remain constant (ECMWF, 2023c).

Furthermore, in recent years there has been an advance towards coupled ocean and sea ice components in NWP models, with dynamic sea ice. Atmosphere-ocean-ice coupling has now been implemented in operational global forecasting systems by several forecasting centres including at ECMWF (Keeley and Mogensen, 2018), which is the focus of Chapter 6, but also at Environment and Climate Change Canada (ECCC; Peterson et al., 2022; Smith et al., 2018), and the United States Naval Research Laboratory (NRL; Barton et al., 2021). Previous works running numerical model experiments have demonstrated that the geometry of the MIZ and ice edge during cold air outbreaks influences the downstream development of the BL (Liu et al., 2006; Spensberger and Spengler, 2021). Hence, coupled NWP models with dynamic sea ice can represent rapid changes in sea ice (e.g. associated with Arctic cyclones, see Section 2.4.3), and therefore have the potential to capture the downstream atmospheric impacts and improve weather forecasts.

2.4.3 Cyclone-sea ice interactions

Very rapid ice loss events (VRILEs) are extreme reductions in sea ice extent (SIE; the areal extent over which SIF exceeds 0.15), on the timescale of days, that are associated

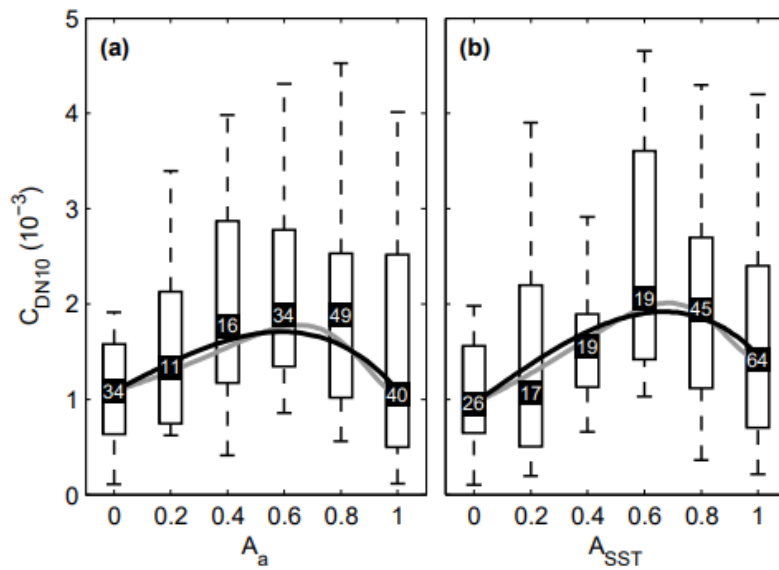


Figure 2.10: Adapted from Elvidge et al. (2016, Figure 2a-b). The drag coefficient (C_{DN10}) as a function of SIF (A) estimated from (a) albedo and (b) sea surface temperature, estimated from aircraft observations collected from the Barents Sea and Fram Strait during the Aerosol-Cloud Coupling And Climate Interactions in the Arctic (ACCACIA) field campaign. The drag coefficient is calculated at 10 m using an eddy covariance method, assuming a parametrization for surface momentum fluxes and neutral stratification. Box and whisker plots show the median (black square), interquartile range (boxes) and 9th and 91st percentiles (whiskers) within each bin (SIF intervals of 0.2). The number in the black box indicates the number of data points in each bin. The black and grey curves illustrate the Lüpkes et al. (2012) parametrization scheme with different parameter settings.

Reproduced under the terms of the Creative Commons Attribution 3.0 License.

with anomalous synoptic activity (e.g. Wang et al., 2020). Cyclones are the key weather systems in the summer-time Arctic that can impact sea ice. For example, C12 tracked over sea ice in the Pacific sector of the Arctic in August 2012 (Lukovich et al., 2021; Simmonds and Rudeva, 2012), and was associated with considerable ice melt (Stern et al., 2020) and reduced SIE (constituting a VRILE; McGraw et al., 2022) that contributed to the record-low SIE minimum that occurred in that year (Zhang et al., 2013).

In the case of C12, sea ice loss was associated with bottom melt due to storm-driven mixing of a ocean warm layer (Stern et al., 2020; Zhang et al., 2013), and surface melting due to warm air advection by strong surface winds (Stern et al., 2020). Peng et al. (2021) also identified a storm-induced increase in ocean turbulent mixing and bottom melt in the C16 case, that lead to accelerated sea ice loss. Although C16 was similar in size and intensity to C12 (Yamagami et al., 2017), it was associated with less sea ice loss due to dynami-

cal convergence of ice in the central Arctic that counteracted the thermodynamic melting (Lukovich et al., 2021). Ultimately, the impact of a cyclone on sea ice is highly dependent on system strength, timing, and location relative to the ice edge (Lukovich et al., 2021). Furthermore, Arctic cyclones do not necessarily need to track over the sea ice in order to impact it. The recent reduction of sea ice in the summer-time Arctic and the growing expanse of open water means that the strong winds produced by cyclones often have a longer fetch, leading to larger and more extreme waves (Asplin et al., 2012; Waseda et al., 2018) that can propagate into the pack ice and break it up. Asplin et al. (2012) presented a case study from September 2009 of large swells caused by cyclones leading to the fracturing of multi-year pack ice, with smaller floes that are more susceptible to lateral melting and decay.

Whilst cyclones can significantly impact sea ice, the sea ice distribution also feeds back on cyclones. For example, sea ice determine surface roughness and surface fluxes, whilst the ice edge can also act as a boundary for cyclogenesis (Inoue and Hori, 2011). Simmonds and Keay (2009) found that the decline in September SIE is related to a trend towards stronger and larger Arctic cyclones in September, although it remains to be established why this may be the case. The more recent work of Valkonen et al. (2021) did not find a consistent link between sea ice and cyclone track frequency or intensity in the summer-time Arctic, suggesting that results are highly dependent on the choice of dataset. The mechanisms by which the surface, and in particular sea ice, impact the dynamical evolution of individual summer-time Arctic cyclone cases, have not previously been examined. However, the framework discussed in Section 2.3.2 provides a suitable methodology to do so, and the application of this is the focus of Chapter 3.

Chapter 3

The role of boundary layer processes in summer-time Arctic cyclones

This chapter has been published in *Weather and Climate Dynamics* with reference:

Croad, H. L., J. Methven, B. Harvey, S. P. E. Keeley, and A. Volonté (2023): The role of boundary layer processes in summer-time Arctic cyclones. *Wea. Climate Dyn.*, **4** (3), 617-638, <https://doi.org/10.5194/wcd-4-617-2023>.

Abstract

Arctic cyclones are the most energetic weather systems in the Arctic, producing strong winds and precipitation that present major weather hazards. In summer, when the sea ice cover is reduced and more mobile, Arctic cyclones can have large impacts on ocean waves and sea ice. While the development of mid-latitude cyclones is known to be dependent on boundary layer (BL) turbulent fluxes, the dynamics of summer-time Arctic cyclones and their dependence on surface exchange processes have not been investigated. The purpose of this study is to characterise the BL processes acting in summer-time Arctic cyclones and understand their influence on cyclone evolution. The study focuses on two cyclone case studies, each characterised by a different structure during growth in the Arctic: (A) low-level-dominant vorticity (warm-core) structure and (B) upper-level-dominant vorticity (cold-core) structure, linked with a tropopause polar vortex. A potential vorticity (PV) framework is used to diagnose the BL processes in model runs from the ECMWF Integrated Forecasting System model. Both cyclones are associated with frictional Ekman pumping and downward sensible heat fluxes over sea ice. However, a third process, the

frictional baroclinic generation of PV, acts differently in A and B due to differences in their low-level temperature structures. Positive PV is generated in Cyclone A near the bent-back warm front, like in typical mid-latitude cyclones. However, the same process produces negative PV tendencies in B, shown to be a consequence of the vertically aligned axisymmetric cold-core structure. This frictional process also acts to cool the lower troposphere, reducing the warm-core anomaly in A and amplifying the cold-core anomaly in B. Both cyclones attain a vertically aligned cold-core structure that persists for several days after maximum intensity, which is consistent with cooling from frictional Ekman pumping, frictional baroclinic PV generation, and downward sensible heat fluxes. This may help to explain the longevity of isolated cold-core Arctic cyclones with columnar vorticity structure.

3.1 Introduction

The rapid loss of sea ice due to anthropogenic global warming (e.g. Comiso, 2012; Meier et al., 2014) is permitting human activity to expand into the summer-time Arctic. For example, reduced sea ice extent and thickness will open up shorter shipping routes through the Arctic between Atlantic and Pacific ports (Melia et al., 2016). This human activity will be exposed to the risks of Arctic weather during the summer, including Arctic cyclones.

Arctic cyclones are synoptic-scale low-pressure systems developing, or moving into, the Arctic. They produce some of the most impactful weather in the Arctic, with strong winds at the surface and sometimes extreme ocean waves (e.g. Thomson and Rogers, 2014; Waseda et al., 2018). Arctic cyclones are also associated with atmospheric forcings that have large impacts on the sea ice (e.g. Asplin et al., 2012; Peng et al., 2021; Simmonds and Keay, 2009; Zhang et al., 2013). As the climate warms the summer-time Arctic is becoming increasingly dominated by the marginal ice zone (MIZ; Strong and Rigor, 2013), a band of fragmented ice floes separating the ice-free ocean and the main ice pack. In recent years the MIZ has widened by 39% (Strong and Rigor, 2013) in summer, with MIZ fraction (MIZ extent divided by total sea ice extent) increasing by more than 50% (Rolph

et al., 2020). Thinner and more mobile ice in the MIZ will result in enhanced surface interactions with Arctic cyclones, with greater surface drag due to ice floe morphology (Elvidge et al., 2016; Lüpkes and Birnbaum, 2005), and enhanced surface sensible and latent heat fluxes due to a greater exposure of the ocean surface. For example, it has been argued that record-low sea ice extent in 2012 was exacerbated by an extremely strong cyclone, the Great Arctic cyclone of 2012 (AC12; Simmonds and Rudeva, 2012), with enhanced ice melt due to increased upward ocean heat transport (Zhang et al., 2013).

Forecast skill in the Arctic is lower, but generally comparable, to that in Northern Hemisphere mid-latitudes (Jung and Matsueda, 2016; Sandu and Bauer, 2018), based on 500 hPa geopotential anomaly correlation scores. Lower predictability in the Arctic is likely related to the relative sparsity of observations there, resulting in larger uncertainties in initial conditions for numerical weather prediction models. Previous work has also demonstrated that the forecast skill of Arctic cyclones is lower than that of mid-latitude cyclones. For instance, Yamagami et al. (2018a) demonstrated that the mean predictability of 10 extraordinary Arctic cyclone cases was 2.5–4.5 days, around 1–2 days less than that of Northern Hemisphere mid-latitude cyclones (Froude, 2010). Furthermore, using ensemble forecasts, Capute and Torn (2021) demonstrated that the ensemble mean root-mean-square error and ensemble standard deviation for cyclone position was higher for 100 selected summer-time Arctic cyclones than for 89 selected winter-time Atlantic mid-latitude cyclones. Yamagami et al. (2018b) examined the predictability of AC12 and found that the position variability was greater than intensity variability between ensemble forecasts. Furthermore, ensemble members that best captured the upper-level vortex merger associated with AC12 produced the best forecasts, demonstrating that an understanding of cyclone dynamics and mechanisms is critical for predictability. Improvements in Arctic cyclone forecasting can likely be achieved through a better understanding of the physical processes that distinguish Arctic cyclones from mid-latitude cyclones, including the different growth mechanisms and interaction with sea ice.

Vessey et al. (2022) demonstrated that the composite structure of intense summer-time Arctic cyclones is distinct to that of intense winter-time Arctic and North Atlantic mid-

latitude cyclones. Summer-time Arctic cyclones undergo a structural transition at the time of maximum intensity, from a tilted baroclinic system to an axisymmetric cold-core structure. The mean lifetime of the summer-time Arctic cyclones was also found to be more than 3 days greater than that of wintertime Arctic cyclones and 4 days greater than that of winter-time North Atlantic mid-latitude cyclones (Vessey et al., 2022). The longevity of some Arctic cyclones and the transition to an axisymmetric cold-core structure have also been documented in several case studies (e.g. Aizawa and Tanaka, 2016; Simmonds and Rudeva, 2012; Tanaka et al., 2012; Tao et al., 2017; Yamagami et al., 2017).

Many of the growth mechanisms of summer-time Arctic cyclones are the same for mid-latitude cyclones, such as baroclinic instability and lee cyclogenesis. However, sustained cyclone interaction with tropopause polar vortices (TPVs), long-lived vortices on the tropopause with horizontal scales of less than 1500 km (Cavallo and Hakim, 2009), is a characteristic of the Arctic (where there is typically an absence of a strong zonal jet stream in the upper troposphere). Gray et al. (2021) classified Arctic cyclones as being either (i) “unmatched” and (ii) “matched” with a TPV during development, using a statistical matching criterion based on a threshold distance between tracked TPVs and low-level cyclones. It was found that unmatched cyclones are initially dominated by low-level vorticity such that vorticity decreases with height. These cyclones occur most commonly along the northern coast of Eurasia (Figure 7 in Gray et al., 2021), in association with high baroclinicity on the Arctic frontal zone (AFZ; Day and Hodges, 2018; Serreze et al., 2001). In contrast, matched cyclones are dominated by upper-level vorticity (vorticity increases with height). Matched cyclones are associated with reduced tilt and baroclinicity, and a single columnar vortex structure at maximum intensity (like the summer-time Arctic cyclone composite in Vessey et al., 2022). Matched cyclones track most frequently along the North American coastline (Fig. 7 in Gray et al., 2021), consistent with the climatological location of TPVs (Cavallo and Hakim, 2010).

In this study, Arctic cyclones will be classified in terms of their vorticity structure during development as either (i) low-level dominant or (ii) upper-level dominant. Note that by thermal wind balance, these cyclones have (i) low-level warm cores (i.e. a horizontal

temperature maximum) and (ii) tropospheric cold cores respectively. This is somewhat similar to the unmatched and matched classification used by Gray et al. (2021) but focuses on the vertical gradient in vorticity rather than the identification of TPVs. These classifications are based on cyclone structure at an instant, in contrast to the Petterssen and Smebye (1971) classification of type A (low-level forcing) and type B (upper-level forcing) cyclones, which describes the development mechanisms.

One of the biggest uncertainties in the modelling of Arctic cyclones is the interaction with the surface and sea ice. Turbulent fluxes of momentum, heat, and moisture in the boundary layer (BL) are critical to understanding the cyclone–sea ice interaction. It is known that BL turbulent fluxes have large impacts on the evolution of mid-latitude cyclones. Here we discuss the momentum fluxes first (sensible heat fluxes are discussed in a later paragraph). Friction acts to reduce the intensity of cyclones, with Valdes and Hoskins (1988) demonstrating that surface drag can reduce the growth rates of baroclinic systems by up to 50%. The dominant physical mechanism responsible for this is often assumed to be Ekman pumping. In Ekman pumping, BL friction causes the near-surface wind to weaken and turn toward the low centre. The subsequent convergence forces ascent at the BL top, which acts to spin down the cyclone via barotropic vortex squashing (Sect. 8.7 in Hoskins and James, 2014, and Sect. 8.4 in Holton and Hakim, 2012).

Previous studies have used a potential vorticity (PV) framework to identify the mechanisms by which BL processes impact mid-latitude cyclones. PV is a central variable in the evolution of baroclinic systems (e.g. Hoskins et al., 1985), considering both vorticity and stratification:

$$P = \frac{1}{\rho} \vec{\zeta}_a \cdot \nabla \theta \quad (3.1)$$

where P is the Rossby-Ertel PV ($\text{K m}^2 \text{kg}^{-1} \text{s}^{-1}$), ρ is density (kg m^{-3}), $\vec{\zeta}_a$ is absolute vorticity (s^{-1}), and θ is potential temperature (K). PV is materially conserved for adiabatic, inviscid motion, but not in the presence of friction and diabatic heating. Lagrangian changes of PV are expected in the BL where friction and diabatic heating are important. The benefit of using a PV framework is that structural changes within a cyclone can be

inferred from any changes in PV, with the constraint of thermal wind balance. A PV framework is used over an energetics framework, for example, where changes in circulation and the constraint of thermal wind balance are not transparent.

The impact of BL friction on a (barotropic) cyclonic vortex can be understood in the PV framework by following an idealised thought experiment from Sect. 17.6 in Hoskins and James (2014). Friction weakens the near-surface winds in a cyclone, reducing the azimuthal cyclone circulation (i.e. the vertical component of vorticity), and therefore reduces PV in the BL near the low centre. In a balanced state, there is both a reduction in cyclonic circulation and BL static stability. To achieve this, in the absence of other non-conservative processes, isentropes must rise, increasing the static stability above the BL. To conserve PV above the BL, vorticity must decrease there. This is the Ekman pumping process, characterised by a negative PV tendency in the BL, and a secondary circulation with inflow within the BL and ascent near the cyclone centre which acts to spin down vorticity in and above the BL.

The PV framework also reveals a second frictional process in mid-latitude cyclones, in which friction acts to alter horizontal vorticity and circulation in the x - z and y - z planes. This process is called “frictional baroclinic PV generation” and is most prominent in regions of strong horizontal temperature gradients where isentropes have significant tilt, such as fronts. In this process, PV is generated in the BL where surface winds oppose the tropospheric thermal wind (Cooper et al., 1992). This frictional baroclinic PV generation occurs mainly to the east and north-east of cyclone centres along the warm front (Adamson et al., 2006; Plant and Belcher, 2007; Stoelinga, 1996; Vanni ere et al., 2016). Boutle et al. (2007) found evidence of both Ekman pumping and baroclinic PV generation in multiple model simulations, with the relative importance of each term depending on cyclone initialisation. In baroclinic wave cyclones with strong low-level temperature gradients, baroclinic generation dominates (Adamson et al., 2006; Boutle et al., 2007). Consistent with this, Stoelinga (1996) found that BL friction generated mainly positive low-level PV in their mid-latitude cyclone modelling study. However, a sensitivity experiment showed that the overall effect of surface drag was to produce a weaker cyclone

due to the reduced development of the upper-level wave (i.e. reduced baroclinicity and mutual growth of the upper and lower waves). This is consistent with the baroclinic PV mechanism described by Adamson et al. (2006), whereby positive PV generated in the BL is ventilated out of the BL by the warm conveyor belt (WCB) and advected above the low centre. This positive PV is associated with increased static stability above the BL, acting as an insulator to reduce the coupling of the upper and lower levels, reducing the cyclone growth rate. Note that both frictional Ekman pumping and the baroclinic PV mechanism have impacts above the BL (in fact Boutle et al., 2015, suggest that these processes act in union to maximise cyclone spin-down), demonstrating that the role of surface friction in a cyclone is more complicated than the simple Ekman spin-down of vorticity in a barotropic vortex.

Sensible heat fluxes have a direct effect on PV by altering static stability in the BL. For example, Chagnon et al. (2013) identified a region of negative BL PV behind the cold front of a mid-latitude cyclone, generated due to strong upward sensible heat fluxes (i.e. the surface losing heat to the overlying atmosphere), associated with reduced BL static stability. Hualand and Spengler (2020) and Bui and Spengler (2021) demonstrated that the direct effect of surface sensible heat fluxes is to weaken mid-latitude cyclone development by reducing low-level baroclinicity, using PV and energy frameworks respectively in idealised modelling setups. However, both studies found that the impact of sensible heat fluxes was relatively small compared to that of latent heating. Sensible heat fluxes also modify the action of friction by altering BL stability and by weakening frontal gradients (Plant and Belcher, 2007).

This PV framework has been used exclusively to study mid-latitude cyclones. The role of BL processes in the evolution of summer-time Arctic cyclones has not yet been investigated. Differences are expected for several reasons: (i) the sea ice surface in summer is characterised by increased surface roughness in the MIZ and variable sensible heat fluxes; (ii) there are longer-lived cyclones in the summer-time Arctic, so BL processes have a longer time to act; and (iii) there are different cyclone growth mechanisms and structures in the summer-time Arctic such that BL processes might impact cyclone evo-

lution in different ways.

In this study we aim to answer the following questions using two case studies from summer 2020:

1. What is the nature of the BL processes acting in contrasting summer-time Arctic cyclones?
2. How does the nature of the BL processes change as the cyclones evolve?
3. What is the impact of the BL processes on Arctic cyclones outside the BL?

The paper is structured as follows. The methodology is described in Section 3.2, including the model setup employed and details of the PV framework. Section 3.3 describes two Arctic cyclone case studies from summer 2020. The main results are presented in Section 3.4, with a qualitative comparison to the existing literature on mid-latitude cyclones. A more general discussion is provided in Section 3.5, and the study is concluded in Section 3.6.

3.2 Methodology

3.2.1 Reanalysis data

The study uses data from the ERA5 dataset, the fifth-generation European Centre for Medium-Range Weather Forecasts (ECMWF) reanalysis product (Hersbach et al., 2017, 2020). ERA5 was produced using the ECMWF's Integrated Forecasting System (IFS) model cycle 41r2, which was operational from 8 May to 21 November 2016. The model has spectral truncation TL639 (horizontal resolution ~ 31 km) and 137 terrain-following hybrid-pressure levels from the surface to 0.01 hPa. The 6-hourly data on a 0.25° regular latitude–longitude grid are used to perform an analysis of Arctic cyclones from the 2020 extended summer (May–September) season.

3.2.2 IFS model runs

The primary tool used in the study is the ECMWF global IFS model, coupled with dynamic ocean and sea ice models. Forecasts were run using IFS model cycle 47r1, with spectral truncation O640 (horizontal resolution ~ 18 km) and 91 terrain-following hybrid-pressure levels up to 0.01 hPa. This is the same setup as the control member of the ECMWF ensemble forecasting system (ENS) which was operational from 30 June 2020 to 10 May 2021. A prognostic dynamic–thermodynamic sea ice model, the Louvain-la-Neuve Ice Model (LIM version 2), is used, incorporated into the dynamical ocean model (NEMO version 3.4; Nucleus for European Modelling of the Ocean). Model runs starting at 00Z are used, with 6-hourly forecasts out to 10 days.

In this study the BL height diagnostic from the IFS model is used, which is determined using a bulk Richardson number (ECMWF, 2020). The BL top is defined as the level at which the bulk Richardson number reaches the critical value of 0.25, i.e. the level at which the flow is no longer turbulent. The surface momentum flux and surface sensible heat flux are also used directly from the IFS model and are computed using bulk formulae with exchange coefficients (ECMWF, 2020).

3.2.3 Arctic cyclone tracking

Tracks of Arctic cyclones are identified from ECMWF ERA5 reanalysis data and from the ECMWF IFS model runs (the control member of ENS, model cycle 47r1) using the TRACK programme developed by Hodges (1994, 1995, 2021). The TRACK algorithm is employed on the T5–63 and T5–42 filtered 850 hPa relative vorticity from ERA5 and the ENS control member respectively, identifying anomalies exceeding 10^{-5} s^{-1} . Only tracks that last longer than 1 day and travel more than 1000 km are retained.

3.2.4 A modified cyclone phase space

A modified cyclone phase space for characterising the structure of Arctic cyclones is proposed. This phase space is based on the thermal asymmetry and thermal wind structure of a cyclone, as in Hart (2003), but is presented in a non-dimensionalised and more direct

way. Thermal asymmetry is quantified here as a non-dimensionalised depth-integrated baroclinicity, B , over the 925–700 hPa layer (assumed to be above the BL but below the “steering” level). As in Hart (2003), this represents the linear variation in temperature across the cyclone (of radius 500 km) by splitting the cyclone into a right (R) and left (L) half:

$$B = \frac{1}{f_0 L N} \frac{g}{\theta_0} \frac{1}{\Delta p} \int_{700 \text{ hPa}}^{925 \text{ hPa}} (\theta_R - \theta_L) dp \quad (3.2)$$

where f_0 is the Coriolis parameter (s^{-1}), L is the cyclone length scale (500 km), N is the Brunt–Väisälä frequency (0.01 s^{-1}), g is the gravitational acceleration (9.81 ms^{-2}), θ_0 is the reference potential temperature (273 K), p is the pressure (hPa), and θ_R and θ_L are the areal mean potential temperature over a semi-circle of radius 500 km to the right and left of the cyclone (K). In the Hart (2003) phase space, the cyclone is split in half by the cyclone motion vector. However, Arctic cyclones can be associated with slow movement and remain quasi-stationary for considerable periods of time, such that the motion vector is not well defined. Hence, here B is calculated at every 10° bearing, with the maximum value of B being used at each time. The larger the value of B , the greater the asymmetry and baroclinicity of a cyclone.

Thermal wind balance can be written in terms of vorticity (Equation 12.6 in Hoskins and James, 2014):

$$\frac{\partial \xi}{\partial z} = \frac{1}{f_0} \nabla^2 b' \quad (3.3)$$

where ξ is relative vorticity (s^{-1}), z is height (m), b' is the buoyancy anomaly ($\frac{g}{\theta_0} \theta'$, m s^{-2}), and θ' is the potential temperature anomaly. A system in the Northern Hemisphere where ξ increases with height ($\frac{\partial \xi}{\partial z} > 0$; upper-level dominant) must be in balance with a cold-core thermal wind structure (negative buoyancy anomaly), as $\nabla^2 b' > 0$ corresponds to $b' < 0$ (since $\nabla^2 b' \sim -\frac{b'}{L^2}$ for systems of length scale L). In contrast, ξ decreases with height (low-level dominant) in warm-core systems. Hence, the thermal wind structure is quantified here as a non-dimensionalised vertical gradient of relative vorticity in the 700–400 hPa layer (assumed to be above the “steering” level but below the tropopause):

$$Ro_T = -\frac{L}{N} \frac{\partial \xi}{\partial z} \quad (3.4)$$

where $\frac{\partial \xi}{\partial z}$ is calculated by a linear regression fit of ξ at 50 hPa intervals between 700 hPa and 400 hPa. The quantity Ro_T is the thermal Rossby number; the non-dimensional ratio of the inertial force due to the thermal wind and the Coriolis force. The form in Equation 3.4 is obtained using the Burger number ($Bu = \frac{NH}{f_0 L}$ where H is the height scale), the non-dimensional ratio of the density stratification and Earth's rotation in the vertical, which is assumed to be 1 for the synoptic scale. A positive Ro_T indicates a low-level dominant cyclone and therefore a warm-core structure, whilst a negative Ro_T corresponds to an upper-level dominant or cold-core structure.

The circularly symmetric component of θ' (and equivalently b') can be expressed in terms of the potential temperature at the cyclone centre, θ_C , and a background potential temperature θ_B (representing the average value at a 500 km radius). Making a second-order finite difference approximation: $\nabla^2 \theta' \approx -\frac{\theta_C - \theta_B}{L^2}$, and substituting into Equation 3.4 using thermal wind balance in Equation 3.3 gives:

$$Ro_T = \frac{1}{f_0 L N} \frac{g}{\theta_0} (\theta_C - \theta_B) \quad (3.5)$$

The appeal of this cyclone phase space is that it is non-dimensionalised, and it is dependent on the potential temperature structure of the cyclone only. Note that in Equations 3.2 and 3.5, the quantities $\theta_R - \theta_L$ and $\theta_C - \theta_B$ are scaled in the same way, such that their magnitudes can be directly compared.

3.2.5 PV framework

In the presence of friction and diabatic heating, the Lagrangian evolution of PV is given by:

$$\frac{DP}{Dt} = -\frac{1}{\rho} \nabla \cdot \vec{J} = \frac{1}{\rho} \left[\left(\nabla \times \vec{F} \right) \cdot \nabla \theta + \vec{\zeta}_a \cdot \nabla \left(\frac{D\theta}{Dt} \right) \right] \quad (3.6)$$

where ρ is density (kg m^{-3}) and \vec{F} is the frictional force vector (m s^{-2}). $\vec{J} = -\vec{F} \times \nabla \theta - \vec{\zeta}_a \frac{D\theta}{Dt}$ is the PV flux arising from non-conservative terms in the Haynes and McIntyre (1987) form. The first term on the RHS of Equation 3.6 represents frictional effects on PV, whilst the second term represents diabatic heating effects, which can be split into

sensible (*shf*) and latent (*lhf*) heat flux contributions. Application of Equation 3.6 in the BL would require full three-dimensional fields of friction and diabatic heating, which would be strongly dependent on the three-dimensional structure of parameterised tendencies and would be difficult to interpret. Therefore a simplified expression for the BL depth-averaged PV tendency was derived by Cooper et al. (1992). It is assumed that the horizontal variation of fluxes is substantially smaller than the vertical variation in the BL such that:

$$\vec{F} = \frac{1}{\rho} \frac{\partial \vec{\tau}}{\partial z}, \quad \left. \frac{D\theta}{Dt} \right|_{shf} = -\frac{\partial H}{\partial z} \quad (3.7)$$

where $\vec{\tau}$ is the momentum flux and H is the sensible heat flux. A linear flux gradient is also assumed in the BL, such that fluxes can be specified as a product of their surface values, $\vec{\tau}_S$ and H_S , decreasing linearly to zero at the top of the BL with height h :

$$\vec{\tau} = \vec{\tau}_S S(z), \quad H = H_S S(z), \quad S(z) = \left(1 - \frac{z}{h}\right) \quad (3.8)$$

where $S(Z)$ is a linear function of height in the BL. Note that the convention used here is that $\vec{\tau}_S$ is taken to be in the same direction as the surface wind (i.e. $\vec{\tau}_S$ is the stress that the atmosphere exerts on the surface). The frictional and sensible heating terms on the RHS of Equation 3.6 can be decomposed into the contributions from the vertical and horizontal components in the dot products (where ∇_H is the horizontal gradient operator):

$$\begin{aligned} \frac{DP}{Dt} = & \frac{1}{\rho_0} \underbrace{\left[(\nabla \times \vec{F}) \cdot \hat{\mathbf{k}} \frac{\partial \theta}{\partial z} \right]}_{(F_{EK})} + \frac{1}{\rho_0} \underbrace{\left[(\nabla \times \vec{F}) \cdot \nabla_H \theta \right]}_{(F_{BG})} \\ & + \frac{1}{\rho_0} \underbrace{\left[\vec{\zeta}_a \cdot \hat{\mathbf{k}} \frac{\partial}{\partial z} \left(\frac{D\theta}{Dt} \right)_{shf} \right]}_{(S_V)} + \frac{1}{\rho_0} \underbrace{\left[\vec{\zeta}_a \cdot \nabla_H \left(\frac{D\theta}{Dt} \right)_{shf} \right]}_{(S_H)} + \frac{1}{\rho_0} \underbrace{\left[\vec{\zeta}_a \cdot \nabla \left(\frac{D\theta}{Dt} \right)_{lhf} \right]}_{(L)} \end{aligned} \quad (3.9)$$

where density is assumed constant ($\rho = \rho_0$) within the BL for simplicity. Equations 3.7 and 3.8 can be substituted into Equation 3.9 to give a new expression in terms of $\vec{\tau}_S$, H_S , and the linear function of height $S(z)$. The following depth-average operator is then applied:

$$\frac{\widehat{DP}}{Dt} = \frac{1}{h} \int_0^h \left(\frac{DP}{Dt} \right) dz \quad (3.10)$$

With some manipulation the BL depth-averaged PV tendency equation from Cooper et al. (1992) is obtained, in the form used in Vanni re et al. (2016):

$$\begin{aligned} \frac{\widehat{DP}}{Dt} = & - \underbrace{\frac{\Delta\theta \hat{\mathbf{k}} \cdot (\nabla \times \vec{\tau}_S)}{\rho_0^2 h^2}}_{(F_{EK})} - \underbrace{\frac{\vec{\tau}_S \cdot (\hat{\mathbf{k}} \times \nabla\theta)_h}{\rho_0^2 h^2}}_{(F_{BG})} - \underbrace{\frac{\hat{\mathbf{k}} \cdot \vec{\zeta}_a(z=h) H_S}{\rho_0 h^2}}_{(S_V)} \\ & - \underbrace{\frac{\Delta\vec{v} \cdot (\hat{\mathbf{k}} \times \nabla H_S)}{\rho_0 h^2}}_{(S_H)} + \underbrace{\frac{1}{\rho_0 h} \int_0^h \vec{\zeta}_a \cdot \nabla\theta_{lat} dz}_{(L)} \end{aligned} \quad (3.11)$$

where subscript h refers to the top of the BL, \vec{v} is the horizontal wind vector, and Δ refers to a change in quantity between the surface and the BL top. Equation 3.11 contains 5 terms, each representing a non-conservative process which gives rise to a Lagrangian tendency of PV in the BL. Note that each term in Equations 3.9 and 3.11 has been prescribed a shorthand name according to whether the term is associated with friction (F), sensible heat fluxes (S), or latent heat fluxes (L). Also note that no assumptions are made about PV conservation or invertibility in this derivation. Although these equations have been derived and used previously in the context of mid-latitude cyclones, the assumptions made regarding turbulent mixing are equally applicable in the Arctic.

The F_{EK} term refers to Ekman friction, capturing the impact of friction on the vertical component of vorticity. This term is proportional to the vertical Ekman pumping, and is negative for a cyclone ($\hat{\mathbf{k}} \cdot (\nabla \times \vec{\tau}_S) > 0$) with a stably stratified BL ($\Delta\theta > 0$). The F_{BG} term is called baroclinic PV generation, capturing the impact of friction on the horizontal components of vorticity relating to vertical wind shear. This term is proportional to the horizontal gradient of potential temperature at the BL top, so is large in the vicinity of fronts. The sign of this term depends on the orientation of the surface stress and the thermal wind above the BL (see Section 3.5). In mid-latitude cyclones F_{BG} is positive along the warm front where the surface winds oppose the tropospheric thermal wind (e.g.

Adamson et al., 2006). The S_V term refers to the impact of sensible heat fluxes on the stratification in the vertical. This term is positive for a cyclone ($\zeta_a^z > 0$) with downward sensible heat fluxes ($H_S < 0$). Term S_H is proportional to the horizontal gradient of sensible heat fluxes. Previous studies have found this term to be negligible compared to the other terms (e.g. Plant and Belcher, 2007; Vanni re et al., 2016). Term L represents the effect of latent heating, which is not discussed in this paper.

3.2.6 Depth-integrated PV budget

To understand how the BL PV tendencies impact cyclone evolution, depth-integrated PV budgets will be considered using control volumes centred on the cyclone. Here we consider the quantity $\langle P \rangle$, which represents the mass-weighted volume average of PV, or the ‘‘amount of PV substance’’, following the terminology of Haynes and McIntyre (1990):

$$\langle P \rangle = \iiint \rho P \, dAdz \quad (3.12)$$

Note that $\langle P \rangle$ equals the depth-integrated circulation around the lateral boundary of the control volume only if the top and bottom boundaries of the volume are isentropic surfaces. Since the baroclinic PV generation term depends on the gradient in potential temperature at the top of the BL (Equation 3.11), when this term is strong it is more precise to refer to $\langle P \rangle$ as PV substance than the depth-integrated circulation.

Consider an atmospheric column modelled as a cylinder centred on a cyclone, split vertically into the BL (height h) and free tropospheric layer above. The vector normal to the BL top is $\hat{\mathbf{n}}$, and $\hat{\mathbf{I}}$ is the outward normal to the lateral boundary of the column. The top of the free tropospheric layer is chosen to be an isentropic surface, θ_{top} (at height $z_{top} = z(\theta_{top})$), near the tropopause, which ensures no PV flux across it due to the impermeability theorem (Haynes and McIntyre, 1987). Here $\theta_{top} = 330$ K is used, as this level is found to reside just above the tropopause in the summer-time Arctic. There can be PV flux across the surface between the two layers (as the BL top is not necessarily an isentropic surface), and there can be PV flux across the lateral boundary. Non-conservative processes in the BL and free troposphere are included in the formulation (although the lat-

ter are not calculated explicitly). Note that whilst non-conservative processes in the free troposphere may occur at mid-levels within Arctic cyclones, in particular latent heating, these are not the subject of this study. However, the changes in $\langle P \rangle$ diagnosed in the IFS model include the effects of all processes, including latent heat release above the BL.

Using this setup, the volume integral in Equation 3.12 can be calculated following the method in Saffin et al. (2021) using Gauss' theorem and the Leibniz rule to obtain:

$$\begin{aligned} \frac{d}{dt} \langle P \rangle_{BL} = & \iint \rho h \frac{\widehat{DP}}{Dt} dA - \iint_{z=h} \rho P (\vec{u} - \vec{u}_b) \cdot \hat{\mathbf{n}} dA \\ & - \int_0^h \oint \rho P (\vec{u} - \vec{u}_b) \cdot \hat{\mathbf{l}} dl dz \end{aligned} \quad (3.13)$$

$$\begin{aligned} \frac{d}{dt} \langle P \rangle_{TROP} = & \int_h^{z_{top}} \iint \rho \frac{DP}{Dt} dAdz + \iint_{z=h} \rho P (\vec{u} - \vec{u}_b) \cdot \hat{\mathbf{n}} dA \\ & - \int_h^{z_{top}} \oint \rho P (\vec{u} - \vec{u}_b) \cdot \hat{\mathbf{l}} dl dz \end{aligned} \quad (3.14)$$

where $\frac{d}{dt} \langle P \rangle_{BL}$ and $\frac{d}{dt} \langle P \rangle_{TROP}$ are the depth-integrated PV tendencies in the BL and free tropospheric layer respectively, \vec{u} is the 3D wind vector (m s^{-1}), and \vec{u}_b is the velocity of the boundary of the control volume (m s^{-1}). In this work we examine the LHS of Equations 3.13 and 3.14, and the non-conservative processes in the BL (the first term on the RHS of Equation 3.13). Non-conservative processes in the free troposphere (the first term on the RHS of Equation 3.14), are not explicitly calculated. The second term on the RHS represents the vertical flux of PV across the surface between the two layers. If the BL top is flat, $(\vec{u} - \vec{u}_b) \cdot \hat{\mathbf{n}}$ can be written as $w - \dot{h}$, where w = vertical velocity (m s^{-1}) and \dot{h} = rate of change of BL height (m s^{-1}). The third term on the RHS represents the horizontal fluxes of PV across the lateral boundary. Note that, along with the non-conservative processes in the free troposphere, the vertical and horizontal fluxes of PV are not explicitly calculated here.

3.3 Arctic cyclone case studies

The 2020 extended summer (May–September) season is used as a sample of Arctic cyclones from which to identify case studies for further analysis. An analysis of the cyclones was performed using the ERA5 dataset (Figure 3.1). Arctic cyclones are identified as vorticity maxima with 850 hPa relative vorticity, ξ_{850} , greater than $8 \times 10^{-5} \text{ s}^{-1}$ in the Arctic ($> 70^\circ\text{N}$) at least once along their track. From manual inspection the ξ_{850} constraint was found to be a good filter for distinguishing synoptic-scale Arctic cyclones from smaller-scale vorticity features.

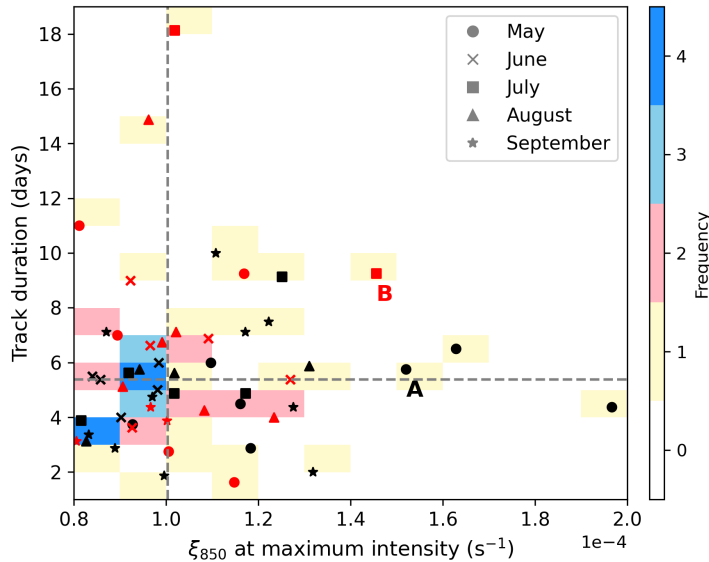


Figure 3.1: 2D histogram of ξ_{850} at maximum intensity (x-axis) and track duration (y-axis) of summer 2020 Arctic cyclones from ERA5. Black and red markers refer to low-level and upper-level-dominant cyclones respectively, as diagnosed by the thermal Rossby number, Ro_T , from the modified cyclone phase space (Section 3.2.4) at the time of maximum growth rate. The shading illustrates the number of cyclones that populate a region of the histogram space. The median values of ξ_{850} at maximum intensity and track duration are demonstrated by the grey dashed lines. Cyclone cases A and B are annotated with the respective letter to the bottom right of the marker.

Using these criteria, 52 Arctic cyclone tracks were identified from the 2020 summer season. The median strength in ξ_{850} was $\sim 10 \times 10^{-5} \text{ s}^{-1}$ at maximum intensity, and the median track duration was approximately 5.4 days (Figure 3.1). In Figure 3.1, Arctic cyclones are also classified as low-level dominant ($Ro_T > 0$; black markers) or upper-level dominant ($Ro_T < 0$; red markers), diagnosed at the time of maximum growth rate. In

2020, 60% of the Arctic cyclones were low-level dominant (31), and 40% were upper-level dominant (21) during development. The median track duration of the low-level-dominant cyclones was 5.13 days, whilst the upper-level-dominant cyclones had a longer median track duration of 6.75 days. The median strength at maximum intensity was similar for both sets of cyclones ($\sim 10 \times 10^{-5} \text{ s}^{-1}$).

For the purposes of this investigation two case studies are chosen, one with low-level-dominant development and the other with upper-level-dominant development. Cyclones A and B (annotated in Figure 3.1) are selected as the strongest cyclones that spend a considerable amount of time over sea ice (note that the two strongest cyclones of the season were not chosen as case studies because the cyclone centres did not track over sea ice). Cyclone A (low-level-dominant development) occurred in May 2020 and was the third strongest cyclone of summer 2020 with $\xi_{850} \sim 15 \times 10^{-5} \text{ s}^{-1}$ at maximum intensity and a lifetime of almost 6 days. Cyclone B (upper-level-dominant development) was the fourth strongest cyclone with $\xi_{850} \sim 14 \times 10^{-5} \text{ s}^{-1}$ at maximum intensity, with a longer track duration of almost 10 days.

The cyclone case studies were analysed in both the ERA5 reanalysis dataset and IFS forecasts (Table 3.1). IFS forecast start times (starting at 00Z) were selected that were closest to, but more than 24 hours before, the time of maximum growth rate of each cyclone. Consequently, 00Z 7 May and 00Z 25 July are the chosen forecast start dates used for Cyclones A and B respectively throughout the paper. The maximum growth rate of Cyclone A occurred at 12Z 8 May in both ERA5 and the IFS forecasts, with the system reaching maximum intensity 12 hours later at 00Z 9 May in ERA5 and 18 hours later at 06Z 9 May in the IFS forecast. In ERA5, Cyclone B underwent maximum growth at 00Z 27 July and reached maximum intensity at 00Z 28 July, compared to 18Z 26 July and 12Z 28 July respectively in the IFS forecast.

Cyclone A developed as part of a baroclinic wave over western Russia before moving northwards into the Kara Sea (Figure 3.2a). In both ERA5 and the IFS forecast, the cyclone develops along an elongated low-level front; however, the tracking algorithm iden-

A	Max. growth rate	Max. intensity	Separation (km)		
			00Z 7 May	12Z 8 May	06Z 9 May
ERA5	12Z 8 May	00Z 9 May	1290	40	63
IFS	12Z 8 May	06Z 9 May			
B	Max. growth rate	Max. intensity	Separation (km)		
			00Z 25 July	18Z 26 July	12Z 28 July
ERA5	00Z 27 July	00Z 28 July	929	96	60
IFS	18Z 26 July	12Z 28 July			

Table 3.1: Summary table of Cyclones A and B tracked using filtered data from ERA5 (T5-63) and the IFS forecasts (T5-42): the time of maximum growth rate, the time of maximum intensity (as evaluated from the tracks), and the great circle separation distance between the cyclone tracks in ERA5 and the IFS forecasts at three selected times (forecast start date, maximum growth rate, and maximum intensity).

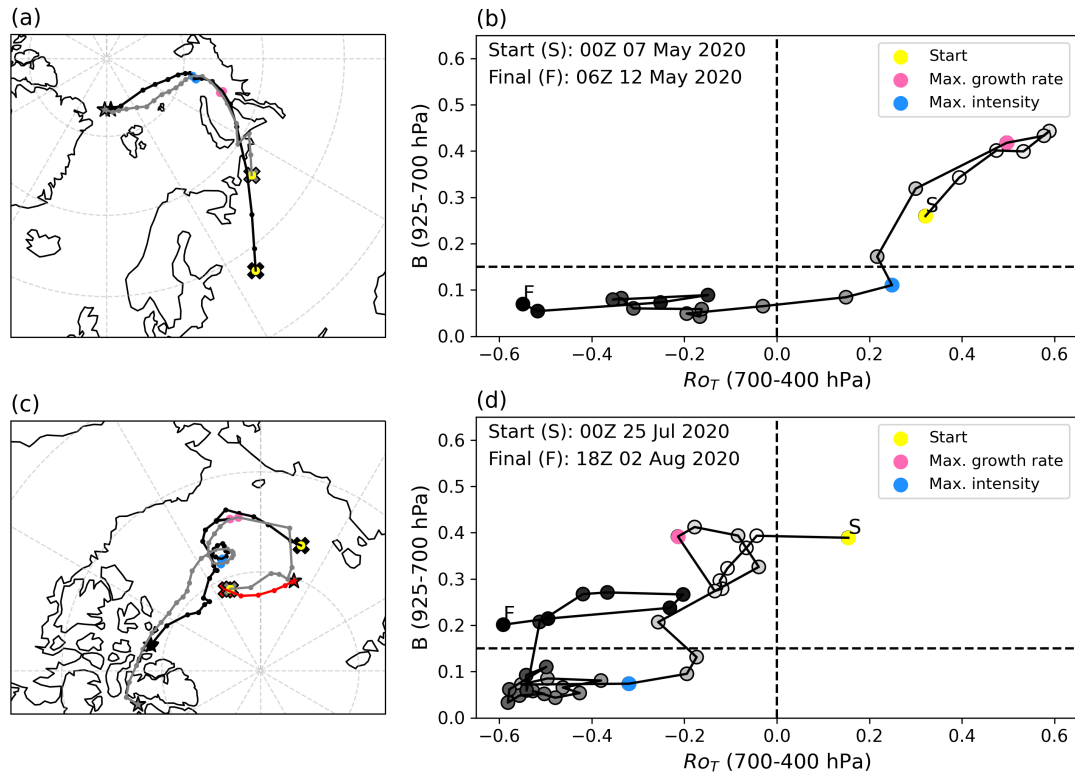


Figure 3.2: (a) The 6-hourly Cyclone A tracks from ERA5 (T5-63; black line) and the IFS run starting 00Z 7 May 2020 (T5-42; grey line) over the shared temporal coverage period 00Z 7 May - 06Z 12 May 2020. The start of the tracks is marked by a cross, whilst the end is marked by a star. The full length of the tracks are 18Z 6 May - 06Z 12 May (ERA5) and 00Z 7 May - 12Z 12 May (IFS). (b) Cyclone A from ERA5 in the adapted cyclone phase-space, from S (start; white) to F (finish; black). The coloured points in (a) and (b) correspond to the times in Table 3.1: 00Z 7 May (yellow), 12Z 8 May (pink), and 06Z 9 May (blue). (c) As in (a) but for Cyclone B, with IFS run starting 00Z 25 July 2020 over the shared temporal coverage period 00Z 25 July - 18Z 2 August 2020. The full length of the tracks are 18Z 24 July - 18Z 2 August (primary ERA5; black line), 06Z 14 July - 06Z 26 July (secondary ERA5; red line), and 00Z 25 July - 12Z 8 August (IFS; grey line). (d) As in (b) but for Cyclone B. The coloured points in (c) and (d) correspond to the times in Table 3.1: 00Z 25 May (yellow), 18Z 26 July (pink), and 12Z 28 July (blue).

tifies the cyclone centres at different places along the feature at 00Z 7 May (likely due to uncertainty in the position of the frontal wave along the front). As the system develops, the tracks converge. This can be seen in Table 3.1, with the separation reducing from 1290 km at the start of the forecast to 40 km at maximum growth rate, and also spatially in Figure 3.2a. The evolution of the cyclone structure is demonstrated by the adapted cyclone phase space (Section 3.2.4) in Figure 3.2b. The system is initially low-level dominant (low-level warm core) with large baroclinicity around the time of maximum growth rate. Approaching maximum intensity, and at subsequent times, the cyclone becomes more axisymmetric and ultimately becomes upper-level dominant (cold core).

Maps of Cyclone A at 6 hours after the time of maximum growth rate from the IFS forecast are presented in Figure 3.3. The surface cyclone is in the Kara Sea at this time, with the warm sector to the south over Russia (identified by the region of the high values of 850 hPa potential temperature to the south of the cyclone) and the warm front on the eastern flank of the warm sector (Figure 3.3a). The cyclone is positioned downstream of an upper-level trough, identified by low potential temperature values on the dynamic tropopause (i.e. the 2 PVU surface; Figure 3.3b). A meridional cross-section is taken through the cyclone centre from 65°N (S) to 89°N (N). In vertical cross-section (Figure 3.3c) the tilted isentropes are indicative of a baroclinic zone to the poleward side of the cyclone associated with a developing bent-back front. The upper-level trough is seen as a lowering of the tropopause to the south of the low-level cyclone (7 km height, 305 K), with the downstream ridge situated north of the low centre (9 km height, 310 K). The dip in the isentropes over the cyclone centre (marked by the red L) indicates a warm-core structure developing, consistent with a low-level-dominant cyclone and the strongest winds just above the BL. The positive PV at low levels above the low centre is reminiscent of that generated due to the frictional baroclinic PV mechanism in mid-latitude cyclones (e.g. Adamson et al., 2006).

Cyclone B initially develops baroclinically north of the AFZ along the Eurasian coastline before interacting with a TPV in the Beaufort Sea (Figure 3.2c). The cyclone track from ERA5 captures the low-level baroclinic growth phase, with the vorticity maximum

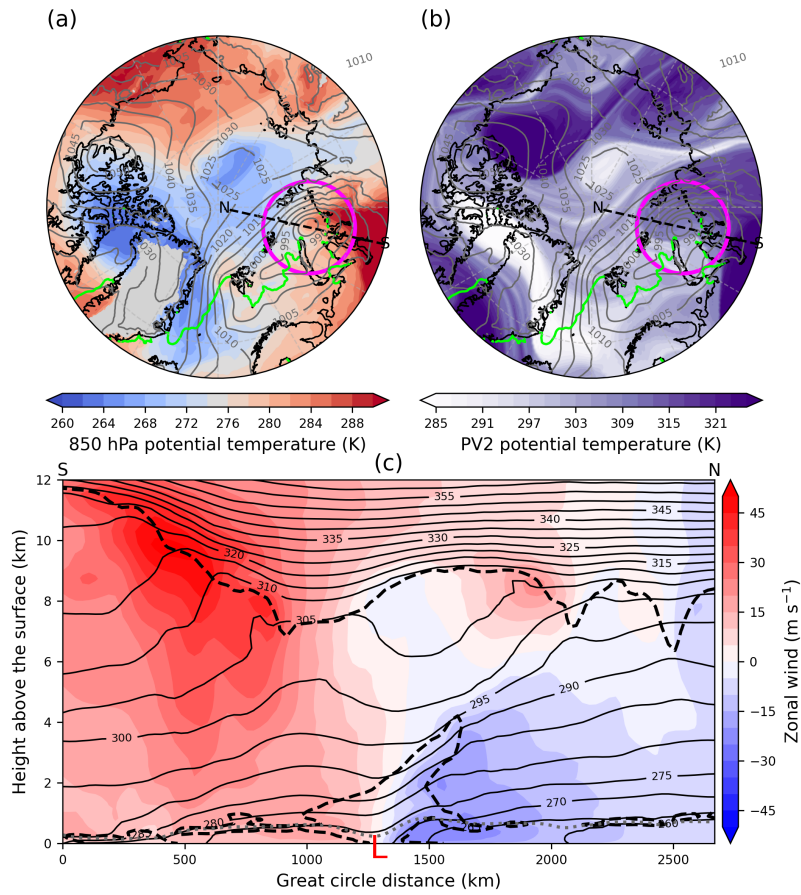


Figure 3.3: Cyclone A at 18Z 8 May 2020 from IFS run starting 00Z 7 May 2020. (a) 850 hPa potential temperature (K; shading) and (b) potential temperature on the PV2 surface (K; shading), overlain with mean sea level pressure (hPa; grey contours), the sea ice edge (0.15 sea ice concentration; green contour). The magenta circle marks the 750 km radius about the cyclone centre as determined by TRACK. The dashed black lines mark the north-south cross-section taken at the longitude of the cyclone centre from south (S; 65 °N) to north (N; 89 °N). (c) Vertical cross-sections linearly interpolated at 100 points between S and N of zonal wind (m s^{-1} ; shading), potential temperature (K; solid black contours), 2 PVU contour (dashed black line) and BL top (dotted grey line). Minimum mean sea level pressure is marked with a red L.

north of the Eurasian coastline (black line in Figure 3.2c). The TPV in this case is very long-lived and can be tracked back to 8 July 2020 (not shown). There is a secondary track from ERA5, following a low-level vorticity maximum below the pre-existing TPV (red track in Figure 3.2c). This track ends once the TPV begins to interact with the low-level baroclinic disturbance at 06Z 26 July. The IFS forecast track (grey track in Figure 3.2c) picks up this vorticity maxima associated with the TPV rather than the initial baroclinic disturbance (likely due to the differences between the reanalysis and forecast or the different spectral filtering employed). As a result, the separation between the tracks is initially

large but reduces as the cyclone develops (Table 3.1). From the ERA5 track in the cyclone phase space, Cyclone B is initially baroclinic and low-level dominant (labelled S) but becomes upper-level dominant due to the interaction with the TPV (Figure 3.1). After maximum intensity the cyclone obtains a long-lived (~ 4 days) axisymmetric cold-core columnar vortex structure in the Beaufort Sea.

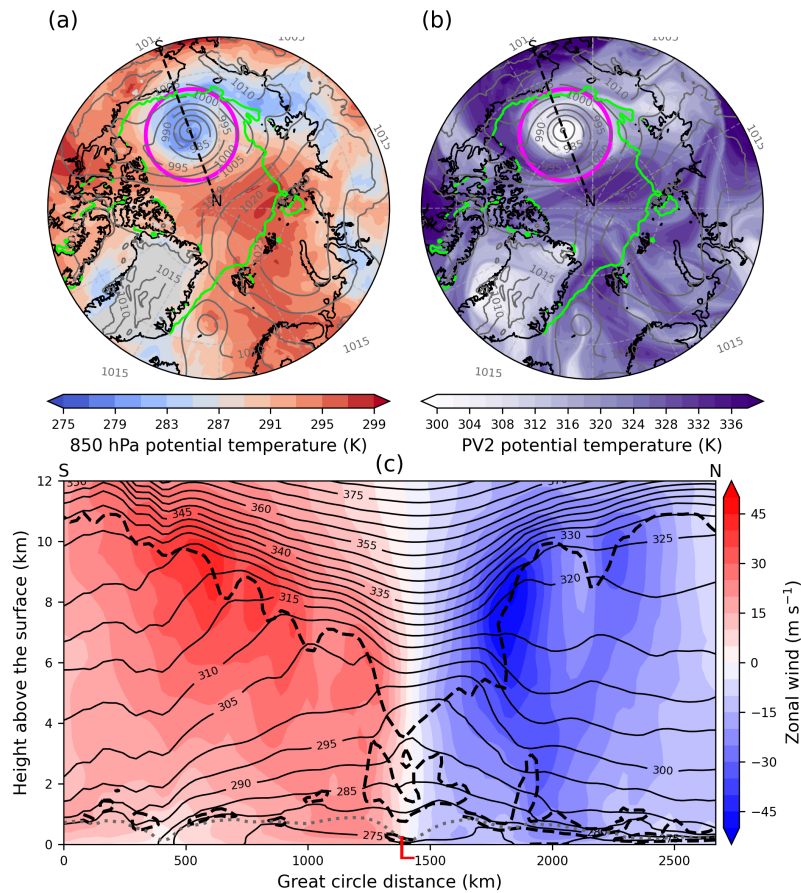


Figure 3.4: As in Figure 3.3, but for Cyclone B from IFS run starting 00Z 25 July 2020, at 12Z 28 July 2020.

Maps of Cyclone B at maximum intensity from the IFS forecast are presented in Figure 3.4. The surface cyclone is located over the sea ice in the Beaufort Sea at this time, associated with a cold air mass at low levels (Figure 3.4a), and the TPV is vertically stacked above the cyclone (low potential temperature values in Figure 3.4b). In the cross-section the axisymmetric cold-core structure is evident with isentropes bowing up throughout the troposphere centred over the cyclone (Figure 3.4c). The TPV is evident as a lowering of the tropopause to ~ 4 km. The peak winds of the system are on the flanks of the TPV,

consistent with the cold-core and upper-level dominant system. The cold-core columnar vortex structure of Cyclone B looks quite different to that of a typical mid-latitude cyclone. There is some low-level PV above the BL in the vicinity of the cyclone but not in a coherent region above the cyclone centre as in Cyclone A.

3.4 Results

3.4.1 Boundary Layer PV tendencies

The BL PV tendencies from Equation 3.11 are presented for Cyclone A at 6 hours before maximum growth rate (Figure 3.5). The Ekman friction term, F_{EK} , is negative over the cyclone centre (Figure 3.5a), indicative of the Ekman pumping mechanism. The frictional baroclinic generation term, F_{BG} , is positive to the north and east of the cyclone centre, along the cyclone bent-back warm front (Figure 3.5b), as seen in the typical developing mid-latitude cyclone. The sensible heat flux term, S_V , is positive over the cyclone centre and in the warm sector (Figure 3.5c), where the atmosphere is warmer than the underlying surface with downward sensible heat fluxes. Note that the S_H term is much smaller than the other terms and is therefore not shown in Figure 3.5. The sum of the BL PV tendencies (Figure 3.5d) resembles the baroclinic generation term, indicating that the Ekman generation is mostly cancelled by the sensible heat flux generation at this time. The BL PV tendencies for Cyclone A resemble those of a typical baroclinic wave mid-latitude cyclone (e.g. Adamson et al., 2006; Boutle et al., 2007).

The BL PV tendencies are presented for Cyclone B at maximum intensity after the cyclone has transitioned to a vertically stacked columnar vortex structure (Figure 3.6). As in Cyclone A, the F_{EK} term is negative over the cyclone centre (Figure 3.6a), as would be expected in a cyclonic weather system. However, unlike Cyclone A (and typical mid-latitude cyclones), the F_{BG} term is negative, with the largest magnitude to the north and east of the cyclone in the WCB region (Figure 3.6b). This is due to the vertically stacked cold-core structure of the cyclone (Figures 3.2d and 3.4), with the cyclonic BL winds oriented in the same direction as the cyclonic winds of the TPV directly aloft (i.e. in the

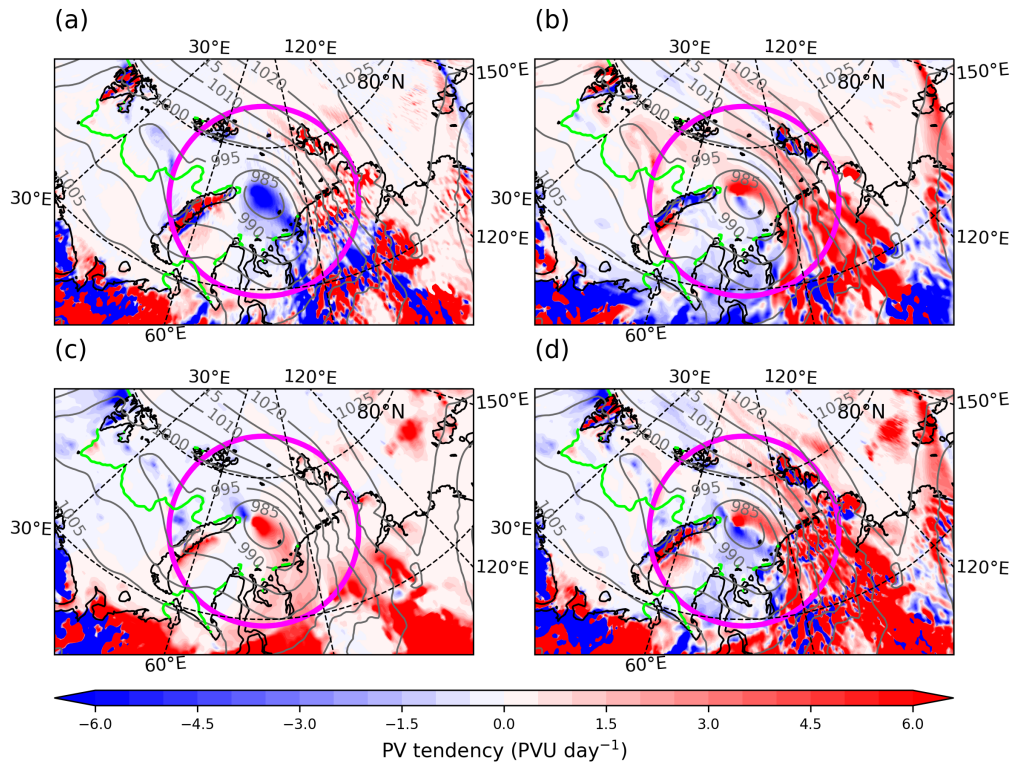


Figure 3.5: BL depth-averaged PV tendencies from Equation 3.11 for Cyclone A at 18Z 8 May 2020 (6 hours before maximum growth rate) from IFS run starting 00Z 7 May 2020. (a) F_{EK} , (b) F_{BG} , (c) S_V , and (d) the sum of F_{EK} , F_{BG} , S_V and S_H (PVU day^{-1} ; shading), mean sea level pressure (hPa; grey contours) and the sea ice edge (0.15 sea ice concentration; green contour). The magenta circle marks 750 km from the cyclone centre.

same direction as the tropospheric thermal wind), in contrast to the tilted frontal structure of Cyclone A (see Section 3.5). The S_V term is positive, with the largest magnitude in the WCB region (Figure 3.6c), indicative of downward sensible heat fluxes over sea ice. This means that the cold air mass associated with the cyclone (Figure 3.4a) is still warmer than the sea ice surface, which is locked at 0°C . Like for Cyclone A, the sum of the BL PV tendencies resembles the F_{BG} term, indicating that F_{EK} is mostly cancelled by S_V , except for the negative PV tendencies at the cyclone centre where F_{EK} is the dominant term. It is the frictional baroclinic PV generation term, F_{BG} , that distinguishes Cyclone B from Cyclone A (and mid-latitude cyclones).

Boutle et al. (2007) demonstrated that in a mid-latitude cyclone initialised without a meridional surface temperature gradient, the (negative) F_{EK} term dominates over (mostly positive) F_{BG} . Cyclone B has some similarities with this experiment, with the sea ice

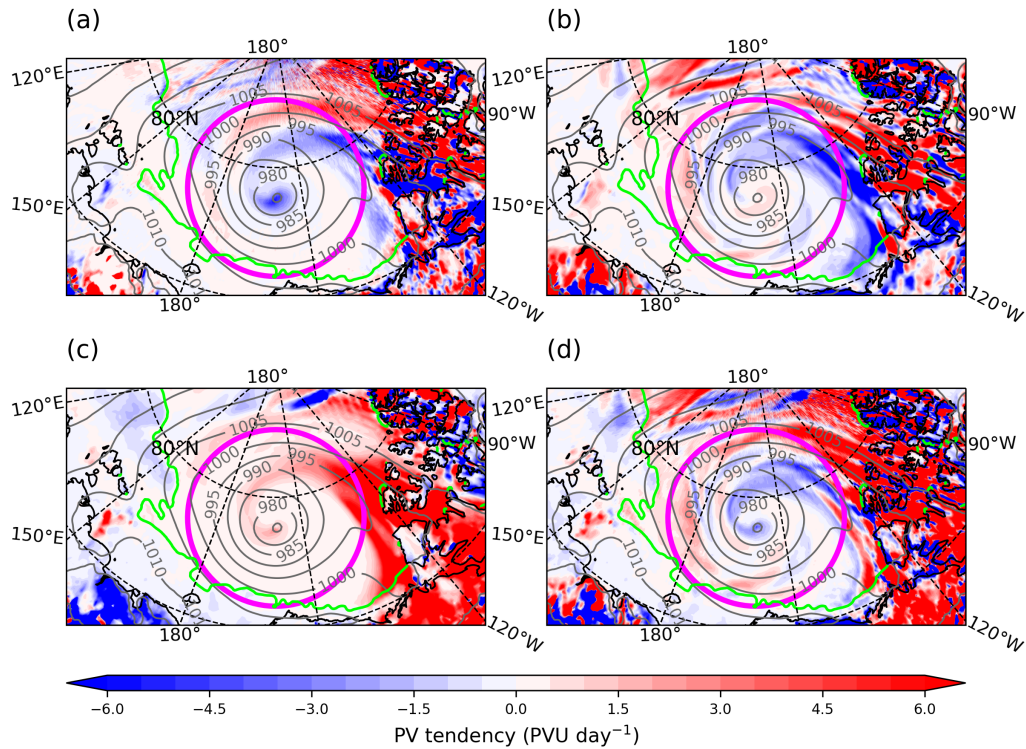


Figure 3.6: As in Figure 3.5, but for Cyclone B from IFS run starting 00Z 25 July 2020 at 12Z 28 July 2020 (maximum intensity).

providing a quasi-uniform surface temperature to limit low-level baroclinicity. However, unlike the Boutle et al. (2007) experiment, the vertically stacked cold-core columnar vortex of Cyclone B results in a large region of negative F_{BG} , which is of a similar magnitude to the F_{EK} term.

3.4.2 Cyclone depth-integrated PV budget

Time series of the terms relevant to the depth-integrated PV budget of Cyclones A and B are presented in Figures 3.7 and 3.8 respectively. The BL PV tendencies in Figures 3.7a and 3.8a have been multiplied by density and BL height to give a BL depth-integrated PV tendency (see first term on RHS of Equation 3.13). Note that the y scale in Figure 3.7a is almost an order of magnitude larger than in Figure 3.8a due to the larger magnitudes of F_{BG} and S_V in Cyclone A during development. The larger magnitude of F_{BG} might be due to greater surface roughness over land or greater baroclinicity. The surface energy balance is also changed over land, resulting in large downward sensible heat fluxes and a large S_V term.

More generally, the magnitude of the BL PV tendencies is impacted by several (interrelated) factors, including the underlying surface, cyclone strength, and BL height, h . For instance, stronger cyclone winds correspond with larger vorticity and surface fluxes and therefore larger PV tendencies (Equation 3.11). Furthermore, the depth-integrated PV tendencies scale by $\frac{1}{h}$ such that the magnitude decreases with increasing h . Cyclone A has stronger low-level winds than upper-level-dominant Cyclone B but with stable shear-driven BLs also has a slightly higher h (with an average value of ~ 800 m at maximum intensity compared to ~ 600 m), with opposing effects on the magnitude of the BL PV tendencies. Clearly, the magnitude of the BL PV tendencies varies with cyclone-specific details, which differ between any two cyclones. However, in this study, we are focused on the fundamental mechanisms in cyclones with contrasting structure, so it is the general evolution and sign of the BL PV tendencies that are the main interest rather than the absolute magnitude. In the subsequent analysis, we focus on the general evolution and sign when comparing the case studies.

In Cyclone A (Figure 3.7a), the Ekman friction (F_{EK}) term is negative throughout the time series, indicative of the Ekman pumping mechanism acting throughout the cyclone evolution. The baroclinic PV generation (F_{BG}) term is large and positive during the baroclinic growth phase before the maximum intensity, with a reduced magnitude after this time (and becoming generally negative). The sensible heat flux (S_V) term is positive before the time of maximum intensity, dominated by the strong downward heat fluxes in the warm sector (Figure 3.5c). After maximum intensity the S_V term has a smaller magnitude. The S_H term (proportional to the horizontal gradient of sensible heat fluxes) is also presented in Figure 3.7a and has a much smaller magnitude than the other non-conservative terms. The sum of the BL PV tendencies is positive during the baroclinic growth phase (before maximum intensity), dominated by F_{BG} , and is negative once the cyclone has matured.

The volume-averaged PV in the BL, $\langle P \rangle_{BL}$ (Section 3.2.6), of Cyclone A (Figure 3.7b) increases during the baroclinic growth phase up to 6 hours before maximum intensity

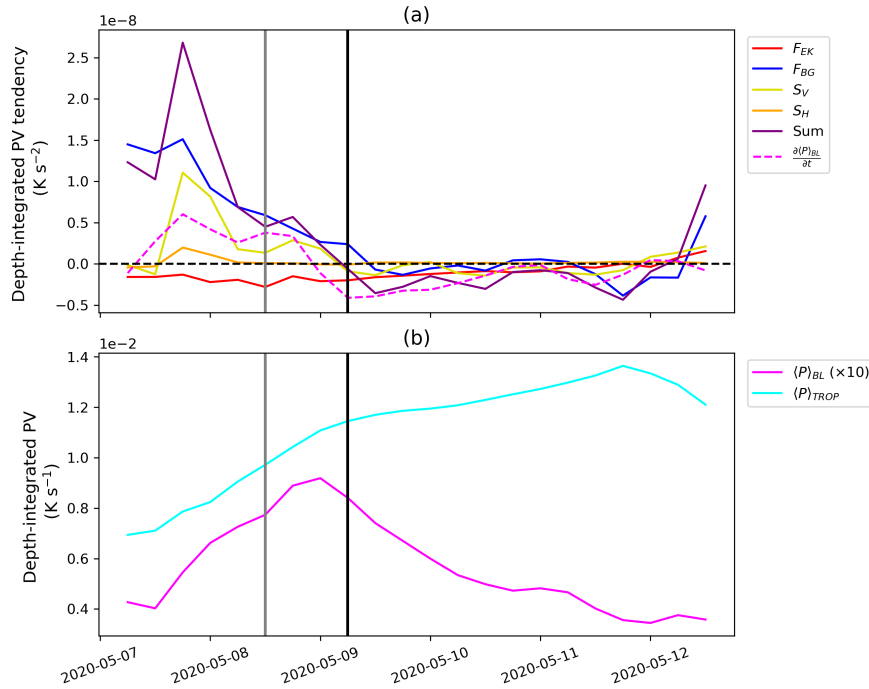


Figure 3.7: Time series of depth-integrated PV and tendencies associated with Cyclone A, from IFS run starting 00Z 7 May 2020, from 00Z 7 May to 12Z 12 May 2020. (a) BL depth-integrated PV tendencies (K s^{-2}): F_{EK} (red line), F_{BG} (blue line), S_V (yellow line), S_H (orange line), sum (purple line) and the BL volume-averaged PV tendency calculated explicitly (LHS of Equation 3.14; dashed magenta line). (b) Volume-averaged PV (K s^{-1}) in the BL and the tropospheric layer with the 330 K isentropic surface as the top of the layer. The grey and black vertical lines correspond to the time of maximum growth rate and maximum intensity.

and decreases after. The rate of change of $\langle P \rangle_{BL}$ is plotted against the BL PV tendency terms in Figure 3.7a (dashed pink line) and corresponds well with the sum of the non-conservative terms (purple line). However, the sum of the non-conservative terms has a larger magnitude before maximum growth rate, which indicates that the vertical and horizontal fluxes of PV into or out of the BL control volume are large at this time, according to Equation 3.13. The volume-averaged PV in the tropospheric layer, $\langle P \rangle_{TROP}$, increases throughout the cyclone lifetime, even after the time of maximum intensity of the low-level cyclone. The increase in $\langle P \rangle_{TROP}$ is dominated by baroclinic wave growth, which in this budget is apparent through the lateral PV fluxes into the volume. Note that $\langle P \rangle_{TROP}$ is approximately 15 times larger than $\langle P \rangle_{BL}$. The fractional rate of growth in the BL and tropospheric layer is similar up to maximum growth rate (i.e. the slopes of $\langle P \rangle_{BL}$ and

$\langle P \rangle_{TROP}$ are similar), which is characteristic of system growth with the BL and upper levels coupled (i.e. lateral PV fluxes in Equations 3.13 and 3.14 are linked due to the baroclinic tilt of the system that is continuous across both layers). Hence, the same BL processes that impact the BL circulation will have an indirect effect on the tropospheric layer also.

In Cyclone B (Figure 3.8) the Ekman friction (F_{EK}) term is negative with maximum magnitude during the baroclinic growth phase at maximum growth rate (Figure 3.8a). The baroclinic PV generation (F_{BG}) term captures two distinct periods of cyclone development. F_{BG} is positive during the baroclinic growth phase but is approximately an order of magnitude smaller than in Cyclone A (Figure 3.7a), indicating reduced baroclinicity. After the time of maximum growth rate, F_{BG} reduces and rapidly becomes strongly negative, decreasing to an absolute minimum 6 hours before maximum intensity. The evolution of F_{BG} differs from that of Cyclone A, with the transition from positive to negative occurring before maximum intensity for Cyclone B and the negative F_{BG} values having a larger magnitude (relative to the magnitude of the positive values before transition). The sensible heat flux (S_V) term is largely positive due to downward sensible heat fluxes over the sea ice. The sum of the non-conservative BL terms is positive before maximum intensity, dominated by the S_V term, and is close to zero afterwards with the positive S_V term reducing in magnitude and having a greater (negative) contribution from F_{BG} . Note that the magnitude of F_{BG} is greater than F_{EK} in Cyclone A (a more baroclinic cyclone; Figure 3.7a), whereas their magnitudes are comparable in Cyclone B due to a more barotropic structure (Figure 3.8a).

Volume-averaged PV in the BL, $\langle P \rangle_{BL}$, of Cyclone B increases during the baroclinic growth phase up to maximum intensity and decreases after (Figure 3.8b), similar to that in Cyclone A in profile and magnitude (Figure 3.7b). The rate of change of $\langle P \rangle_{BL}$ (Figure 3.8a) corresponds well with the sum of the BL non-conservative terms. The differences between the two series are likely due to vertical and horizontal PV flux terms and also possibly latent heating (which is not explicitly calculated here). Unlike in Cyclone A, $\langle P \rangle_{TROP}$ is relatively constant (Figure 3.8b). This is related to the pre-existing TPV as-

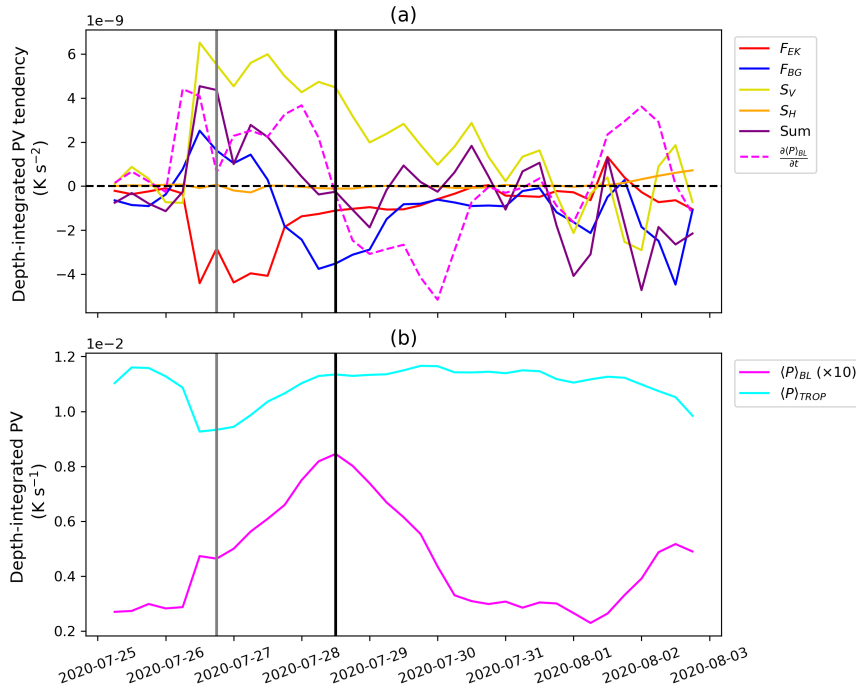


Figure 3.8: As in Figure 3.7, but for Cyclone B from IFS run starting 00Z 25 July 2020, from 00Z 25 July to 00Z 2 August. Note that the y-scale in (a) is an order of magnitude smaller than that of Figure 3.7a.

sociated with Cyclone B. Applying a similar reasoning used in Martínez-Alvarado et al. (2016), if the control volume containing the TPV is in an isentropic layer (i.e. the BL top is an isentropic surface as well as the top boundary), and all the non-conservative processes lie within the circuit, then the circulation is conserved if the lateral boundary is a material surface. When the system (TPV and low-level cyclone) becomes a cut-off axisymmetric circuit, this condition is satisfied, and the circulation ($\langle P \rangle$) is conserved. Cyclone B largely satisfies this condition, except during the baroclinic growth phase (i.e. the dip in $\langle P \rangle_{TROP}$ in Figure 3.8b at maximum growth rate), when the cyclone and TPV start to interact. The coupling between the BL and tropospheric layer is reduced such that the BL processes do not significantly impact the free-tropospheric circulation at this stage. This is very different to the evolution of the system $\langle P \rangle$ in Cyclone A (Figure 3.7).

This analysis has revealed how the magnitude and sign of the cyclone-average BL PV tendencies evolve in time and how the baroclinic PV generation term, F_{BG} , differs between

the cyclones. A key question is the extent to which this difference modifies the subsequent evolution of the cyclones. Whilst a quantitative assessment of this effect, which would require a piecewise PV inversion procedure, is beyond the scope of this work, in the following section the impacts of the BL processes are qualitatively inferred by analysing the 3-D structure of the cyclones and their associated PV fields. In Section 3.5 the F_{BG} term is examined in more detail.

3.4.3 Cyclone structural evolution

Low-level (up to 700 hPa) north–south cross-sections of Cyclone A at selected times are presented in Figure 3.9. The panel below each cross-section shows the profile of the (depth-averaged) BL PV tendency terms interpolated along the section (just shown within 750 km of the cyclone centre for clarity). At the time of maximum growth rate (Figure 3.9a) the cyclone has a baroclinic tilted structure, with tilted isentropes associated with positive PV over the cyclone centre. Winds exceed 15 m s^{-1} in the BL at this time. F_{EK} is negative below the cyclone centre, whilst F_{BG} is positive to the north (where the BL winds are strongest). S_V is positive to the south of the cyclone centre, where there are downward sensible heat fluxes in the warm sector. This is consistent with a region of positive PV in the BL on the southern end of the cross-section. The sum of the BL PV tendencies is positive to the north of the cyclone and negative to the south.

At the time of maximum intensity (Figure 3.9b), the system has obtained a warm-core axisymmetric structure over the sea ice, with isentropes dipping down over the low-pressure centre. The system is very strong at low levels at this time, with winds speeds exceeding 30 m s^{-1} in the BL. There is large positive PV above the BL constrained within a ~ 200 km radius of the cyclone centre, associated with enhanced static stability, and is likely indicative of the frictional baroclinic PV mechanism. As at maximum growth rate, F_{EK} is negative over the cyclone centre, whilst F_{BG} is positive to the north of the cyclone below the strongest BL winds. The magnitude of S_V is reduced at this time. The BL height peaks where the winds are strongest, indicative of a wind-driven BL and consistent with small sensible heat fluxes. The sum of the BL PV tendencies is again positive to the north of the cyclone, consistent with positive PV there, and negative to the south of the cyclone,

where there is negative PV.

At 24 hours after the time of maximum intensity (Figure 3.9c), the cyclone has lost its warm core and has now developed a larger-scale cold-core structure, with the isentropes bowing upwards. This resembles the composite cold-core axisymmetric structure of summer-time Arctic cyclones after maximum intensity from Vessey et al. (2022). The isentropes have moved upward, taking the low-level positive PV from 950 hPa up to 800 hPa. The wind field is now upper-level dominant but with a deep structure such that winds still exceed 20 m s^{-1} in the BL. The BL PV tendencies are now reduced in magnitude (due to weaker winds), but the F_{BG} term is notably the dominant term and is predominantly negative. The negative F_{BG} term is also seen in Figure 3.7 after maximum intensity and likely reflects the cyclone's transition to an axisymmetric cold-core structure. The cyclone retains this cold-core axisymmetric structure for 2 more days before dissipating (Figure 3.2b).

This cross-section analysis is also performed for Cyclone B (Figure 3.10). At the time of maximum growth rate (Figure 3.10a), the cold-core structure of the pre-existing TPV is evident in the isentropes. There are baroclinic zones to the north and south of the TPV, with tilted isentropes and positive near-surface PV. Cyclone B develops on the baroclinic zone to the south of the TPV. The TPV is associated with a strong cyclonic wind field at the tropopause, but this does not extend to the BL at this time. The BL PV tendency terms are largest to the south of the section over the ocean. F_{EK} is positive, which is consistent with the cyclone centre (as diagnosed by ξ_{850}) not being co-located with the minimum in sea level pressure at this time (not shown). F_{BG} is positive, consistent with the system undergoing baroclinic growth. With S_V also being positive, there is net positive PV being generated over the cyclone centre.

At the time of maximum intensity (Figure 3.10b), the cyclone has obtained an axisymmetric cold-core structure. The cyclonic winds about the system now extend to the lower levels, with winds greater than 20 m s^{-1} in the BL. PV is small within the BL at this time. The magnitude of the BL PV tendency terms in Cyclone B is approximately half that of

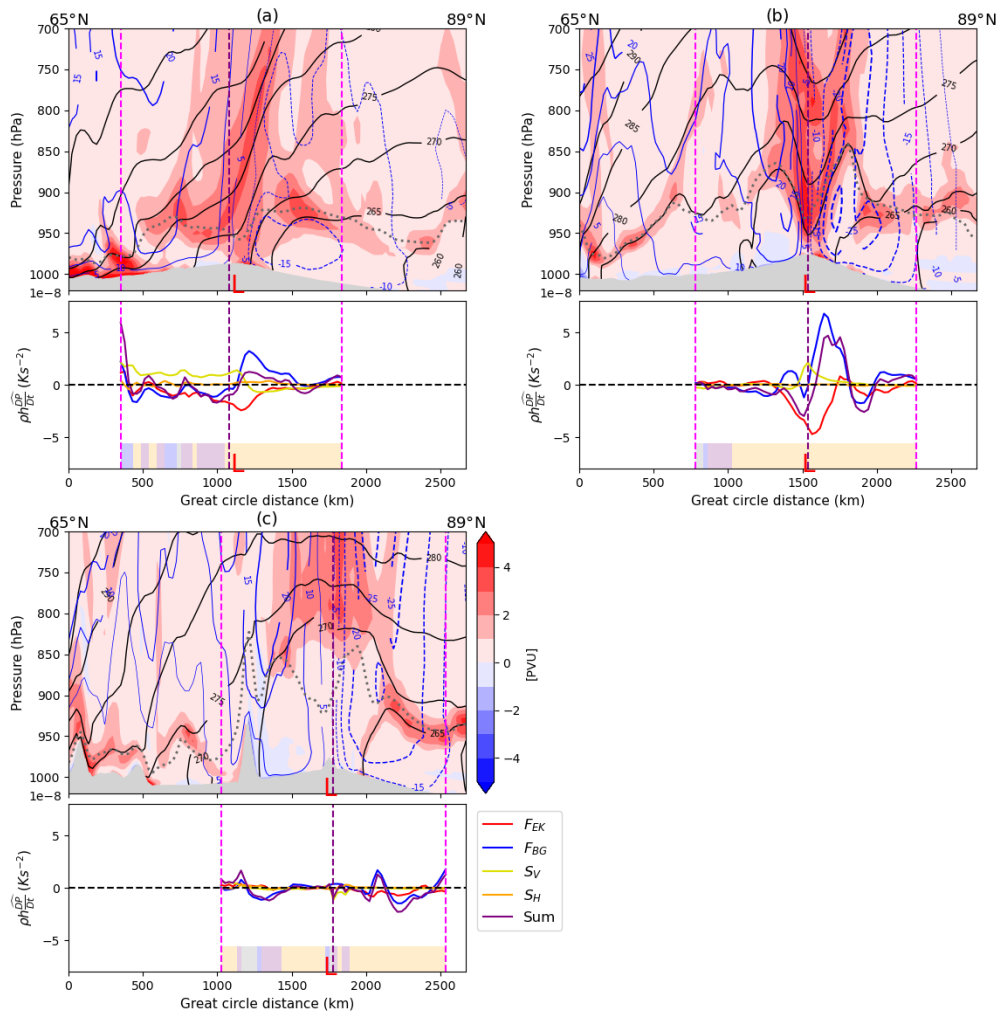


Figure 3.9: North-south cross-sections of Cyclone A, from IFS run starting 00Z 7 May 2020, at the longitude of the cyclone centre from 65°N to 89°N at (a) 12Z 8 May (maximum growth rate), (b) 06Z 9 May (maximum intensity), and (c) 06Z 10 May 2020 (24 hours after maximum intensity). The top panels display potential vorticity (PVU; shading), potential temperature (K; black solid contours), zonal wind (m s^{-1} ; blue contours), and the BL top (grey dotted line). The bottom panels display the BL PV tendency terms (scaled to depth-integrated PV tendencies) due to friction and sensible heat fluxes, within 750 km radius of the cyclone centre. The background shading denotes the surface type: land (grey), ocean (blue; sea ice concentration < 0.15), marginal ice zone (purple; sea ice concentration > 0.15 and < 0.8), and pack ice (orange; sea ice concentration > 0.8). The purple vertical line marks the cyclone centre from TRACK (Section 3.2.3), and the magenta lines mark 750 km distance from the cyclone centre. Minimum sea level pressure along the section is marked with a red L.

Cyclone A, likely due to the system being upper-level dominant with weaker winds at the surface. F_{EK} is negative over the cyclone centre, and F_{BG} is negative on the northern flank of the cyclone. S_V is small but consistently positive over the cyclone.

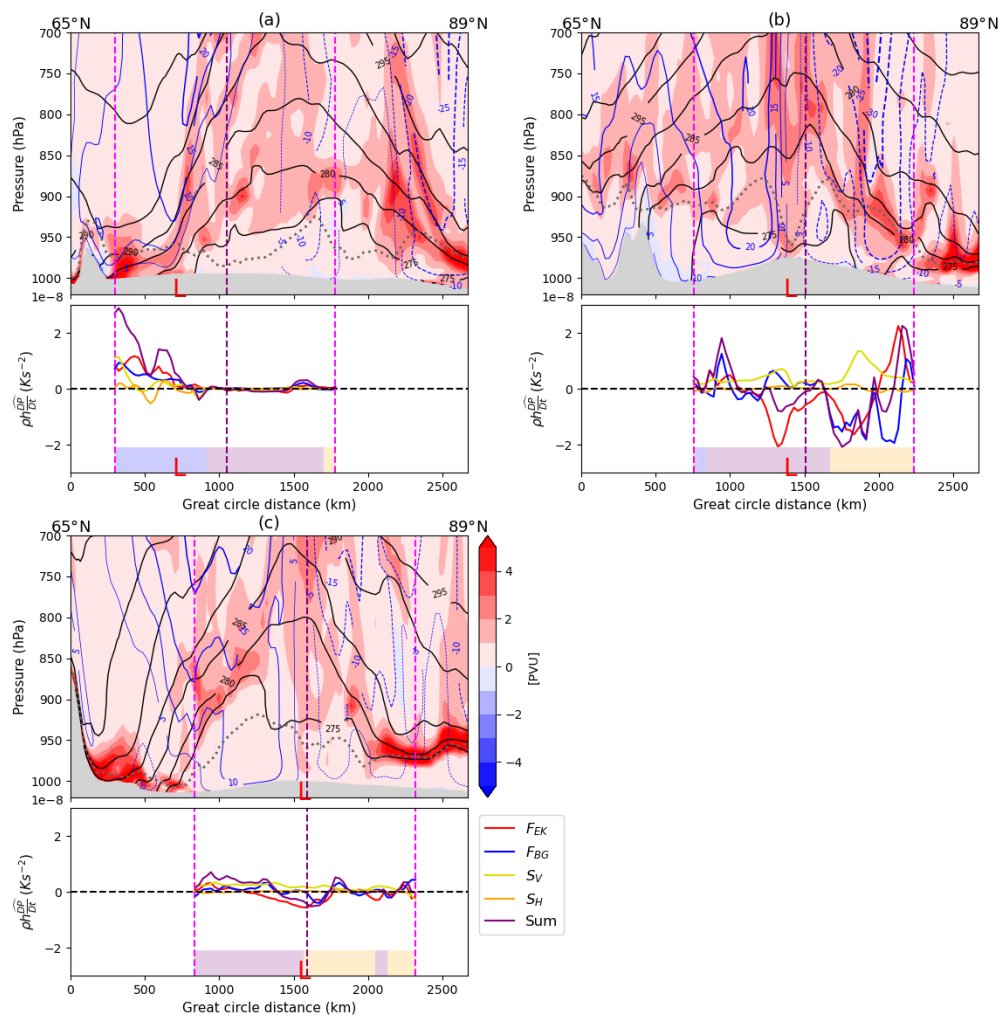


Figure 3.10: As in Figure 3.9, but for Cyclone B, from IFS run starting 00Z 25 July 2020, at (a) 18Z 26 July (maximum growth rate), (b) 12Z 28 July (maximum intensity), (c) 12Z 31 July (72 hours after maximum intensity).

At 72 hours after the time of maximum intensity (Figure 3.10c), whilst the surface cyclone has weakened (with BL winds of $\sim 10 \text{ m s}^{-1}$), the axisymmetric cold-core structure has amplified, with a steeper isentropic tilt on the flanks of the system. The BL PV tendencies are small at this time, although F_{EK} is notably negative over the cyclone centre, indicative of Ekman pumping. Note that the system is not associated with a coherent accumulation of PV above the BL like in Cyclone A, and consequently there is reduced static stability above the BL here (i.e. the isentropic surfaces are spaced further apart).

3.5 Discussion

From the results, the BL process that most obviously differs between Cyclones A and B is frictional baroclinic PV generation, i.e. the F_{BG} term. Physically, the F_{BG} term is governed by the orientation of the surface winds and the low-level thermal wind above the BL. Another form of thermal wind balance is:

$$\left(\hat{\mathbf{k}} \times \nabla\theta\right) = \frac{f_0\theta_0}{g} \frac{\partial\vec{v}}{\partial z} \quad (3.15)$$

where $\frac{\partial\vec{v}}{\partial z}$ is the thermal wind vector, \vec{v}_T , just above the BL. Substituting Equation 3.15 into the F_{BG} term in Equation 3.11 gives F_{BG} explicitly in terms of the thermal wind just above the BL:

$$F_{BG} = \frac{f_0\theta_0}{g\rho_0^2h^2} (-\vec{\tau}_S \cdot \vec{v}_T) = -\frac{f_0\theta_0}{g\rho_0^2h^2} |\vec{\tau}_S| |\vec{v}_T| \cos\phi \quad (3.16)$$

where ϕ is the angle between $\vec{\tau}_S$ and \vec{v}_T , and $\vec{\tau}_S$ is in the same direction as the surface wind (\vec{v}_S). Schematics of low-level dominant and upper-level dominant cyclones are presented in Figure 3.11. In the low-level dominant case (Figure 3.11a), in the warm front region, the cyclonic BL wind opposes the low-level thermal wind vector just above the BL. Hence, $\vec{\tau}_S$ and \vec{v}_T are opposed (i.e. $90^\circ < \phi < 180^\circ$). According to Equation 3.16, this would yield a positive Lagrangian PV tendency (F_{BG}), consistent with that in Cyclone A. Now consider an axisymmetric upper-level dominant cyclone (Figure 3.11b). The cyclonic BL wind is oriented in the same direction as the low-level thermal wind vector just above the BL. This means that $\vec{\tau}_S$ and \vec{v}_T are oriented in the same direction (i.e. $0^\circ < \phi < 90^\circ$) such that the Lagrangian PV tendency (F_{BG}) in Equation 3.16 is negative. This is consistent with the sign of F_{BG} associated with Cyclone B.

In essence, F_{BG} represents changes in PV due to BL friction altering the horizontal components of vorticity. F_{BG} can be written as the Lagrangian derivative of the horizontal component (considering only the y -component for simplicity) of Equation 3.1:

$$F_{BG} = \frac{D}{Dt} \left(\frac{1}{\rho} \zeta_a^y \frac{\partial\theta}{\partial y} \right) = \frac{1}{\rho} \left(\frac{D(\zeta_a^y)}{Dt} \frac{\partial\theta}{\partial y} + \zeta_a^y \frac{D(\frac{\partial\theta}{\partial y})}{Dt} \right) \quad (3.17)$$

where the product rule has been applied to give the RHS, and variations in density have been neglected. The horizontal vorticity in the BL, ζ_a^y , is associated with the (zonal) vertical wind shear between the surface winds and the thermal wind just above the BL. Therefore F_{BG} depends on the vertical wind shear across the BL (ζ_a^y), and the horizontal temperature gradient just above the BL top ($\frac{\partial\theta}{\partial y}$).

Once again, consider the warm front region of a low-level dominant cyclone, where the cyclonic BL wind opposes the low-level thermal wind vector (Figure 3.11a). In this setup, $\zeta_a^y > 0$, and $\frac{\partial\theta}{\partial y} < 0$. Friction will act to slow down the BL winds, such that the vertical wind shear over the BL is reduced: $\frac{D(\zeta_a^y)}{Dt} < 0$. If the system is to remain in thermal wind balance, the temperature gradient (just above the BL) across the cyclone must also weaken: $\frac{D(\frac{\partial\theta}{\partial y})}{Dt} > 0$ (note that this yields $F_{BG} > 0$ from Equation 3.17). The reduction of the temperature gradient across the cyclone means that the cyclone warm core decays.

Now consider an axisymmetric upper-level dominant, or cold-core cyclone (Figure 3.11b), where the cyclonic BL wind is oriented in the same direction as the low-level (cyclonic) thermal wind vector above the BL. Here, $\zeta_a^y < 0$, and $\frac{\partial\theta}{\partial y} > 0$. Friction slows down the BL winds, which in this configuration, will increase the vertical wind shear over the BL: $\frac{D(\zeta_a^y)}{Dt} < 0$. To remain in thermal wind balance, the temperature gradient (just above the BL) across the cyclone must increase: $\frac{D(\frac{\partial\theta}{\partial y})}{Dt} > 0$ (note that this yields $F_{BG} < 0$ from Equation 3.17). The increase in the temperature gradient across the cyclone means that the cyclone cold-core intensifies.

It has been shown that F_{BG} has the opposite impact on cyclone thermal structure. In low-level dominant cyclones, the thermal anomaly is weakened, whereas in upper-level dominant cyclones, the thermal anomaly is amplified. The analysis demonstrates that the impact of friction depends on the cyclone structure. In both cases, F_{BG} is acting to cool the thermal anomaly.

For Cyclone A, the analysis above demonstrates that F_{BG} acts to decay the low-level warm-core (and amplify the cold-core anomaly once established; see negative F_{BG} after

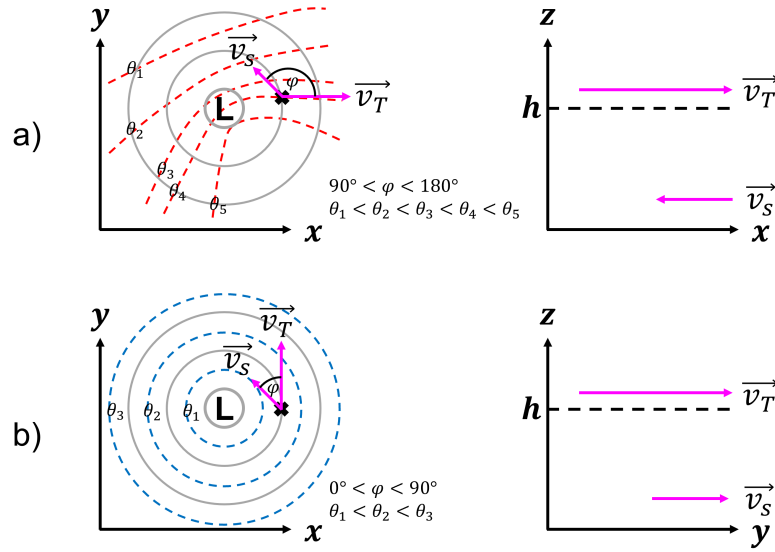


Figure 3.11: Schematics of (a) low-level dominant (warm-core) and (b) upper-level dominant (cold-core) cyclone structures. Left panels show a plan view with mean sea level pressure (grey solid contours) and potential temperature (θ ; dashed contours). At the point marked by the black cross, the orientation of the surface wind vector (\vec{v}_S ; in the same direction as the surface stress, $\vec{\tau}_S$) and the thermal wind vector above the BL (\vec{v}_T) are demonstrated by the magenta arrows, with an angle ϕ between them. Right panels show vertical wind structure at this point, with the horizontal axis aligned with the largest component of \vec{v}_T (in (a) this is the x-direction, in (b) this is the y-direction). The orientation of \vec{v}_S and \vec{v}_T are demonstrated with magenta arrows. The BL top is marked by the black dashed line (height h). The idealised cyclone structure in (a) is associated with positive F_{BG} , whilst (b) is associated with negative F_{BG} .

maximum intensity in Figure 3.7). Ekman pumping is also acting, which will also cool the system due to the rising of air and adiabatic cooling (Ekman pumping is also acting to spin-down the cyclone as it becomes stacked in the vertical). The positive S_V term (before maximum intensity; Figure 3.7), indicative of downward sensible heat fluxes, also contributes to cooling with the atmosphere losing heat to the surface. For Cyclone B, F_{BG} acts to amplify the cold-core, with Ekman pumping and sustained downward sensible heat fluxes over the sea ice (as indicated by negative F_{EK} and positive S_V ; Figure 3.8) also contributing to low-level cooling. Hence, all of the BL PV tendencies in both cyclones are contributing to cooling the system. Low-level cooling in an axisymmetric cyclone will result in a reduction in low-level vorticity, and therefore a reduction in surface winds. This can be shown using Equation 3.3; for example, in a cold-core cyclone $b' < 0$ will increase in magnitude, and therefore $\frac{\partial \xi}{\partial z} > 0$ will increase. Assuming upper-level vorticity and the layer depth stays constant, this means the low-level vorticity must decrease. Hence, the

frictional processes and sensible heat fluxes are contributing to weakening the low-level cyclone after maximum intensity. Although the low-level cyclone is weakening, friction is acting to amplify a cold-core anomaly above the BL in both cyclones once they have matured. What this means for the subsequent system evolution is still an open question.

Consistent with all of the BL processes contributing to cooling the system, both cyclones obtain a vertically stacked cold-core structure after maximum intensity (Figures 3.9c and 3.10c) which persists for several days (Figures 3.2b and 3.2d). This structural evolution is not seen in maturing mid-latitude cyclones. The barotropic cold-core structure after maximum intensity resembles the structural transition of summer-time Arctic cyclones in Vessey et al. (2022). Vessey et al., 2022 find that their summer-time Arctic cyclone composite does not undergo occlusion, and suggest that summer-time Arctic cyclones may lack the dynamical forcing from the occlusion process that typically leads to the dissipation of mid-latitude cyclones. One hypothesis is that this may extend the lifetime of summer-time Arctic cyclones. This will allow BL processes (which all act to cool the thermal anomaly in Cyclones A and B) to act over a longer time period than in mid-latitude cyclones, permitting the cold-core structure to develop and persist over many days.

In Cyclone A, Ekman pumping and the baroclinic PV mechanism are both acting to increase the static stability above the BL (Boutle et al., 2015). This acts to reduce the coupling of the lower and upper levels, and eventually weaken the cyclone. In Cyclone B, the static stability above the BL is reduced compared to Cyclone A (see the large vertical spacing of the isentropes above the BL in Figure 3.10c). The lower static stability would result in enhanced coupling of the lower and upper levels for longer (compared to Cyclone A), and might explain the longer lifetime of Cyclone B (almost 10 days), compared to Cyclone A (~ 6 days).

3.6 Conclusions

Previous studies have demonstrated that the evolution of mid-latitude cyclones is sensitive to BL turbulent fluxes (e.g. Valdes and Hoskins, 1988), and identified the BL processes

by which the surface influences mid-latitude cyclones (e.g. Adamson et al., 2006; Cooper et al., 1992). However, the influence of the surface and the relevant dynamical mechanisms have not yet been investigated in the context of Arctic cyclones. Differences are expected for several reasons. Firstly, surface properties (and therefore turbulent fluxes) are highly variable in the summer-time Arctic, over land, ocean, marginal ice and pack ice. Secondly, Arctic cyclones are longer lived than mid-latitude cyclones, allowing BL processes to act for longer. Thirdly, there are different cyclone growth mechanisms and morphologies in the Arctic, such that the BL processes may have different impacts on cyclone evolution.

The purpose of this study is to characterise the BL processes acting in summer-time Arctic cyclones, and understand how they influence the structural evolution. A PV framework (derived by Cooper et al., 1992, in the Vanni re et al., 2016, form) has been used, as has been used in previous studies for mid-latitude cyclones (e.g. Adamson et al., 2006; Plant and Belcher, 2007). This PV framework in Equation 3.11 reveals four BL PV tendencies, each representing a BL process, associated with friction or sensible heat fluxes: F_{EK} (Ekman friction), F_{BG} (frictional baroclinic PV generation), S_V (sensible heat fluxes), and S_H (proportional the horizontal gradient of sensible heat fluxes – typically smaller than the other terms). In this work, unlike previous studies, summer-time Arctic cyclones are categorised by their vorticity structure during development, as either (i) low-level dominant (low-level warm core) or (ii) upper-level dominant (tropospheric cold-core). In this study, BL processes (and their impact on cyclone evolution) acting in two contrasting cyclone case studies from summer 2020 are investigated and compared. Cyclone A occurred in May 2020 and was low-level dominant (developing as part of a baroclinic wave off the Eurasian coastline), whilst Cyclone B occurred in July 2020 and was upper-level dominant (developing with a TPV in the Beaufort Sea). The primary tool used is the ECMWF global IFS model, focusing on a single model run for each cyclone.

The first research question (defined in Section 3.1) was to determine the nature of the BL processes in the different types of Arctic cyclones, and the second was to understand how these evolve with time. Both Cyclones A and B are associated with negative F_{EK} ,

and therefore Ekman pumping, which acts to spin down the cyclones throughout their lifetime (as would be expected in cyclonic weather systems). Furthermore, both cyclones are associated with positive S_V due to downward sensible heat fluxes over sea ice (i.e. the atmosphere losing heat to the underlying surface), representing the generation of PV due to increased static stability. Cyclone A is associated with positive S_V before maximum intensity in the warm sector (over land and sea ice). Cyclone B is associated with positive S_V over the sea ice for most of its lifetime. It is the frictional baroclinic PV generation, the F_{BG} term, that differs between Cyclones A and B. The F_{BG} term is positive in Cyclone A along the warm front region during the baroclinic growth phase, where the BL winds oppose the lower-tropospheric thermal wind. After maximum intensity this term reduces in magnitude and becomes weakly negative. In Cyclone B, F_{BG} is initially positive during the baroclinic growth phase (but with a reduced magnitude compared to Cyclone A, suggesting reduced baroclinicity). As the system approaches maximum intensity, the F_{BG} term becomes strongly negative, as the cyclone becomes vertically stacked, with BL winds in the cyclone oriented in the same direction as the cyclonic thermal wind associated with the TPV above the BL. In both cyclones the sum of the BL PV tendencies are positive before maximum intensity, and negative afterwards.

Comparisons of the BL processes acting in Cyclones A and B with those in mid-latitude cyclones were made throughout the manuscript. The evolution of Cyclone A resembles that of mid-latitude cyclones, consistent with the same frictional processes, with negative F_{EK} and positive F_{BG} . There is also evidence of the baroclinic PV mechanism, the dominant frictional spin-down mechanism in baroclinic wave cyclones, with a region of high PV just above the BL over the low centre in Cyclone A (e.g. Adamson et al., 2006). In contrast, Cyclone B is associated with negative F_{BG} due to the vertically stacked nature of the system with a TPV, suggesting that friction is acting differently compared to Cyclone A and typical mid-latitude cyclones. Both cyclones are associated with predominantly positive S_V due to downward sensible heat fluxes over the sea ice, unlike mid-latitude cyclones. The S_V term is generally small in Cyclone A (except over land), consistent with the finding from Hualand and Spengler (2020) that sensible heat fluxes only have a minor impact on baroclinic wave development. In contrast, the S_V term is more dominant

in Cyclone B, with downward sensible heat fluxes over sea ice over the entire cyclone.

Finally, the third research question was to understand the impact of the BL processes on the Arctic cyclone interior evolution. It has been shown that the F_{BG} term has the opposite impact on cyclone structure above the BL, depending on the cyclone type. In Cyclone A (low-level dominant), F_{BG} acts to decay the warm-core thermal anomaly, whereas F_{BG} acts to amplify the cold-core thermal anomaly in Cyclone B (upper-level dominant). In fact, all of the BL processes associated with friction and sensible heat fluxes are contributing to lower tropospheric cooling, and therefore a reduction in low-level vorticity by thermal wind balance. Although the low-level circulation of the cyclone is weakening, friction is acting to amplify a cold-core anomaly above the BL. Consistent with the BL processes contributing to cooling, both Cyclones A and B obtain a cold-core structure which persists for several days after maximum intensity, unlike the evolution of mid-latitude cyclones. Vessey et al. (2022) have suggested that Arctic cyclones may lack the dynamical forcing to dissipate as quickly as mid-latitude cyclones, and it is hypothesised that this may allow the BL processes to act over a longer period of time. This may permit the cold-core structure to develop and persist over several days. Finally, it is hypothesised that in Cyclone B, because frictional baroclinic PV generation does not result in high PV (and high static stability) over the cyclone centre, the coupling of the lower and upper levels is prolonged, and therefore so is cyclone lifetime (~ 10 days), compared to Cyclone A (~ 6 days).

Moist processes and diabatic effects in the free troposphere (in particular latent heat release coupled with the vertical motion) have not been considered here. Although we may expect latent heating to be less important in the Arctic than lower latitudes due to reduced absolute humidity, Terpstra et al. (2015) demonstrated that low-level disturbances are able to amplify in a high-latitude moist baroclinic environment in the absence of other processes (upper-level perturbations, surface fluxes or radiation) using an idealised baroclinic channel model. This suggests that latent heating can be significant for the development of polar cyclones. The work here is focused on characterising the effects of friction and sensible heat fluxes at the lower boundary on Arctic cyclones in two cases

with contrasting structure. Further study is being conducted by the co-authors to quantify the response of the 3-D wind field within the cyclones to the BL processes explored here, and the amplification of ascent by latent heat release, using the diagnostic tool of Cullen (2018) assuming semi-geostrophic balance dynamics. Quantifying the relative importance of non-conservative processes in the BL and free troposphere in the evolution of Arctic cyclones, and understanding the sensitivity of cyclone evolution to surface properties, are also areas for future research.

Acknowledgements

Hannah L. Croad acknowledges funding and support from the SCENARIO NERC Doctoral Training Partnership, with co-supervision and super-computing support from ECMWF. The authors thank Kevin Hodges for providing cyclone tracks from the TRACK algorithm for use in this study. The authors would also like to acknowledge ECMWF for the production of the ERA5 reanalysis dataset.

Financial support

This research has been supported by PhD studentship funding from SCENARIO NERC Doctoral Training Partnership grant NE/S007261/1 and the Arctic Summer-time Cyclones: Dynamics and Sea-ice Interaction NERC standard grant NE/T006773/1.

Chapter 4

A climatology of summer-time Arctic cyclones using a modified phase space

This chapter has been published in *Geophysical Research Letters* with reference:

Croad, H. L., J. Methven, B. Harvey, S. P. E. Keeley, A. Volonté, and K. I. Hodges (2023): A Climatology of Summer-time Arctic Cyclones Using a Modified Phase Space. *Geophys. Res. Lett.*, **50** (22), e2023GL105993, <https://doi.org/10.1029/2023GL105993>.

Abstract

We perform a climatological analysis of summer-time Arctic cyclone structure in reanalysis data using a phase space approach. A classification scheme for Arctic cyclones is proposed, dependent on whether vorticity structure during development is low-level-dominant (LLD) or upper-level-dominant (ULD). During growth, LLD cyclones (65.5%) exhibit warm-core asymmetric structures, whereas ULD cyclones (34.5%) have cold-core asymmetric structures. LLD cyclones typically have greater thermal asymmetry during growth. However, a transition to a persistent cold-core axisymmetric structure after maturity is characteristic of summer-time Arctic cyclones, regardless of structure during growth. LLD cyclones are typically stronger and preferentially track on the Russian coastline where there is high baroclinicity, whereas ULD cyclones tend to be longer-lived and preferentially track in the Pacific sector, where they can interact with tropopause polar vortices. This study provides a platform for further research into different classes of Arctic cyclones and associated hazardous weather, and ultimately for developing conceptual models.

Plain language summary

We investigate the structure of cyclones, large-scale low-pressure systems, in the summer-time Arctic, using observations-based data of the atmosphere. A phase space is used to represent two aspects of cyclone structure, specifically (a) the low-level horizontal temperature contrast (i.e., whether there is a distinct warm sector), and (b) the vertical change in wind. We classify Arctic cyclones based on their vertical structure as they develop, as either low-level-dominant (LLD), where winds decrease with height, or upper-level-dominant (ULD), where winds increase with height. During growth, LLD cyclones (65.5%) exhibit warm-core structures whereas ULD cyclones (34.5%) have cold-core structures, both with strong low-level temperature contrasts. LLD cyclones tend to have a stronger warm sector contrast during development. However, after maximum intensity, when a cyclone matures and begins to weaken, both subsets of cyclones typically evolve to have long-lasting cold-core structures without a warm sector. LLD cyclones are typically stronger and preferentially track on the Russian coastline, whereas ULD cyclones tend to be longer-lived, and preferentially track in the Pacific sector of the Arctic. This study provides a platform for further research into different classes of Arctic cyclones, and ultimately for developing conceptual models, which are key for anticipating associated hazardous weather.

4.1 Introduction

Arctic cyclones are the major weather hazard to the increasing human activity in the summer-time Arctic (e.g., Babin et al., 2020; Li et al., 2021), and can be associated with extreme surface winds, ocean waves (e.g., Thomson and Rogers, 2014; Waseda et al., 2018, 2021), and the break-up and melting of sea ice (e.g., Asplin et al., 2012; Lukovich et al., 2021; Peng et al., 2021). Furthermore, Arctic cyclones in summer can be long-lived, exacerbating the impact of any associated hazards. For example, the Great Arctic cyclone of 2012 (henceforth C12) lasted for almost 13 days (Simmonds and Rudeva, 2012), and an Arctic cyclone in August 2016 was maintained for over 1 month through repeated cyclone mergings (Yamagami et al., 2017).

The structural development of mid-latitude cyclones is well-established, with conceptual models such as the Norwegian (Bjerknes, 1919) and Shapiro-Keyser (Shapiro and Keyser, 1990) models, which are key for anticipating hazardous weather within a cyclone. However, the structural evolution of Arctic cyclones is not as well understood. Studies of extreme summer-time cases suggest that Arctic cyclones can have different structures to mid-latitude cyclones (e.g., Aizawa and Tanaka, 2016; Tanaka et al., 2012; Tao et al., 2017). However, climatological studies are needed to complement these works and assess how typical these cases are. Previously, climatologies of Arctic cyclones (e.g., Vessey et al., 2020; Zhang et al., 2004) did not consider cyclone structure. In more recent work, Vessey et al. (2022) showed that summer-time Arctic cyclones undergo a transition at maximum intensity from a tilted baroclinic to an axisymmetric cold-core structure. However, the composite approach used did not permit for different varieties of cyclone structural evolution.

Gray et al. (2021) performed a climatological analysis of summer-time Arctic cyclones and tropopause polar vortices (TPVs), long-lived vortices on the tropopause which are common in the summer-time Arctic due to the lack of wind shear (Cavallo and Hakim, 2009, 2010). It was shown that Arctic cyclones that develop with a TPV (“matched”) have a distinct structure to those that do not (“unmatched”). In a similar vein, Croad et al. (2023a) focused on two summer-time cyclones with contrasting structure from summer 2020. Cyclone A (henceforth C20A) developed as a baroclinic wave along the northern coast of Russia on the Arctic frontal zone (AFZ; Day and Hodges, 2018; Serreze et al., 2001). The cyclone had a low-level-dominant (LLD) vorticity structure during development, with a structural evolution resembling a mid-latitude cyclone. In contrast, Cyclone B (henceforth C20B) developed with a TPV, with an upper-level-dominant (ULD) vorticity structure. Whilst Cyclone A had stronger winds, Cyclone B attained a cold-core columnar vortex structure that persisted for several days, looking quite different to a typical mid-latitude cyclone. The hypothesis is that cyclones A and B from Croad et al. (2023a) represent two archetypal structural evolutions of Arctic cyclones.

Here we investigate summer-time Arctic cyclone structure using a modified form of the Hart (2003) cyclone phase space. This is a flexible approach to classifying cyclone structure, as it allows for a continuum of structures. In this study cyclones are categorized as having LLD or ULD development, determined by their vorticity structure at maximum growth rate. Note that this may have some similarities with the unmatched/matched classification from Gray et al. (2021), but here the focus is on general evolution of cyclone structure, rather than feature-based identification of TPVs. In this work we aim to answer the following:

1. What are the characteristic cyclone structures in the summer-time Arctic?
2. How does LLD/ULD growth determine subsequent cyclone structural evolution, and how frequently does each type of growth occur?
3. How is LLD/ULD growth related to cyclone strength, longevity, and location?

4.2 Methodology

4.2.1 Reanalysis data

The study uses ERA5, the fifth-generation European Centre for Medium-Range Weather Forecasts (ECMWF) reanalysis data set (Hersbach et al., 2017, 2020), produced using the ECMWF’s Integrated Forecasting System model cycle 41r2. The model has spectral truncation TL639 (~ 31 km horizontal grid spacing at the equator), and 137 terrain-following hybrid-pressure levels from the surface to 0.01 hPa. 6-hourly data on a 0.25° regular latitude-longitude grid during 1979–2021 is used.

4.2.2 Arctic cyclone tracking

Arctic cyclone tracks are identified from ERA5 data using the TRACK algorithm (Hodges, 1994, 1995, 2021). This is employed on 1-hourly spectrally truncated (T5-63; removing total wavenumbers less than 5 and more than 63) 850 hPa relative vorticity (ξ_{850}). Maxima exceeding 10^{-5} s^{-1} are identified and initialized into a set of tracks using a nearest neighbor search with a maximum displacement distance of 2° (geodesic, 222 km) in a time step.

These are subsequently refined by minimizing a cost function for track smoothness. Only tracks that last longer than 1 day and travel more than 1000 km are retained. Arctic cyclones are identified as those tracks with filtered $\xi_{850} > 8 \times 10^{-5} \text{ s}^{-1}$ for at least 12 hours whilst located north of 70°N . For each track, only sections north of 55°N are retained (deemed relevant to the Arctic), from which time of maximum growth rate and maximum intensity are identified. There is no special treatment for merging/splitting tracks, as this introduces added subjectivity. Spatial track density of cyclones was computed with cosine-shaped kernels on a polar domain (500 km bandwidth) using the scikit-learn Python library (Pedregosa et al., 2011).

4.2.3 A modified cyclone phase space

A modified cyclone phase space for characterizing the structure of Arctic cyclones was proposed in Croad et al. (2023a), adapted from Hart (2003). The modified phase space differs from the Hart (2003) version in that the parameters have been non-dimensionalised by the natural scalings of quasi-geostrophic (QG) dynamics. The modified phase space has also been reduced from three to two dimensions for simplicity, considering the thermal asymmetry in the lower troposphere, and the thermal wind structure in the upper troposphere only, and not also in the lower troposphere as in Hart (2003). This is justified as we are primarily interested in the presence of low-level baroclinicity and TPVs in the upper levels. Furthermore, suitable pressure levels are used to define the layers in the modified phase space to account for the shallower troposphere in the Arctic. The modified phase space is also no longer dependent on the cyclone motion vector (as some Arctic cyclones are associated with slow movement such that the motion vector is not well defined), thereby producing smoother trajectories.

The thermal asymmetry is quantified as a non-dimensionalized depth-integrated baroclinic asymmetry, B , over the 925–700 hPa layer (assumed to be above the boundary layer but below the “steering” level), calculated by splitting the cyclone into two halves:

$$B = \frac{1}{f_0 LN} \frac{g}{\theta_0} \frac{1}{\Delta p} \int_{700\text{hPa}}^{925\text{hPa}} (\theta_R - \theta_L) dp \quad (4.1)$$

where f_0 = Coriolis parameter (s^{-1}), L = horizontal length scale (500 km), N = Brunt-Väisälä frequency (0.01 s^{-1}), g = gravitational acceleration (9.81 m s^{-2}), θ_0 = reference potential temperature (273 K), p = pressure (hPa), θ_R and θ_L = areal mean potential temperature over a semi-circle (radius 500 km) to the right and left side of the cyclone (K). At each time, Equation 4.1 is calculated by splitting the cyclone at every 10° bearing, with the maximum value of B being used.

The thermal wind structure is quantified as a non-dimensionalised vertical gradient of relative vorticity (ξ ; s^{-1}) in the 700–400 hPa layer (assumed to be above the “steering” level but below the tropopause):

$$Ro_T = -\frac{L}{N} \frac{\partial \xi}{\partial z} \quad (4.2)$$

where z = height (m) and Ro_T is a thermal Rossby number (the ratio of the vertical contrast in relative vorticity to planetary vorticity, noting that $\frac{L}{N} \sim \frac{H}{f_0}$ in QG scaling, where H = height scale). From thermal wind balance, a positive Ro_T indicates a warm-core structure, whilst a negative Ro_T corresponds to a cold-core structure.

In Croad et al. (2023a), Equation 4.1 was calculated with data at 25 hPa intervals, and Equation 4.2 was estimated by a linear regression fit of ξ at 50 hPa intervals. However, here the parameters are calculated by finite difference using data at 925, 700 and 400 hPa only (reducing data storage requirements). Differences between the two methods were very small for the cyclone cases in Croad et al. (2023a), justifying the decision to use fewer pressure levels.

The modified cyclone phase space is presented in Figure 4.1a, with four quadrants defined by the boundaries $Ro_T = 0$ and $B = 0.15$. The latter is equivalent to a ~ 2 K difference across a cyclone, above which a cyclone is considered to be asymmetric, and below which a cyclone is considered to be symmetric. This choice is justified a posteriori using the statistics at the time of maximum intensity shown in Figure 4.2b.

4.3 Results

4.3.1 Cyclone structure and evolution

During 1979–2021, 1658 Arctic cyclones were identified in the extended summer (May–September) using the criteria in Section 4.2.2 (≈ 39 per year on average). All (6-hourly) tracked points of these cyclones are presented in the modified phase space in Figure 4.1a. The highest point density is in the lower-left quadrant (39.8%), indicative of cold-core cyclone structures with low asymmetry. There are also a considerable number of points in the top two quadrants, with 29.0% and 23.5% exhibiting warm-core and cold-core cyclone structures respectively with high asymmetry. The region of highest point density slants from the lower-left to the upper-right, indicating that cyclones with warm-core structures typically have greater low-level asymmetry than cold-core cyclones.

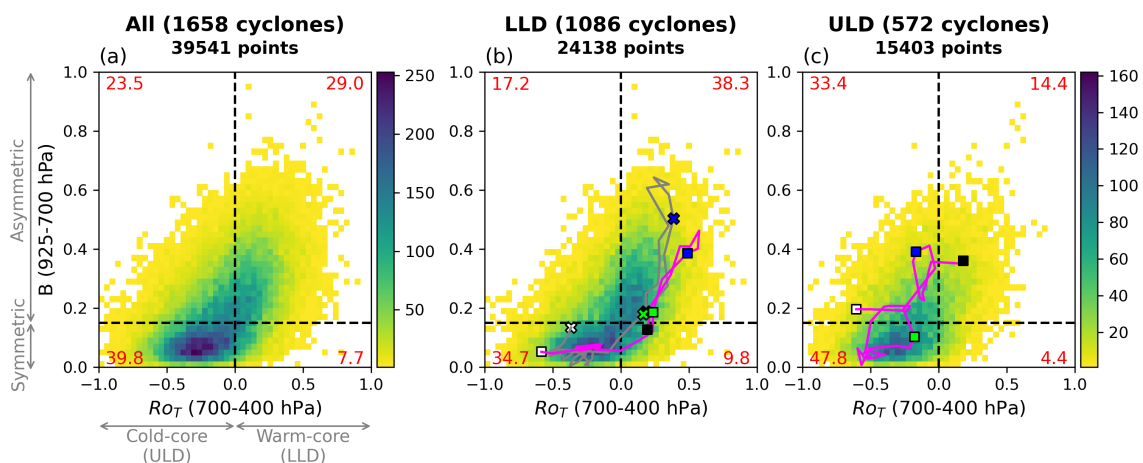


Figure 4.1: Point density in the modified cyclone phase space of all track points for (a) all, (b) LLD, and (c) ULD Arctic cyclones. Overlaid are the trajectories of three cyclone case studies; C12 and C20A are overlain on (b) in gray and magenta respectively, and C20B is overlain on (c) in magenta. The black, blue, green and white markers (crosses for C12, squares for C20A and C20B) refer to the start point, maximum growth rate, maximum intensity and final point respectively. The percentage of the total points in each quadrant is written in red.

Figure 4.1a indicates a positive correlation between B and Ro_T , reflecting the differing dependencies of LLD and ULD cyclones on their respective forcing mechanisms. LLD cyclones ($Ro_T > 0$) require environments with strong low-level baroclinicity (large B) to exist, whereas ULD cyclones ($Ro_T < 0$) have strong upper-level forcing, and so can exist even with weak low-level baroclinicity (small B). Although the use of two parameters to

characterise cyclone structure may be conducive to four classes of cyclone (corresponding to each quadrant of the phase space), the observed positive correlation between B and Ro_T justifies why only two classes – LLD and ULD – are sufficient to capture the first-order variability in summer-time Arctic cyclone occurrence.

The sample is split into two subsets, depending on whether a cyclone is LLD (i.e., warm-core; $Ro_T > 0$) or ULD (i.e., cold-core; $Ro_T < 0$) at the time of maximum growth rate (Figures 4.1b and 4.1c). 65.5% (1086) of the cyclones are LLD at maximum growth rate, whilst 34.5% (572) are ULD. Note that this partition is similar to that of cyclones that are unmatched and matched with TPVs in Gray et al. (2021). The LLD cyclones (Figure 4.1b) have a higher proportion of warm-core asymmetric structures than climatology (38.3% compared to 29.0%), and a lower fraction of cold-core structures. In contrast, the ULD subset (Figure 4.1c) has a considerably lower fraction of warm-core asymmetric structures than climatology (14.4% compared to 29.0%), with the region of highest point density on the cold-core half of the phase space (and lower average asymmetry). The ULD subset has a higher proportion of cold-core asymmetric (33.4% compared to 23.5%) and cold-core symmetric (47.8% compared to 39.8%) structures than climatology.

The trajectories of the three aforementioned Arctic cyclone cases are overlaid in Figures 4.1b and 4.1c. C12 and C20A (Figure 4.1b; LLD development) have warm-core asymmetric structures at maximum growth rate (blue marker), with a reduction in asymmetry as they approach maximum intensity (green markers). After maximum intensity, the cyclone trajectories move into the lower-left quadrant, illustrating the transition to a cold-core axisymmetric structure, and remain there for several days. In contrast, C20B (Figure 4.1c; ULD development) has a cold-core structure at maximum growth rate, with high asymmetry (reduced compared to C12 but comparable to C20A). Although C20B has a contrasting development to C12 and C20A, it undergoes a transition around the time of maximum intensity to a cold-core symmetric structure that persists for several days, like C12 and C20A.

The evolution of structure throughout cyclone lifetime is highlighted in Figure 4.2. Con-

sidering the full cyclone sample, at maximum growth rate (Figure 4.2a), the highest point density is in the warm-core asymmetric (60.0%) and cold-core asymmetric (30.5%) quadrants. At maximum intensity (Figure 4.2b), the highest point density has moved to the left and downwards in the diagram, positioned on the central point between the quadrants, representing a reduction in asymmetry and a reduction in the fraction of warm-core structures as cyclones mature. At the final track point (Figure 4.2c), the highest point density is in the cold-core symmetric quadrant (62.0%). This represents the transition to a cold-core axisymmetric structure, like that seen in C12, C20A and C20B. The results indicate that a transition to a cold-core axisymmetric structure after maximum intensity occurs commonly in summer-time Arctic cyclones, consistent with Vessey et al. (2022).

Note that the highest point density at maximum growth rate (Figure 4.2a) is unimodal, even though in this study the cyclones are partitioned into two types depending on their structure at this time. This illustrates how in reality, cyclone structure is a continuum, rather than being constrained by distinct types (with many “unconventional” cyclones). However, it is still useful to apply broad classification schemes for the purpose of understanding characteristic cyclone structures and behaviors. The merit of this classification scheme is demonstrated in Figure 4.1, with the LLD and ULD subsets exhibiting different characteristic structures.

Figures 4.2d–4.2f and 4.2g–4.2i show the evolution of the LLD and ULD subsets respectively. At maximum growth rate, the LLD (Figure 4.2d) and ULD (Figure 4.2g) subsets have warm-core and cold-core structures respectively, by definition, with high asymmetry. At maximum intensity, the highest point density has moved downwards in the phase space in both subsets (Figures 4.2e and 4.2h), indicating reduced asymmetry as the cyclones mature. The LLD subset (Figure 4.2e) also moves to lower Ro_T values, although 67.7% of the cyclones still have warm-core structures at this time. This demonstrates that LLD cyclones tend to undergo their transition from warm-core to cold-core structures after maximum intensity, like C12 and C20A (Figure 4.1b). At the final track point, the LLD (Figure 4.2f) and ULD (Figure 4.2i) subsets have their highest point density in the cold-core symmetric quadrant, with 59.1% and 67.5% of the points respectively. This

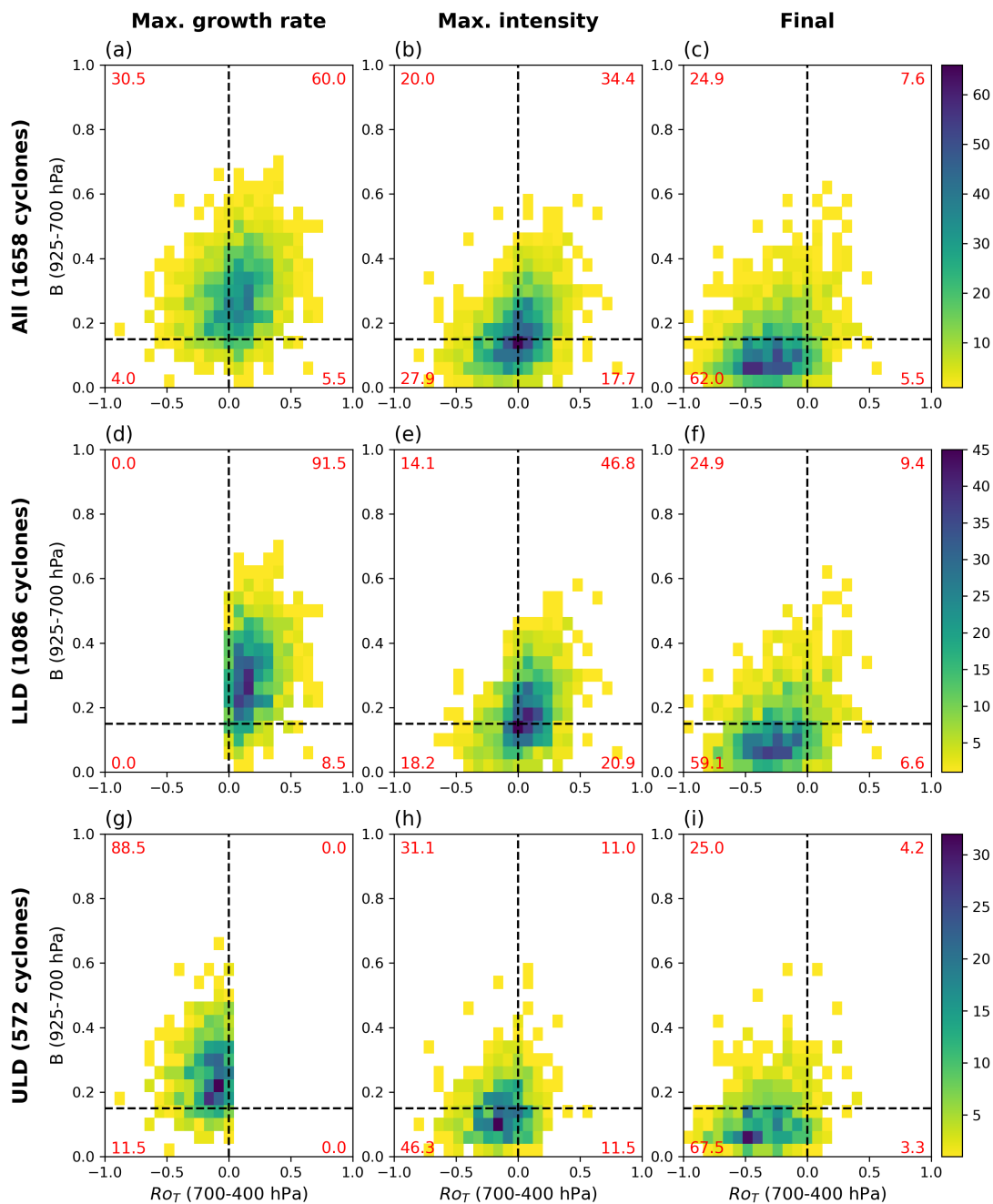


Figure 4.2: Point density in the modified cyclone phase space for (a–c) all identified Arctic cyclones at (a) maximum growth rate, (b) maximum intensity, and (c) the final point of each track. Panels (d–f) and (g–i) are the same as panels (a–c), but for LLD and ULD cyclones respectively. The percentage of the total points in each quadrant is written in red.

suggests that both LLD and ULD cyclones often undergo the transition to a cold-core axisymmetric structure, although a cyclone that had a ULD development is more likely to do so.

4.3.2 Cyclone characteristics

Having illustrated the differences in structural evolution between LLD and ULD cyclones, we now consider how the cyclone subsets compare with regards to strength and duration (Figure 4.3).

The distributions of maximum strength for the LLD and ULD cyclones are presented in Figure 4.3a. The median value of ξ_{850} at maximum intensity (denoted by the dashed vertical lines) is higher for the LLD cyclones ($10.5 \times 10^{-5} \text{ s}^{-1}$) than the ULD cyclones ($9.9 \times 10^{-5} \text{ s}^{-1}$). Furthermore, the ULD histogram has a higher peak at low values of ξ_{850} compared to the LLD histogram, which is flatter in shape and has higher frequencies at larger ξ_{850} values. A two-sample Kolmogorov-Smirnov (KS) test confirms that the two distributions are robustly different ($p\text{-value} = 2.6 \times 10^{-7}$). This demonstrates that LLD cyclones are typically stronger than ULD cyclones, and that the strongest cyclones are more likely to have a LLD development.

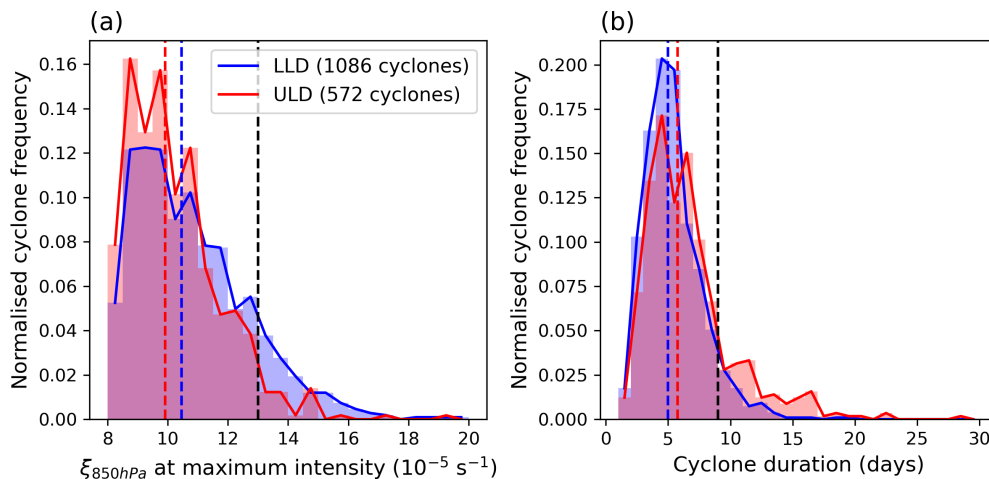


Figure 4.3: Histograms of Arctic cyclone (a) maximum strength according to ξ_{850} at maximum intensity and (b) duration, partitioned into the LLD (blue) and ULD (red) subsets. The histograms are normalized by the number of cyclones in each subset. The blue and red vertical dashed lines mark the median value for the LLD and ULD subsets respectively. The black vertical dashed line marks the 90th percentile value of all the cyclones.

An equivalent analysis is provided in Figure 4.3b for cyclone lifetime. The median duration is greater for ULD cyclones (6 days) than LLD cyclones (5 days). Moreover, the LLD

histogram has a higher peak at short durations compared to the ULD histogram, which has a longer tail and higher frequencies at longer durations. A two-sample KS test confirms that the distributions are robustly different (p-value = 3.8×10^{-10}). This demonstrates that ULD cyclones tend to be longer-lived than LLD cyclones, and, that the longest-lived cyclones are more likely to have an ULD development.

4.3.3 Extreme cyclones

Here we focus on the cyclones that exceed the 90th percentile in strength and duration, which were found to be $13.0 \times 10^{-5} \text{ s}^{-1}$ and 9.0 days respectively (marked by the black vertical dashed lines in Figure 4.3).

The strongest cyclones subset is comprised predominantly of LLD cyclones (140; 12.9% of the LLD subset), with only 26 ULD cyclones (4.5% of the ULD subset). Accordingly, the distribution in the phase space (Figure 4.4a) resembles that of the LLD subset (Figure 4.1b). In contrast, the longest-lived cyclone subset is comprised of 67 LLD cyclones (6.2% of the LLD subset) and 95 ULD cyclones (16.6% of the ULD subset). The distribution in the phase space (Figure 4.4b) exhibits more cold-core structures than the strongest subset (Figure 4.4a), more closely resembling the ULD subset (Figure 4.1c). These results are consistent with LLD cyclones being stronger on average than ULD cyclones, and ULD cyclones being longer-lived. Both the strongest and longest-lived cyclone subsets have a greater fraction of cold-core axisymmetric structures than climatology (42.4% and 50.9% respectively compared to 39.8%). This is likely related to longer persistence after maximum intensity, either due to stronger cyclones taking longer to dissipate, or due to cyclones being maintained by upper-level forcing. Note that only 17 cyclones ($\sim 10\%$ of the sample size) are in both the strongest and longest-lived subsets, suggesting that extremely strong cyclones do not tend to be extremely long-lived.

The strongest cyclones most frequently develop and track in the Barents and Kara Seas (Figure 4.4c), consistent with baroclinic development on the AFZ. Some of the strongest cyclones develop on the Laptev Sea coastline instead, highlighting a secondary baroclinic zone on the AFZ. In contrast, the longest-lived cyclones preferentially track in the Pa-

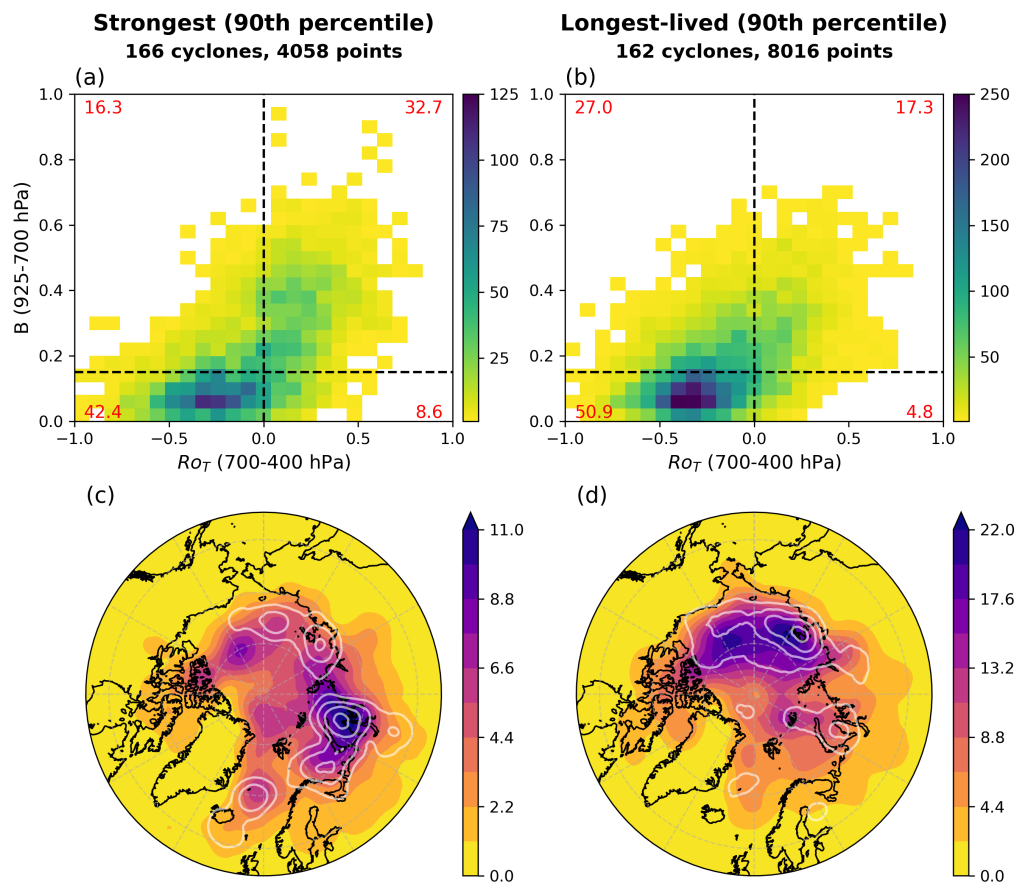


Figure 4.4: Arctic cyclones in the 90th percentile of strength (left) and duration (right). (Top) Density plots of the (a) strongest and (b) longest-lived cyclones in the modified cyclone phase space. (Bottom) Feature density maps (using spherical cosine kernels with 500 km bandwidth) of the (c) strongest and (d) longest-lived cyclone tracks for all track points (shading) and at the time of maximum growth rate (white contours at 0.2 intervals), with units of points per million km^2 per season.

cific sector of the Arctic Ocean, with a main development region in the Laptev and East Siberian Seas that extends across the entire Pacific sector (Figure 4.4d). This suggests that the longest-lived cyclones tend to undergo baroclinic development on this eastern portion of the AFZ (i.e., distinct from the AFZ in the Barents/Kara Seas region). The Pacific sector is likely a hotspot for long-lived cyclones due to the proximity of this baroclinic zone with TPVs, which most commonly occur in this region (Cavallo and Hakim, 2010). The track densities of cyclones that are matched and unmatched with TPVs from Gray et al. (2021, Figures 7c and 7d respectively) are broadly similar to that of the longest-lived (Figure 4.4d) and strongest (Figure 4.4c) cyclone subsets here, further suggesting a link with TPVs.

Generally speaking, the strongest cyclones tend to have LLD development, whilst the longest-lived cyclones tend to have ULD development. However, this is not true in all cases. For example, C12 had a LLD development, and is in the strongest subset, but it was also very long-lived (and in the longest-lived subset) due to interaction with a TPV. This highlights that processes outside of a cyclone's main development can be important. This is especially relevant to extremely long-lived cyclones in the summer-time Arctic. Cyclones in the Pacific sector may be longer-lived (regardless of structure during growth) as they are more likely to encounter TPVs. Cyclones that interact with TPVs (forming a cold-core columnar vortex) have more opportunity for complex track evolutions exhibiting periods of re-intensification later in the life cycle.

4.4 Conclusions

In this study we have performed a climatological analysis of summer-time (May-September) Arctic cyclone structure using ERA5 reanalysis (1979–2021), and a modified version of the Hart (2003) cyclone phase space. Motivated by the contrasting life cycles of some notable Arctic cyclone case studies, the focus was how structure at maximum growth rate relates to the subsequent evolution. The findings are summarized below, with reference to the research questions defined in Section 4.1:

1. Cold-core axisymmetric structures are the most common cyclone structure in the summer-time Arctic, accounting for 39.8% of the track points. Asymmetric warm-core (29.0%) and cold-core (23.5%) structures are also common.
2. Low-level-dominant (LLD; 65.5%) and upper-level-dominant (ULD; 34.5%) cyclones follow distinct developmental trajectories in the phase space. During growth, LLD cyclones exhibit warm-core asymmetric structures, whereas ULD cyclones have cold-core asymmetric structures. LLD cyclones tend to have greater asymmetry during growth. However, Arctic cyclones typically exhibit a characteristic transition to a cold-core axisymmetric structure after maturity, regardless of structure at maximum growth rate.

3. LLD cyclones are on average stronger, whilst the ULD cyclones tend to be longer-lived. The strongest cyclones (which are predominantly LLD) preferentially track on the northern coast of Russia, consistent with high baroclinicity on the AFZ. The longest-lived cyclones (typically ULD) tend to track over the Pacific side of the Arctic Ocean basin, likely related to the climatological location of TPVs near North America.

LLD and ULD cyclones have different characteristics consistent with the dominant growth mechanisms for each type. LLD cyclones grow on greater low-level baroclinicity (with weaker tropopause disturbances) and so the near-surface cyclone is strong, but only for a limited time whilst the low-level baroclinic environment exists. ULD cyclones are dominated by some upper-level disturbance (e.g., a TPV), such that the low-level baroclinicity might be weaker, but the system can be maintained for longer if the upper-level feature remains (which can be a considerable length of time for TPVs in the summer-time Arctic), and by the lower tropospheric processes described in Croad et al. (2023a).

This article has proposed a classification scheme for Arctic cyclones, working toward conceptual models which are key for our understanding of cyclone characteristics and hazards. However, some cyclones do not fit into the proposed classification, and these unconventional cyclones may be prevalent in the summer-time Arctic due to the lack of dynamical forcing (i.e., wind shear) for dissipation. Future work should focus on establishing the processes acting in LLD and ULD cyclones. For example, it has been shown that summer-time Arctic cyclones often attain persistent cold-core axisymmetric structures after maturity. Croad et al. (2023a) demonstrated that friction and sensible heat fluxes over sea ice contributed to the maintenance of the cold-core structures of Arctic cyclones in their mature stages, but more work is needed to quantify how large these effects are on cyclone strength and longevity.

Acknowledgements

HLC acknowledges PhD studentship funding from SCENARIO Natural Environment Research Council (NERC) Doctoral Training Partnership grant NE/S007261/1, with co-

supervision by SPEK and super-computing support from ECMWF. JM, BH, and AV were funded by the Arctic Summer-time Cyclones: Dynamics and Sea-Ice Interaction NERC standard grant NE/T006773/1. BH was also supported by the National Centre for Atmospheric Science, which is funded by NERC under contract R8/H12/83. The authors also acknowledge the ECWMF for the production of the ERA5 reanalysis data set.

Chapter 5

The stability of axisymmetric vortex columns with friction and relevance to summer-time Arctic cyclones

This chapter is the most recent version of a draft paper in progress for submission in *Journal of the Atmospheric Sciences*:

Croad, H. L., B. Harvey, and J. Methven: The stability of axisymmetric vortex columns with friction and relevance to summer-time Arctic cyclones. In prep. for *J. Atmos. Sci.*.

Abstract

Summer-time Arctic cyclones commonly undergo a transition to a long-lived axisymmetric columnar vortex structure after maturity, with the low-level cyclone becoming vertically stacked below a tropopause polar vortex (TPV) at upper levels. Previous works examining this cyclone structure have been largely descriptive, but here we focus on understanding the vortex dynamics. TPVs are associated with a positive potential vorticity (PV) anomaly at upper levels, whilst at low levels the damping of surface winds by friction acts to cool the lower troposphere via the Ekman pumping mechanism. Such a setup (with the low-level cold anomaly interpreted as a negative PV anomaly) exhibits opposing radial gradients of PV at upper and lower levels, thereby satisfying the Charney-Stern-Pedlosky necessary condition for baroclinic instability. Here we investigate the dynamical instability of this idealised axisymmetric columnar vortex setup using a two-layer quasi-geostrophic (QG) model with friction in the lower layer. It is shown that vortex states

consisting of a vortex in the upper layer with winds reduced to zero in the lower layer are indeed unstable, but only for vortices larger than a “short-scale cutoff”, a vortex radius equal to 1.2 times the Rossby radius of deformation. Furthermore, numerical simulations indicate that friction can act to destabilise vortices that are initially stable by cooling the lower troposphere over time. In both cases, the instability leads to a splitting of the vortex into several smaller ones, each being smaller than the small-scale cutoff and therefore being stable. From examination of two real summer-time Arctic cyclone cases, we deduce the values of physical parameters that govern the dynamics and find that predictions for the most unstable wavenumber are consistent with observed disturbances to the vortex columns. Further work is required to examine the importance of this instability mechanism in real summer-time Arctic cyclone cases.

5.1 Introduction

Arctic cyclones are the most energetic weather system in the summer-time Arctic, producing strong winds, ocean waves (Thomson and Rogers, 2014; Waseda et al., 2018, 2021), and rapid changes to sea ice cover (Asplin et al., 2012; Lukovich et al., 2021; Peng et al., 2021), all of which pose major hazards to the increasing human activity in the region. A particularly notable quality of summer-time Arctic cyclones that distinguishes them from their winter-time Arctic and mid-latitude counterparts is their longevity (Vessey et al., 2022). For example, a famous case in August 2012 had a lifetime of ~ 13 days (Simmonds and Rudeva, 2012), whilst the longest-lived cyclone in the climatology by Croad et al. (2023b) had a lifetime of almost one month.

Whilst the mid-latitude flow is dominated by Rossby waves, Woollings et al. (2023) demonstrated that Rossby wave activity is reduced in the polar regions (due to a weaker meridional gradient of planetary vorticity), with isolated vortices often dominating. One such example is tropopause polar vortices (TPVs), coherent circulation features on the tropopause with horizontal scales of less than 1500 km, and lifetimes that can exceed one month (Cavallo and Hakim, 2010). For example, the longest-lived TPV identified in the climatological study of Gray et al. (2021) had a lifetime of 43 days. TPVs are a common

feature of the summer-time Arctic due to the lack of a zonal jet stream and wind shear (that would destroy such features in the mid-latitudes), and they are known to excite and interact with surface cyclones (Gray et al., 2021). Woollings et al. (2023) also demonstrated that high-latitude Rossby waves are less dispersive, such that weather phenomena may be more persistent in the polar regions.

Croad et al. (2023b) performed a climatology of summer-time Arctic cyclone structure, and classified cyclones as being either low-level dominant (LLD) or upper-level dominant (ULD) in terms of vorticity structure during growth. Around two thirds of the summer-time Arctic cyclones from 1979–2021 were found to be LLD during growth, and these systems tended to be stronger, whilst the remaining third were found to be ULD, and these systems were on average longer-lived. Similarly, in the climatological analysis of Gray et al. (2021) it was shown that one third of all summer-time Arctic cyclones develop in the vicinity of TPVs, suggesting that the ULD cyclones identified in Croad et al. (2023b) likely develop with TPVs. However, regardless of structure during growth, a transition to a persistent cold-core axisymmetric structure after maturity is characteristic of summer-time Arctic cyclones (Croad et al., 2023b). This axisymmetric columnar vortex structure that can persist for many days after maturity has also been reported in a climatology of extreme cyclones (Vessey et al., 2022), and in several extreme summer-time Arctic cyclone cases, with the low-level cyclone becoming vertically stacked below a TPV at upper levels (e.g. Tanaka et al., 2012; Tao et al., 2017). This evolution is unlike that of mid-latitude cyclones, which exhibit a tilted structure during growth and do not last long after maturity due to non-linear Rossby wave breaking or the influence of other large-scale disturbances.

The previous works describing the axisymmetric columnar vortex structure of mature summer-time Arctic cyclones have largely been descriptive in nature, with less focus on the dynamics of these systems. TPVs are associated with positive potential vorticity (PV) anomalies on the tropopause (Cavallo and Hakim, 2010), whilst friction is associated with negative PV tendencies in the boundary layer (BL; Croad et al., 2023a). Furthermore, Croad et al., 2023a demonstrated that during this mature stage friction (and sensible heat fluxes if located over sea ice, although not considered here) acts to cool the cyclone ther-

mal anomaly in the lower troposphere. If a surface cold anomaly is established, this can be thought of as resulting from a negative PV anomaly concentrated at the surface (Bretherton, 1966). Hence, this setup features opposing radial gradients of PV at upper and lower levels, thereby satisfying the necessary (but not sufficient) Charney-Stern-Pedlosky (CSP) condition for baroclinic instability (Vallis, 2017).

Here we investigate the dynamical instability of this axisymmetric columnar vortex setup, with a focus on the impact of friction, and how this relates to the persistence of mature summer-time Arctic cyclones. We do this by employing an idealised modelling approach, which permits for parameter space of the dynamics to be fully explored. The quasi-geostrophic (QG) model is a commonly-used framework to describe baroclinic instability in the atmosphere for phenomena that occur on synoptic scales, such that hydrostatic and geostrophic balances are approximately valid. An often-used model is the two-layer QG model (Flierl, 1978; Pedlosky, 1987). The model is comprised of two vertical layers in which the dynamics is governed by the evolution of quasi-geostrophic potential vorticity (QGPV). The two layers interact via the circulation induced by one QGPV anomaly on the other (“action at a distance”). This two-layer QG model has been used to study the baroclinic instability of parallel flows (e.g. Phillips, 1954) and of circular vortices (e.g. Carton et al., 2010; Flierl, 1988) in replicating atmospheric and oceanic phenomena such as the mid-latitude jet stream and ocean eddies.

Previous studies have extended the classical Eady and Charney models, which are both essentially QG layer models applied to a parallel flow basic state (Hoskins and James, 2014), to include friction (e.g. Card and Barcilon, 1982; Williams and Robinson, 1974), and it has been shown that friction acts to reduce the growth rate of baroclinic waves. Furthermore, Boutle et al. (2009) demonstrated that inclusion of friction in the Eady model reduced the growth rates of unstable modes, but that it also introduced instability at short wavelengths where there was previously no instability, thereby removing the so-called “short-wave cutoff”.

In this study we investigate the instability of vertically-stacked circular vortices in the two-

layer QG model, meant to replicate the structure of mature summer-time Arctic cyclones, with friction prescribed to act in the lower layer. To the authors' knowledge, this is the first study to investigate the stability of the axisymmetric vortex phase of summer-time Arctic cyclones, and more generally to consider the impact of friction in axisymmetric vortex setups in the two-layer QG model.

A TPV in the presence of friction will tend towards a steady state with zero surface winds. We first analyse the linear stability of this zero wind steady state with and without friction, and then perform non-linear simulations to (i) verify the linear stability analysis, and (ii) explore how the instability develops into its non-linear phase. In reality, we expect friction to damp the cyclonic surface winds gradually over time. The non-steady background state in this case means that a linear stability analysis cannot be performed. However, non-linear simulations are run in which a TPV is initially associated with some low-level winds, to examine whether friction can lead to instability in that case. We aim to answer the following questions:

1. Under what circumstances are vortex columns unstable?
2. What is the impact of friction on the vortex instability?
3. How does the instability evolve non-linearly at large amplitude?
4. To what extent are the results applicable to real world cases?

The paper is structured as follows. The methodology is described in Section 5.2, including details of the two-layer QG model (and the method, developed by Ben Harvey, for numerically integrating this equation set in time). Two summer-time Arctic cyclone case studies are then examined in Section 5.3, to aid selection of relevant physical parameters and scalings for the problem. The main results are then presented, with a linear stability analysis performed in Section 5.4, and the non-linear numerical simulations discussed in Section 5.5. A discussion relating the results to the real world is provided in Section 5.6. The study is concluded in Section 5.7.

5.2 Methodology

5.2.1 The two-layer QG model

QGPV is a quantity whose advection on horizontal surfaces mimics the advection of the full Rossby-Ertel PV on isentropic surfaces. QG theory and QGPV are suitable for the study of atmospheric phenomena that are close to geostrophic balance (e.g. Chapter 5 in Vallis, 2017). The flow is determined by the geostrophic stream function ψ_g (henceforth the g subscript is dropped for brevity) which specifies the winds $\vec{v} = (u, v)$ and buoyancy anomaly b' by:

$$u = -\frac{\partial\psi}{\partial y} \quad v = \frac{\partial\psi}{\partial x} \quad b' = f_0 \frac{\partial\psi}{\partial z} \quad (5.1)$$

and the QGPV anomaly from the background planetary vorticity (f) via:

$$q = QGPV - f = \underbrace{\nabla_H^2 \psi}_{\xi} + \frac{f_0^2}{N^2} \frac{\partial^2 \psi}{\partial z^2} \quad (5.2)$$

where the Boussinesq approximation has been made such that density, ρ , and the Brunt-Väisälä frequency, $N = \sqrt{\frac{g}{\theta} \frac{\partial\theta}{\partial z}}$, are assumed to be approximately constant. $\nabla_H^2 = \frac{\partial^2}{\partial x^2} + \frac{\partial^2}{\partial y^2}$ is the horizontal Laplacian, and ξ is the geostrophic relative vorticity. A constant f is assumed (a reasonable approximation in the polar regions where the meridional gradient of planetary vorticity is small), with a value f_0 . q is conserved following the geostrophic flow in the absence of friction and diabatic effects. Hence, q is advected horizontally by the geostrophic wind and modified by the frictional force \vec{F} and diabatic heating S :

$$\frac{Dq}{Dt} = \hat{\mathbf{k}} \cdot (\nabla \times \vec{F}) + \frac{\partial S}{\partial z} \quad (5.3)$$

A two-layer model setup is employed (e.g. Flierl, 1978; Pedlosky, 1987), with the lower and upper layers denoted by subscripts 1 and 2 respectively. This study focuses on the impact of friction, and so considers the case of no diabatic heating ($\frac{\partial S}{\partial z} = 0$). Rayleigh friction is prescribed in the bottom layer, with the frictional force parametrized as being directly proportional to the wind speed, $\vec{F} = -\frac{1}{\tau_E}(u, v)$ (equivalent to integrating the eddy diffusion term vertically over an Ekman BL), where τ_E is the Ekman friction spin-down

timescale:

$$\frac{Dq_1}{Dt} = -\frac{1}{\tau_E} \nabla_{H^2} \psi_1, \quad \frac{Dq_2}{Dt} = 0 \quad (5.4)$$

5.2.2 Numerical integration of the two-layer QG model

Numerical simulations are generated by integrating the two-layer QG model equations numerically in time. The method used, as outlined in this section, was developed by Ben Harvey. To integrate the two-layer QG equations numerically, Equation 5.2 is discretised in each layer as follows:

$$q_1 = \nabla_{H^2} \psi_1 + \frac{f_0^2}{N^2} \frac{\psi_2 - \psi_1}{H_s^2}, \quad q_2 = \nabla_{H^2} \psi_2 - \frac{f_0^2}{N^2} \frac{\psi_2 - \psi_1}{H_s^2} \quad (5.5)$$

where H_s is the relevant height scale (assumed to be half the depth of the troposphere). At each time step, the q_1 and q_2 fields are inverted to find ψ_1 and ψ_2 . The inversion at each time step is performed on a doubly periodic domain using Fourier transforms, using a modified form of the code used in Harvey et al. (2018). The resulting winds are used to advect q_1 and q_2 to the next time step using a semi-Lagrangian advection scheme (Durran, 2013). A Lifschitz condition is applied to obtain a dynamically varying time step ensuring the model remains numerically stable.

All numerical simulations are performed on a square grid comprised of 256 grid points in the x and y directions. The domain lengths are set to be 20 times the vortex radius, to minimise the impact of the boundaries on the vortex dynamics, and a constant model height of $2H_s$ is set in all runs. Small-magnitude random noise (with maximum magnitude 50 times smaller than the initial QGPV anomaly in each layer) is added to both layers of each model run, replicating small perturbations in the real world that kick off baroclinic instability. The same small-magnitude random noise is applied to each model run, to ensure that any observed differences are not due to different initial conditions.

5.2.3 Reanalysis data

Two summer-time Arctic cyclone cases are examined in ERA5, the fifth-generation European Centre for Medium-Range Weather Forecasts (ECMWF) reanalysis (Hersbach et al., 2017, 2020), to inform choice of physical parameters and scales for the subsequent analysis. ERA5 is produced using the ECMWF’s Integrated Forecasting System model cycle 41r2. The model has spectral truncation TL639 (~ 31 km resolution at the equator), and 137 terrain-following hybrid-pressure levels from the surface to 0.01 hPa. We use data transformed onto a regular 0.25° latitude-longitude grid on pressure levels.

5.3 Key physical parameters and scales

Parameters and scales must be selected to physically interpret the (non-dimensionalised) QG model output. In the Arctic, a uniform planetary vorticity of $f = 1.4 \times 10^{-4} \text{ s}^{-1}$ is assumed. The atmosphere is prescribed to have typical values for static stability of $N = 10^{-2} \text{ s}^{-1}$, and BL eddy viscosity coefficient of $A = 5 \text{ m}^2 \text{ s}^{-1}$ (e.g. Chapter 8 in Holton and Hakim, 2012).

Two summer-time Arctic cyclone case studies that exhibit axisymmetric structures are examined to obtain physically reasonable vortex parameters. The Great Arctic cyclone of August 2012 (Simmonds and Rudeva, 2012) initially exhibited a tilted baroclinic structure during growth and at maximum intensity (with an asymmetric and low-level dominant structure; Croad et al., 2023b). However, by 36 hours after maximum intensity the cyclone is vertically-stacked below a broad upper-level positive PV anomaly, with the system attaining a cold-core columnar vortex structure in the central Arctic (Figure 5.1a). A cross-section through the system at this time highlights that the vortex has a span of almost 2000 km (i.e. a radius of 1000 km), judging by the distance between the wind maxima on the flanks of the upper-level feature, with wind speeds of up to 50 m s^{-1} (Figure 5.1b). A July 2020 cyclone (which was also examined in Croad et al., 2023a) had lower asymmetry and an upper-level dominant structure during growth (Croad et al., 2023b), and therefore more quickly obtained an axisymmetric structure after maturity. At 24 hours after maximum intensity the cyclone is positioned in the Pacific sector of the

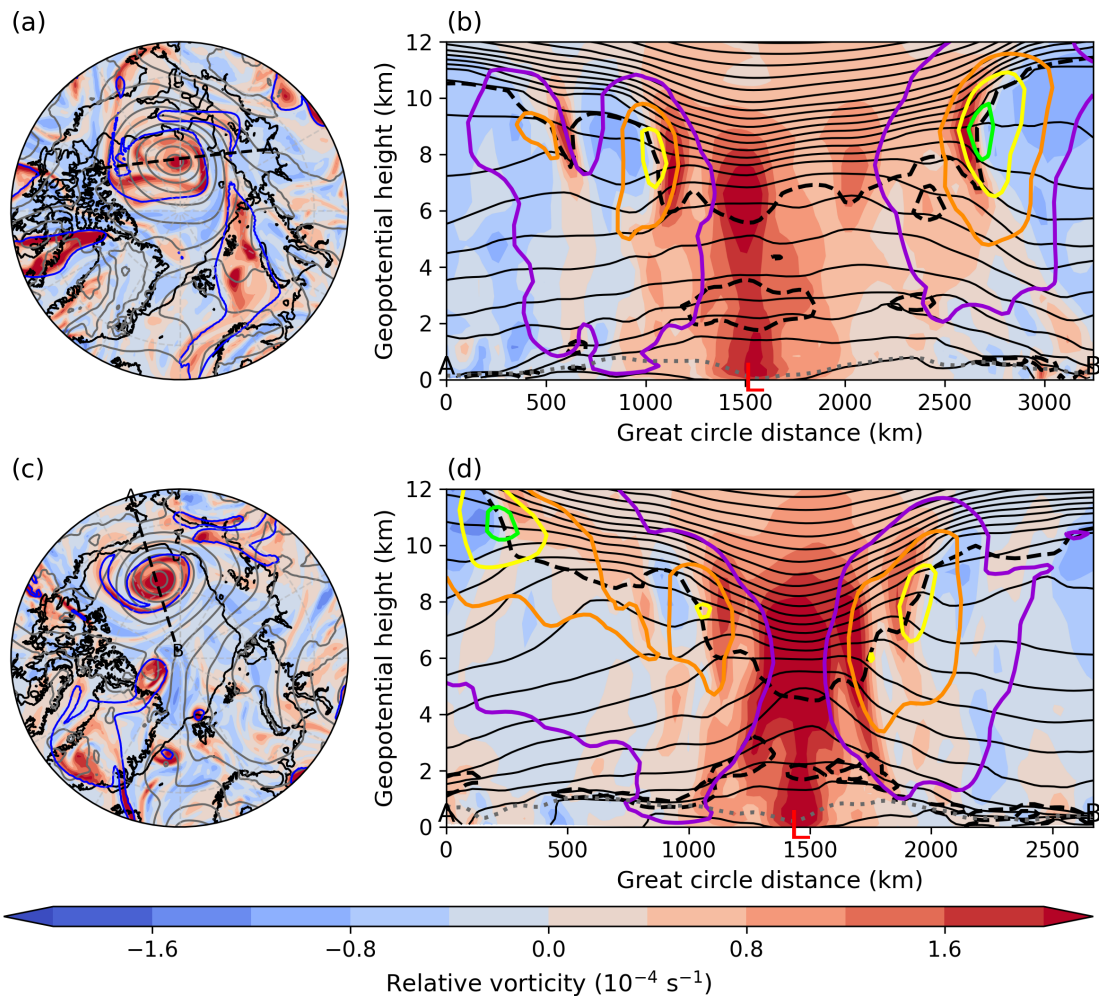


Figure 5.1: Summer-time Arctic cyclone case studies from ECMWF ERA5 reanalysis at (top) 12Z 7 August 2012 and (bottom) 00Z 29 July 2020. (a,c) 400 hPa relative vorticity (shading), overlain with mean sea level pressure (grey contours), the sea ice edge (0.15 sea ice fraction; black contour), and 310 K potential temperature on the PV2 surface (blue contours). The black dashed lines mark the transect of the cross-sections in panels b and d. (b,d) Vertical cross-sections linearly interpolated at 100 points between A and B of relative vorticity (shading), potential temperature (solid black contours), 2 PVU contour (dashed black line), the BL top (dotted grey line), and wind speed (with purple, orange, yellow and green lines denoting 20, 30, 40, and 50 m s^{-1} respectively). Minimum mean sea level pressure is marked with a red L.

Arctic with a cold-core axisymmetric structure (Figure 5.1c). A cross-section through the system at this time demonstrates a vortex of radius ~ 500 km with winds exceeding 40 m s^{-1} on the flanks of the upper-level TPV (Figure 5.1d). The vortex exhibits relative vorticity in the upper-levels of $\sim 2 \times 10^{-4} \text{ s}^{-1}$ (Figure 5.1d). The cyclone cross-sections indicate tropopause depths of approximately 7000 m.

For this study a constant tropopause depth of 7000 m is assumed such that $H_s = 3500$ m.

This gives a Rossby radius of deformation, the length scale at which rotational effects become as important as buoyancy effects in the flow evolution, of $L_R = \frac{NH_s}{f} = 250$ km. For scaling purposes, a horizontal length scale of $L_s = L_R = 250$ km, and a horizontal wind scale of $U_s = 20 \text{ m s}^{-1}$ are taken. This gives a time scale $t_s = \frac{L_s}{U_s} = 3.5$ hours.

Fundamentally, Arctic cyclone structures are characterised by 3 scales; radius (R_a^*), depth (H^*), and wind speed (U^*), where the * superscript refers to dimensional quantities. The August 2012 cyclone has $R_a^* = 1000$ km, $U^* = 30 \text{ m s}^{-1}$ over a broad region, and $H^* = 7000$ m (Figure 5.1b), which corresponds to Rossby number $Ro = \frac{U^*}{fR_a^*} \approx 0.2$ and Froude number $Fr = \frac{U^*}{NH^*} \approx 0.4$. Both of these non-dimensional parameters being less than 1 indicates that QG theory is an appropriate framework for this problem. A dimensional radius of $R_a^* = 1000$ km corresponds to a non-dimensional radius of $R_a = \frac{R_a^*}{L_s} = 4$. In cross-section (Figure 5.1b) the maximum dimensional winds are $\max(U^*) = 50 \text{ m s}^{-1}$, or non-dimensional value $\max(U) = \frac{\max(U^*)}{U_s} = 2.5$.

The July 2020 cyclone has $R_a^* = 500$ km and $\max(U^*) = 40 \text{ m s}^{-1}$, with approximately the same average wind speed and tropopause depth as the August 2012 case (Figure 5.1d), corresponding to Rossby number $Ro = \frac{U^*}{fR_a^*} \approx 0.4$, and the same Froude number $Fr = \frac{U^*}{NH^*} \approx 0.4$. These numbers again suggest that a QG framework is appropriate for modelling this cyclones. The system has non-dimensional radius $R_a = \frac{R_a^*}{L_s} = 2$ and non-dimensional maximum winds of $\max(U^*) = \frac{\max(U^*)}{U_s} = 2$.

The vertical Ekman number for $A = 5 \text{ m}^2 \text{ s}^{-1}$ is $Ek = \frac{A}{fH_s^2} \approx 2.9 \times 10^{-3}$, indicating that the Coriolis force dominates over friction (as in the real atmosphere). The Ekman spin-down timescale is $\tau_E = \frac{H_s}{\sqrt{Af}} \approx 1.5$ days, which is long compared to $\frac{1}{f}$, as in the real atmosphere. Following Pedlosky (1987), non-dimensionalising the inverse of the Ekman spin-down timescale gives a coefficient of friction $\kappa = \frac{1}{\tau_E} \frac{L_s}{U_s} \approx 0.1$.

5.4 Linear stability analysis

Consider the evolution of a vortex column in the two-layer QG model (with cyclonic flow in both layers) with friction only in the lower layer. Friction will act to spin down the vorticity and azimuthal flow in the lower layer towards zero. While the upper-layer QGPV is unaffected by friction and continues to induce a cyclonic circulation in the layer below, zero wind in the lower layer must eventually be achieved by the appearance of a negative QGPV anomaly in the lower layer, which induces an anticyclonic flow with a structure that precisely cancels the cyclonic flow induced by the upper vortex. This negative QGPV anomaly in the lower-layer results in a radial QGPV gradient with the opposite sign to the upper layer, therefore satisfying the CSP necessary criterion for instability (Vallis, 2017). A linear stability analysis is performed here with the aim to understand whether this circular steady state is unstable to friction acting in the lower layer. Note that the background state would not be steady if the relative vorticity in the lower layer was non-zero (due to the action of friction). Hence the stability analysis is conducted for the special case in which there are zero low-level winds, taken to represent the mature stage of a summer-time Arctic cyclone. Note that the linear stability analysis results are only valid for small-amplitude perturbations (i.e. at early stages in the evolution). The QG model is used later (Section 5.5) to evaluate the results of the linear stability analysis and investigate later stages in the evolution, which can be non-linear.

From now on, we will refer to the non-dimensionalised two-layer QGPV model, which is obtained from Equation 5.5 by scaling the parameters as $q^* = q \frac{U_s}{L_s}$, $\psi^* = \psi U_s L_s$, $\nabla_H^* = \nabla_H \frac{1}{L_s}$, and $z^* = z H_s$ (as in Section 6.16 of Pedlosky, 1987):

$$q_2 = \nabla_H^2 \psi_2 - \frac{\psi_2 - \psi_1}{(L_R/L_s)^2}, \quad q_1 = \nabla_H^2 \psi_1 + \frac{\psi_2 - \psi_1}{(L_R/L_s)^2} \quad (5.6)$$

5.4.1 Defining the basic state

To construct the basic state described above, we prescribe the upper layer QGPV profile $q_2 = Q_2(r)$ and that the lower layer winds are zero ($\psi_1 = \Psi_1(r) = 0$), where the upper case symbols denote the basic state. We solve in cylindrical coordinates to find $q_1 =$

$Q_1(r)$ and $\psi_2 = \Psi_2(r)$:

$$Q_2 = \frac{1}{r} \frac{\partial}{\partial r} \left(r \frac{\partial \Psi_2}{\partial r} \right) - \frac{\Psi_2}{(L_R/L_s)^2} \quad (5.7)$$

$$Q_1 = \frac{\Psi_2}{(L_R/L_s)^2} \quad (5.8)$$

Solving Equation 5.7 for $\Psi_2(r)$ given $Q_2(r)$ yields $Q_1(r)$ via Equation 5.8. Since the differential equations are linear, a Green's function method can be employed. Setting the right hand side (RHS) of Equation 5.7 equal to $\delta(r - r_0)$, where δ is the Dirac delta function, and solving for Ψ_2 will yield the Green's function for this equation. Expanding the RHS of Equation 5.7 and using $R = \frac{r}{(L_R/L_s)}$ gives:

$$\frac{1}{(L_R/L_s)^2} \left[\frac{\partial^2 \Psi_2}{\partial R^2} + \frac{1}{R} \frac{\partial \Psi_2}{\partial R} - \Psi_2 \right] = (L_R/L_s) \delta(R - R_0) \quad (5.9)$$

If the RHS is zero, this is the modified Bessel equation, which has two independent solutions $K_0(R)$ and $I_0(R)$. We find separate solutions for $R < R_0$ and $R > R_0$ (where the RHS is zero), and ensure they match at R_0 . For a bounded solution:

$$\Psi_2(R; R_0) = \begin{cases} c_1 I_0(R) & \text{for } R < R_0 \\ c_2 K_0(R) & \text{for } R > R_0 \end{cases} \quad (5.10)$$

for some constants c_1 and c_2 . To determine these constants we impose two boundary conditions; firstly that $\Psi_2(r)$ is continuous at $R = R_0$, and secondly that it's slope jumps at $R = R_0$ by L_R/L_s . The solution is:

$$\Psi_2(r; r_0) = G_0(r; r_0) = -r_0 \begin{cases} K_0 \left(\frac{r_0}{(L_R/L_s)} \right) I_0 \left(\frac{r}{(L_R/L_s)} \right) & \text{for } r < r_0 \\ I_0 \left(\frac{r_0}{(L_R/L_s)} \right) K_0 \left(\frac{r}{(L_R/L_s)} \right) & \text{for } r > r_0 \end{cases} \quad (5.11)$$

where G_0 is the Green's function. This method can be used to invert any QGPV profile $Q_2(r)$ by writing:

$$Q_2(r) = \int_0^\infty Q_2(r_0) \delta(r - r_0) dr_0 \quad (5.12)$$

$$\Psi_2(r) = \int_0^\infty Q_2(r_0) G_0(r; r_0) dr_0 \quad (5.13)$$

The basic state of the idealised TPV setup with $R_a = 2$ (i.e. $R_a^* = 500$ km) is presented in Figure 5.2. The positive QGPV anomaly in the upper layer and zero winds in the lower layer are consistent with positive (i.e. cyclonic) winds in the upper layer, and a negative QGPV anomaly in the lower layer. An upper layer QGPV anomaly with a maximum value of 5.2 was selected to give upper-level maximum winds of $U_2 = 2$ with relative vorticity $\xi_2 \sim 2$, which corresponds to dimensional values of $U_2^* = U_2 U_s = 40$ m s⁻¹ and $\xi_2^* = \xi_2 \frac{U_s}{L_s} = 1.6 \times 10^{-4}$ s⁻¹. These dimensional values match closely with those in the July 2020 Arctic cyclone (Figure 5.1d). The basic state is consistent with a negative QGPV anomaly in the lower layer of $Q_1 \sim -3.5$.

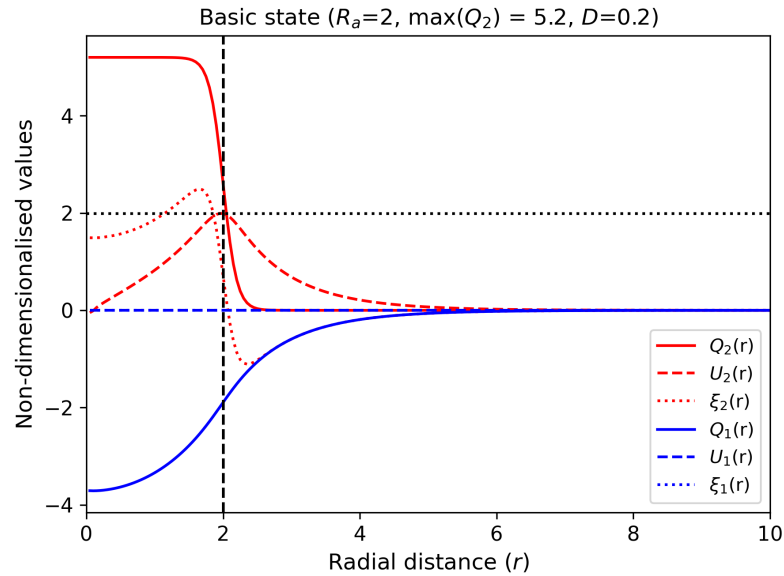


Figure 5.2: The basic state achieved by prescribing a positive upper-layer QGPV anomaly of the form $Q_2(r) = \frac{\max(Q_2)}{2} (1 - \tanh(\frac{r-R_a}{D}))$ and the lower-layer streamfunction $\Psi_1 = 0$, where $R_a = 2$, $\max(Q_2) = 5.2$ and $D = 0.2$. Q_2 (red solid line), U_2 (red dashed line) and ξ_2 (red dotted line) refer to the upper-layer basic state QGPV, azimuthal wind and relative vorticity respectively, whilst Q_1 (blue solid line) and U_1 (blue dashed line) and ξ_1 refer to the lower-layer equivalents. The vertical black dashed line marks the vortex radius R_a , and the horizontal black dotted line marks the maximum value of $U_2 = 2$.

5.4.2 Characterising the instability of the basic state

To understand if this basic state is unstable, we add a small wave-like perturbation and see if this grows in time. The mathematical methods are provided in Appendix A, with a qualitative discussion of the results discussed here. We calculate the growth rates of perturbations that grow due to the coupling of the upper and lower layers (i.e. baroclinic instability). The growth rates of the fastest growing mode as a function of perturbation wavenumber (i.e. the number of perturbations about the edge of the vortex) for different vortex radii are presented in Figure 5.3. The growth rates are non-zero for many wavenumber-radius combinations, indicating instability. For $R_a = 2$, the fastest growing mode occurs at perturbation wavenumber 2.

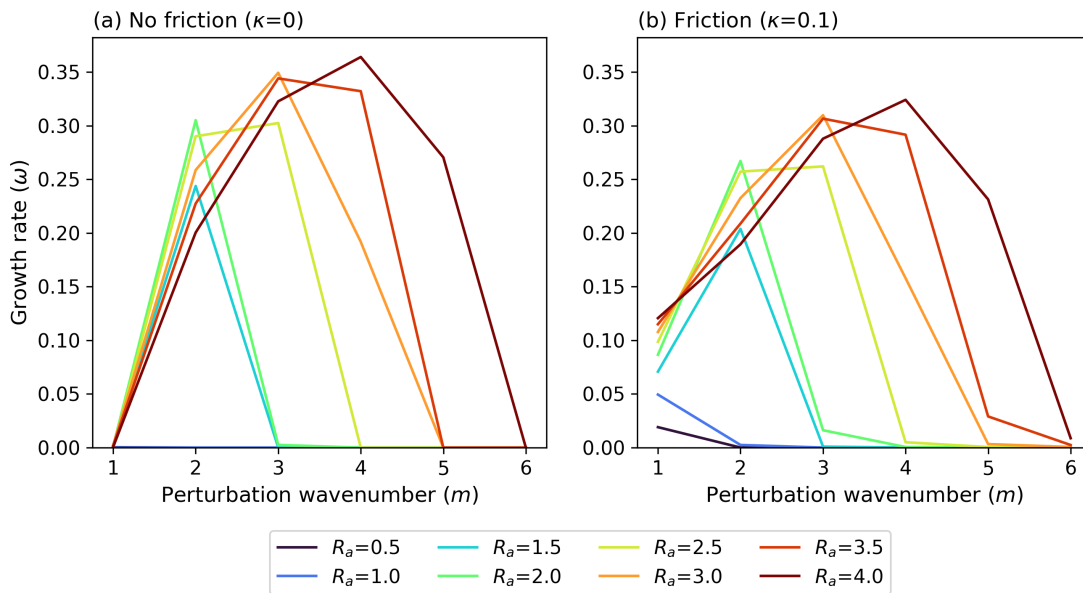


Figure 5.3: The non-dimensionalised growth rate of the linear fastest growing mode for the form of the basic state in Figure 5.2 as a function of perturbation wavenumber (m) for vortex radii (R_a) 0.5–4.0 (with increasing radii from blue to red coloured lines). Panel (a) is the no-friction solution, whilst panel (b) is the solution with Rayleigh friction included ($\kappa = 0.1$).

For the wavenumbers that are unstable without friction (Figure 5.3a), friction acts to decrease the growth rate (Figure 5.3b). However, friction also destabilises some wavenumbers that were stable in the frictionless system, with the growth rate curves having longer tails in Figure 5.3b, indicating that friction has led to instability at higher and lower wavenumbers where in the frictionless case there was none. For example, a vortex of

radius $R = 1$ is stable for all wavenumbers when there is no friction (Figure 5.3a), but exhibits instability at $m = 1$ when friction is included (Figure 5.3b). The impact of adding friction in the Eady model is qualitatively the same (e.g. Boutle et al., 2009).

The growth rates presented here are dimensionalised by $\omega^* = \omega \frac{U_s}{L_s}$. If $\omega = 0.25$, this gives $\omega^* = 2 \times 10^{-5} \text{ s}^{-1} \approx 1.7 \text{ day}^{-1}$. This growth rate is comparable to the typical mid-latitude Eady growth rate of the order of 1 day^{-1} (e.g. Vallis, 2017).

Stability within parameter space is further examined in Figure 5.4, with growth rate curves as a function of vortex radii for different QGPV anomaly magnitudes (i.e. $\max(Q_2)$) and coefficients of friction (κ). Figure 5.4a demonstrates that halving the magnitude of the QGPV anomaly results in half the growth rate. That is to say that the growth rate of instability is directly proportional to the magnitude of the QGPV anomaly. In Figure 5.4a, for each wavenumber, non-zero growth rates are only present above a certain vortex radius, indicating a “short-scale cutoff” for instability. For systems smaller than the short-scale cutoff, the streamfunctions induced by the upper and lower layer QGPV anomalies do not have sufficient vertical extent for coupling and for mutual growth of perturbations (i.e. baroclinic instability). For perturbation wavenumber $m = 2$, the short-scale cutoff occurs at $R_a = 1.2$, indicating that this vortex instability only occurs for vortices with radius greater than $R_a^* = 300 \text{ km}$. For higher perturbation wavenumbers, this short-scale cutoff occurs at higher values of R_a (e.g. for $m = 3$ only vortices with radius greater than $R_a = 2$ or $R_a^* = 500 \text{ km}$ are unstable).

Figure 5.4b demonstrates that increasing the coefficient of friction reduces the maximum growth rates associated with this vortex instability. The inclusion of friction also permits some instability below the short-scale cutoff, although the instability is typically much smaller than above the short-scale cutoff. In the no-friction solutions, there is no instability for perturbation wavenumber $m = 1$ (Figure 5.4a). However, the addition of friction leads to instability at $m = 1$ for all vortex radii greater than $R_a \approx 0.3$.

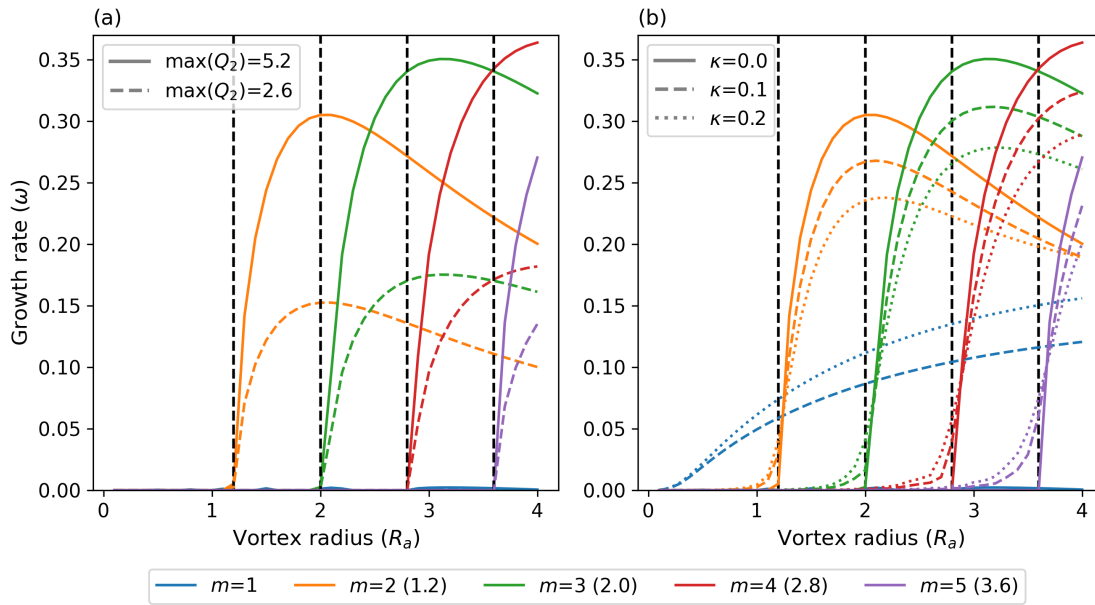


Figure 5.4: The non-dimensionalised growth rate of the linear fastest growing mode for the form of the basic state in Figure 5.2 as a function of vortex radii for perturbation wavenumbers 1 (blue), 2 (orange), 3 (green), 4 (red) and 5 (purple). In (a) the growth rates are plotted for $\max(Q_2) = 5.2$ (solid) and $\max(Q_2) = 2.6$ (dashed) with $\kappa = 0$ and $D = 0.2$. In (b) the growth rates are plotted for $\kappa = 0.0$ (solid), $\kappa = 0.1$ (dashed), and $\kappa = 0.2$ (dotted), with $\max(Q_2) = 5.2$ and $D = 0.2$. Black dashed vertical lines denote the shortscale cutoff (for $\kappa = 0$) for each perturbation wavenumber, the value of which is given in the legend.

5.5 Non-linear numerical simulation results

In this section, the non-linear evolution of the instability is examined with numerical integrations of the QG equations. Firstly, model runs are performed with an initial setup identical to the form of the basic state used in the linear stability analysis (i.e. zero wind in the lower layer, replicating a mature cyclone stage), to test whether the observed behaviour is consistent with the linear stability analysis (Section 5.5.1). Subsequently, simulations are run with cyclonic surface winds present in the initial condition (Section 5.5.2), representing earlier stages of the cyclone lifecycle, which are subsequently damped by friction.

5.5.1 Comparison with the linear stability analysis

The QG model has been run without and with friction for vortex radii $R_a = 1 - 4$, with a selection of plots here chosen to highlight the key findings: the short-scale cutoff, the

role of friction, and the dominant wavenumber of perturbations. The results from the QG model are consistent with the results from the linear stability analysis in the early stages of the simulations.

Firstly, the short-scale cutoff is examined in the QG model without friction in Figure 5.5. Figures 5.5a and 5.5b show vortices with radii $R_a = 1.0$ and $R_a = 1.5$ at the start time ($t = 0$), with a circular positive QGPV anomaly in the top layer vertically stacked on a circular negative QGPV in the bottom layer. According to the linear stability analysis, a vortex with radius $R = 1$ should be stable (because it is smaller than the short-scale cutoff), whilst a vortex with radius $R = 1.5$ should be unstable with a wavenumber 2 dominance (Figure 5.4). At $t = 30$ ($t^* = t_s t \sim 4.4$ days), the $R = 1.0$ vortex is largely unchanged from its initial state (Figure 5.5c). However, the $R = 1.5$ vortex has undergone wavenumber 2 instability, with the lower layer QGPV anomaly splitting into two parts (Figure 5.5d). This is consistent with there being a short-scale cutoff for instability, as initially identified in the linear stability analysis.

The impact of friction on a $R_a = 2$ vortex in the QG model is demonstrated in Figure 5.6. According to the linear stability analysis, a vortex of this size should be unstable with a wavenumber 2 dominance (Figure 5.4). Figures 5.6a and 5.6b show the vortex without and with friction ($\kappa = 0.1$) respectively at $t = 20$ ($t^* = t_s t \sim 2.9$ days), with both vortices undergoing wavenumber 2 instability and beginning to shear into two parts (consistent with the linear stability analysis). The no-friction run (Figure 5.6a) has undergone more of a deformation from the initially circular state than the friction run (Figure 5.6b), consistent with friction acting to reduce the growth rates of vortex instability.

By $t = 40$ ($t^* = t_s t \sim 5.8$ days), the main vortex has split into several smaller components in both the no-friction (Figure 5.6c) and friction (Figure 5.6d) runs. In both cases the main vortex has broadly split into three separate vortices, one remaining at the centre of the domain with two linear filaments, and two others splitting off and moving away from the centre of the domain (each with an upper layer positive QGPV anomaly and corresponding lower layer negative QGPV). This suggests that the vortex instability ul-

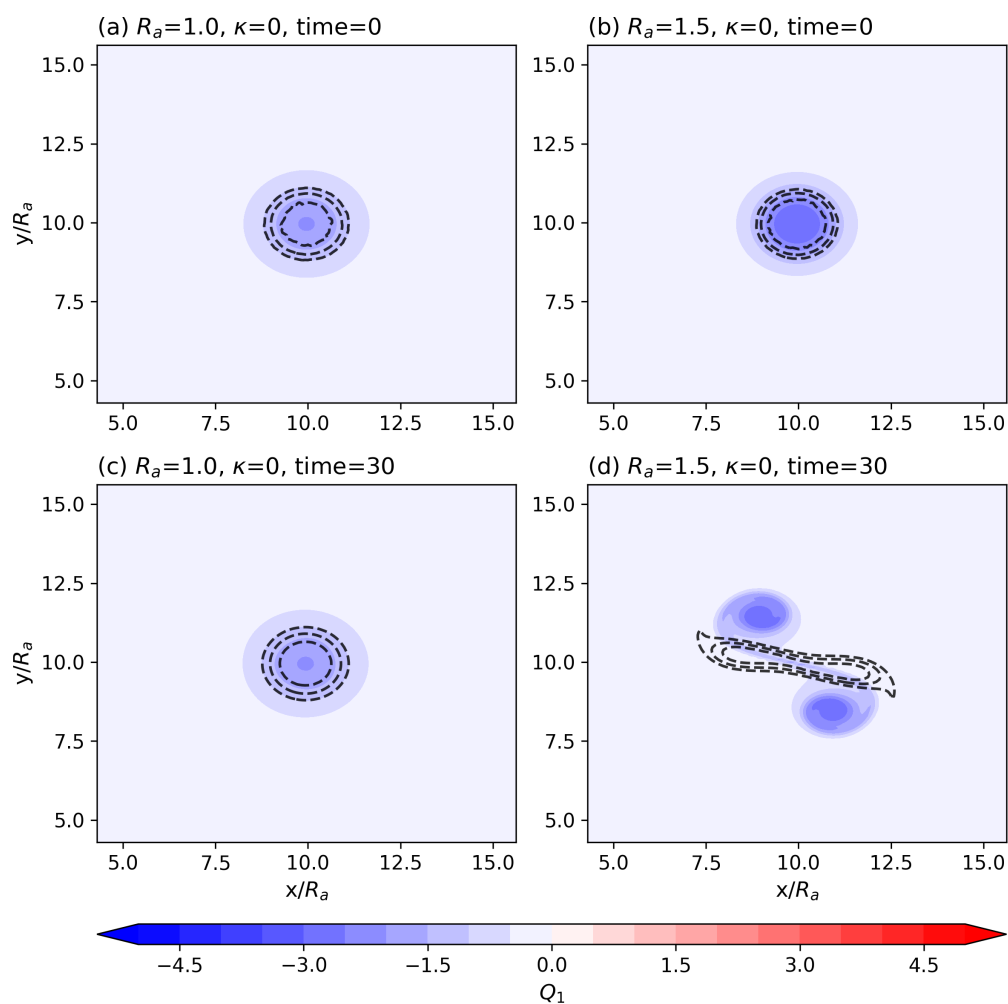


Figure 5.5: QG model runs with the same initial setup as the linear stability analysis ($\max(Q_2) = 5.2$, $D = 0.2$), showing the lower layer QGPV (Q_1 ; shading) and the upper layer QGPV (Q_2 ; black dashed contours starting at +2 with a contour interval of 2) on the QG model grid (zoomed in to focus on vortex). The panels show snapshots of the QG model runs with no friction ($\kappa = 0$) for (a) $t = 0$ and $R_a = 1.0$, (b) $t = 0$ and $R_a = 1.5$, (c) $t = 30$ and $R_a = 1.0$, and (d) $t = 30$ and $R_a = 1.5$.

timately leads to a splitting of the main vortex (a highly non-linear state that the linear stability analysis cannot describe), into smaller vortices that are smaller than the small-scale cutoff, and are therefore stable. Note that friction has acted to slow down the vortex split, with low-level negative QGPV that is smaller in magnitude (Figure 5.6d) than the frictionless run (Figure 5.6c).

Section 5.4 indicates that larger vortex radii are associated with a larger dominant perturbation wavenumbers, and this is also seen in the QG model (Figure 5.7). For vortices

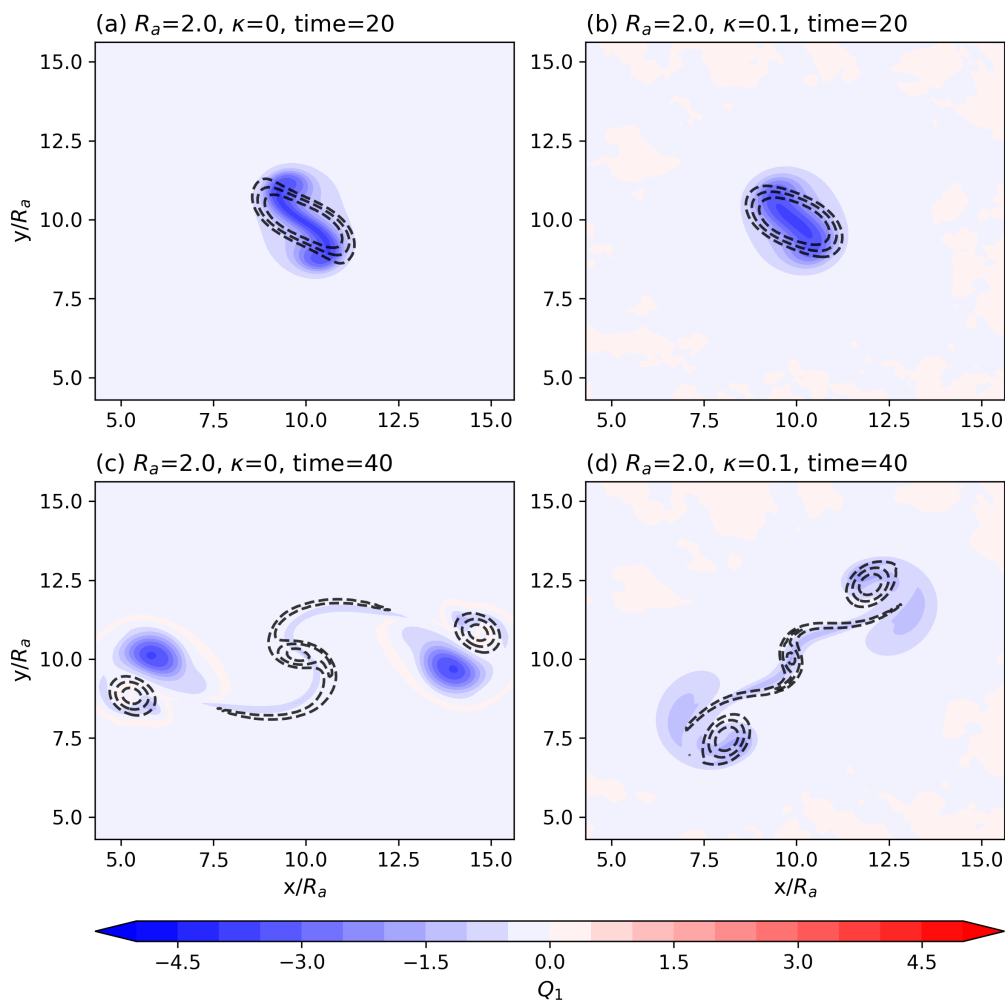


Figure 5.6: As in Figure 5.5 but for QG model runs with vortex radius $R_a = 2.0$ for (a) $t = 20$ and $\kappa = 0$, (b) $t = 20$ and $\kappa = 0.1$, (c) $t = 40$ and $\kappa = 0$, and (d) $t = 40$ and $\kappa = 0.1$.

larger than $R_a = 2$, instability is possible for more than one perturbation wavenumber, and exactly which wavenumber dominates is highly dependent on the initial random noise applied (not shown), and the eventual non-linear evolution of the vortex. One example model run (with friction) shows a $R_a = 3$ vortex initially undergoing wavenumber 3 instability (Figure 5.7a). As the vortex evolves, the 3 filaments pinch off such that the main vortex becomes smaller. By $t = 50$, the main vortex is undergoing wavenumber 2 instability and is beginning to split into two (Figure 5.7b). The dominant wavenumber of instability depends to some extent on the initial random noise, particularly when several wavenumbers are unstable. For example a $R_a = 4$ vortex initially undergoes wavenumber 4 instability in the model runs shown in Figures 5.7c–d, but in other model runs with different initial random noise (not shown here) has initially undergone wavenumber 3 in-

stability.

Ultimately, in all cases examined, this instability mechanism is acting to split up a large unstable vortex into smaller stable ones, with different wavenumber instabilities possible for vortices of size $R_a = 2$ and larger, depending on initial noise and eventual non-linear evolution. Note that the $R_a = 4$ vortex exhibits wavenumber 4 instability without (Figure 5.7c) and with friction (Figure 5.7d), suggesting that friction does not impact the wavenumber of instability, and simply acts to reduce the growth rates of instability.

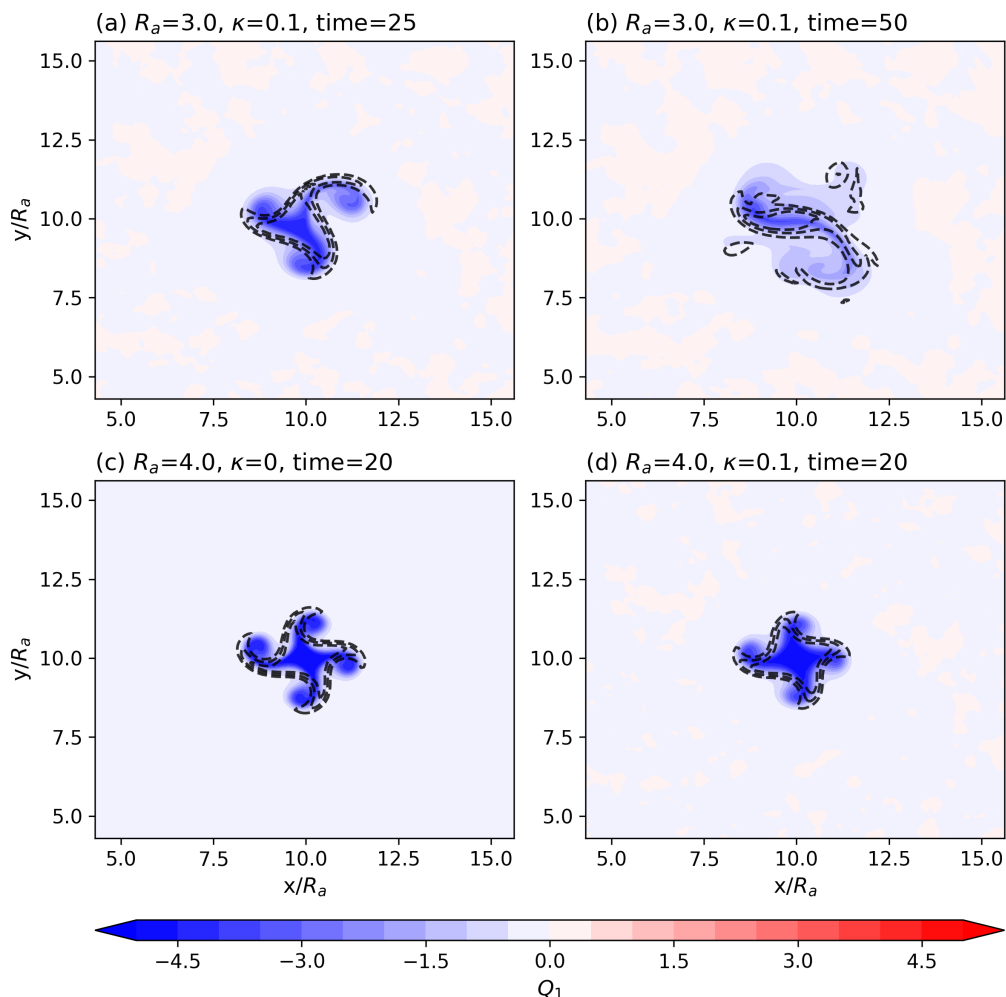


Figure 5.7: As in Figure 5.5 but for QG model runs with for $R_a = 3.0$ and $\kappa = 0.1$ at (a) $t = 25$ and (b) $t = 50$, and for $R_a = 4.0$ at $t = 20$ with (c) $\kappa = 0$ and (d) $\kappa = 0.1$.

5.5.2 Earlier stages in cyclone lifecycle

Having demonstrated the suitability of the QG model for investigating these axisymmetric vortex columns (evidenced by the general agreement with the linear stability analysis), we can now investigate the stability of a transiently evolving vortex state in which surface winds are initially present but are gradually damped to zero by the presence of friction, aiming to mimic an earlier stage in the cyclone lifecycle. In these model runs, the upper-layer QGPV anomaly is the same as that in the linear stability analysis (Figure 5.2), but the lower-layer QGPV anomaly is now prescribed as being positive (such that there will be cyclonic winds in the lower layer). Specifically, QG model runs with friction and vortex radius $R_a = 2$ have been performed (Figure 5.8) with initial axisymmetric states of an upper-layer positive QGPV vertically stacked above lower-layer positive QGPV anomalies with magnitudes $Q_1 = \frac{Q_2}{2}$ (Figure 5.8a) and $Q_1 = Q_2$ (Figure 5.8b). These setups might represent the structure of summer-time Arctic cyclones at the time of maximum intensity. Note that if there is no friction in these runs, there is no instability (since the setup does not feature opposing PV gradients in the vertical and therefore does not satisfy the CSP instability condition) and the vortex does not significantly evolve with time.

By $t = 25$ ($t^* = t_s t \sim 3.6$ days) friction has acted to spin down the lower layer winds and turn the lower layer QGPV negative. The QGPV is more negative in the $Q_1 = \frac{Q_2}{2}$ run (Figure 5.8c) than the $Q_1 = Q_2$ (Figure 5.8d), with friction in the latter case taking longer to spin down the initially stronger low-level vortex and induce the cyclone structural evolution. Here the vortex setup is unstable, satisfying the CSP instability condition with opposing PV gradients in the vertical. After this stage the vortex undergoes wavenumber 2 instability, with the vortex splitting into two at $t = 50$. The splitting is more advanced at this time in the $Q_1 = \frac{Q_2}{2}$ run (Figure 5.8e), with the $Q_1 = Q_2$ run (Figure 5.8f) lagging behind, but ultimately undergoing the same evolution.

These simulations have illustrated that, whilst friction acts to damp the growth of perturbations on an unstable vortex, thereby having an intuitive stabilising effect, the action of friction on the low-level vortex winds as a whole can cause the vortex to evolve towards an unstable state, and so be a destabilising effect.

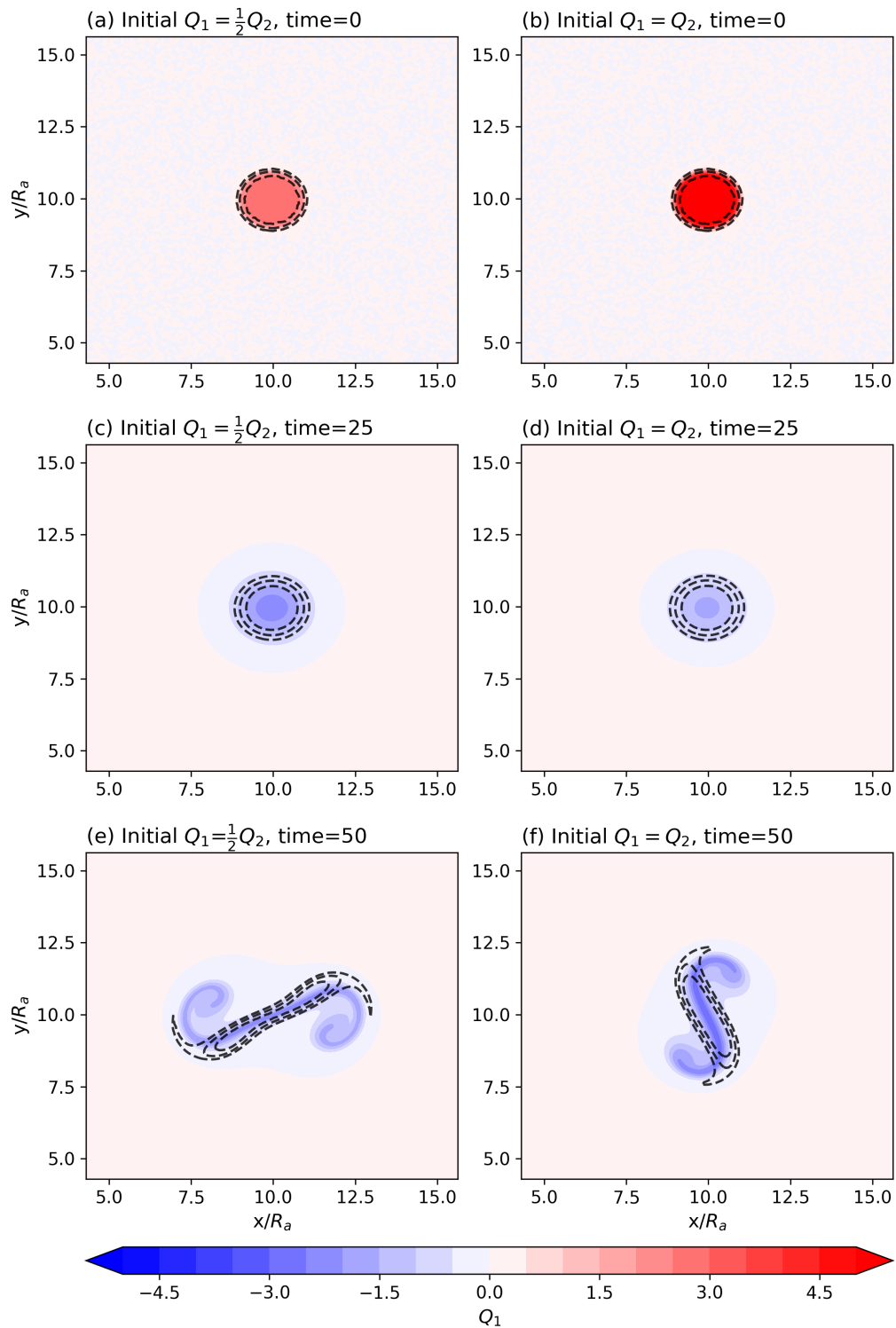


Figure 5.8: As in Figure 5.5 with the same initial upper-layer QGPV anomaly ($\max(Q_2) = 5.2$, $D = 0.2$), but with prescribed initial positive lower layer QGPV of the same form, with vortex radius $R_a = 2$. The panels show snapshots of the QG model runs with friction ($\kappa = 0.1$) for $\max(Q_1) = \max(Q_2)/2$ at (a) $t = 0$, (c) $t = 20$, and (e) $t = 40$. (b, d, f) are as (a, c, e) but for $\max(Q_1) = \max(Q_2)$.

5.6 Discussion

In this section we relate the results from the linear stability analysis and QG model to the real atmosphere. Firstly, in real Arctic cyclone cases, it is not clear whether sufficient low-level negative PV anomalies are generated (as a result of the surface cold anomaly and friction) to result in a negative horizontal PV gradient at low-levels, such that the CSP instability condition is satisfied. The results of this work suggest that if this instability does occur in the real atmosphere, it would only do so for the largest systems, those that exceed a radius of $R_a \sim 1.2$, or $R_a^* \sim 300$ km. This short-scale cutoff indicates a critical threshold size for TPVs, above which this instability mechanism would act to split up the vortex into several smaller vortices (in the absence of other processes). The summer-time Arctic cyclone cases examined in this work exceed this short-scale cutoff, but are on the extreme end of the spectrum in terms of strength, longevity and size (Croad et al., 2023b, 2023a; Simmonds and Rudeva, 2012). The average size of a mature summer-time Arctic cyclone with an axisymmetric columnar vortex structure is not well established, and so it is not clear whether the instability discussed in this work would be a relevant mechanism to a large number of cyclone cases. This instability mechanism might act to limit the maximum size or lifetime of mature summer-time Arctic cyclones in nature.

The QG model results suggest that large summer-time Arctic cyclones with axisymmetric columnar vortex structures after maturity could be significantly distorted by baroclinic instability on the order of a few days (with the exact length of time being dependent on the size and initial noise). However, the basic state described in this work does not perfectly replicate the axisymmetric columnar vortex structure of real systems. In the atmosphere, cyclones with columnar vortex structures are not perfectly circular, and are not totally isolated from other atmospheric features. Furthermore, in the two-layer QG model, friction is prescribed to act in a layer that represents half the depth of the troposphere. In reality, friction acts in the BL, which has a depth much shallower than this (on the order of one-tenth of the depth of the troposphere). A three-layer QG model, with friction acting in the bottom layer, and cyclonic winds in the middle and upper layers, would permit for a better representation of real summer-time Arctic cyclone cases, and will be the focus of

future work.

Although a systematic investigation into whether this instability mechanism occurs in many real summer-time Arctic cyclone cases is beyond the scope of this dynamical study, we have briefly examined whether it occurs in the two case studies examined in this work. Figure 5.9 shows selected maps of the July 2020 cyclone, positioned in the Pacific sector of the Arctic during its mature stage. The cyclone has non-dimensional radius $R_a \sim 2$, or $R^* \approx 500$ km, as discussed in Section 5.3. This means that, according to Figure 5.4, we would expect wavenumber 2 instability (or wavenumber 3, if R_a is slightly larger than 2). At 36 hours after maximum intensity (Figure 5.9a) the upper-level TPV is vertically stacked above the low-level cyclone, and exhibits a triangular shape, with linear filaments pinching off at the three corners. 30 hours later (Figure 5.9b), the upper-level TPV has been stretched in one direction, but has been squashed in the other. These snapshots resemble the wavenumber 3 and 2 instability that was observed in the QG model (Figures 5.5–5.8) respectively. This suggests that the instability mechanism may be occurring in the July 2020 case. However, Figure 5.4 indicates that for a vortex of this size, wavenumber 2 instability would be dominant (rather than wavenumber 3). The discrepancy may be due to the system deviating from a perfect circular basic state (i.e. with large initial noise), or perhaps because the Rossby radius of deformation (L_R) is actually smaller in the Arctic atmosphere than defined in this study (here $L_R = 250$ km). Furthermore, although the vortex becomes increasingly distorted over time, it does not split in isolation, as in the QG model runs. 5 days after maximum intensity, it begins to interact with another upper-level feature and ultimately becomes stretched out into a linear feature (not shown).

The evolution of the July 2020 cyclone suggests that the instability mechanism may be happening, but not in the idealised fashion seen in the main body of this work. Perhaps if the cyclone was uninterrupted for a longer period of time, it may have ultimately split into smaller vortices on its own accord, as seen in the QG model runs. However, in the real Arctic atmosphere, it is likely that long-lived structures will ultimately encounter other atmospheric features. Further work is required to determine the relative importance of, and understand the interplay between, vortex-vortex interactions and the instability

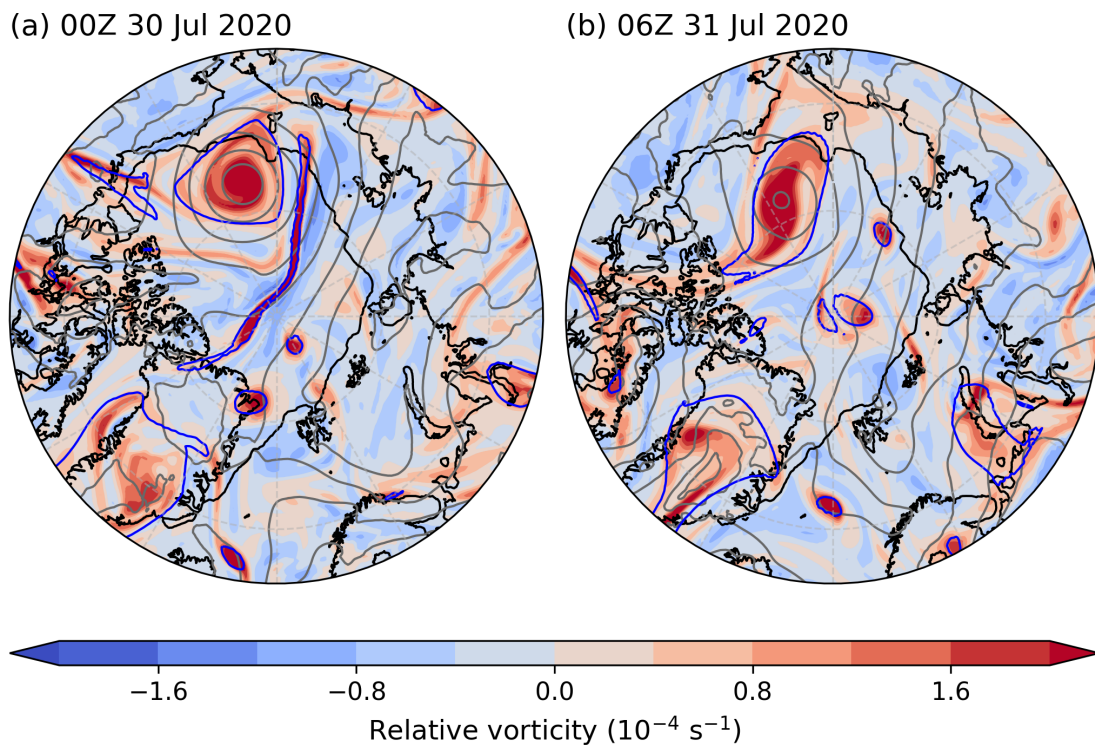


Figure 5.9: Maps of the July 2020 Arctic cyclone case study at (a) 00Z 30 July and (b) 06Z 31 July from ECMWF ERA5 reanalysis data. The maps show 400 hPa relative vorticity (shading), 310 K potential temperature on the PV2 surface (blue contours) mean sea level pressure (grey contours), and the sea ice edge (0.15 sea ice fraction; black contours).

of individual (large) vortices. Examination of Figure 3.8 in Chapter 3 demonstrates that frictional generation of negative PV after maximum intensity is continuously occurring in this cyclone, although it has a relatively small magnitude. It is not clear this is sufficient to result in a negative QGPV anomaly in the lower layer in this case (so that a negative horizontal PV gradient is established). Further examination is required to determine whether the CSP instability criterion is satisfied for several days. The August 2012 cyclone also appears to exhibit wavenumber 4 instability after maturity (not shown), which is consistent with the prediction of the dominant perturbation wavenumber for a vortex of radius $R_a = 4$ from Figure 5.4. Again, further examination and more rigorous attribution to the instability mechanism is left for future work.

In Chapter 3 it was argued that friction acts to amplify the cold-core structure of mature summer-time Arctic cyclones, through the action of both Ekman pumping and frictional

baroclinic PV generation (although only Ekman pumping can be represented in the QG model), and this may contribute to the long lifetime of summer-time Arctic cyclones. The amplification of the cold-core structure of axisymmetric columnar vortex cyclones is also seen in the two-layer QG model (e.g. Figure 5.8), although the role of Ekman pumping in amplifying a cold anomaly at low- and mid-levels would be better demonstrated by running a three-layer QG model. As discussed in this work, the low-level cooling is consistent with a negative PV anomaly at the lower boundary (Bretherton, 1966), satisfying the CSP condition. Hence, this work builds on Chapter 3 by proposing a mechanism by which friction acts to destabilise summer-time Arctic cyclones and ultimately lead to their dissipation. The QG model results suggest that this can occur on the order of a few days (which is consistent with the lifetime of mature summer-time Arctic cyclones), but further efforts are required to determine accurate time scales of instability in the real world.

5.7 Conclusions

Cyclones with cold-core axisymmetric columnar vortex structures are commonly observed in the summer-time Arctic after maturity (e.g. Croad et al., 2023b), with the low-level cyclone vertically stacked below a TPV at upper levels (e.g. Tanaka et al., 2012; Tao et al., 2017). A TPV is associated with a positive PV anomaly at upper levels, whilst friction can lead to a low-level cold anomaly that is consistent with negative PV at low-levels. Hence, the axisymmetric columnar vortex structure can feature opposing PV gradients in the vertical, thereby satisfying the CSP condition of baroclinic instability (Vallis, 2017). In this work we investigate the instability of this axisymmetric columnar vortex structure, using a two-layer QG model.

Firstly, two summer-time Arctic cyclone cases were examined to inform appropriate physical parameters and scales for the basic state of this problem, and demonstrate that the QG model is an appropriate framework for this investigation (Section 5.3). A linear stability analysis was performed (Section 5.4), to understand if the axisymmetric basic states (meant to replicate mature summer-time Arctic cyclones) with friction were unstable to small-amplitude wavy perturbations on the vortex edge, and if so how this depended on

the vortex characteristics and coefficient of friction. The non-linear QG model was then run with several different vortex setups to examine how instability would impact the long-term evolution of axisymmetric columnar vortices (Section 5.5). Finally, the results from the two-layer QG model were related to the real world in Section 5.6. The findings are summarised below, with reference to the research questions (posed in Section 5.1):

1. Under what circumstances are vortex columns unstable?

The linear stability analysis suggests that instability is possible for vortices with radius greater than 1.2 times the Rossby radius of deformation, which we estimate to be ~ 300 km. Vortices smaller than this short-scale cutoff are too vertically separated for the upper and lower QGPV anomalies to interact and for instabilities to grow. It was shown that above the short-scale cutoff, the dominant perturbation wavenumber of instability increases with vortex radius, with wavenumbers 2–4 being most likely for summer-time Arctic cyclone cases with observed radii ranging from 500–1000 km. Each perturbation wavenumber has its own short-scale cutoff. The growth rates of this instability mechanism were found to be comparable to the Eady growth rate of baroclinic instability on the mid-latitude jet. The growth rates were found to be directly proportional to the magnitude of the QGPV anomalies (i.e. doubling the magnitude of the upper-level QGPV anomaly leads to a doubling of the growth rate).

2. What is the impact of friction on the vortex instability?

Friction acts to damp the low-level cyclonic winds of idealised vortex columns that are initially stable, cooling the lower troposphere due to Ekman pumping, and leading to the formation of a negative QGPV anomaly. This causes the CSP instability criterion to be satisfied, and for instabilities to grow. Friction damps the growth rates of this instability, whilst also introducing some instability below the short-scale cutoff. Friction does not impact the wavenumber of instability, but does slow down the eventual non-linear evolution of the vortex.

3. How does the instability evolve non-linearly at large amplitude?

In the QG model, the axisymmetric columnar vortex setups initially evolve as pre-

dicted by the linear stability analysis. The instability is seen in the simulations as the main axisymmetric vortex splitting into a number of smaller vortices which depends on the dominant perturbation wavenumber of instability. At this point the evolution is non-linear, and is therefore not described by the linear stability analysis. For vortices with radii larger than two times the Rossby radius of deformation (~ 500 km), instability is possible for more than one perturbation wavenumber, and exactly which wavenumber dominates is highly dependent on the initial random noise applied and eventual non-linear evolution. Ultimately, the instability mechanism is acting to split up a large unstable vortex into smaller stable ones (that are smaller than the short-scale cutoff). The QG model results suggests that vortex instability may be visible on the order of a few days.

4. To what extent are the results applicable to real world cases?

Provided the CSP condition is satisfied in the real atmosphere (it remains to be determined how often this occurs), the results indicate a critical threshold size for TPVs in the Arctic, above which this mechanism would act to split the system into smaller vortices. From examination of two real summer-time Arctic cyclone cases, we find that predictions of the most unstable wavenumber, according to their radius, are broadly consistent with the observed disturbances to the vortex columns. However, further investigation is needed to rigourously demonstrate this. It may well be that whilst this instability mechanism is occurring in the atmosphere, vortex-vortex interactions are also important and may ultimately dominate the dynamics.

It was suggested in Chapter 3 that friction acts to amplify the cold-core structure of mature summer-time Arctic cyclones above the BL which, given that we think of friction as acting to damp atmospheric weather systems, is a somewhat counterintuitive result. This study proposes a frictional instability mechanism which acts against this, with friction ultimately leading to destabilisation and dissipation of cold-core axisymmetric columnar vortex structures. Further investigation is required to quantify this instability and understand how it would present itself in the real atmosphere, where vortices are not isolated from other atmospheric phenomena. Furthermore, the two cyclone case studies may not be representative of summer-time Arctic cyclones, with their characteristics being suffi-

ciently notable to lead to their selection as case studies in previous work (e.g. Croad et al., 2023a; Simmonds and Rudeva, 2012). Further analysis is required to understand the size distribution of summer-time Arctic cyclones and provide an estimate for how many cyclones this vortex instability may be a relevant mechanism (i.e. those that are larger than the short-scale cutoff).

The two-layer QG model used in this study leads to an idealised and simplistic representation of the Arctic environment. There are future plans to run the QG model with three layers, with friction acting in the bottom layer, and cyclonic winds in the middle and upper layers. This permits for a more complex initial vortex state in which the lower frictional layer more closely resembles a BL, and therefore a better representation of the vertical structure of mature summer-time Arctic cyclones. In future work, the numerical QG model could be extended to include the impact of diabatic processes, permitting investigation of their impact on summer-time Arctic cyclones. For example, diabatic forcing terms could be included (in the bottom model layer) to replicate the impact of surface turbulent heat fluxes over sea ice, but also (in the top model layer) to replicate the impact of longwave radiative cooling, which is known to intensify TPVs (e.g. Cavallo and Hakim, 2013). In the future, one could also consider the use of a semi-geostrophic framework that would better represent the dynamics of the real atmosphere, and also permit for a more realistic representation of friction, capturing both Ekman pumping and baroclinic PV generation as was described in Chapter 3.

Chapter 6

Examining the sensitivity of ECMWF IFS weather forecasts to sea ice coupling for the summer-time Arctic and cyclones

This chapter has been published in *Quarterly Journal of the Royal Meteorological Society* with reference:

Croad, H. L., S. P. E. Keeley, J. Methven, B. Harvey, and A. Volonté (2025): Examining the sensitivity of ECMWF IFS weather forecasts to sea-ice coupling for the summer-time Arctic and cyclones. *Quart. J. Roy. Meteor. Soc.*, **151(766)**, e4899, <https://doi.org/10.1002/qj.4899>.

Abstract

In recent years there has been an advance towards coupled Earth system models for weather forecasting. For example, the European Centre for Medium-Range Weather Forecasts now implement ocean-ice coupling with dynamic sea ice in the Integrated Forecasting System (IFS) at all time ranges. This has the potential to improve weather forecasts in the polar regions where sea ice directly influences the overlying atmosphere by turbulent exchange, especially in the rapidly warming summer-time Arctic where thinner and more mobile ice is susceptible to rapid change. In this study, we investigate the sensitivity of IFS (cycle 47r1) weather forecasts to sea ice coupling representation in the summer-time Arctic by comparing three sets of forecasts that are coupled with: (i) dynamic sea ice in operational configuration, (ii) static sea ice, and (iii) dynamic sea ice with additional

thermodynamic (surface temperature and albedo) coupling. It is found that dynamic sea ice improves predictions of sea ice and the ice edge, compared to persistence, especially in the vicinity of Arctic cyclones. The dynamic sea ice forecasts exhibit lower near-surface temperatures (up to 0.5°C) compared to static sea ice forecasts where ice loss has occurred, and differences in near-surface winds of up to 0.5 m s^{-1} , consistent with changing surface roughness over the marginal ice zone. The forecasts with additional thermodynamic coupling have near-surface temperatures that are up to 1°C cooler over ice than the operational configuration (correcting a known warm bias), consistent with a more stable boundary layer (BL) and weaker near-surface winds. The influence of sea ice coupling above the BL is small, with differences in cyclone forecasts being smaller than the spread of the operational ensemble. This study highlights the influence of ocean-ice coupling in weather forecasts for the summer-time Arctic, and the potential gains from improving its representation.

6.1 Introduction

Since 1979 the Arctic has warmed nearly four times faster than the global average (Rantanen et al., 2022), and the associated rapid decline of sea ice (e.g. Meier and Stroeve, 2022) is driving increasing interest in socio-economic activities in the Arctic, including resource extraction, shipping, and tourism (Stephenson et al., 2011). Hence, there is a growing demand for accurate forecasts of Arctic weather and sea ice on a range of timescales to support human activity in the region.

In recent years dynamical forecast systems for sea ice predictions on seasonal timescales and longer have been established (Guemas et al., 2016), exhibiting some predictive skill for pan-Arctic (and regional) sea ice extent and volume out to a few months ahead (e.g. Bushuk et al., 2019). Predictability at these time scales is beneficial for forecasting the sea ice state itself, but also for capturing important feedbacks on atmospheric circulation and precipitation (Balmaseda et al., 2010; Screen, 2013). For predictions on subseasonal timescales, Zampieri et al. (2018) demonstrated a wide range in skill across operational forecasting systems with coupled sea ice, with the best showing predictive skill out to 1.5

months. The need for coupled sea ice on shorter timescales relevant to weather forecasts (1–10 days) has received less attention, although Mohammadi-Aragh et al. (2018) indicated some potential in this regard.

Until recently, operational numerical weather prediction (NWP) systems typically have kept sea ice fields fixed for weather forecasts, based on the assumption that changes in sea ice are slow and that models would not be able to beat a persistence forecast. However, Keeley and Mogensen (2018) demonstrated that static sea ice is a poor assumption for NWP, especially in summer, with on average more than 5% of the Arctic ice field exhibiting significant changes over 5-day periods during June–November 2017. One way in which this may be realised is through very rapid ice loss events (VRILEs), extreme reductions in sea ice extent on the timescale of days, which are associated with anomalous synoptic activity (e.g. Wang et al., 2020). For example, an extremely strong Arctic cyclone in August 2012 (Simmonds and Rudeva, 2012) was associated with substantial ice melt (Stern et al., 2020) and ultimately reduced ice extent that constituted a VRILE (McGraw et al., 2022).

The presence of sea ice has a strong influence on the atmospheric boundary layer (BL; Notz, 2012). The marginal ice zone (MIZ), a heterogeneous band of fragmented ice floes separating the ice-free ocean and main ice pack, is associated with gradients in roughness, temperature and humidity that result in turbulent exchange of momentum, heat and moisture. Momentum fluxes and surface roughness peak in the MIZ at sea ice fraction (SIF) values of 0.5–0.8 (Elvidge et al., 2016; Lüpkes and Birnbaum, 2005), primarily due to form drag over ice floe edges. Off-ice flow (e.g. during cold-air outbreaks) is typically associated with cold air moving over the warm ocean surface, with upward surface sensible and latent heat fluxes, and a transition from a BL that is stable or neutral to unstable (e.g. Renfrew and Moore, 1999). In contrast, the BL is cooled and dried during on-ice flow, such as during warm air intrusions (e.g. Pithan et al., 2018). In recent years physical parameterizations that depend on SIF for surface momentum, heat and moisture fluxes have been shown to improve representation of surface turbulent exchange in NWP (Elvidge et al., 2021, 2023; Renfrew et al., 2019). However, correctly capturing the loca-

tion and geometry of the ice edge is also important, due to the strong influence of this in the development of the downstream BL (e.g. Liu et al., 2006; Spensberger and Spengler, 2021). Hence, coupled NWP models with dynamic sea ice that can capture rapid changes in sea ice (e.g. during VRILEs) have the potential to predict these downstream impacts and improve weather forecasts in the Arctic.

Accordingly, in recent years there have been ongoing efforts towards coupled ocean and ice components in NWP models. Building on positive results from regional coupled NWP systems (e.g. Pellerin et al., 2004; Smith et al., 2013), operational centres including Environment and Climate Change Canada (ECCC; e.g. Peterson et al., 2022; Smith et al., 2018), the European Centre for Medium-Range Weather Forecasts (ECMWF; e.g. Keeley and Mogensen, 2018), and the United States Naval Research Laboratory (NRL; Barton et al., 2021) have now implemented atmosphere-ocean-ice coupling in their operational global weather forecasting systems. ECMWF, the focus of this study, implemented atmosphere-ocean-ice coupling in the Integrated Forecasting System (IFS) in their ensemble prediction system (EPS) in November 2016, and then in their high-resolution deterministic forecasts in June 2018 (Keeley and Mogensen, 2018). This is facilitated by coupling the IFS to a dynamic ocean model (NEMO; Nucleus for European Modelling for the Ocean), which incorporates a dynamic-thermodynamic sea ice model (LIM2; Louvain-la-Neuve version 2). Focusing on a winter evaluation period, Day et al. (2022) demonstrated that this atmosphere-ocean-ice coupling in the IFS generally improves medium-range forecasts of the sea ice edge and the downstream BL in the Arctic, compared to the previous uncoupled system. However, some localised regions see a degradation in forecast skill, demonstrating that challenges remain with the atmosphere-ocean-ice coupling.

No corresponding evaluation of this coupled system has been performed in summer, when the Arctic is most accessible and therefore there is the greatest demand for weather forecasts to support human activity. Surface turbulent exchange near the ice edge in summer differs from that in winter, with typically much smaller turbulent heat fluxes due to the atmosphere and ocean having more similar temperatures than in winter (when turbulent heat fluxes can be on the order of 100 W m^{-2} during off-ice flow; e.g. Elvidge et al., 2021;

Renfrew and Moore, 1999). Instead, surface exchange over ice might be dominated by surface drag and turbulent momentum fluxes. The summer-time Arctic is becoming increasingly dominated by the MIZ (Rolph et al., 2020; Strong and Rigor, 2013), which, due to more mobile and rough ice, may enhance surface exchange and interactions with Arctic weather systems. In particular, Arctic cyclones are associated with strong winds and ocean waves that have large impacts on the thinning sea ice cover in summer (e.g. Asplin et al., 2012; Peng et al., 2021). How this interaction with sea ice feeds back on the cyclones is less clear, and has not previously been examined in NWP models with coupled sea ice.

In this study we build on the work by Day et al. (2022) by examining the sensitivity of IFS forecasts in the summer-time Arctic (with a focus on cyclones) to sea ice coupling representation. With regards to surface drag over ice in the IFS, the surface roughness is represented via a roughness length that is dependent on SIF (ECMWF, 2020). However, ocean wave propagation is suppressed in the model for SIF greater than 0.3 (ECMWF, 2023b), which is likely a key process for surface drag in the MIZ. Furthermore, comparison with observations from the Arctic Ocean 2018 expedition highlights that surface and near-surface temperatures over sea ice in the IFS are too warm during summer, with biases of +0.5°C and +0.5-1.0°C respectively such that both are above zero in spite of ongoing melt (Tjernström et al., 2021). In the current ECMWF operational setup, the only sea ice variable coupled to the atmosphere is SIF. The surface temperature over sea ice is not coupled, with the surface energy balance calculated on the sea ice tile in the land surface scheme (Keeley and Mogensen, 2018). Using a more comprehensive thermodynamic coupling over sea ice would aim to produce more physical solutions and improved forecasts.

In this study we examine and compare three sets of 10-day forecast experiments run with the IFS that differ only in their sea ice coupling configurations, starting daily at 00Z during 20 July–25 August 2020. The 2020 summer was selected as the period of interest due to the regular passage of Arctic cyclones; Croad et al. (2023a) identified 52 Arctic cyclones during the extended summer season (May–September), compared to an average

of ~ 39 cyclones per summer during 1979–2021 (Croad et al., 2023b). The dates selected were chosen as a period with rapid sea ice loss, and to capture the occurrence of a known extreme cyclone in July that was examined in Croad et al. (2023a). The three sets of IFS forecast experiments to be compared are coupled with (i) “dynamic sea ice”, in operational configuration (henceforth C_{oper}), (ii) “static sea ice”, where the sea ice cannot evolve throughout the forecast as was operational prior to November 2016 (henceforth C_{static}), and (iii) dynamic sea ice with additional “thermodynamic coupling” (henceforth C_{thermo}) over sea ice in an experimental setup. We aim to answer the following questions:

1. Where does dynamic coupling with the ocean-sea ice model have the greatest impact on sea ice forecasts?
2. How does dynamic sea ice impact the forecast BL compared to static sea ice?
3. How does additional thermodynamic coupling impact the forecast BL compared to dynamic sea ice alone?
4. What is the impact of sea ice coupling on Arctic cyclone forecasts?

The paper is structured as follows. The methodology is described in Section 6.2, including details of the sea ice coupling configuration in each set of IFS forecast experiments. The results are presented in Section 6.3, where forecasts of sea ice, BL quantities and Arctic cyclones are evaluated. The study is concluded in Section 6.4.

6.2 Methodology

6.2.1 Experiments

The three sets of forecast experiments were run using IFS model cycle 47r1 (Cy47r1), which employs a spectral model with an octahedral reduced Gaussian grid $T_{CO}639$ (horizontal resolution ~ 18 km), and 91 terrain-following hybrid pressure levels up to 0.01 hPa. This is the same setup as the ensemble members in the ECMWF’s operational EPS for the cycle, although the forecasts used in this study are deterministic (i.e. a single control member is run for each experiment at each start time). In all three sets of forecasts

the ocean and sea ice fields are initialised from ECMWF OCEAN5 analysis (Zuo et al., 2019; see more details in Section 6.2.2), and the atmosphere is initialised from ECMWF operational control analysis. The experiments all have the same ocean-atmosphere coupling as that in the operational EPS, with sea surface temperatures (SSTs) being fully coupled in the tropics but only partially coupled in the extratropics for the first 4 days (ECMWF, 2024). Roughness lengths for momentum, heat and moisture are prescribed in each experiment as in the operational configuration of IFS Cy47r1 (ECMWF, 2020). Over sea ice, the roughness length for momentum depends on SIF (with a maximum value at 0.5 SIF), whilst the scalar roughness lengths are constants. For the fields shown in this study, we use 6-hourly forecast data interpolated to a 0.25° regular latitude-longitude grid.

Figure 6.1 describes the sea ice coupling in the three sets of forecast experiments. In the first set of forecasts, C_{oper} , the IFS atmospheric model is coupled to the ocean-sea ice (NEMO-LIM2) models consistent with the operational implementation of Cy47r1. The only sea ice variable coupled to the atmosphere is SIF (ECMWF, 2020). A uniform climatological sea ice albedo value (assuming bare ice in summer) from Ebert and Curry (1993) is used rather than using the albedo from the sea ice model, which can be too high in summer due to the lack of melt pond processes in the LIM2 model (Keeley and Mogenssen, 2018). Coupling between the atmosphere and ocean-sea ice models occurs once per hour, rather than every atmospheric model time step. Hence, SIF is updated every coupling step (informing the surface albedo and roughness lengths for momentum, heat and moisture), with the sea ice tile in the surface scheme being used to adjust the surface energy balance and surface temperature on faster timescales (left panel in Figure 6.1).

The second set of forecasts, C_{static} , is identical to C_{oper} except that the sea ice field is persisted from the start of the forecast (middle panel in Figure 6.1).

The third set of forecasts, C_{thermo} , is an experimental setup that is identical to C_{oper} except that the sea ice is also coupled thermodynamically, with albedo and surface temperature from the LIM2 sea ice model being coupled to the atmosphere as well as SIF (similar to the “Tight” coupling experiment in Arduini et al., 2022, but with albedo coupled also).

In this setup the surface temperature and albedo over ice in the atmospheric model are fixed to those from the LIM2 sea ice model (with the thermodynamic calculations on the sea ice tile in the surface scheme being disabled). This surface temperature is physically consistent with the surface energy balance that is calculated in LIM2 within each coupling step, including the phase transitions of sea ice and snow. However, the system is still not fully coupled, with the surface temperature over ice being held constant for each hourly coupling step (right panel in Figure 6.1) so that fluctuations on faster timescales are not possible. There is also potential for surface albedos that are too high as the LIM2 implementation does not represent melt ponds. Note that the forecasts have the same initial conditions as the other experiments (i.e. analyses produced by a data assimilation system in which there is no thermodynamic coupling with the sea ice model). Hence, the thermodynamic coupling leads to an imbalance between the ocean-sea ice model and atmosphere at the first coupling step, driving rapid adjustments in surface fluxes to establish a new thermodynamical balance. This initialisation shock could accelerate the development of errors in the forecast. Hence, this thermodynamic coupling is not implemented operationally, but these experiments explore the potential benefits of doing so.

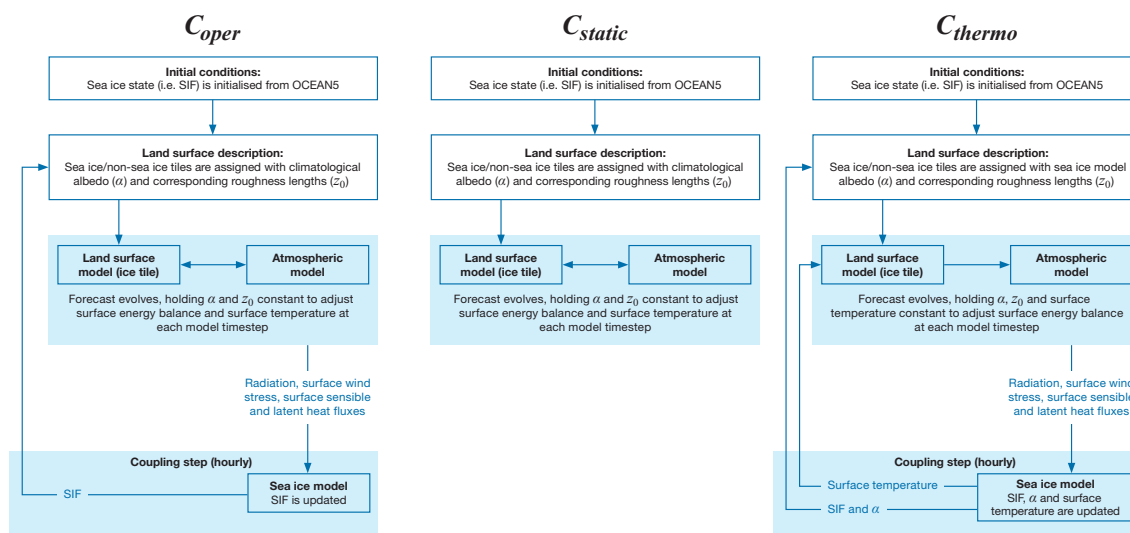


Figure 6.1: A schematic diagram describing the coupled sea ice configuration in the 3 experiments, (left) C_{oper} , (middle) C_{static} and (right) C_{thermo} .

6.2.2 Evaluation

This study is primarily focused on comparing the different forecast experiments and understanding the model response to changing sea ice coupling representation, rather than verification against a truth dataset. This is because our knowledge of the true atmospheric state is limited over ice, with sparse in situ observations (in space and time) and reanalysis products having known deficiencies (e.g. Graham et al., 2017; Wesslén et al., 2014). For example, ERA5 reanalysis has a known warm bias over sea ice (Wang et al., 2019). Evaluation of reanalyses over ice is a complicated matter in its own right (beyond the scope of this paper), so here we focus on investigating model sensitivity to sea ice coupling.

That being said, a brief evaluation of sea ice forecasts from the experiments is performed against the OCEAN5 analysis used to initialise forecasts at the same valid time. OCEAN5 estimates the state of the sea ice and ocean using the same ocean-sea ice model configuration as C_{oper} and a 3D variational assimilation system, assimilating OSTIA (Operational Sea Surface Temperature and Sea Ice Analysis; Donlon et al. 2012) gridded sea ice concentrations and SSTs (more precisely, it relaxes towards them) in addition to other ocean observations (see Zuo et al. 2019 for more details).

Although the atmospheric forecasts are not compared to a “truth” dataset, we benchmark the differences between the experiments to the spread of the operational forecasts from the EPS ensemble members initialised at the same time. The EPS is comprised of 51 ensemble members with the same setup as C_{oper} except that perturbations are applied to the ocean and atmospheric initial conditions, and atmospheric physical parametrization tendencies. This accounts for forecast uncertainty related to the initial conditions, and the forecast model itself, in terms of subgrid scale phenomena that are not captured in the formulation of physical parametrizations.

6.2.3 Cyclone tracks

Cyclone tracks are identified in ERA5, the fifth-generation ECMWF reanalysis data set (Hersbach et al., 2017, 2020), produced using the ECMWF’s Integrated Forecasting Sys-

tem (Cy41r2). The model has spectral truncation T_L639 (~ 31 km resolution at the equator), and 137 terrain-following hybrid-pressure levels from the surface to 0.01 hPa.

Arctic cyclone tracks are obtained from ERA5 reanalysis using the TRACK algorithm (Hodges, 1994, 1995, 2021). The algorithm is employed on 1-hourly spectrally truncated (T5-63; removing total wavenumbers less than 5 and more than 63) 850 hPa relative vorticity. Maxima exceeding 10^{-5} s^{-1} are identified, initialized into a set of tracks using a nearest neighbour search with a maximum great circle displacement distance of 2° in a time step, and are subsequently refined by minimizing a cost function for track smoothness. Arctic cyclones are identified as those tracks where filtered 850 hPa relative vorticity exceeds $8 \times 10^{-5} \text{ s}^{-1}$ for at least 12 hours whilst located north of 70°N . Cyclone tracks are presented at 6-hourly intervals interpolated onto a 0.25° regular latitude-longitude grid. Spatial track density of cyclones was computed with cosine-shaped kernels on a polar domain (500 km bandwidth) using the scikit-learn Python library (Pedregosa et al., 2011).

6.3 Results

6.3.1 Forecasts of sea ice

In this section the extent to which dynamic coupling impacts sea ice forecasts is examined, by comparing the C_{oper} and C_{static} forecasts (note C_{oper} and C_{thermo} forecasts have virtually identical sea ice fields; Section 6.3.2). In Figure 6.2, maps of the differences in SIF between C_{oper} and C_{static} , averaged over all forecast start dates, are presented at 3-day (Figure 6.2a) and 10-day (Figure 6.2b) lead times. The differences in SIF are largely negative, reflecting a loss of sea ice in C_{oper} (as would be expected in this summer melting period) that is not possible in C_{static} . Here we focus on two regions in which large differences occur. The first region is to the north of the Bering Strait, which shall henceforth be referred to as the “Pacific” sector (demarcated by the purple box), with reduced SIF in C_{oper} over a broad area. The second region is to the north of the Greenland-Barents-Kara Seas region, and shall henceforth be referred to as the “Eurasian” sector (demarcated by

the green box). The reduced SIF in C_{oper} is limited to a relatively thin region close to the ice edge.

The Pacific sector experiences the highest density of cyclone activity during this period, with 4 Arctic cyclone tracks (Figure 6.2c) contributing to a high track density (Figure 6.2d) over the sea ice in this region. Furthermore, there is considerable cyclone activity in the Greenland-Barents-Kara Seas region (Figure 6.2c and 6.2d), which would likely be associated with across-ice edge flow to the north in the Eurasian sector. Hence, the largest differences in SIF forecasts from C_{oper} and C_{static} (Figure 6.2a and 6.2b) occur in the vicinity of Arctic cyclones. These systems are associated with strong winds and/or warm intrusions that can result in rapid losses of sea ice. The sea ice in the C_{oper} forecasts can respond to these atmospheric forcings, but not in C_{static} .

Forecasts of the sea ice area (SIA; sea ice extent weighted by grid box SIF) from C_{oper} and C_{static} are compared to that from the ECMWF operational OCEAN5 analysis at the same valid time in Figure 6.3. Note that in this study sea ice grid points are those with $SIF > 0.15$, whilst all non-land grid points with $SIF < 0.15$ are considered to be ocean. The operational analysis and the C_{oper} forecasts show a consistent reduction in SIA with time, as would be expected in this late summer melting period. Figure 6.3 highlights that the C_{oper} forecasts produce much improved SIA predictions compared to C_{static} , with the root mean square errors (relative to the operational analysis) reduced by approximately a half in all sectors. This highlights how poor an assumption static sea ice can be on weather timescales during the summer. However, the reduction in SIA from the C_{oper} forecasts is typically underestimated compared to the operational analysis over the whole Arctic (Figure 6.3a). The SIA loss in C_{oper} is particularly underestimated in the Pacific sector (Figure 6.3b). It is known that the LIM2 sea ice model tends to melt sea ice too slowly, particularly where the analysis overestimates sea ice thickness (ECMWF, 2023a), since heat transfer within the ice model assumes a constant thickness of 1.5 m (ECMWF, 2020). Previous studies have noted that sea ice thickness is overestimated in the ECMWF model in the Pacific sector (Balan-Sarajini et al., 2021; Xiu et al., 2022), which would be consistent with the underestimation of the ice loss rate we have identified in this re-

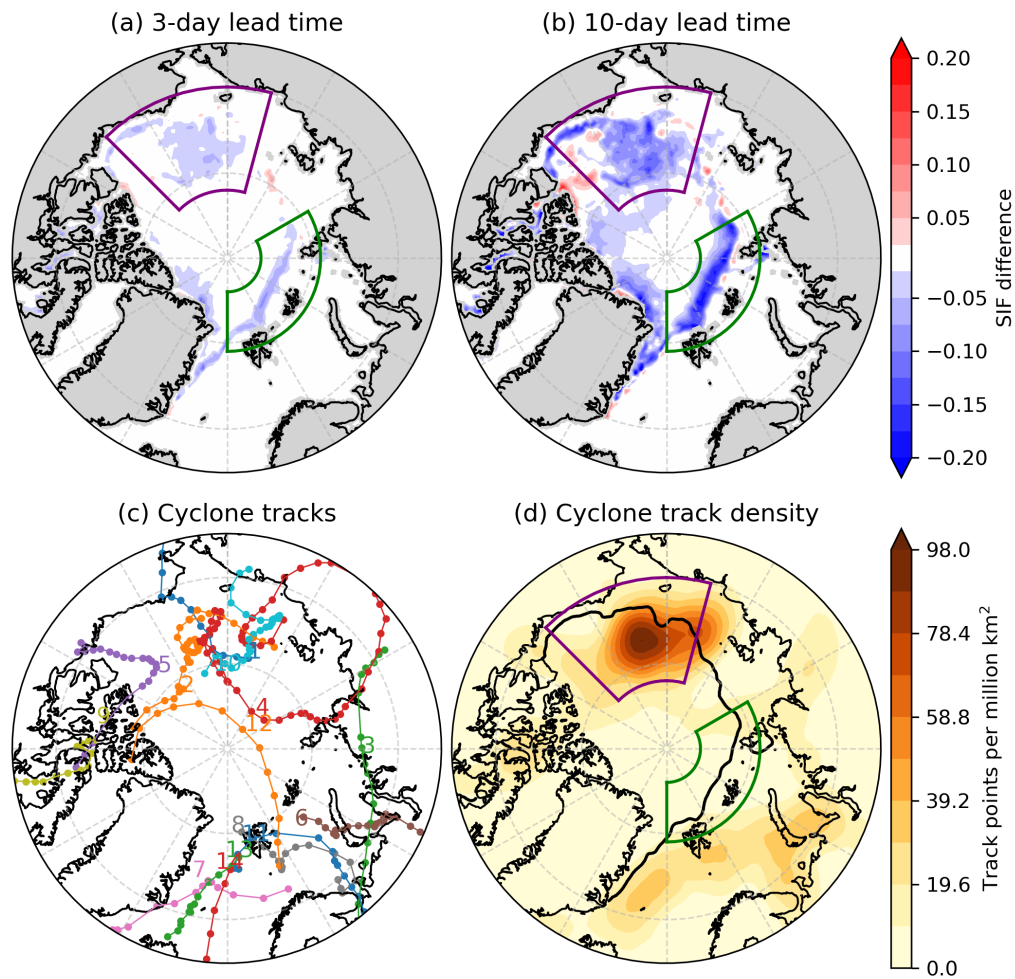


Figure 6.2: The difference in sea ice fraction ($C_{oper} - C_{static}$), averaged over all forecast start dates, at (a) 3-day and (b) 10-day lead times. The 6-hourly tracks of Arctic cyclones identified in ERA5 reanalysis during the study period are presented as (c) individual trajectories, and (d) as a feature track density map using spherical cosine kernels with bandwidth 500 km (shading; track points per million km^2), with the composite mean sea ice edge (black contour; 0.15 SIF) overlain. The regions marked with purple and green borders are the Pacific and Eurasian sectors respectively.

gion. Furthermore, the forecasts do not represent ocean wave propagation into the sea ice, which is an important process in the break up of sea ice in reality. In contrast, the SIA forecasts from C_{oper} are more similar to the operational analysis in the Eurasian sector, although the SIA loss is occasionally overestimated (Figure 6.3c). This is consistent with the underestimation of sea ice thickness in the ECMWF model in the Eurasian sector (Balan-Sarojini et al., 2021; Xiu et al., 2022).

A more user-relevant verification metric for sea ice, given the dependence of the down-

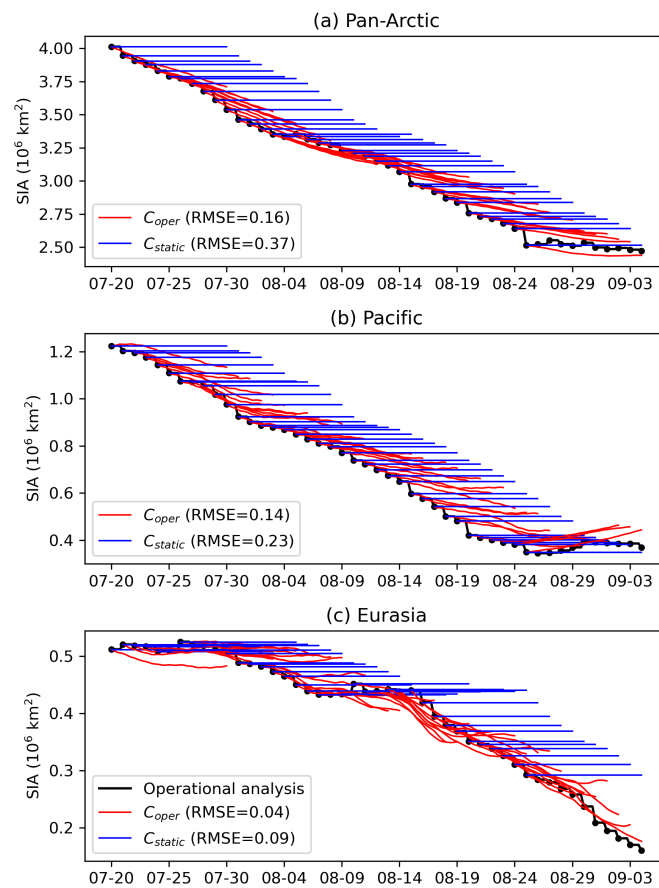


Figure 6.3: Time series of sea ice area (SIA) from the ECMWF operational analysis (black lines) for the (a) Pan-Arctic, (b) Pacific sector and (c) Eurasian sectors, and 10-day forecasts from C_{oper} (red lines) and C_{static} (blue lines) starting at 00Z daily (indicated by black markers). The root mean square error (RMSE) for C_{oper} and C_{static} relative to the operational analysis at day 10 is presented in the legend for each region.

stream BL on the location and geometry of the ice edge, is the integrated ice edge error (IIEE; Goessling et al., 2016). The IIEE of a forecast is the sum of the areas of sea ice that are overestimated and underestimated compared to the truth, here the ECMWF operational OCEAN5 analysis. In Figure 6.4 it is seen that the IIEE in C_{oper} is reduced compared to C_{static} at all lead times for the Pan-Arctic (Figure 6.4a), and in the Pacific (Figure 6.4b) and Eurasian (Figure 6.4c) sectors. Consistent with the comparison of SIA forecasts in Figure 6.3, the reduction in IIEE in C_{oper} compared to C_{static} is more marked in the Eurasian sector (Figure 6.4c) than the Pacific sector (Figure 6.4b; where in general the SIF is reduced but the ice cover is not completely removed). In all regions, the rate of growth in IIEE in C_{oper} is particularly reduced compared to C_{static} in the first 5 days of the forecasts. During days 5–10, the lines in Figure 6.4 are roughly parallel, indicating

that the rate of growth of IIEE in both experiments is similar.

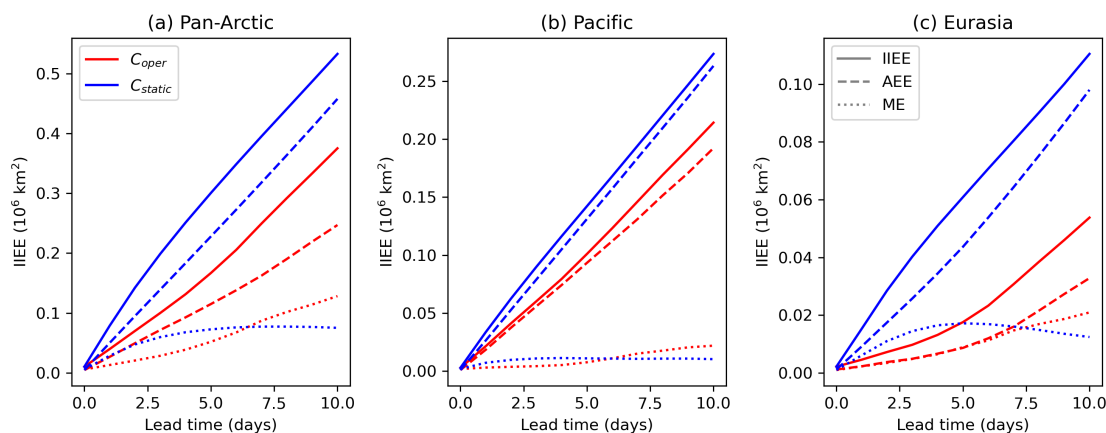


Figure 6.4: The integrated ice edge error (IIEE) of the C_{oper} (red) and C_{static} (blue) forecasts relative to the ECMWF OCEAN5 operational analysis averaged over all forecasts as a function of lead time for the (a) Pan-Arctic, (b) Pacific sector, and (c) Eurasian sectors. The solid lines denote the full IIEE metric, whilst the dashed and dotted lines denote the absolute extent error (AEE) and misplacement error (ME) respectively.

The IIEE can also be decomposed into the sum of the absolute extent error (AEE) and misplacement error (ME). The AEE is the absolute difference between the overestimated and underestimated sea ice areas, representing the common difference in sea ice extent (Goessling et al., 2016). The ME is the residual (i.e. IIEE minus AEE), indicative of too much ice in one place and too little in another. In the C_{oper} and C_{static} forecasts the IIEE is generally dominated by the AEE (Figure 6.4), indicating that the underestimation of sea ice loss is dominating the signal in this summer period. The only exception is the C_{oper} forecasts in the Eurasian sector (red lines in Figure 6.4c), where the AEE and ME are of comparable magnitudes.

6.3.2 Forecasts of the atmospheric boundary layer

In this section we examine the impact of different sea ice coupling configurations on forecasts of the atmospheric BL. To start with we want to identify any systematic differences in the pan-Arctic atmospheric BL between the three sets of forecasts. To do this, we compute the differences in selected BL quantities averaged over all forecast start dates as a function of lead time (Figure 6.5). For this initial investigation the differences are

considered over grid points north of 65°N that are ocean ($\text{SIF} < 0.15$) and sea ice ($\text{SIF} > 0.15$), at the start of the forecasts, separately.

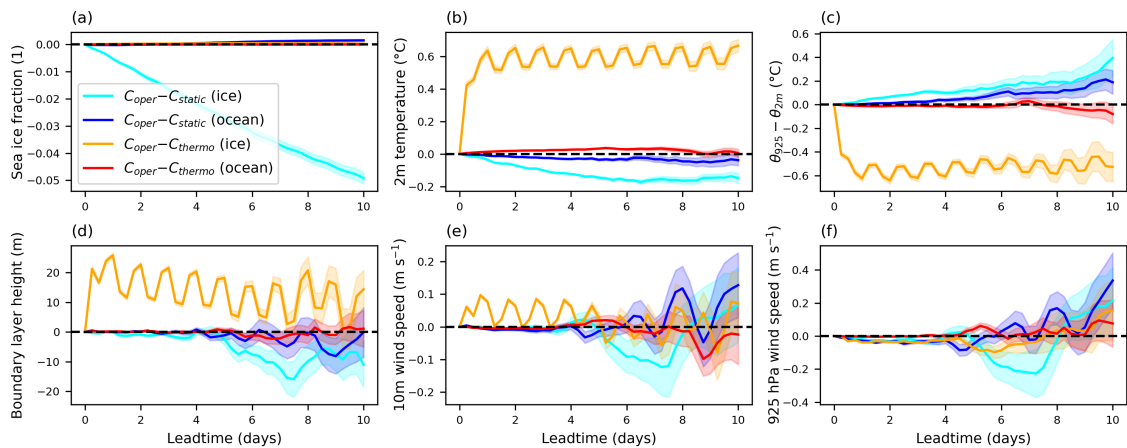


Figure 6.5: The pan-Arctic differences between forecast experiments averaged over all forecasts in (a) sea ice fraction, (b) 2 m temperature, (c) low-level stability as diagnosed by the difference in potential temperature (θ) between 925 hPa and 2m ($\theta_{925} - \theta_{2m}$), (d) boundary layer height, (e) 10 m wind speed, (f) 925 hPa wind speed, as a function of lead time. The differences are calculated as areal averages (over grid points north of 65°N that are ocean and sea ice at the forecast starts separately) for each forecast, and then averaged over all forecast start dates. The differences are presented for $C_{oper} - C_{static}$ over sea ice (cyan profiles) and ocean (blue profiles), and for $C_{oper} - C_{thermo}$ over sea ice (orange profiles) and ocean (red profiles). The solid lines denote the composite mean, and the shading denotes the standard error (calculated as the standard deviation in areal average differences divided by the square root of the number of forecasts).

Over ice, the C_{oper} forecasts are associated with a reduction in SIF that grows with time compared to C_{static} , consistent with the analysis in Section 6.3.1 (Figure 6.5a; note that over ocean there is a slight increase in SIF in C_{oper} representing the formation of sea ice in some regions). The reduced SIF in C_{oper} is associated with a systematically cooler 2 m temperatures compared to C_{static} (Figure 6.5b). This difference grows with time through the forecast and is larger over sea ice than ocean, approaching a magnitude of $\sim 0.2^\circ\text{C}$ and $\sim 0.05^\circ\text{C}$ at day 10 over ice and ocean respectively. Note that this difference is also seen in the skin temperature, with a comparable magnitude (not shown). The reduced surface and near-surface temperatures are a consequence of the melting ice in C_{oper} , with a greater fraction of exposed ocean surface (which will have a SST of -1.8°C , the freezing point of saline water) resulting in a reduced warm bias in the grid box average temperature. The BL over sea ice is stable in the experiments (not shown) due to the overlying atmosphere

being warmer than the surface. C_{oper} is associated with even greater low-level stability than C_{static} , as indicated by a greater contrast in potential temperature (θ) from 925 hPa to 2 m ($\theta_{925} - \theta_{2m}$), particularly over ice but also over the ocean (Figure 6.5c). The difference in low-level stability has the same order of magnitude as the difference in 2 m temperature, suggesting that the low-level cooling due to sea ice loss causes the increased BL stability in the C_{oper} forecasts. This is consistent with lower BL heights in C_{oper} (due to reduced turbulent mixing), although differences that are distinguishable from zero are not seen until after day 4 (Figure 6.5d). C_{oper} is also associated with slightly weaker winds at 10 m (Figure 6.5e) and 925 hPa (Figure 6.5f) over sea ice between days 5 and 8. The BL height difference profiles in Figure 6.5d follow similar patterns to those of the low-level wind in Figures 6.5e and 6.5f, suggesting that the BL turbulence is wind-driven. Although weaker winds are consistent with a more stable BL in C_{oper} , the differences are of very low magnitude (on the order of 0.1 m s^{-1}), with a relatively large standard error. This indicates that there is not a systematic difference in wind speed between the two experiments.

The SIF in C_{oper} is virtually identical to that in C_{thermo} , with the orange and red lines being indistinguishable from zero at all lead times in Figure 6.5a. However, C_{thermo} exhibits 2 m temperatures over ice that are $\sim 0.6^\circ\text{C}$ cooler than in C_{oper} (Figure 6.5b), consistent with greater low-level stability (Figure 6.5c). This suggests reduced BL turbulent mixing in C_{thermo} , which is consistent with lower BL heights (Figure 6.5d) and weaker 10 m winds (Figure 6.5e; at least in the first 5 days of the forecasts). The difference in 2 m temperature exhibits a diurnal cycle, that also feeds into low-level stability, BL height and 10 m wind. This occurs due to there being a larger diurnal variation in C_{oper} (where temperatures can exceed zero over ice) than in C_{thermo} . The reduction in low-level temperatures of $\sim 0.6^\circ\text{C}$ is similar in magnitude to the warm bias in Tjernström et al. (2021), indicating that the surface temperature and albedo coupling eliminates the warm bias. The C_{thermo} near-surface temperatures are the same as the other experiments at the initial time (with the same warm bias over ice), and then rapidly cool at the first coupling step, explaining the sharp change between days 0 and 1 in Figure 6.5b (this is the “initialisation shock” described in Section 6.2.1). Again, the same differences are seen in the skin temperature,

with the same magnitude (not shown). The cooler temperatures in C_{thermo} largely remain local to the sea ice, with only small differences over the ocean (Figure 6.5b). The differences in 925 hPa wind between C_{oper} and C_{thermo} are rather small with large standard errors (Figure 6.5f), indicating that there is no systematic difference.

The differences in Figure 6.5 are small, due to taking pan-Arctic averages over all forecasts. To better understand the impact of the sea ice coupling, we must examine selected forecasts in more detail in time and space. To maximize the potential signal, here we will examine forecast start dates where the surfaces in C_{oper} and C_{static} are most different, as presumably this will prompt the greatest impact on the overlying atmosphere. Forecasts will be compared in the previously defined Pacific and Eurasian sectors separately, providing two case periods with different sea ice conditions and meteorology. Note that we will use the same dates for comparison of the C_{thermo} forecasts for continuity. The focus hereafter is on 3-day forecasts, as at longer lead times the atmospheric forecasts were found to have diverged significantly in some cases due to the chaotic nature of the system, making direct attribution to model differences more difficult.

The differences in SIF between C_{oper} and C_{static} over 3-day forecasts in the Pacific and Eurasian sectors are presented in Figure 6.6. In both regions, the greatest SIF difference between the two experiments at 3 days is found to occur over 4 consecutive forecasts (exceeding the 90th percentile of difference), and these are chosen as case periods for further study. In the Pacific, the greatest difference in SIF between the forecasts occurs in late July, in association with cyclone “2” (Figure 6.6a). Note that this is the aforementioned cyclone that was studied in Croad et al. (2023a). The “Pacific case period” for further examination is comprised of 3-day forecasts starting 26–29 July. In the Eurasian sector, the greatest difference in SIF between the forecasts occurs in mid-August, associated with cyclones “7” and “8” (Figure 6.6b). The “Eurasian case period” is comprised of 3-day forecasts starting 13–16 August.

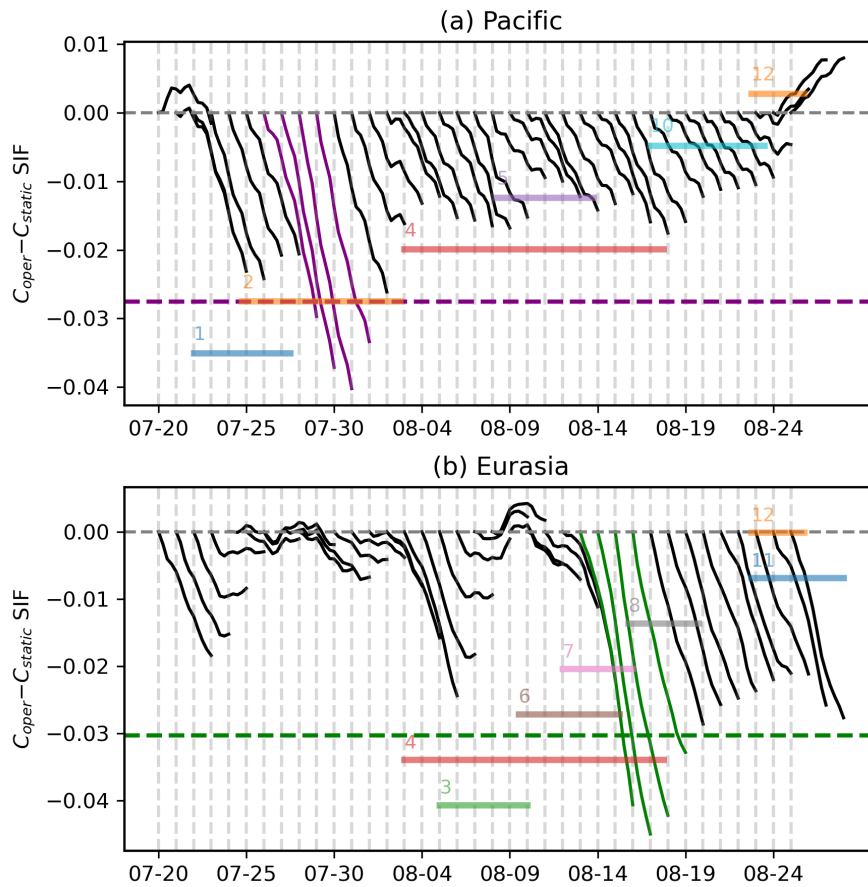


Figure 6.6: Time series of the areal average difference in SIF ($C_{oper} - C_{static}$) over 3-day forecasts in the (a) Pacific and (b) Eurasian sectors. The dashed horizontal lines mark the 90th percentile of 3-day differences for each region, and the solid lines coloured in purple and green denote the forecast start dates that exceed this threshold in the (a) Pacific and (b) Eurasian sectors respectively. The semi-transparent horizontal lines refer to the passage of cyclones, with the colours and numbers matching those in Figure 6.2c.

Pacific case period: forecasts starting 26–29 July

Composite maps describing the surface in the Pacific sector from 3-day forecasts starting 26–29 July are presented in Figure 6.7. In this region the MIZ spans a broad meridional extent in C_{oper} from 70–80°N, with the SIF being largely between 0.5 and 0.8, with a very sharp drop off to 0.15 approaching the ice edge (Figure 6.7a). Cyclone 2 is seen in the mean sea level pressure (MSLP) field, positioned directly over the MIZ during this time, with the cyclone centre over a small gap in the ice (where the SIF has fallen below 0.5). Beneath the cyclone, C_{oper} is associated with reduced SIF compared to C_{static} (Figure 6.7b), suggesting that cyclone 2 is associated with the break up and melting of ice in the coupled forecasts. C_{oper} has greater SIF along the ice edge to the west of the

Pacific sector, which is likely associated with the advection of ice by large-scale off-ice flow associated with the cyclone. C_{thermo} is associated with slightly higher SIF than C_{oper} (perhaps due to the colder surface and near-surface temperatures identified in Figure 6.5 inhibiting melting), but the differences are approximately an order of magnitude smaller than the differences between C_{oper} and C_{static} (Figure 6.7c). C_{oper} and C_{thermo} have an areal average SIF in the Pacific sector (i.e. the purple box) that is almost identical to the EPS ensemble mean, whereas C_{static} has a higher areal average SIF than any of the ensemble members (Figure 6.7d).

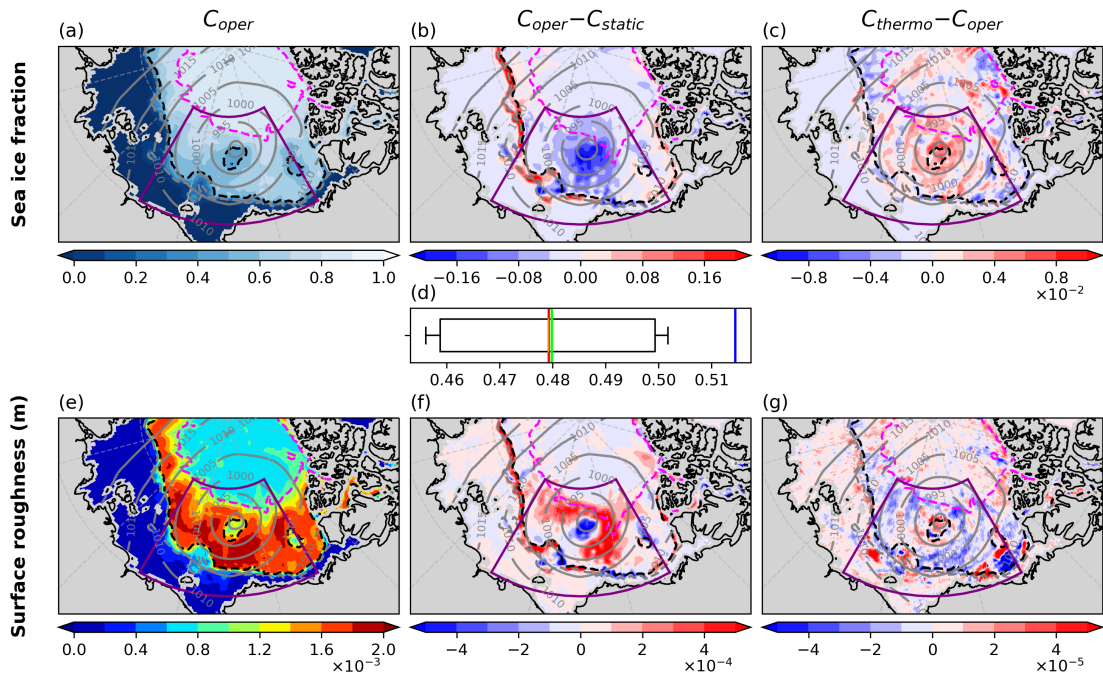


Figure 6.7: Composite mean SIF and surface roughness lengths for 3-day forecasts starting 26–29 July 2020. The top panels are maps of (a) average SIF in C_{oper} , (b) the average difference in SIF between C_{oper} and C_{static} , and (c) the average difference in SIF between C_{thermo} and C_{oper} . (d) The average SIF in the purple region from C_{oper} (red line), C_{static} (blue line), C_{thermo} (lime green line), and each EPS ensemble member presented as a box plot (with whiskers extending to the maximum and minimum values). The bottom panels (e-g) are as (a-c) but for surface roughness length. Note the differences in order of magnitude when comparing panels (b) and (c), and (f) and (g). Contours of SIF (0.15, grey dashed; 0.5, black dashed; 0.8, magenta dashed) and mean sea level pressure (grey solid) from (a,e) C_{oper} , (b,f) C_{static} , (c,g) C_{thermo} are overlain.

The MIZ region is associated with relatively large surface roughness lengths compared to the surrounding ocean and pack ice (Figure 6.7e). This is because in the IFS Cy47r1 the roughness length for momentum depends on SIF, and peaks when SIF is approximately

0.5 (ECMWF, 2020). C_{oper} has reduced SIF compared to C_{static} (Figure 6.7b), and given that the SIF is largely between 0.5 and 0.8 (Figure 6.7a), this means that the SIF in C_{oper} is moving closer to 0.5 with a greater surface roughness lengths than C_{static} (Figure 6.7f). This is generally true except in the small gap of ice in C_{oper} where the SIF moves away from 0.5. In this region C_{oper} has reduced roughness lengths compared to C_{static} , as the SIF falls below 0.5. The slightly greater SIF in C_{thermo} than C_{oper} means that the surface roughness lengths are reduced in C_{thermo} , but the differences are an order of magnitude smaller than those between C_{oper} and C_{static} (Figure 6.7g).

Maps of the differences in BL quantities from the three sets of forecasts are presented in Figure 6.8. As seen from Figure 6.5b, the near-surface temperatures are reduced in C_{oper} compared to C_{static} over almost the entire domain (Figure 6.8a). The magnitude of this cooling is greatest where the SIF has been reduced in C_{oper} compared to C_{static} , with a value of $\sim 0.5^\circ\text{C}$ in the gap in the sea ice in the middle of the domain. Differences in surface sensible and latent heat fluxes between the experiments are found to have the same sign and have similar magnitudes, so are combined into one field for this analysis. The lower near-surface temperatures over the centre of the domain are associated with surface sensible and latent heat fluxes that are more negative in C_{oper} than in C_{static} (Figure 6.7b), indicating greater heat and moisture transfer from the atmosphere to the surface. This is consistent with a more stable BL over ice in C_{oper} . There is also a notable reduction in near-surface temperature in the off-ice flow to the west of the Pacific sector in the Laptev Sea (Figure 6.8a). This results in more positive sensible and latent heat fluxes in C_{oper} than in C_{static} (Figure 6.8b), with more heat and moisture transfer from the surface to the atmosphere due to a greater temperature contrast between the ocean surface and the air. In this case over the ocean, the BL is more unstable in C_{oper} . Furthermore, the 10 m wind speeds in the cyclone are found to be $\sim 0.5 \text{ m s}^{-1}$ lower in C_{oper} than in C_{static} (Figure 6.8c). The weaker winds are associated with greater surface momentum fluxes over the MIZ on the eastern flank of the cyclone (Figure 6.8d). This indicates that the weaker winds in C_{oper} are linked to increased surface roughness and surface drag in the MIZ.

The C_{thermo} forecasts have near-surface temperatures that are up to 1.0°C cooler over

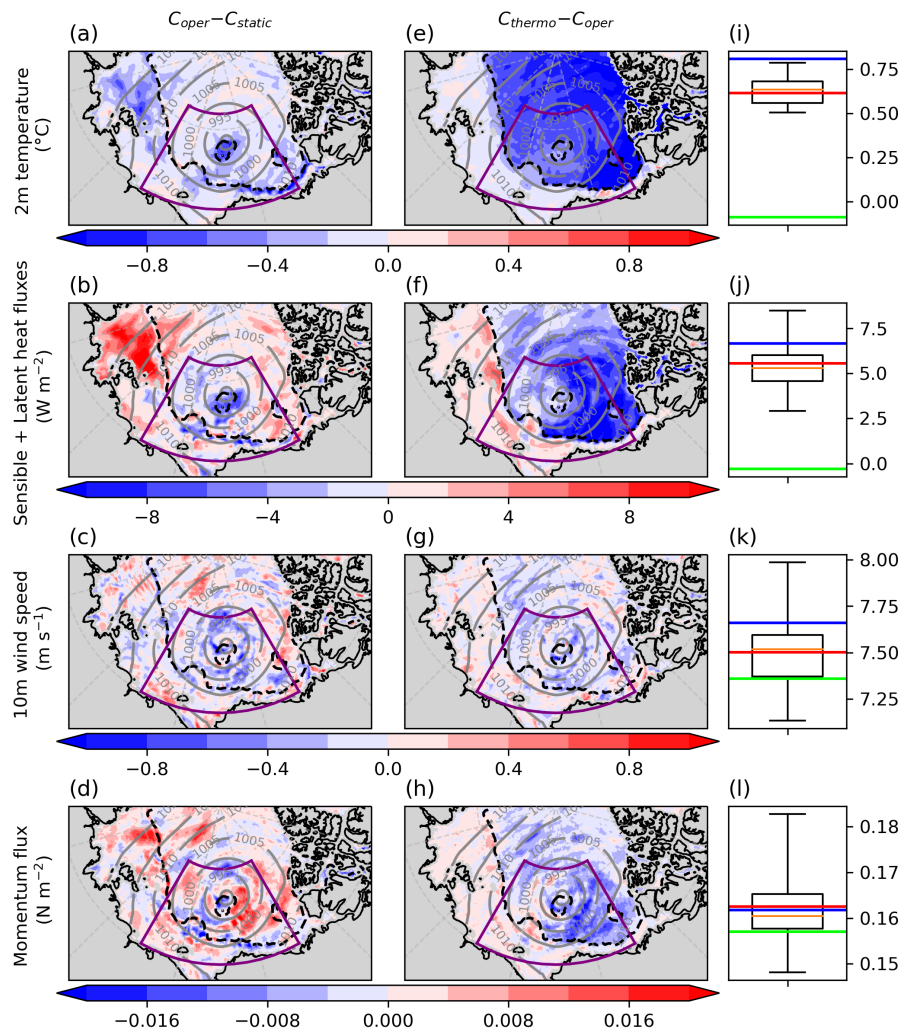


Figure 6.8: Composite mean differences in BL quantities for 3-day forecasts starting 26–29 July 2020. The top row shows the 2 m temperature, with (a) the average difference between C_{oper} and C_{static} , (e) the average difference between C_{thermo} and C_{oper} , and (i) the areal average value over sea ice grid points at the forecast starts in the purple region from C_{oper} (red line), C_{static} (blue line), C_{thermo} (lime green line), and each EPS ensemble member presented as a box plot (with whiskers extending to the maximum and minimum values). Panels (b,f,j), (c,g,k), and (d,h,l) are as (a,e,i) but for the sum of surface sensible and latent heat fluxes, 10 m wind speed, and momentum flux respectively. Contours of 0.5 SIF (black dashed) and mean sea level pressure (grey solid) from C_{oper} are overlain on each map.

ice compared to C_{oper} (Figure 6.8e). This large difference in near-surface temperature is associated with sensible and latent heat fluxes that are more negative over all ice in C_{thermo} (Figure 6.8f) meaning greater heat and moisture transfer from the atmosphere to the surface, consistent with a more stable BL. Also note that there are slightly colder temperatures over the ocean in C_{thermo} (Figure 6.8e), associated with more positive heat sensible and latent heat fluxes (Figure 6.8f). This indicates greater heat and moisture

transfer from the ocean surface to the overlying atmosphere, in the opposite sense to the fluxes over ice. C_{thermo} is consistently associated with slightly weaker winds than C_{oper} over the ice (Figure 6.8g), but also reduced surface momentum flux (Figure 6.8h). This indicates that the weaker winds in C_{thermo} are related to increased BL stability over ice.

This analysis demonstrates differences in BL quantities between the forecast experiments that are physically consistent with the changes at the surface. The differences in near-surface temperature between the experiments are relatively large compared to the spread of the EPS ensemble, with C_{static} being slightly warmer than any other ensemble member, C_{oper} aligning with the ensemble mean, and C_{thermo} being much cooler than any other ensemble member (Figure 6.8i). Note that the average 2 m temperature over ice has been reduced from ~ 0.6 °C in C_{oper} to just below 0 °C in C_{thermo} , demonstrating that the C_{thermo} configuration has corrected for the known warm bias over ice. The difference in the sum of the surface sensible and latent heat fluxes between C_{oper} and C_{static} has a regional dependence (Figure 6.8b), and so the average difference is small compared to the spread of the EPS ensemble (Figure 6.8j). In contrast, the systematically more negative sensible and latent heat fluxes over ice in C_{thermo} than in C_{oper} (Figure 6.8f), with an average value of approximately 0 W m^{-2} compared to $\sim 5 \text{ W m}^{-2}$, is a relatively large difference compared to the spread of the EPS ensemble (Figure 6.8j). The differences in 10 m wind (Figure 6.8k) and surface momentum flux (Figure 6.8l) between the three sets of experiments are small compared to the spread of the EPS ensemble.

Eurasian case period: forecasts starting 13–16 August

Figure 6.9 shows composite maps describing the surface in the Eurasian sector from 3-day forecasts starting 13–16 August. The sea ice field differs from that during the Pacific case period, with a sharp drop in SIF from pack ice to open ocean, constituting a very narrow MIZ (Figure 6.9a). The MSLP field highlights a cyclone to the south-east of Svalbard, resulting in on-ice flow in the Eurasian sector (Figure 6.9a; note that cyclones 7 and 8 merge into one system south of Svalbard, see tracks in Figure 6.2c). The cyclonic flow is likely responsible for transporting heat poleward, resulting in the reduction of SIF in a narrow band at the ice edge in C_{oper} compared to C_{static} (Figure 6.9b). There is also a

complicated change in ice edge geometry in the off-ice flow to the west of the domain, with increased SIF to the north of Greenland (likely related to transport of ice by the wind forcing), and reduced SIF to the east of Greenland (perhaps usual summer melting) in C_{oper} compared to C_{static} . The differences in SIF between C_{thermo} and C_{oper} are again an order of magnitude smaller than that between C_{oper} and C_{static} (Figure 6.9c). The areal average SIF in the green box from C_{oper} and C_{thermo} is almost identical to the EPS ensemble mean, whereas C_{static} has a high areal average SIF than any other ensemble member (Figure 6.9d).

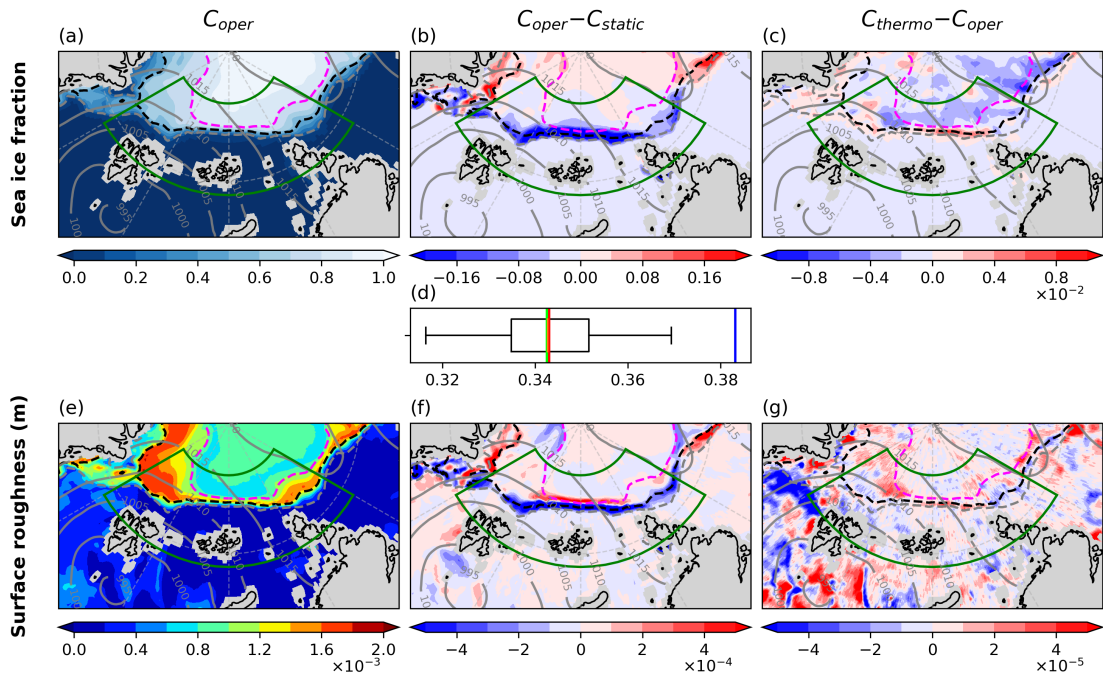


Figure 6.9: As in Figure 6.7 but for 3-day forecasts starting 13–16 August 2020 in the Eurasian sector. Note the differences in order of magnitude when comparing panels (b) and (c), and (f) and (g).

The surface roughness over ice is generally lower than during the Pacific case period, due to the narrower MIZ region (Figure 6.9e). The reduction in SIF at the ice edge in C_{oper} (Figure 6.9b) is associated with a dipole in the difference in the surface roughness lengths compared to C_{static} , with lower surface roughness where the SIF falls below 0.5 at the outermost edge, and greater surface roughness behind where SIF falls closer to 0.5 (Figure 6.9f). The differences in surface roughness between C_{oper} and C_{thermo} are again small (Figure 6.9g).

C_{oper} is associated with reduced 2 m temperatures compared to C_{static} where ice loss has occurred, on the ice edge and in the off-ice flow to the west of the domain (Figure 6.10a). The reduced near-surface temperatures are again associated with more negative surface sensible and latent heat fluxes in C_{oper} than C_{static} (Figure 6.10b), indicating a more stable BL in C_{oper} in these regions. C_{oper} is associated with a thin band of enhanced 10 m wind speeds on the ice edge compared to C_{static} (Figure 6.10c) where SIF has been reduced below 0.5 and therefore the surface is less rough (Figure 6.9b,f), with reduced surface momentum fluxes (Figure 6.10d). This demonstrates that the reduced surface roughness over ice in C_{oper} compared to C_{static} results in a local increase in 10 m wind speed due to reduced surface drag. The 10 m wind speed is also enhanced in C_{oper} in the off-ice flow to the west of the domain (Figure 6.10c), which may be associated with the reduced surface roughness in this region (Figure 6.9f).

As in the Pacific case period, C_{thermo} is associated with reduced near-surface temperatures over ice than in C_{oper} (Figure 6.10e), with a difference of $\sim 0.5^\circ\text{C}$. These cooler temperatures are associated with sensible and latent heat fluxes that are more negative over ice in the on-ice flow, but more positive over ocean in the off-ice flow (Figure 6.10f) in C_{thermo} , as was seen in the Pacific case period (Figure 6.8f). The on-ice flow in C_{thermo} (where BL stability is greater) is associated with slightly weaker 10 m winds (Figure 6.10g) and reduced surface momentum fluxes (Figure 6.10h) compared to C_{oper} , but the differences are generally small.

Again, the differences in BL quantities are physically consistent with the changes at the surface. The differences in the 2 m temperature are again relatively large compared to the spread of the EPS ensemble (Figure 6.10i), but the differences in surface sensible and latent heat fluxes, 10 m wind and surface momentum fluxes (Figure 6.10j,k,l) are relatively small compared to the EPS ensemble and the Pacific case period. Note again at the C_{thermo} configurations corrects the known warm bias over ice, with the average 2 m temperatures being below zero in contrast to the C_{oper} and C_{static} configurations (Figure 6.10i). The differences are generally smaller in this case due to the domain of interest

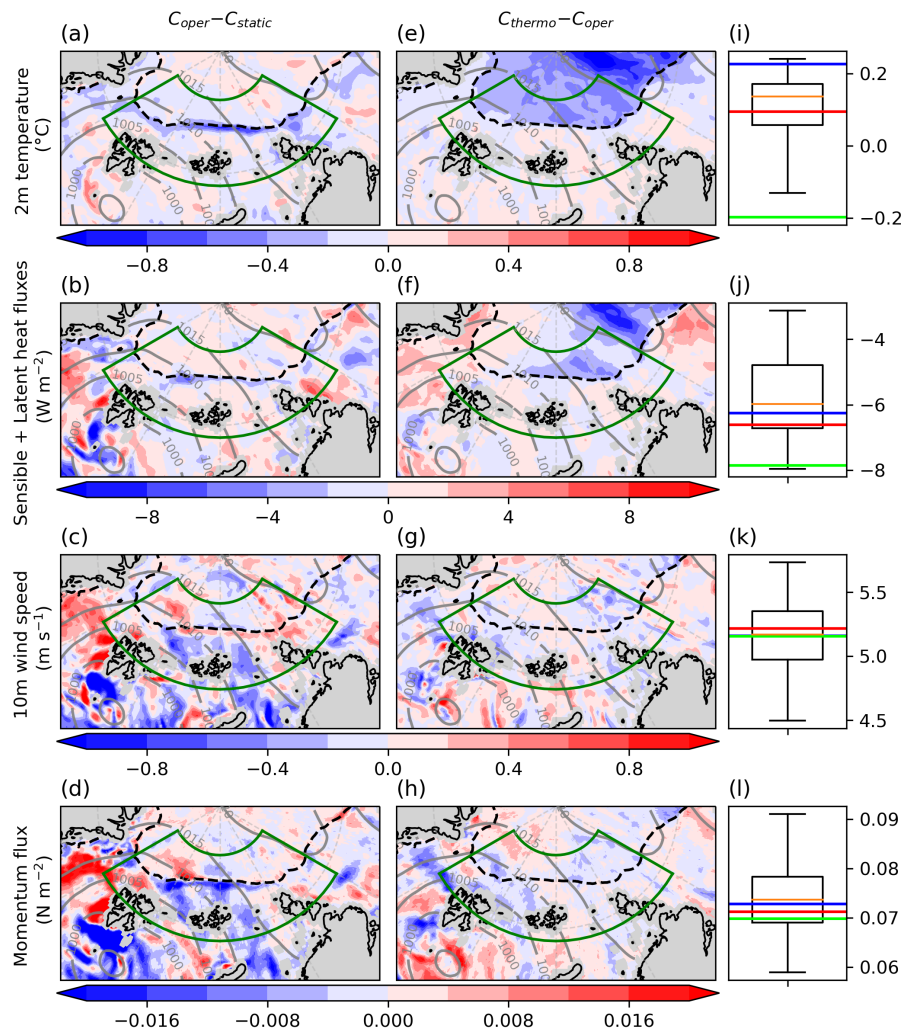


Figure 6.10: As in Figure 6.8 but for 3-day forecasts starting 13–16 August 2020 in the Eurasian sector.

containing less sea ice, and due to any differences in the sea ice surface between C_{oper} and C_{static} occupying a smaller areal extent (compared to the Pacific case period). This analysis demonstrates that the impact of sea ice coupling largely remains local to the sea ice itself, and that the size of the impact is dependent on the areal extent of the ice (when comparing C_{oper} and C_{thermo}) and the areal extent of the sea ice changes (when comparing C_{oper} and C_{static}).

6.3.3 Forecasts of Arctic cyclones

The MSLP fields in Figures 6.7 and 6.9 indicate that the differences between the cyclones in the three sets of forecasts are small, but in this section we examine the impact of sea

ice coupling on Arctic cyclones in more detail. Firstly, maps of cyclone 2 from 3-day forecasts starting 26 July (valid 29 July) are presented in Figure 6.11. The forecasts of 850 hPa relative vorticity are remarkably similar from C_{oper} , C_{static} and C_{thermo} (Figures 6.11a–c), with large positive values at the centre of the cyclone and banded features further from the centre. There are some small discernible differences in the 10 m wind speed to the south of the cyclone, with C_{static} having slightly stronger winds over a larger area than C_{oper} , which has slightly stronger winds than C_{thermo} (seen by focusing on the 15 m s^{-1} contours in Figures 6.11a–c). These differences in wind speed at 10 m are consistent with the analysis in Section 6.3.2. The EPS ensemble mean map is much smoother in 850 hPa relative vorticity than the individual forecast experiments (Figure 6.11d), indicating variability in the cyclone placement amongst the ensemble members. This suggests that the differences between the EPS ensemble members are larger than that between the C_{oper} , C_{static} , and C_{thermo} forecasts.

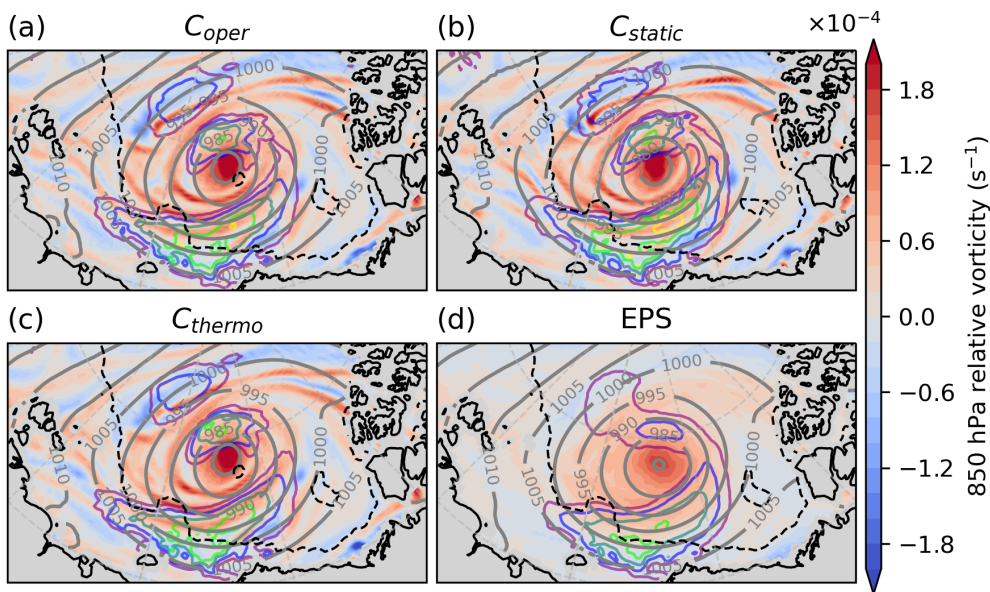


Figure 6.11: Maps of cyclone 2 from 3-day forecasts starting 26 July (valid 29 July). The maps display 850 hPa relative vorticity (shading), 10 m wind speed speeds (solid coloured contours from 10–15 m s^{-1}), mean sea level pressure (grey contours) and 0.5 SIF fraction (black dashed contours) from (a) C_{oper} , (b) C_{static} and (c) C_{thermo} , and (d) the EPS ensemble mean.

Time series of cyclone intensity, as diagnosed by minimum MSLP, from 3-day forecasts are presented in Figure 6.12. The minimum MSLP in each forecast is found by searching for the minimum value within a 500 km radius of the ERA5 cyclone centre determined

by TRACK (see Section 6.2.3). Forecasts of strength for cyclone 2 during the Pacific case period (Figure 6.12a) are remarkably similar across different forecast experiments and forecast start times. C_{static} consistently has the lowest minimum MSLP and C_{thermo} consistently has the highest, however, the differences at 3 days are on the order of only 1 hPa. Understanding whether these differences are statistically significant would require running ensemble forecasts of the experiments, which is beyond the scope of this study. However, what can be said is that the differences in cyclone strength at 3 days are smaller than the spread of the EPS ensemble, shown by the boxplots in Figure 6.12a. Forecasts of strength for cyclones 7 and 8 (combined into one track here) during the Eurasian case period (Figure 6.12b) exhibit larger differences between the forecast experiments and forecast start times, indicative of a more uncertain situation due to the merger of the two systems. This is reflected by the larger spread of the EPS ensemble in Figure 6.12b. Again, the differences in cyclone strength at 3 days are smaller than the spread of the EPS ensemble.

This analysis demonstrates that the impact of the sea ice coupling on the forecasts of Arctic cyclones is smaller than the impact of the noise of the initial condition and stochastic perturbations to the ensemble members in the prediction system. From Section 6.3.2 changing the sea ice coupling can have locally large impacts on the near-surface temperature (up to 1°C) and near-surface winds (up to 0.5 m s⁻¹) in the BL, but these impacts are generally isolated to the sea ice (when comparing C_{oper} and C_{thermo}), or to regions where sea ice change has occurred (when comparing C_{oper} and C_{static}). Hence, the overall impact of the sea ice coupling on the larger scales above the BL is very small. Cyclone 2 during the Pacific case period represents a set up that should maximise the differences between the three sets of forecast experiments, with the cyclone being positioned over the MIZ for several days (Figure 6.7). However, the cyclone has a similar position and strength in each forecast experiment (Figures 6.11 and 6.12a). The analysis here and in Section 6.3.2 has focused on 3 day forecasts. Similar results were found with 6 day forecasts, although the impact of the sea coupling had a weaker signal, with the forecasts diverging due to chaos (not shown).

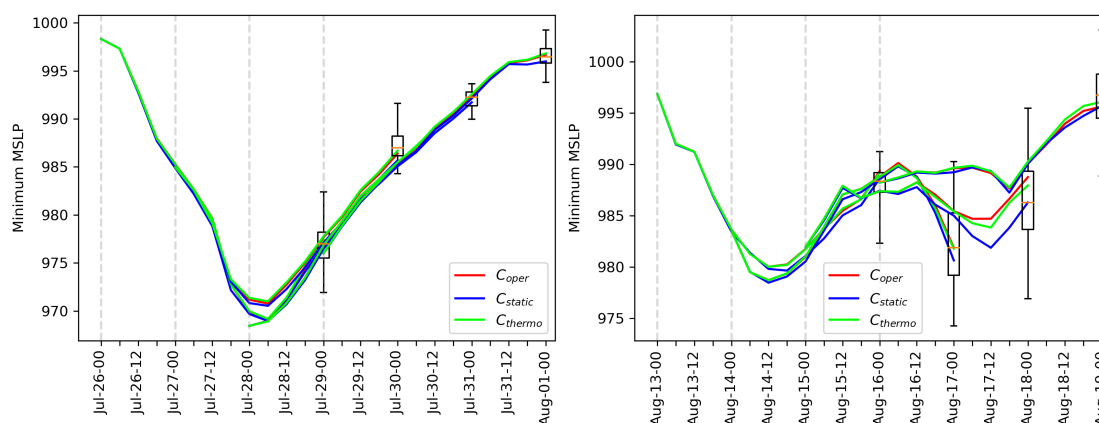


Figure 6.12: The minimum mean sea level pressure from 3-day forecasts for (a) cyclone 2 during the Pacific case period with forecast start dates 26–29 July, and (b) cyclones 7 and 8 (combined into a single cyclone track) during the Eurasian case period with forecast start dates 13–16 August, from C_{oper} (red), C_{static} (blue) and C_{thermo} (lime green). The EPS ensemble at day 3 is presented by the box plots (with whiskers extending to the maximum and minimum values).

6.4 Conclusions

With climate change, sea ice is becoming thinner and more mobile in the summer-time Arctic, making it more susceptible to break up and melting by atmospheric forcings such as cyclones. Hence, static sea ice for weather forecasts is an increasingly poor assumption in the summer-time Arctic. In recent years, the ECMWF have implemented ocean-ice-atmosphere coupling with dynamic sea ice in the IFS at all time ranges. Day et al. (2022) demonstrated that dynamic sea ice in the IFS generally improved medium-range forecasts in the Arctic in a winter case study. However, no corresponding evaluation for summer has been published in the literature. Despite recent advances, the IFS has a known warm bias over sea ice in summer (Tjernström et al., 2021), which may be related to the fact that the sea ice is not coupled thermodynamically.

In this study we examine the sensitivity of IFS weather forecasts to sea ice coupling in the summer-time Arctic, by comparing 3 sets of 10-day forecast experiments from IFS Cy47r1 that differ only in their sea ice coupling configurations. The results are based on the period 20 July–25 August 2020, although we expect that the qualitative conclusions could be extended to the broader Arctic summer period, in a melting regime. The first set of forecasts, C_{oper} , is identical to the control member of the operational EPS ensemble

used at the time, with “dynamic sea ice”. The second set of forecasts, C_{static} , is identical to C_{oper} except that it has “static sea ice”, where the sea ice field cannot evolve from the start of the forecast as was operational in the EPS prior to November 2016. The third set of forecasts, C_{thermo} , is an experimental setup which is identical to C_{oper} except with additional “thermodynamic coupling” (sea ice surface temperature and albedo coupled to the atmosphere as well as SIF).

The first research question was to understand where the dynamic coupling with the ocean-sea ice model has the greatest impact on sea ice forecasts (Section 6.3.1). It was found that dynamic sea ice had the greatest impact in the vicinity of Arctic cyclones. The dynamic sea ice forecasts capture cyclone-induced break up and melting of sea ice due to strong winds and warm air intrusions, whereas the static sea ice forecasts cannot. However, ice loss was underestimated in the dynamic sea ice forecasts, which may be attributed to missing ocean wave processes or model biases in sea ice thickness. Despite this, the dynamic sea ice forecasts produced much improved sea ice field and ice edge predictions compared to the static sea ice forecasts.

The second and third research questions were to understand the impact of dynamic sea ice and additional thermodynamic coupling on forecasts of the atmospheric BL (Section 6.3.2). The forecasts with dynamic sea ice were found to have colder near-surface temperatures than the static sea ice forecasts (up to $\sim 0.5^{\circ}\text{C}$ in regions where sea ice cover is reduced), with consistent changes in surface heat fluxes, and BL stability. Differences in surface momentum fluxes and low-level winds were found to depend on changes to the surface roughness of the sea ice when comparing the dynamic and static sea ice forecasts. For example, an extreme cyclone in late July (cyclone 2) was positioned over the MIZ for several days, with rougher sea ice in the dynamic sea ice forecasts resulting in a reduction in 10 m winds of $\sim 0.5 \text{ m s}^{-1}$ over a broad area. The forecasts with additional thermodynamic coupling had near-surface temperatures over sea ice that were up to $\sim 1.0^{\circ}\text{C}$ cooler than the operational forecasts, correcting the known warm bias over ice. This was found to be consistent with a more stable BL and weaker 10 m winds over sea ice of up to $\sim 0.5 \text{ m s}^{-1}$.

While the sea ice coupling was found to have locally large impacts on near-surface temperature and winds, the impacts were generally limited to near the sea ice surface. The size of impact was dependent on the areal extent of sea ice and sea ice changes. For example, larger differences were found in a Pacific case period where a cyclone was positioned over the MIZ for several days, than in a Eurasian case period where the cyclone centre was located south of the ice edge. In general, other than near-surface temperature, the differences between the three experiments were found to be smaller than the spread of the EPS ensemble.

The final research question was to understand if sea ice coupling impacted forecasts of Arctic cyclones (Section 6.3.3). Examining two case periods, it was determined that the differences between the cyclones in the three forecasts were smaller than the spread of the operational ensemble. This suggests that any impact of sea ice coupling on the larger scales above the BL is very small in the model, compared with the growth of forecast uncertainty from initial conditions and model physics.

In summary, this work demonstrates the benefits of increasingly sophisticated sea ice coupling representations in a NWP model in the summer-time Arctic, with physically consistent impacts on forecasts. This work has also highlighted the limitations of the sea ice coupling used operationally in the IFS, with the simplistic SIF coupling not capturing any ocean wave interactions, and not correcting for a surface energy balance that leads to a low-level warm bias. The latter was addressed by implementing an experimental configuration with additional thermodynamic coupling. The impact of closer thermodynamic coupling (including the representation of snow on ice), and how this can be employed with adaption to the current data assimilation systems, is being assessed across all ECMWF forecast systems for future implementation, as part of continuously ongoing efforts to improve Earth system interactions in the IFS. This study, along with observations-based evaluations of surface exchange parametrizations over ice (e.g. Elvidge et al., 2016; Elvidge et al., 2021, 2023; Srivastava et al., 2022), highlight the need to revisit how surface exchange is modelled in the coupled system.

With regards to the cyclone-sea ice interaction in the model, the results of this work suggest that cyclones have a larger impact on sea ice than sea ice does on cyclones during summer. Whether this result is model-specific (e.g. due to the underestimation of ice loss with missing processes in the model), or if it is relevant to the physical world, should be determined. The emphasis for future work should be placed on evaluation of NWP model output in the Arctic, key to which is real-world observations. In particular, forecast experiments should be re-run for previous summer-time Arctic field campaign periods. For example, evaluation against the observations discussed in Tjernström et al. (2019) would permit an examination of whether the increasingly sophisticated sea ice coupling representations result in improved model performance in the case of warm air advection events and surface-based inversions in summer.

Acknowledgements

HLC acknowledges PhD studentship funding from the SCENARIO NERC Doctoral Training Partnership grant NE/S007261/1, with co-supervision by SPEK and super-computing support from ECMWF. JM, BH and AV were funded by the Arctic Summer-time Cyclones: Dynamics and Sea-Ice Interaction NERC standard grant NE/T006773/1. BH was also supported by the National Centre for Atmospheric Science, which is funded by NERC under contract R8/H12/83. The authors thank Kevin Hodges for providing cyclone tracks from the TRACK algorithm for use in this study. The authors also acknowledge ECMWF for the production of the ERA5 reanalysis dataset.

Chapter 7

Conclusions

This thesis set out to further our understanding of the physical mechanisms acting in summer-time Arctic cyclones with regards to their atmospheric dynamics and interaction with sea ice. Another aim was to assess the impact of atmosphere-ocean-sea ice coupling, that has recently been implemented in an operational NWP model, on forecasts of summer-time Arctic cyclones. The main outcomes of the thesis and how they answer the four key questions outlined in Chapter 1 are summarised in Section 7.1. The implications and limitations of the findings are then discussed in Section 7.2, alongside suggestions for future work.

7.1 Summary and Discussion

KQ1: What is the variability in the occurrence of summer-time Arctic cyclones, and can they be categorized into classes with distinct structural evolutions and characteristics?

Previously, case studies and composite analyses of extreme cyclones indicated that summer-time Arctic cyclones can have a different lifecycle to mid-latitude cyclones, attaining a long-lived axisymmetric columnar vortex structure after maturity (e.g. Aizawa and Tanaka, 2016; Simmonds and Rudeva, 2012; Vessey et al., 2022). However, it was not clear how typical these cases were, and whether different varieties of cyclone evolutions occur in the summer-time Arctic (unlike mid-latitude cyclones, for which conceptual models are well established; e.g. Bjerknes, 1919; Shapiro and Keyser, 1990). Answering KQ1 was the

focus of Chapter 4, by performing a climatology of summer-time Arctic cyclone structure during May–September 1979–2021. In this chapter a cyclone phase space, based on Hart (2003) but adapted for application in the Arctic, was used to represent a continuum of cyclone structures.

The identified summer-time Arctic cyclones were classified as being low-level dominant (LLD; relative vorticity decreasing with height) or upper-level dominant (ULD; relative vorticity increasing with height) at the time of maximum growth. It was found that 65.5% of cyclones were LLD, whilst the remaining 34.5% were ULD. Classifying summer-time Arctic cyclones in this way produced two cyclone subsets with different structural evolutions and characteristics. LLD cyclones are typically stronger, and preferentially grow and track on the Russian coastline where there is strong low-level baroclinicity on the AFZ. In contrast, ULD cyclones tend to be longer-lived, and preferentially track in the Pacific sector of the Arctic, where they likely interact with TPVs. Note that the partition of ULD/LLD cyclones found in this work is similar to the partition of cyclones that were matched/unmatched with TPVs in Gray et al. (2021), strongly suggesting a link between TPVs and the ULD cyclones identified in this classification scheme.

During growth, LLD cyclones exhibit warm-core asymmetric structures, whereas ULD cyclones have cold-core asymmetric structures. This temperature anomaly in the troposphere (above the surface cyclone) is a direct consequence of thermal wind balance. LLD cyclones typically have greater thermal asymmetry during growth. However, a transition to a persistent cold-core axisymmetric structure after maturity was found to be characteristic of summer-time Arctic cyclones, regardless of structure during growth. This result is consistent with the composite analysis of Vessey et al. (2022), and builds on the study by demonstrating that the structural transition occurs more commonly for cyclones that are ULD during development. Furthermore, the chapter highlighted that cyclones with unconventional lifecycles may be common in the summer-time Arctic, due to the lack of dynamical forcing for dissipation (as discussed in Woollings et al., 2023) and therefore a greater opportunity for re-intensification outside of their main development phase, particularly if interacting with TPVs.

KQ2: By what mechanisms does the surface impact summer-time Arctic cyclone evolution?

The interaction between Arctic cyclones and sea ice is important in summer, when ice extent and thickness is reduced. Whilst it is well understood that cyclones can have large impacts on sea ice (e.g. Asplin et al., 2012; Lukovich et al., 2021; Peng et al., 2021), the mechanisms by which the surface impacts cyclone evolution in the Arctic have received less attention. Chapter 3 set out to address KQ2 by examining the BL processes occurring in two summer-time Arctic cyclone case studies (that tracked over sea ice) with contrasting structure, one being LLD and the other being ULD (the latter developing with a TPV). A PV framework, that has been applied previously to examine the impact of BL friction and sensible heat fluxes on mid-latitude cyclones (Adamson et al., 2006; Cooper et al., 1992), was used.

Both cyclone cases were found to be associated with frictional Ekman pumping and downward sensible heat fluxes over sea ice. However, frictional baroclinic generation of PV (arising from the impact of the frictional slow-down of near-surface winds on horizontal components of vorticity across the BL) was found to be different in the cases, due to the opposing thermal wind structure of the cyclones. Positive PV was generated in the LLD cyclone along the bent-back warm front, like in typical mid-latitude cyclones (e.g. Adamson et al., 2006; Vanni re et al., 2016). However, the same process produced negative PV tendencies in the ULD cyclone, due to the vertically-aligned axisymmetric cold-core structure. This demonstrated that the role of friction in cyclonic weather systems is dependent on the existing cyclone structure.

The use of a PV framework meant that the impact of BL friction and diabatic heating on cyclone structure above the BL could be deduced. In particular, frictional Ekman pumping, frictional baroclinic PV generation, and downward sensible heat fluxes over sea ice all act to cool the cyclone thermal anomaly above the BL. It was suggested that these processes working in unison act to amplify the cold-core columnar vortex structure that

both cyclones exhibited for several days after maximum intensity (unlike mid-latitude cyclones, which more quickly dissipate), although this remains to be demonstrated and quantified in a dynamical model.

KQ3: Which physical parameters determine the dynamics and stability of summer-time Arctic cyclones during their axisymmetric columnar vortex phase, and what is the impact of surface processes?

The cold-core axisymmetric columnar vortex structure of mature summer-time Arctic cyclones (discussed in Chapter 4) has been described in case studies as the low-level cyclone becoming vertically stacked below a TPV (Tanaka et al., 2012; Tao et al., 2017). However, no previous studies have investigated the vortex dynamics of this long-lived cyclone structure. A TPV is associated with a positive PV anomaly on the tropopause (e.g. Cavallo and Hakim, 2010), whilst Chapter 3 demonstrated that at low levels friction generates negative PV anomalies and acts to cool the lower troposphere. Such a setup (with the low-level cold anomaly interpreted as a negative PV anomaly) features opposing radial gradients of PV at upper and lower levels, thereby satisfying the Charney-Stern-Pedlosky necessary condition for baroclinic instability. The focus of Chapter 5 was to answer KQ3 by investigating the stability of the axisymmetric columnar vortex structure of mature summer-time Arctic cyclones, using an idealised two-layer QG model, with a focus on the impact of friction.

The QG model results indicated that this axisymmetric columnar vortex structure is unstable, but only if the vortex radius exceeds a short-scale cutoff (estimated to be ~ 300 km in the Arctic). The growth rate of instability scales with the magnitude of the QGPV anomalies, but decreases with increasing friction coefficient. It is also demonstrated that friction can act to destabilise an initially stable vortex column (by cooling the lower troposphere over time and generating negative PV anomalies) in the QG model, on the timescale of a few days.

Further investigation is required to quantify this instability and understand how it would

present itself in the real atmosphere, where vortices are not isolated from other atmospheric phenomena. For example, this instability mechanism might suggest a limit on the lifetime of mature summer-time Arctic cyclones.

KQ4: How does sea ice coupling representation impact weather forecasts of summer-time Arctic cyclones in NWP?

Whilst Chapters 3–5 were focused on the atmospheric dynamics of summer-time Arctic cyclones, Chapter 6 took a different approach, with a focus on examining the cyclone-sea ice interaction in an operational NWP model. It might be expected that the recent progress in implementing atmosphere-ocean-sea ice coupling in NWP models should benefit Arctic cyclone forecasts. However, this had yet to be established. Answering KQ4 was the focus of Chapter 6, by investigating the sensitivity of weather forecasts produced by the ECMWF IFS to sea ice coupling representation in the summer-time Arctic. Three sets of coupled forecasts were compared with (i) dynamic sea ice in operational configuration, (ii) static sea ice (as used to be operational), and (iii) dynamic sea ice with additional thermodynamic coupling in an experimental setup.

The dynamic sea ice forecasts produced much improved forecasts of sea ice, compared to static sea ice, particularly in the vicinity of Arctic cyclones that track over the ice. Furthermore, the dynamic sea ice forecasts produced lower near surface temperatures (up to 0.5°C), consistent with a more stable BL, and differences in near-surface wind (up to 0.5 m s^{-1}) that are consistent with changing surface roughness over the ice. The forecasts with additional thermodynamic coupling produced temperatures that were up to 1°C cooler over sea ice than the operational configuration, correcting a known warm bias in the IFS, and also associated with a more stable BL and weaker near-surface winds. The results suggest that more physically complete representations of the sea ice coupling can lead to more physical solutions. However, any differences above the BL were found to be small, with differences in forecasts of cyclone strength and position being smaller than the spread of the operational forecast ensemble.

With regards to a cyclone-sea ice interaction in the model, the results suggested that cyclones have a larger influence on sea ice than sea ice does on cyclones at present. It is not clear whether this result is specific to the IFS, or if it is also relevant to the physical world. Efforts are continuously ongoing to develop the model, including the atmosphere-ocean-sea ice coupling, and these conclusions may change in the future as the model improves.

7.2 Implications and future work

As summarised in the previous section, this thesis has contributed to advancing our understanding of summer-time Arctic cyclones in several different aspects. The climatological work presented in Chapter 4 (addressing KQ1) has provided a broader perspective of summer-time Arctic cyclone occurrence, extending beyond the case-study approach of previous literature. Chapters 3 and 5 (addressing KQs 2 and 3) have illuminated aspects of the summer-time Arctic atmosphere that had not previously been explored. Chapter 6 (addressing KQ4) has provided an evaluation of an operational NWP model with coupled sea ice in the summer-time Arctic, and shed light on the model behaviour with regards to the cyclone-sea ice interaction. More specific implications, limitations, and suggestions for future work are provided for each chapter in turn below.

In the following discussion details of ongoing efforts from the closely-linked “Arctic Summer-time Cyclones: Dynamics and Sea-Ice Interaction” (henceforth ASC) NERC project (UK Research and Innovation, 2024; project reference NE/T006773/1), that are complimentary but separate from the work presented in this thesis, are briefly discussed. The ASC project had an associated field campaign (THINICE; with a summary article submitted to the *Bulletin of the American Meteorological Society* and currently under review), based in Svalbard in July–August 2022, which used two research aircraft to obtain measurements related to Arctic cyclone structure and near-surface fluxes of momentum, heat and moisture over sea ice. More details about the project and field campaign are available at <https://research.reading.ac.uk/arctic-summertime-cyclones/>.

Chapter 4 (KQ1): In this work a simple classification scheme for Arctic cyclones was pro-

posed. Formulation of a more complex classification scheme was limited by the minimal number of pressure levels used to deduce cyclone structure (a data storage compromise made in return for increased temporal coverage). A more detailed perspective of cyclone structure in the vertical should be considered in the future. Furthermore, a cyclone phase space approach simply describes instantaneous cyclone structure, from which the dynamics are implied. Alternatively, one could use a methodology that places more of an emphasis on cyclone dynamics, such as the height-attributable QG vertical-motion diagnostic that has been used previously to classify mid-latitude cyclones as Type A, B and C (e.g. Deveson et al., 2002; Gray and Dacre, 2006). Future work should ultimately lead to the formulation of conceptual models, which are key for communicating typical cyclone behaviour and hazards, and therefore provide value in forecasting applications (as they do for mid-latitude cyclones). One approach for achieving this would be to perform spatial composite analysis of LLD and ULD cyclones at different stages in their lifecycles. Furthermore, there are many opportunities for extending the analysis presented in Chapter 4, for example, examining other climatological characteristics of cyclones including size, origin, and month of occurrence. Examining trends in cyclone behaviour is another potential avenue for future work, especially in the context of climate change and sea ice decline.

Chapter 3 (KQ2): The mechanisms by which friction and sensible heat fluxes over ice impact Arctic cyclones were deduced from PV and thermal wind arguments. In particular, the cooling action of friction and sensible heat fluxes on the cyclone thermal anomaly above the BL was realised, and it was hypothesised that this may contribute to amplifying cold-core columnar vortex structure of long-lived summer-time Arctic cyclones. However, more work is required to demonstrate this mechanism using a dynamical model, and understand if this any bearing on the cyclone longevity. For example, work is ongoing in the ASC project (building on Chapter 3 in this thesis) to investigate the impact of BL friction and other diabatic processes on the evolution of summer-time Arctic cyclones, using PV tracers (e.g. Saffin et al., 2016) in the UK Met Office's Unified Model. Future work should also use a PV inversion tool to directly attribute the PV tendencies from BL friction and sensible heat fluxes to the impacts on cyclone structure (circulation and stratification). For example, the diagnostic tool of Cullen, 2018, which assumes semi-geostrophic bal-

ance dynamics, would be suitable for this. On this point, latent heat release and other moist processes, which have largely not been considered in this thesis, likely play an important role in the evolution of summer-time Arctic cyclones (e.g. Fearon et al., 2023) and should be the subject of future work. Furthermore, the terms in the PV framework used in this study were calculated from NWP model output. The measurements collected during the THINICE field campaign are sufficient to estimate some of these terms from observations, and therefore provide a rare opportunity to verify the NWP model.

Chapter 5 (KQ3): The impact of friction on idealised columnar vortices (meant to replicate the mature stage of summer-time Arctic cyclones) was examined in a reduced dynamics model. The next step with this work is to expand the QG model from 2 to 3 layers, which would permit for more complex initial vortex structures that more closely resemble summer-time Arctic cyclone structures in nature (with the lowest frictional layer having a smaller vertical extent, like the BL in the real world). In the future, one could also consider the use of a semi-geostrophic framework that would better represent the dynamics of the real atmosphere, with the added benefit that the frictional baroclinic PV generation term identified in Chapter 3 could be represented as well as the Ekman friction term (therefore providing a closer link to Chapter 3). Two different mechanisms by which friction impacts summer-time Arctic cyclone evolution have been proposed in this thesis, with Chapter 3 suggesting that friction acts to amplify and persist a cold-core structure after maturity, and Chapter 5 proposing that friction can ultimately act to destabilise this structure. Future work should focus on evidencing and quantifying these processes acting in real summer-time Arctic cyclone cases. With regards to understanding whether the vortex instability mechanism occurs in the real world, a first step would be to examine the structure (including PV gradients), size and vortex behaviour of a broader range of summer-time Arctic cyclones in nature. This analysis would indicate whether the instability condition is satisfied in real cases, and whether we see vortex behaviour that resembles the instability seen in the idealised model.

Chapter 6 (KQ4): A comparison of forecast experiments produced by the ECMWF IFS suggested that sea ice coupling representation can have large impacts on sea ice and the

BL, but has very little impact on forecasts of summer-time Arctic cyclones. The work is somewhat limited because an evaluation against a truth dataset has not been performed, with no in situ observations available for the period of study and there being large uncertainties with regards to the quality of reanalysis datasets in the Arctic (e.g. Graham et al., 2017; Wesslén et al., 2014). Clearly, increasing the quantity and quality of observations in the Arctic is a key focus for all aspects of Arctic research and weather forecasting. The results suggest that summer-time Arctic cyclones have a larger impact on sea ice than the sea ice does on the cyclones. It is not clear whether this characterisation of the cyclone-sea ice interaction is specific to the choice of model, or is a fact of the real world. Work undertaken within the ASC project to investigate the impact of sea ice coupling in a different NWP model (the UK Met Office Unified Model) on forecasts of summer-time Arctic cyclones, has yielded different results and suggests that sensitivity to sea ice coupling is model specific. To understand the cyclone-sea ice interaction in a more theoretical sense, it may be that more idealised sensitivity experiments need to be conducted. For example, forecasts should be run with more dramatic changes to sea ice (e.g. changing the surface roughness, or even removing the sea ice altogether) to fundamentally understand the cyclone-sea ice interaction.

In the future, global temperatures will continue to rise with climate change and sea ice will continue to decline (Meredith et al., 2019). Extrapolation of recent sea ice volume data and climate model projections indicate that the Arctic will be practically ice-free in summer by mid-century (Overland and Wang, 2013), at less than 2°C global warming relative to pre-industrial levels (Notz and Stroeve, 2018). This will make the summer-time Arctic increasingly accessible to human activity, for example, with shipping routes across the central Arctic projected to be available by mid-century (Melia et al., 2016).

Although it remains unclear whether summer-time Arctic cyclone activity has changed significantly in recent decades (e.g. Valkonen et al., 2021; Zhang et al., 2023), the dramatic environmental transformation in the Arctic due to climate change is likely to influence the dynamics of Arctic cyclones in the future. For instance, sea ice loss is likely to alter the magnitude and location of low-level temperature gradients that influence cyclo-

genesis. Warmer surface temperatures in the central Arctic due to the loss of sea ice may contribute to a weakening temperature gradient across the AFZ, although this could be offset by enhanced warming over land surfaces to the south. Moreover, the greater exposure of the ocean surface, and a warmer Arctic atmosphere, means that moist processes are likely to play a greater role in cyclone dynamics in the future. The accelerated warming of the Arctic relative to lower latitudes (i.e. Arctic Amplification) is hypothesised to impact the broader atmospheric circulation, including the mid-latitude jet stream (e.g. Francis and Vavrus, 2015). Future research is needed to understand these changes and their implications for summer-time Arctic cyclone dynamics. Anticipating future changes in Arctic cyclones will be critical for mitigating the risks associated with increased human activity in the summer-time Arctic.

With increasing human activity in the summer-time Arctic will come an increasing demand for accurate forecasts to support operations, with the primary weather hazard being Arctic cyclones. Continued research on the dynamics and impacts of summer-time Arctic cyclones, building on the work presented in this thesis, will be important for obtaining a comprehensive understanding of these weather systems and their prediction, and to guide efforts in ultimately improving weather forecasts.

Appendix A

Appendix to Chapter 5: Linear stability analysis

The following linear stability analysis was formulated by Ben Harvey.

A.1 Adding a perturbation

Consider the case of smooth basic state QGPV profiles, $Q_1(r)$ and $Q_2(r)$ (e.g. as in Figure 5.2). We define general perturbations in the lower layer $\eta_1(a, \phi)$ and upper layer $\eta_2(a, \phi)$ (where a = radial distance and ϕ = angle), as displacements of the QGPV field in polar coordinates where each circular contour $r = a$ is perturbed to $r = a + \eta_1(a, \phi)$ (lower layer) and $r = a + \eta_2(a, \phi)$ (upper layer). Considering each perturbation wavenumber m separately:

$$\eta_1(r, \phi) = \hat{\eta}_1(r)e^{im\phi} \quad \eta_2(r, \phi) = \hat{\eta}_2(r)e^{im\phi} \quad (\text{A.1})$$

The QGPV anomalies associated with these perturbations (to linear accuracy) are then:

$$q'_1(r, \phi) = -\frac{dQ_1}{dr}\hat{\eta}_1(r)e^{im\phi}, \quad q'_2(r, \phi) = -\frac{dQ_2}{dr}\hat{\eta}_2(r)e^{im\phi} \quad (\text{A.2})$$

To invert the QGPV anomalies, we define barotropic and baroclinic components of QGPV, q_{BT} and q_{BC} respectively:

$$q_{BT} = \frac{q_1 + q_2}{2} = \nabla^2\psi_{BT} \quad (\text{A.3})$$

$$q_{BC} = \frac{q_2 - q_1}{2} = \nabla^2 \psi_{BC} - \frac{2\psi_{BC}}{(L_R/L_s)^2} \quad (\text{A.4})$$

This is a mathematical trick to decouple the two-layer QGPV equations, meaning we can solve for the two components separately. We do this using the same Green's function approach as before. For the barotropic component, we put $q_{BT} = \delta(r - r_0)e^{im\phi}$ and try for a solution of the form $\psi_{BT}(r, \phi) = \widehat{\psi}_{BT}(r)e^{im\phi}$. Substituting into Equation (A.3) and solving as before gives:

$$\widehat{\psi}_{BT}(r; r_0) = \widehat{G}_{BT,m}(r; r_0) = -\frac{r_0}{2m} \begin{cases} \left(\frac{r}{r_0}\right)^m & \text{for } r < r_0 \\ \left(\frac{r_0}{r}\right)^m & \text{for } r > r_0 \end{cases} \quad (\text{A.5})$$

Hence, for a general perturbation to the barotropic QGPV of the form $q_{BT} = \widehat{q}_{BT}(r)e^{im\phi}$, the streamfunction is:

$$\psi_{BT}(r) = \int_0^\infty \widehat{q}_{BT}(r_0) \widehat{G}_{BT,m}(r; r_0) dr_0 \quad (\text{A.6})$$

Similarly for the baroclinic component, we put $q_{BC} = \delta(r - r_0)e^{im\phi}$ and try for a solution of the form $\psi_{BC}(r, \phi) = \widehat{\psi}_{BC}(r)e^{im\phi}$ in Equation (A.4):

$$\widehat{\psi}_{BC}(r; r_0) = \widehat{G}_{BC,m}(r; r_0) = -r_0 \begin{cases} K_m \left(\frac{\sqrt{2}r_0}{L_R} \right) I_m \left(\frac{\sqrt{2}r}{(L_R/L_s)} \right) & \text{for } r < r_0 \\ I_m \left(\frac{\sqrt{2}r_0}{L_R} \right) K_m \left(\frac{\sqrt{2}r}{(L_R/L_s)} \right) & \text{for } r > r_0 \end{cases} \quad (\text{A.7})$$

Hence, for a general perturbation to the baroclinic QGPV of the form $q_{BC} = \widehat{q}_{BC}(r)e^{im\phi}$, the streamfunction is:

$$\psi_{BC}(r) = \int_0^\infty \widehat{q}_{BC}(r_0) \widehat{G}_{BC,m}(r; r_0) dr_0 \quad (\text{A.8})$$

Hence, for a general perturbation $\widehat{\eta}_1(r), \widehat{\eta}_2(r)$ the perturbation streamfunction is:

$$\widehat{\psi}_1(r) = \widehat{\psi}_{BT}(r) - \widehat{\psi}_{BC}(r) = \int_0^\infty \widehat{q}_{BT}(r_0) \widehat{G}_{BT,m}(r; r_0) - \widehat{q}_{BC}(r_0) \widehat{G}_{BC,m}(r; r_0) dr_0 \quad (\text{A.9})$$

$$\widehat{\psi}_2(r) = \widehat{\psi}_{BT}(r) + \widehat{\psi}_{BC}(r) = \int_0^\infty \widehat{q}_{BT}(r_0) \widehat{G}_{BT,m}(r; r_0) + \widehat{q}_{BC}(r_0) \widehat{G}_{BC,m}(r; r_0) dr_0 \quad (\text{A.10})$$

where

$$\widehat{q}_{BT}(r) = -\frac{1}{2} \left(\frac{dQ_1}{dr} \widehat{\eta}_1(r) + \frac{dQ_2}{dr} \widehat{\eta}_2(r) \right) \quad (\text{A.11})$$

$$\widehat{q}_{BC}(r) = \frac{1}{2} \left(\frac{dQ_1}{dr} \widehat{\eta}_1(r) - \frac{dQ_2}{dr} \widehat{\eta}_2(r) \right) \quad (\text{A.12})$$

A.2 Time evolution of the perturbation without friction

To get the time evolution of the perturbation, here we derive the linearised contour evolution equation in each layer (i.e. advection of anomalies around the vortex by the basic state wind U , and advection in the radial direction by the perturbation wind v):

$$\frac{Dq_k}{Dt} = 0 \quad \text{where} \quad \frac{D}{Dt} = \frac{\partial}{\partial t} + \frac{U}{r} \frac{\partial}{\partial \phi} + v \frac{\partial}{\partial r} \quad (\text{A.13})$$

and

$$q_k = Q_k(r) - \frac{dQ_k}{dr} \eta_k(r, \phi) \quad (\text{A.14})$$

Substituting Equation (A.14) into Equation (A.13), expanding, and neglecting terms that are products of perturbations gives the linearised contour evolution equation:

$$\frac{\partial \eta_k}{\partial t} + \frac{U_k}{r} \frac{\partial \eta_k}{\partial \phi} = v_k \quad (\text{A.15})$$

We seek a normal-mode solution, with the form $\eta_k = \widehat{\eta}_k e^{i(m\phi - \omega t)}$, $\psi_k = \widehat{\psi}_k e^{i(m\phi - \omega t)}$ where ω is the wave frequency (i.e. assuming that the shape of the perturbation is fixed

with time). Using $v = -\frac{1}{r} \frac{\partial \psi}{\partial \phi}$ gives:

$$\omega \widehat{\eta}_k = \frac{m}{r} \left(\widehat{\psi}_k + U \widehat{\eta}_k \right) \quad (\text{A.16})$$

In general ω will be complex, and it is the imaginary component that indicates wave growth or decay. In practice perturbations do evolve in time so the assumption made is not valid. However, this process is still very useful. These types of equations always exhibit a particular set of solutions which do preserve their shape in time (each with their own ω), and these normal mode solutions are complete, meaning that a general perturbation can be written as a sum of the normal modes. Hence, a basic state profile is stable if and only if all the normal modes have real ω s.

We can find the normal modes and their corresponding ω s numerically on a $N \times N$ grid. Firstly, discretise $\widehat{\eta}_k$ at each grid point $r = j\delta$ for $j = 1, 2, 3, \dots, N$ (where δ is the grid resolution) to give vectors $\vec{\widehat{\eta}}_1$ and $\vec{\widehat{\eta}}_2$. Then the inversion integrals in Equations (A.9)-(A.12) become:

$$\vec{\widehat{\psi}}_1 = M_{11} \vec{\widehat{\eta}}_1 + M_{21} \vec{\widehat{\eta}}_2 \quad (\text{A.17})$$

$$\vec{\widehat{\psi}}_2 = M_{12} \vec{\widehat{\eta}}_1 + M_{22} \vec{\widehat{\eta}}_2 \quad (\text{A.18})$$

where the M s are $N \times N$ matrices that represent discretised versions of the integrals:

$$M_{11}^{yz} = -\frac{1}{2} \frac{dQ_1}{dr}(r_y) \left(\widehat{G}_{BT,m}(r_z; r_y) + \widehat{G}_{BC,m}(r_z; r_y) \right) \delta \quad (\text{A.19})$$

$$M_{21}^{yz} = -\frac{1}{2} \frac{dQ_2}{dr}(r_y) \left(\widehat{G}_{BT,m}(r_z; r_y) - \widehat{G}_{BC,m}(r_z; r_y) \right) \delta \quad (\text{A.20})$$

$$M_{12}^{yz} = -\frac{1}{2} \frac{dQ_1}{dr}(r_y) \left(\widehat{G}_{BT,m}(r_z; r_y) - \widehat{G}_{BC,m}(r_z; r_y) \right) \delta \quad (\text{A.21})$$

$$M_{22}^{yz} = -\frac{1}{2} \frac{dQ_2}{dr}(r_y) \left(\widehat{G}_{BT,m}(r_z; r_y) + \widehat{G}_{BC,m}(r_z; r_y) \right) \delta \quad (\text{A.22})$$

The evolution equation (A.16) then becomes a $2N \times 2N$ matrix equation:

$$\omega \begin{pmatrix} \vec{\widehat{\eta}}_1 \\ \vec{\widehat{\eta}}_2 \end{pmatrix} = \frac{m}{r} \begin{pmatrix} M_{11} + U_{11} & M_{21} \\ M_{12} & M_{22} + U_{22} \end{pmatrix} \begin{pmatrix} \vec{\widehat{\eta}}_1 \\ \vec{\widehat{\eta}}_2 \end{pmatrix} \quad (\text{A.23})$$

where the U s are $N \times N$ diagonal matrices given by:

$$U_{11}^{nm} = \begin{cases} U_1(r_z) & \text{if } y = z \\ 0 & \text{otherwise} \end{cases} \quad (\text{A.24})$$

$$U_{22}^{nm} = \begin{cases} U_2(r_z) & \text{if } y = z \\ 0 & \text{otherwise} \end{cases} \quad (\text{A.25})$$

Equation (A.23) is an eigenvalue equation, which we can solve using the SciPy Python library. There will be $2N \times 2N$ eigenvectors, each with their own eigenvalue ω , and these are the normal modes. We are interested in the fastest growing normal mode, which is the one with the largest imaginary component of ω .

A.3 Time evolution of the perturbation with friction

Friction will act on the perturbation wind in the lower level. The inclusion of Rayleigh friction will change the linearised contour evolution equation in the lower layer since:

$$\frac{Dq_1}{Dt} = -\kappa \nabla^2 \psi_1 \quad (\text{A.26})$$

where κ is the coefficient of friction. Substituting in Equation (A.14) and neglecting terms that are products of perturbations:

$$\frac{\partial \eta_1}{\partial t} + \frac{U_1}{r} \frac{\partial \eta_1}{\partial \phi} = v_1 + \frac{\kappa \nabla^2 \psi_1}{\frac{dQ_1}{dr}} \quad (\text{A.27})$$

whilst the upper-level equation is unchanged. Substituting in $\nabla^2 \psi_1 = q_1 - \frac{\psi_2 - \psi_1}{L_R^2}$ gives:

$$\frac{\partial \eta_1}{\partial t} + \frac{U_1}{r} \frac{\partial \eta_1}{\partial \phi} = v_1 + \frac{\kappa}{\frac{dQ_1}{dr}} \left(q_1 - \frac{\psi_2 - \psi_1}{L_R^2} \right) \quad (\text{A.28})$$

We seek a normal-mode solution with the form $\eta_1 = \hat{\eta}_1 e^{i(m\phi - \omega t)}$, $\psi_1 = \hat{\psi}_1 e^{i(m\phi - \omega t)}$, $\psi_2 = \hat{\psi}_2 e^{i(m\phi - \omega t)}$, and use the fact that $q_1 = -\frac{dQ_1}{dr} \hat{\eta}_1 e^{i(m\phi - \omega t)}$:

$$\omega \hat{\eta}_1 = \frac{m}{r} \left(\hat{\psi}_1 + U \hat{\eta}_1 \right) - i\kappa \left(\hat{\eta}_1 + \frac{\hat{\psi}_2 - \hat{\psi}_1}{\frac{dQ_1}{dr} L_R^2} \right) \quad (\text{A.29})$$

Hence, the discretised evolution equation becomes:

$$\omega \begin{pmatrix} \vec{\hat{\eta}}_1 \\ \vec{\hat{\eta}}_2 \end{pmatrix} = \left[\frac{m}{r} \begin{pmatrix} M_{11} + U_{11} & M_{21} \\ M_{12} & M_{22} + U_{22} \end{pmatrix} - i\kappa \begin{pmatrix} I + \frac{(M_{12}-M_{11})}{\frac{dQ_1}{dr} L_R^2} & \frac{(M_{22}-M_{21})}{\frac{dQ_1}{dr} L_R^2} \\ 0 & 0 \end{pmatrix} \right] \begin{pmatrix} \vec{\hat{\eta}}_1 \\ \vec{\hat{\eta}}_2 \end{pmatrix} \quad (\text{A.30})$$

As in the case of Equation (A.23), this is an eigenvalue equation which can be solved numerically to find ω .

References

- Adamson, D., Belcher, S. E., Hoskins, B. J., & Plant, R. S. (2006). Boundary-layer friction in midlatitude cyclones. *Quart. J. Roy. Meteor. Soc.*, *132*(614), 101–124.
- Ahmadi-Givi, F., Graig, G., & Plant, R. (2004). The dynamics of a midlatitude cyclone with very strong latent-heat release. *Quart. J. Roy. Meteor. Soc.*, *130*(596), 295–323.
- Aizawa, T., & Tanaka, H. (2016). Axisymmetric structure of the long lasting summer Arctic cyclones. *Polar Sci.*, *10*(3), 192–198.
- Andreas, E. L., et al. (1996). *The atmospheric boundary layer over polar marine surfaces*. Cold Regions Research; Engineering Laboratory (US).
- Andreas, E. L., Horst, T. W., Grachev, A. A., Persson, P. O. G., Fairall, C. W., Guest, P. S., & Jordan, R. E. (2010). Parametrizing turbulent exchange over summer sea ice and the marginal ice zone. *Quart. J. Roy. Meteor. Soc.*, *136*(649), 927–943.
- Andrew, R. (2014). *Socio-economic drivers of change in the Arctic*. AMAP technical report no. 9. Arctic Monitoring; Assessment Programme (AMAP).
- Arctic Council. (2009). Arctic marine shipping assessment 2009 report.
- Arctic Portal. (2024). Arctic definitions. <https://arcticportal.org/education/quick-facts/the-arctic/3448-arctic-definitions>
- Arduini, G., Keeley, S., Day, J. J., Sandu, I., Zampieri, L., & Balsamo, G. (2022). On the importance of representing snow over sea-ice for simulating the Arctic boundary layer. *J. Adv. Model. Earth Syst.*, *14*(7), e2021MS002777.
- Aschwanden, A., Fahnestock, M. A., Truffer, M., Brinkerhoff, D. J., Hock, R., Khroulev, C., Mottram, R., & Khan, S. A. (2019). Contribution of the Greenland ice sheet to sea level over the next millennium. *Sci. Adv.*, *5*(6), eaav9396.

-
-
- Asplin, M. G., Galley, R., Barber, D. G., & Prinsenberg, S. (2012). Fracture of summer perennial sea ice by ocean swell as a result of Arctic storms. *J. Geophys. Res. Oceans*, *117*(C6).
- Babin, J., Lasserre, F., & Pic, P. (2020). Arctic shipping and polar seaways. *Encyclopedia of water: Sciences, technology and society*.
- Balan-Sarojini, B., Tietsche, S., Mayer, M., Balmaseda, M., Zuo, H., De Rosnay, P., Stockdale, T., & Vitart, F. (2021). Year-round impact of winter sea ice thickness observations on seasonal forecasts. *The Cryosphere*, *15*, 325–344.
- Balmaseda, M. A., Ferranti, L., Molteni, F., & Palmer, T. N. (2010). Impact of 2007 and 2008 Arctic ice anomalies on the atmospheric circulation: Implications for long-range predictions. *Quart. J. Roy. Meteor. Soc.*, *136*(652), 1655–1664.
- Barry, T., Berteaux, D., Bültmann, H., Christiansen, J. S., Cook, J. A., Dahlberg, A., Daniëls, F. J., Ehrich, D., Fjeldså, J., Fridriksson, F., et al. (2013). *Arctic biodiversity assessment: Status and trends in Arctic biodiversity*. Conservation of Arctic Flora; Fauna (CAFF). <https://oaarchive.arctic-council.org/items/b32baf29-d9d7-4c9e-8598-877db37141da>
- Barton, N., Metzger, E. J., Reynolds, C. A., Ruston, B., Rowley, C., Smedstad, O. M., Ridout, J. A., Wallcraft, A., Frolov, S., Hogan, P., et al. (2021). The Navy's Earth system prediction capability: A new global coupled atmosphere-ocean-sea ice prediction system designed for daily to subseasonal forecasting. *Earth Space Sci.*, *8*(4), e2020EA001199.
- Bird, K. J., Charpentier, R. R., Gautier, D. L., Houseknecht, D. W., Klett, T. R., Pitman, J. K., Moore, T. E., Schenk, C. J., Tennyson, M. E., & Wandrey, C. R. (2008). *Circum-Arctic resource appraisal: Estimates of undiscovered oil and gas north of the Arctic circle* (tech. rep.). US Geological Survey.
- Bjerknes, J. (1919). On the structure of moving cyclones. *Mon. Wea. Rev.*, *47*(2), 95–99.
- Bjerknes, J., & Solberg, H. (1922). Life cycle of cyclones and the polar front theory of atmospheric circulation. *Geophys. Publ.*, *3*, 1–18.
- Boutle, I., Beare, R., Belcher, S. E., & Plant, R. S. (2007). A note on boundary-layer friction in baroclinic cyclones. *Quart. J. Roy. Meteor. Soc.*, *133*(629), 2137–2141.
-
-

-
-
- Boutle, I., Belcher, S. E., & Plant, R. S. (2015). Friction in mid-latitude cyclones: An Ekman-PV mechanism. *Atmos. Sci. Lett.*, *16*(2), 103–109.
- Boutle, I., Belcher, S. E., Plant, R. S., Beare, R., & Brown, A. (2009). *Boundary-layer processes in mid-latitude cyclones* [Doctoral dissertation, University of Reading].
- Box, J. E., Colgan, W. T., Wouters, B., Burgess, D. O., O’Neel, S., Thomson, L. I., & Mernild, S. H. (2018). Global sea-level contribution from Arctic land ice: 1971–2017. *Env. Res. Lett.*, *13*(12), 125012.
- Bretherton, F. P. (1966). Critical layer instability in baroclinic flows. *Quart. J. Roy. Meteor. Soc.*, *92*(393), 325–334.
- Bromaghin, J. F., McDonald, T. L., Stirling, I., Derocher, A. E., Richardson, E. S., Regehr, E. V., Douglas, D. C., Durner, G. M., Atwood, T., & Amstrup, S. C. (2015). Polar bear population dynamics in the southern Beaufort Sea during a period of sea ice decline. *Ecol. Appl.*, *25*(3), 634–651.
- Brown, J., Ferrians, O., Heginbottom, J. A., & Melnikov, E. (2002). Circum-Arctic map of permafrost and ground-ice conditions, version 2 [Date Accessed 04-24-2024]. <https://doi.org/10.7265/skbg-kf16>
- Bui, H., & Spengler, T. (2021). On the influence of sea surface temperature distributions on the development of extratropical cyclones. *J. Atmos. Sci.*, *78*(4), 1173–1188.
- Bushuk, M., Msadek, R., Winton, M., Vecchi, G., Yang, X., Rosati, A., & Gudgel, R. (2019). Regional Arctic sea–ice prediction: Potential versus operational seasonal forecast skill. *Climate Dyn.*, *52*, 2721–2743.
- Capute, P. K., & Torn, R. D. (2021). A comparison of Arctic and Atlantic cyclone predictability. *Mon. Wea. Rev.*, *149*(11), 3837–3849.
- Card, P., & Barcilon, A. (1982). The Charney stability problem with a lower Ekman layer. *J. Atmos. Sci.*, *39*(10), 2128–2137.
- Carton, X., Flierl, G. R., Perrot, X., Meunier, T., & Sokolovskiy, M. A. (2010). Explosive instability of geostrophic vortices. Part 1: Baroclinic instability. *Theor. Comput. Fluid Dyn.*, *24*, 125–130.
- Cavallo, S. M., & Hakim, G. J. (2009). Potential vorticity diagnosis of a tropopause polar cyclone. *Mon. Wea. Rev.*, *137*(4), 1358–1371.
-
-

-
-
- Cavallo, S. M., & Hakim, G. J. (2010). Composite structure of tropopause polar cyclones. *Mon. Wea. Rev.*, *138*(10), 3840–3857.
- Cavallo, S. M., & Hakim, G. J. (2012). Radiative impact on tropopause polar vortices over the Arctic. *Mon. Wea. Rev.*, *140*(5), 1683–1702.
- Cavallo, S. M., & Hakim, G. J. (2013). Physical mechanisms of tropopause polar vortex intensity change. *J. Atmos. Sci.*, *70*(11), 3359–3373.
- Chagnon, J., Gray, S., & Methven, J. (2013). Diabatic processes modifying potential vorticity in a North Atlantic cyclone. *Quart. J. Roy. Meteor. Soc.*, *139*(674), 1270–1282.
- Charney, J. G., & Stern, M. E. (1962). On the stability of internal baroclinic jets in a rotating atmosphere. *J. Atmos. Sci.*, *19*(2), 159–172.
- Chylek, P., Folland, C., Klett, J. D., Wang, M., Hengartner, N., Lesins, G., & Dubey, M. K. (2022). Annual mean Arctic amplification 1970–2020: Observed and simulated by CMIP6 climate models. *Geophys. Res. Lett.*, *49*(13), e2022GL099371.
- Clark, P. A., & Gray, S. L. (2018). Sting jets in extratropical cyclones: A review. *Quart. J. Roy. Meteor. Soc.*, *144*(713), 943–969.
- Comiso, J. C. (2012). Large decadal decline of the Arctic multiyear ice cover. *J. Climate*, *25*(4), 1176–1193.
- Cooper, I. M., Thorpe, A. J., & Bishop, C. H. (1992). The role of diffusive effects on potential vorticity in fronts. *Quart. J. Roy. Meteor. Soc.*, *118*(506), 629–647.
- Crawford, A. D., & Serreze, M. C. (2016). Does the summer Arctic frontal zone influence Arctic ocean cyclone activity? *J. Climate*, *29*(13), 4977–4993.
- Croad, H. L., Keeley, S. P., Methven, J., Harvey, B., & Volonté, A. (2025). Examining the sensitivity of ECMWF IFS weather forecasts to sea-ice coupling for the summer-time arctic and cyclones. *Quart. J. Roy. Meteor. Soc.*, *151*(766), e4899.
- Croad, H. L., Methven, J., Harvey, B., Keeley, S. P. E., & Volonté, A. (2023a). The role of boundary layer processes in summer-time Arctic cyclones. *Wea. Climate Dyn.*, *4*(3), 617–638.
- Croad, H. L., Methven, J., Harvey, B., Keeley, S. P. E., Volonté, A., & Hodges, K. (2023b). A climatology of summer-time Arctic cyclones using a modified phase space. *Geophys. Res. Lett.*, *50*(22), e2023GL105993.
-
-

-
-
- Cullen, M. (2018). The use of semigeostrophic theory to diagnose the behaviour of an atmospheric GCM. *Fluids*, 3(4), 72.
- Davis, C. A., Stoelinga, M. T., & Kuo, Y.-H. (1993). The integrated effect of condensation in numerical simulations of extratropical cyclogenesis. *Mon. Wea. Rev.*, 121(8), 2309–2330.
- Day, J. J., & Hodges, K. I. (2018). Growing land-sea temperature contrast and the intensification of Arctic cyclones. *Geophys. Res. Lett.*, 45(8), 3673–3681.
- Day, J. J., Keeley, S., Arduini, G., Magnusson, L., Mogensen, K., Rodwell, M., Sandu, I., & Tietsche, S. (2022). Benefits and challenges of dynamic sea ice for weather forecasts. *Wea. Climate Dyn.*, 3(3), 713–731.
- Deveson, A., Browning, K., & Hewson, T. (2002). A classification of FASTEX cyclones using a height-attributable quasi-geostrophic vertical-motion diagnostic. *Quart. J. Roy. Meteor. Soc.*, 128(579), 93–117.
- Donlon, C. J., Martin, M., Stark, J., Roberts-Jones, J., Fiedler, E., & Wimmer, W. (2012). The operational sea surface temperature and sea ice analysis (OSTIA) system. *Remote Sens. Env.*, 116, 140–158.
- Durrán, D. R. (2013). *Numerical methods for wave equations in geophysical fluid dynamics* (Vol. 32). Springer Science & Business Media.
- Ebert, E. E., & Curry, J. A. (1993). An intermediate one-dimensional thermodynamic sea ice model for investigating ice-atmosphere interactions. *J. Geophys. Res. Oceans*, 98(C6), 10085–10109.
- ECMWF. (2020). IFS documentation Cy47r1, PART IV: PHYSICAL PROCESSES. <https://www.ecmwf.int/en/elibrary/81189-ifs-documentation-cy47r1-part-iv-physical-processes>
- ECMWF. (2023a). Forecast user guide: Section 2.1.4.8 water-surface temperature and ice concentration. <https://confluence.ecmwf.int/display/FUG/Section+2.1.4.8+Water-surface+temperature+and+ice+concentration>
- ECMWF. (2023b). Forecast user guide: Section 2.2 ocean wave model - ecwam. <https://confluence.ecmwf.int/display/FUG/Section+2.2+Ocean+Wave+Model+-+ECWAM#Section2.2OceanWaveModelECWAM-Nearseaice>
-
-

-
-
- ECMWF. (2023c). IFS documentation Cy48r1, PART IV: PHYSICAL PROCESSES. <https://www.ecmwf.int/en/elibrary/81370-ifs-documentation-cy48r1-part-iv-physical-processes>
- ECMWF. (2024). Forecast user guide: Section 2.1.4.3 modelling ocean surfaces. <https://confluence.ecmwf.int/display/FUG/Section+2.1.4.3+Modelling+ocean+surfaces>
- Elvidge, A. D., Renfrew, I., Weiss, A., Brooks, I., Lachlan-Cope, T., & King, J. (2016). Observations of surface momentum exchange over the marginal ice zone and recommendations for its parametrization. *Atmos. Chem. Phys.*, *16*(3), 1545–1563.
- Elvidge, A. D., Renfrew, I. A., Brooks, I. M., Srivastava, P., Yelland, M. J., & Prytherch, J. (2021). Surface heat and moisture exchange in the marginal ice zone: Observations and a new parameterization scheme for weather and climate models. *J. Geophys. Res. Atmos.*, *126*(17), e2021JD034827.
- Elvidge, A. D., Renfrew, I. A., Edwards, J. M., Brooks, I. M., Srivastava, P., & Weiss, A. I. (2023). Improved simulation of the polar atmospheric boundary layer by accounting for aerodynamic roughness in the parameterization of surface scalar exchange over sea ice. *J. Adv. Model. Earth Syst.*, *15*(3), e2022MS003305.
- Emanuel, K. A., & Rotunno, R. (1989). Polar lows as arctic hurricanes. *Tellus A: Dyn. Meteor. and Oceanogr.*, *41*(1), 1–17.
- Ertel, H. (1942). Ein neuer hydrodynamischer wirbelsatz. *Meteor. Z.*, *59*, 277–282.
- Fearon, M. G., Doyle, J. D., & Finocchio, P. M. (2023). Soil moisture influences on summer Arctic cyclones and their associated poleward moisture transport. *Mon. Wea. Rev.*, *151*(7), 1699–1716.
- Flierl, G. R. (1978). Models of vertical structure and the calibration of two-layer models. *Dyn. Atmos. Oceans*, *2*(4), 341–381.
- Flierl, G. R. (1988). On the instability of geostrophic vortices. *J. Fluid Mech.*, *197*, 349–388.
- Francis, J. A., & Vavrus, S. J. (2015). Evidence for a wavier jet stream in response to rapid arctic warming. *Env. Res. Lett.*, *10*(1), 014005.
- Froude, L. S. (2010). TIGGE: Comparison of the prediction of Northern Hemisphere extratropical cyclones by different ensemble prediction systems. *Wea. Forecasting*, *25*(3), 819–836.
-
-

-
-
- Froude, L. S. (2011). TIGGE: Comparison of the prediction of Southern Hemisphere extratropical cyclones by different ensemble prediction systems. *Wea. Forecasting*, 26(3), 388–398.
- Gautier, D. L., Bird, K. J., Charpentier, R. R., Grantz, A., Houseknecht, D. W., Klett, T. R., Moore, T. E., Pitman, J. K., Schenk, C. J., Schuenemeyer, J. H., et al. (2009). Assessment of undiscovered oil and gas in the Arctic. *Science*, 324(5931), 1175–1179.
- Goessling, H. F., Tietsche, S., Day, J. J., Hawkins, E., & Jung, T. (2016). Predictability of the Arctic sea ice edge. *Geophys. Res. Lett.*, 43(4), 1642–1650.
- Graham, R. M., Rinke, A., Cohen, L., Hudson, S. R., Walden, V. P., Granskog, M. A., Dorn, W., Kayser, M., & Maturilli, M. (2017). A comparison of the two Arctic atmospheric winter states observed during N-ICE2015 and SHEBA. *J. Geophys. Res. Atmos.*, 122(11), 5716–5737.
- Gray, S. L., Hodges, K. I., Vautrey, J. L., & Methven, J. (2021). The role of tropopause polar vortices in the intensification of summer Arctic cyclones. *Wea. Climate Dyn.*, 2(4), 1303–1324.
- Gray, S. L., & Dacre, H. F. (2006). Classifying dynamical forcing mechanisms using a climatology of extratropical cyclones. *Quart. J. Roy. Meteor. Soc.*, 132(617), 1119–1137.
- Guemas, V., Blanchard-Wrigglesworth, E., Chevallier, M., Day, J. J., Déqué, M., Doblans-Reyes, F. J., Fučkar, N. S., Germe, A., Hawkins, E., Keeley, S., et al. (2016). A review on Arctic sea-ice predictability and prediction on seasonal to decadal time-scales. *Quart. J. Roy. Meteor. Soc.*, 142(695), 546–561.
- Guest, P. S., & Davidson, K. L. (1991). The aerodynamic roughness of different types of sea ice. *J. Geophys. Res. Oceans*, 96(C3), 4709–4721.
- Hart, R. E. (2003). A cyclone phase space derived from thermal wind and thermal asymmetry. *Mon. Wea. Rev.*, 131(4), 585–616.
- Harvey, B., Methven, J., & Ambaum, M. H. (2018). An adiabatic mechanism for the reduction of jet meander amplitude by potential vorticity filamentation. *J. Atmos. Sci.*, 75(12), 4091–4106.
-
-

-
-
- Hualand, K. F., & Spengler, T. (2020). Direct and indirect effects of surface fluxes on moist baroclinic development in an idealized framework. *J. Atmos. Sci.*, *77*(9), 3211–3225.
- Hauser, D. D., Whiting, A. V., Mahoney, A. R., Goodwin, J., Harris, C., Schaeffer, R. J., Schaeffer, R., Laxague, N. J., Subramaniam, A., Witte, C. R., et al. (2021). Co-production of knowledge reveals loss of indigenous hunting opportunities in the face of accelerating Arctic climate change. *Env. Res. Lett.*, *16*(9), 095003.
- Haynes, P. H., & McIntyre, M. E. (1987). On the evolution of vorticity and potential vorticity in the presence of diabatic heating and frictional or other forces. *J. Atmos. Sci.*, *44*(5), 828–841.
- Haynes, P. H., & McIntyre, M. (1990). On the conservation and impermeability theorems for potential vorticity. *J. Atmos. Sci.*, *47*(16), 2021–2031.
- Heifetz, E., Bishop, C., Hoskins, B., & Methven, J. (2004). The counter-propagating Rossby-wave perspective on baroclinic instability. I: Mathematical basis. *Quart. J. Roy. Meteor. Soc.*, *130*(596), 211–231.
- Hersbach, H., Bell, B., Berrisford, P., Hirahara, S., Horányi, A., Muñoz-Sabater, J., Nicolas, J., Peubey, C., Radu, R., Schepers, D., et al. (2017). Complete ERA5 from 1979: Fifth generation of ECMWF atmospheric reanalyses of the global climate [(Accessed on 24-06-22)].
- Hersbach, H., Bell, B., Berrisford, P., Hirahara, S., Horányi, A., Muñoz-Sabater, J., Nicolas, J., Peubey, C., Radu, R., Schepers, D., et al. (2020). The ERA5 global reanalysis. *Quart. J. Roy. Meteor. Soc.*, *146*(730), 1999–2049.
- High North News. (2021). *Early winter freeze traps ships in Arctic ice, highlighting weak safety regime*. Retrieved April 21, 2024, from <https://www.highnorthnews.com/en/early-winter-freeze-traps-ships-arctic-ice-highlighting-weak-safety-regime>
- Hodges, K. (1994). A general method for tracking analysis and its application to meteorological data. *Mon. Wea. Rev.*, *122*(11), 2573–2586.
- Hodges, K. (1995). Feature tracking on the unit sphere. *Mon. Wea. Rev.*, *123*(12), 3458–3465.
- Hodges, K. (2021). TRACK tracking and analysis system for weather, climate and ocean data. <https://gitlab.act.reading.ac.uk/track/track>
-
-

-
-
- Holton, J., & Hakim, G. (2012). *An introduction to dynamic meteorology (5th edition)*. Elsevier.
- Hoskins, B. J., & James, I. N. (2014). *Fluid dynamics of the mid-latitude atmosphere*. John Wiley & Sons.
- Hoskins, B. J., McIntyre, M. E., & Robertson, A. W. (1985). On the use and significance of isentropic potential vorticity maps. *Quart. J. Roy. Meteor. Soc.*, *111*(470), 877–946.
- Inoue, J., & Hori, M. E. (2011). Arctic cyclogenesis at the marginal ice zone: A contributory mechanism for the temperature amplification? *Geophys. Res. Lett.*, *38*(12).
- Irrgang, A. M., Lantuit, H., Gordon, R. R., Piskor, A., & Manson, G. K. (2019). Impacts of past and future coastal changes on the Yukon coast—threats for cultural sites, infrastructure, and travel routes. *Arctic Sci.*, *5*(2), 107–126.
- Isaev, V., Koshurnikov, A., Pogorelov, A., Amangurov, R., Podchasov, O., Sergeev, D., Buldovich, S., Aleksyutina, D., Grishakina, E., & Kioka, A. (2019). Cliff retreat of permafrost coast in south-west Baydaratskaya Bay, Kara Sea, during 2005–2016. *Permafrost Periglac. Process.*, *30*(1), 35–47.
- Jaskólski, M. W. (2021). For human activity in Arctic coastal environments—a review of selected interactions and problems. *Miscellanea Geographica*, *25*(2), 127–143.
- Jung, T., Gordon, N., Klebe, S., Bauer, P., Bromwich, D., Day, J., Doblus-Reyes, F., Fairall, C., Hines, K., Holland, M., Iversen, T., Lemke, P., Mills, B., Nurmi, P., Renfrew, I., Smith, G., Svensson, G., & Tolstykh, M. (2013). WWRP Polar Prediction Project: Implementation Plan. *WWRP/PPP No. 2*. <https://library.wmo.int/records/item/49973-wwrp-polar-prediction-project-implementation-plan?offset=2241>
- Jung, T., Kasper, M. A., Semmler, T., & Serrar, S. (2014). Arctic influence on subseasonal midlatitude prediction. *Geophys. Res. Lett.*, *41*(10), 3676–3680.
- Jung, T., & Matsueda, M. (2016). Verification of global numerical weather forecasting systems in polar regions using TIGGE data. *Quart. J. Roy. Meteor. Soc.*, *142*(695), 574–582.
-
-

-
-
- Karjalainen, O., Aalto, J., Luoto, M., Westermann, S., Romanovsky, V. E., Nelson, F. E., Etzelmüller, B., & Hjort, J. (2019). Circumpolar permafrost maps and geohazard indices for near-future infrastructure risk assessments. *Scientific Data*, *6*(1), 1–16.
- Keeley, S., & Mogensen, K. (2018). Dynamic sea ice in the IFS. *ECMWF Newsletter*, *156*, 23–29.
- Laidre, K. L., Born, E. W., Atkinson, S. N., Wiig, Ø., Andersen, L. W., Lunn, N. J., Dyck, M., Regehr, E. V., McGovern, R., & Heagerty, P. (2018). Range contraction and increasing isolation of a polar bear subpopulation in an era of sea-ice loss. *Ecol. Evol.*, *8*(4), 2062–2075.
- Lawrence, H., Bormann, N., Sandu, I., Day, J., Farnan, J., & Bauer, P. (2019). Use and impact of Arctic observations in the ECMWF numerical weather prediction system. *Quart. J. Roy. Meteor. Soc.*, *145*(725), 3432–3454.
- Li, X., Otsuka, N., & Brigham, L. W. (2021). Spatial and temporal variations of recent shipping along the Northern Sea Route. *Polar Sci.*, *27*, 100569.
- Liu, A., Moore, G., Tsuboki, K., & Renfrew, I. (2006). The effect of the sea-ice zone on the development of boundary-layer roll clouds during cold air outbreaks. *Boundary-layer Meteor.*, *118*, 557–581.
- Lukovich, J. V., Stroeve, J. C., Crawford, A., Hamilton, L., Tsamados, M., Heorton, H., & Massonnet, F. (2021). Summer extreme cyclone impacts on Arctic sea ice. *J. Climate*, *34*(12), 4817–4834.
- Lüpkes, C., & Birnbaum, G. (2005). Surface drag in the Arctic marginal sea-ice zone: A comparison of different parameterisation concepts. *Boundary-layer Meteor.*, *117*(2), 179–211.
- Lüpkes, C., Gryanik, V. M., Hartmann, J., & Andreas, E. L. (2012). A parametrization, based on sea ice morphology, of the neutral atmospheric drag coefficients for weather prediction and climate models. *J. Geophys. Res. Atmos.*, *117*(D13).
- Martínez-Alvarado, O., Gray, S. L., & Methven, J. (2016). Diabatic processes and the evolution of two contrasting summer extratropical cyclones. *Mon. Wea. Rev.*, *144*(9), 3251–3276.
-
-

-
-
- McGraw, M. C., Blanchard-Wrigglesworth, E., Clancy, R. P., & Bitz, C. M. (2022). Understanding the forecast skill of rapid Arctic sea ice loss on subseasonal time scales. *J. Climate*, *35*(4), 1179–1196.
- Meier, W. N., Hovelsrud, G. K., Van Oort, B. E., Key, J. R., Kovacs, K. M., Michel, C., Haas, C., Granskog, M. A., Gerland, S., Perovich, D. K., et al. (2014). Arctic sea ice in transformation: A review of recent observed changes and impacts on biology and human activity. *Rev. Geophys.*, *52*(3), 185–217.
- Meier, W. N., & Stroeve, J. (2022). An updated assessment of the changing Arctic sea ice cover. *Oceanography*, *35*(3/4), 10–19.
- Melia, N., Haines, K., & Hawkins, E. (2016). Sea ice decline and 21st century trans-Arctic shipping routes. *Geophys. Res. Lett.*, *43*(18), 9720–9728.
- Meredith, M., Sommerkorn, M., Cassotta, S., Derksen, C., Ekaykin, A., Hollowed, A., Kofinas, G., Mackintosh, A., Melbourne-Thomas, J., Muelbert, M. M. C., Ottersen, G., Pritchard, H., & Schuur, E. A. G. (2019). Polar regions. In H.-O. Pörtner, D. C. Roberts, V. Masson-Delmotte, P. Zhai, M. Tignor, E. Poloczanska, K. Mintenbeck, A. Alegría, M. Nicolai, A. Okem, J. Petzold, B. Rama, & N. M. Weyer (Eds.), *IPCC special report on the ocean and cryosphere in a changing climate* (pp. 203–320). Cambridge University Press. <https://doi.org/10.1017/9781009157964.005>
- Mohammadi-Aragh, M., Goessling, H., Losch, M., Hutter, N., & Jung, T. (2018). Predictability of Arctic sea ice on weather time scales. *Scientific reports*, *8*(1), 6514.
- Moreno-Ibáñez, M., Laprise, R., & Gachon, P. (2021). Recent advances in polar low research: Current knowledge, challenges and future perspectives. *Tellus A: Dyn. Meteor. and Oceanogr.*, *73*(1), 1–31.
- Naakka, T., Nygård, T., Tjernström, M., Vihma, T., Pirazzini, R., & Brooks, I. M. (2019). The impact of radiosounding observations on numerical weather prediction analyses in the Arctic. *Geophys. Res. Lett.*, *46*(14), 8527–8535.
- National Snow and Ice Data Center. (2023). *The sun sets on the arctic melt season*. Retrieved April 21, 2024, from <https://nsidc.org/sea-ice-today/analyses/sun-sets-arctic-melt-season>
-
-

-
-
- Nicu, I. C., Stalsberg, K., Rubensdotter, L., Martens, V. V., & Flyen, A.-C. (2020). Coastal erosion affecting cultural heritage in Svalbard. a case study in Hiorthhamn (Adventfjorden)—an abandoned mining settlement. *Sustainability*, *12*(6), 2306.
- Nordregio. (2019). *Components of the cryosphere in the Arctic*. Retrieved April 21, 2024, from <https://nordregio.org/maps/components-of-the-cryosphere-in-the-arctic/>
- Notz, D. (2012). Challenges in simulating sea ice in Earth system models. *Wiley Interdisciplinary Reviews: Climate Change*, *3*(6), 509–526.
- Notz, D., & Stroeve, J. (2018). The trajectory towards a seasonally ice-free Arctic Ocean. *Current climate change reports*, *4*, 407–416.
- Overland, J. E., & Wang, M. (2013). When will the summer Arctic be nearly sea ice free? *Geophys. Res. Lett.*, *40*(10), 2097–2101.
- Pedlosky, J. (1964). The stability of currents in the atmosphere and the ocean: Part i. *J. Atmos. Sci.*, *21*(2), 201–219.
- Pedlosky, J. (1987). *Geophysical fluid dynamics*. Springer Science & Business Media.
- Pedregosa, F., Varoquaux, G., Gramfort, A., Michel, V., Thirion, B., Grisel, O., Blondel, M., Prettenhofer, P., Weiss, R., Dubourg, V., Vanderplas, J., Passos, A., Cournapeau, D., Brucher, M., Perrot, M., & Duchesnay, E. (2011). Scikit-learn: Machine learning in Python. *J. Mach. Learn. Res.*, *12*, 2825–2830.
- Pellerin, P., Ritchie, H., Saucier, F. J., Roy, F., Desjardins, S., Valin, M., & Lee, V. (2004). Impact of a two-way coupling between an atmospheric and an ocean-ice model over the Gulf of St. Lawrence. *Mon. Wea. Rev.*, *132*(6), 1379–1398.
- Peng, L., Zhang, X., Kim, J.-H., Cho, K.-H., Kim, B.-M., Wang, Z., & Tang, H. (2021). Role of intense Arctic storm in accelerating summer sea ice melt: An in situ observational study. *Geophys. Res. Lett.*, *48*(8), e2021GL092714.
- Perovich, D. K., & Polashenski, C. (2012). Albedo evolution of seasonal Arctic sea ice. *Geophys. Res. Lett.*, *39*(8).
- Persson, O., & Vihma, T. (2017). The atmosphere over sea ice. *Sea ice*, 160–196.
- Persson, P. O. G., Fairall, C. W., Andreas, E. L., Guest, P. S., & Perovich, D. K. (2002). Measurements near the atmospheric surface flux group tower at SHEBA: Near-surface conditions and surface energy budget. *J. Geophys. Res. Oceans*, *107*(C10), SHE-21.
-
-

-
-
- Peterson, K. A., Smith, G. C., Lemieux, J.-F., Roy, F., Buehner, M., Caya, A., Houtekamer, P. L., Lin, H., Muncaster, R., Deng, X., et al. (2022). Understanding sources of Northern Hemisphere uncertainty and forecast error in a medium-range coupled ensemble sea-ice prediction system. *Quart. J. Roy. Meteor. Soc.*, *148*(747), 2877–2902.
- Petterssen, S., & Smebye, S. (1971). On the development of extratropical cyclones. *Quart. J. Roy. Meteor. Soc.*, *97*(414), 457–482.
- Phillips, N. A. (1954). Energy transformations and meridional circulations associated with simple baroclinic waves in a two-level, quasi-geostrophic model. *Tellus*, *6*(3), 274–286.
- Pithan, F., Svensson, G., Caballero, R., Chechin, D., Cronin, T. W., Ekman, A. M., Neggers, R., Shupe, M. D., Solomon, A., Tjernström, M., et al. (2018). Role of air-mass transformations in exchange between the Arctic and mid-latitudes. *Nat. Geosci.*, *11*(11), 805–812.
- Plant, R., & Belcher, S. (2007). Numerical simulation of baroclinic waves with a parameterized boundary layer. *J. Atmos. Sci.*, *64*(12), 4383–4399.
- Plant, R., Craig, G. C., & Gray, S. (2003). On a threefold classification of extratropical cyclogenesis. *Quart. J. Roy. Meteor. Soc.*, *129*(594), 2989–3012.
- Rantanen, M., Karpechko, A. Y., Lipponen, A., Nordling, K., Hyvärinen, O., Ruosteenoja, K., Vihma, T., & Laaksonen, A. (2022). The Arctic has warmed nearly four times faster than the globe since 1979. *Commun. Earth & Environ.*, *3*(1), 168.
- Renfrew, I. A., Elvidge, A. D., & Edwards, J. M. (2019). Atmospheric sensitivity to marginal-ice-zone drag: Local and global responses. *Quart. J. Roy. Meteor. Soc.*, *145*(720), 1165–1179.
- Renfrew, I. A., & Moore, G. (1999). An extreme cold-air outbreak over the Labrador Sea: Roll vortices and air–sea interaction. *Mon. Wea. Rev.*, *127*(10), 2379–2394.
- Rhines, P. B. (1975). Waves and turbulence on a beta-plane. *J. Fluid Mech.*, *69*(3), 417–443.
- Rolph, R. J., Feltham, D. L., & Schröder, D. (2020). Changes of the Arctic marginal ice zone during the satellite era. *The Cryosphere*, *14*(6), 1971–1984.
-
-

-
-
- Rossby, C.-G. (1940). Planetary flow patterns in the atmosphere. *Quart. J. Roy. Meteor. Soc.*, 66, 68–87.
- Saffin, L., Methven, J., & Gray, S. (2016). The non-conservation of potential vorticity by a dynamical core compared with the effects of parametrized physical processes. *Quart. J. Roy. Meteor. Soc.*, 142(696), 1265–1275.
- Saffin, L., Methven, J., Bland, J., Harvey, B., & Sanchez, C. (2021). Circulation conservation in the outflow of warm conveyor belts and consequences for Rossby wave evolution. *Quart. J. Roy. Meteor. Soc.*, 147(740), 3587–3610.
- Sandu, I., & Bauer, P. (2018). Improving prediction and climate monitoring of polar regions—challenges and priorities. *ECMWF Science Blog*. <https://www.ecmwf.int/en/about/mediacentre/science-blog/2018/improving-prediction-and-climate-monitoring-polar-regions>
- Schultz, D. M., Keyser, D., & Bosart, L. F. (1998). The effect of large-scale flow on low-level frontal structure and evolution in midlatitude cyclones. *Mon. Wea. Rev.*, 126(7), 1767–1791.
- Schultz, D. M., & Vaughan, G. (2011). Occluded fronts and the occlusion process: A fresh look at conventional wisdom. *Bull. Amer. Meteor. Soc.*, 92(4), 443–466.
- Schuur, E. A., McGuire, A. D., Schädel, C., Grosse, G., Harden, J. W., Hayes, D. J., Hugelius, G., Koven, C. D., Kuhry, P., Lawrence, D. M., et al. (2015). Climate change and the permafrost carbon feedback. *Nature*, 520(7546), 171–179.
- Screen, J. A. (2013). Influence of Arctic sea ice on European summer precipitation. *Env. Res. Lett.*, 8(4), 044015.
- Serreze, M. C., Lynch, A. H., & Clark, M. P. (2001). The Arctic frontal zone as seen in the NCEP-NCAR reanalysis. *J. Climate*, 14(7), 1550–1567.
- Shapiro, M. A., & Keyser, D. (1990). Fronts, jet streams and the tropopause. In C. W. Newton & E. O. Holopainen (Eds.), *Extratropical cyclones: The erik palmén memorial volume* (pp. 167–191). American Meteorological Society. https://doi.org/10.1007/978-1-944970-33-8_10
- Simmonds, I., & Keay, K. (2009). Extraordinary September Arctic sea ice reductions and their relationships with storm behavior over 1979–2008. *Geophys. Res. Lett.*, 36(19).
-
-

-
-
- Simmonds, I., & Rudeva, I. (2012). The great Arctic cyclone of August 2012. *Geophys. Res. Lett.*, *39*(23).
- Smith, G. C., Bélanger, J.-M., Roy, F., Pellerin, P., Ritchie, H., Onu, K., Roch, M., Zadra, A., Colan, D. S., Winter, B., et al. (2018). Impact of coupling with an ice–ocean model on global medium-range NWP forecast skill. *Mon. Wea. Rev.*, *146*(4), 1157–1180.
- Smith, G. C., Roy, F., & Brasnett, B. (2013). Evaluation of an operational ice–ocean analysis and forecasting system for the Gulf of St Lawrence. *Quart. J. Roy. Meteor. Soc.*, *139*(671), 419–433.
- Spensberger, C., & Spengler, T. (2021). Sensitivity of air-sea heat exchange in cold-air outbreaks to model resolution and sea-ice distribution. *J. Geophys. Res. Atmos.*, *126*(5), e2020JD033610.
- Srivastava, P., Brooks, I. M., Prytherch, J., Salisbury, D. J., Elvidge, A. D., Renfrew, I. A., & Yelland, M. J. (2022). Ship-based estimates of momentum transfer coefficient over sea ice and recommendations for its parameterization. *Atmos. Chem. Phys.*, *22*(7), 4763–4778.
- Stephenson, S. R., Smith, L. C., & Agnew, J. A. (2011). Divergent long-term trajectories of human access to the Arctic. *Nat. Climate Change*, *1*(3), 156–160.
- Stern, D. P., Doyle, J. D., Barton, N. P., Finocchio, P. M., Komaromi, W. A., & Metzger, E. J. (2020). The impact of an intense cyclone on short-term sea ice loss in a fully coupled atmosphere-ocean-ice model. *Geophys. Res. Lett.*, *47*(4), e2019GL085580.
- Stoelinga, M. T. (1996). A potential vorticity-based study of the role of diabatic heating and friction in a numerically simulated baroclinic cyclone. *Mon. Wea. Rev.*, *124*(5), 849–874.
- Strong, C., & Rigor, I. G. (2013). Arctic marginal ice zone trending wider in summer and narrower in winter. *Geophys. Res. Lett.*, *40*(18), 4864–4868.
- Stull, R. B. (1988). *An introduction to boundary layer meteorology* (Vol. 13). Springer Science & Business Media.
- Tanaka, H. L., Yamagami, A., & Takahashi, S. (2012). The structure and behavior of the Arctic cyclone in summer analyzed by the JRA-25/JCDAS data. *Polar Sci.*, *6*(1), 55–69.
-
-

-
-
- Tao, W., Zhang, J., & Zhang, X. (2017). The role of stratosphere vortex downward intrusion in a long-lasting late-summer Arctic storm. *Quart. J. Roy. Meteor. Soc.*, *143*(705), 1953–1966.
- Terpstra, A., Spengler, T., & Moore, R. W. (2015). Idealised simulations of polar low development in an Arctic moist-baroclinic environment. *Quart. J. Roy. Meteor. Soc.*, *141*(691), 1987–1996.
- The Barents Observer. (2021). *A critical situation might be in the making on the northern sea route*. Retrieved April 21, 2024, from <https://thebarentsobserver.com/en/arctic/2021/11/critical-situation-might-be-making-northern-sea-route>
- Thomson, J., & Rogers, W. E. (2014). Swell and sea in the emerging Arctic ocean. *Geophys. Res. Lett.*, *41*(9), 3136–3140.
- Tjernström, M., Shupe, M. D., Brooks, I. M., Achtert, P., Prytherch, J., & Sedlar, J. (2019). Arctic summer airmass transformation, surface inversions, and the surface energy budget. *J. Climate*, *32*(3), 769–789.
- Tjernström, M., Svensson, G., Magnusson, L., Brooks, I. M., Prytherch, J., Vüllers, J., & Young, G. (2021). Central Arctic weather forecasting: Confronting the ECMWF IFS with observations from the Arctic Ocean 2018 expedition. *Quart. J. Roy. Meteor. Soc.*, *147*(735), 1278–1299.
- UK Research and Innovation. (2024). Arctic summer-time cyclones: Dynamics and sea-ice interaction [Accessed: 2024-06-27]. <https://gtr.ukri.org/projects?ref=NE%2FT006773%2F1>
- U.S. National Ice Center, Fetterer, F., Savoie, M., Helfrich, S., & Clemente-Colón, P. (2010). Multisensor analyzed sea ice extent - Northern Hemisphere (MASIE-NH), version 1 [Date Accessed 04-24-2024]. <https://doi.org/10.7265/N5GT5K3K>
- Valdes, P. J., & Hoskins, B. J. (1988). Baroclinic instability of the zonally averaged flow with boundary layer damping. *J. Atmos. Sci.*, *45*(10), 1584–1593.
- Valkonen, E., Cassano, J., & Cassano, E. (2021). Arctic cyclones and their interactions with the declining sea ice: A recent climatology. *J. Geophys. Res. Atmos.*, *126*(12), e2020JD034366.
- Vallis, G. K. (2017). *Atmospheric and oceanic fluid dynamics*. Cambridge University Press.
-
-

-
-
- Vanni re, B., Czaja, A., Dacre, H., Woollings, T., & Parfitt, R. (2016). A potential vorticity signature for the cold sector of winter extratropical cyclones. *Quart. J. Roy. Meteor. Soc.*, *142*(694), 432–442.
- Vessey, A. F., Hodges, K. I., Shaffrey, L. C., & Day, J. J. (2022). The composite development and structure of intense synoptic-scale Arctic cyclones. *Wea. Climate Dyn.*, *3*(3), 1097–1112.
- Vessey, A. F., Hodges, K. I., Shaffrey, L. C., & Day, J. J. (2020). An inter-comparison of Arctic synoptic scale storms between four global reanalysis datasets. *Climate Dyn.*, *54*(5), 2777–2795.
- Wang, C., Graham, R. M., Wang, K., Gerland, S., & Granskog, M. A. (2019). Comparison of ERA5 and ERA-Interim near-surface air temperature, snowfall and precipitation over Arctic sea ice: Effects on sea ice thermodynamics and evolution. *The Cryosphere*, *13*(6), 1661–1679.
- Wang, Z., Walsh, J., Szymborski, S., & Peng, M. (2020). Rapid Arctic sea ice loss on the synoptic time scale and related atmospheric circulation anomalies. *J. Climate*, *33*(5), 1597–1617.
- Waseda, T., Nose, T., Kodaira, T., Sasmal, K., & Webb, A. (2021). Climatic trends of extreme wave events caused by Arctic cyclones in the western Arctic ocean. *Polar Sci.*, *27*, 100625.
- Waseda, T., Webb, A., Sato, K., Inoue, J., Kohout, A., Penrose, B., & Penrose, S. (2018). Correlated increase of high ocean waves and winds in the ice-free waters of the Arctic ocean. *Scientific reports*, *8*(1), 1–9.
- Wessl n, C., Tjernstr m, M., Bromwich, D., De Boer, G., Ekman, A. M., Bai, L.-S., & Wang, S.-H. (2014). The Arctic summer atmosphere: An evaluation of reanalyses using ASCOS data. *Atmos. Chem. Phys.*, *14*(5), 2605–2624.
- Williams, G. P., & Robinson, J. B. (1974). Generalized Eady waves with Ekman pumping. *J. Atmos. Sci.*, *31*(7), 1768–1776.
- Woollings, T., Li, C., Drouard, M., Dunn-Sigouin, E., Elme stekawy, K. A., Hell, M., Hoskins, B., Mbengue, C., Patterson, M., & Spengler, T. (2023). The role of Rossby waves in polar weather and climate. *Wea. Climate Dyn.*, *4*(1), 61–80.
-
-

-
-
- Xiu, Y., Luo, H., Yang, Q., Tietsche, S., Day, J., & Chen, D. (2022). The challenge of Arctic sea ice thickness prediction by ECMWF on subseasonal time scales. *Geophys. Res. Lett.*, *49*(8), e2021GL097476.
- Yamagami, A., Matsueda, M., & Tanaka, H. L. (2017). Extreme Arctic cyclone in August 2016. *Atmos. Sci. Lett.*, *18*(7), 307–314.
- Yamagami, A., Matsueda, M., & Tanaka, H. L. (2018a). Medium-range forecast skill for extraordinary Arctic cyclones in summer of 2008–2016. *Geophys. Res. Lett.*, *45*(9), 4429–4437.
- Yamagami, A., Matsueda, M., & Tanaka, H. L. (2018b). Predictability of the 2012 great Arctic cyclone on medium-range timescales. *Polar Sci.*, *15*, 13–23.
- Zampieri, L., Goessling, H. F., & Jung, T. (2018). Bright prospects for Arctic sea ice prediction on subseasonal time scales. *Geophys. Res. Lett.*, *45*(18), 9731–9738.
- Zhang, J., Lindsay, R., Schweiger, A., & Steele, M. (2013). The impact of an intense summer cyclone on 2012 Arctic sea ice retreat. *Geophys. Res. Lett.*, *40*(4), 720–726.
- Zhang, X., Tang, H., Zhang, J., Walsh, J. E., Roesler, E. L., Hillman, B., Ballinger, T. J., & Weijer, W. (2023). Arctic cyclones have become more intense and longer-lived over the past seven decades. *Commun. Earth & Environ.*, *4*(1), 348.
- Zhang, X., Walsh, J. E., Zhang, J., Bhatt, U. S., & Ikeda, M. (2004). Climatology and interannual variability of Arctic cyclone activity: 1948–2002. *J. Climate*, *17*(12), 2300–2317.
- Zuo, H., Balmaseda, M. A., Tietsche, S., Mogensen, K., & Mayer, M. (2019). The ECMWF operational ensemble reanalysis–analysis system for ocean and sea ice: A description of the system and assessment. *Ocean Sci.*, *15*(3), 779–808.